



HAL
open science

Prototyping of in-situ optical methods to characterize organic molecular crystals

Simon Clevers

► **To cite this version:**

Simon Clevers. Prototyping of in-situ optical methods to characterize organic molecular crystals. Analytical chemistry. Université de rouen, 2014. English. NNT : . tel-01957285

HAL Id: tel-01957285

<https://theses.hal.science/tel-01957285>

Submitted on 17 Dec 2018

HAL is a multi-disciplinary open access archive for the deposit and dissemination of scientific research documents, whether they are published or not. The documents may come from teaching and research institutions in France or abroad, or from public or private research centers.

L'archive ouverte pluridisciplinaire **HAL**, est destinée au dépôt et à la diffusion de documents scientifiques de niveau recherche, publiés ou non, émanant des établissements d'enseignement et de recherche français ou étrangers, des laboratoires publics ou privés.



Normandie Université

PhD THESIS

In view to obtain the degree of Doctor of Philosophy in Sciences

Materials Chemistry

Submitted to the Faculty of Sciences - University of Rouen Normandie in partial fulfilment of the requirements for the degree

Prototyping of *in-situ* optical methods to characterize organic molecular crystals

Presented and defended by
Simon CLEVERS

Defended the October, 29th 2014

in front of the dissertation committee composed of

M. Yves Geerts	Pr. Université Libre de Bruxelles	Reviewer
M. Jürg Hulliger	Pr. Université de Bern	Reviewer
M. Claude Lecomte	Pr. Université de Lorraine	Reviewer
M. Jean Marie Le Breton	Pr. Université de Rouen Normandie	Co-Supervisor
Mme. Valérie DUPRAY	Maître de Conférences. Université de Rouen Normandie	Co-supervisor
M. Gérard COQUEREL	Pr. SMS Université de Rouen Normandie	President

Supervised by Jean Marie LE BRETON and Valérie DUPRAY, Laboratory Sciences et Méthodes Séparatives (SMS)



Acknowledgments

First, I want to thank Professor Gérard Coquerel for allowing me to do my thesis in the SMS laboratory but also for making me discover a part of science that had so far escaped me. Thank you for sharing with me your knowledge on heterogeneous equilibria but also your vision of science and anecdotes! I'm not a big talker but I come away enriched by the interactions we have had.

I thank Dr. Valerie Dupray, the optician of the laboratory, who gave me his knowledge in nonlinear optics. I discovered a person with whom it was immediately easy to talk. Her advice, criticism and ideas were during those three years a source of inspiration and a force for successful work.

In this adventure, I also have to thank Dr. Virginia Nachbaur who was my Master 2 supervisor and Professor Jean-Marie Le Breton (Director of the Magnetism Team in the GPM Laboratory). The story can not be change, but in a parallel universe (without executive and delivery delay), I am sure that cooperation initially specified in DIXCUR project would not have been as successful.

I thank all the permanent members of the laboratory (Nicolas Couvrat, Morgane Sanselme, Yohann Cartigny, Samuel Petit, Gabin Gabode and Pascal Cardinael and colleagues of chromatography team) for the discussions we have stink and constructive criticism that have given me, seminar or in their offices. They were a source of questioning and thus allowed me to build my best results. I thank all the members of the laboratory that allow daily to advance the science and Françoise and Ghislaine and all trainees who have crossed my path and helped to research and to the life of laboratory.

This thesis would not have been possible without the help of my friends. For their funniness, their support, their advice, debates, laughs that are good, encounters, surprises, Nutella and pastries, thank all PhD students of the laboratory: Grace, Emily, Melanie, Lina, Elodie, Aurélien, Benjamin and Quentin. I extend a special thanks to those I met during my university studies and who are, over the past three years, become increasingly close: Jean Christophe

Debray, Julien Mahieux and Florent Simon. And then there's the friend, the great friend of always Clement Brandel; thank you.

Finally I thank my family: my parents Joel and Veronique, my grandma Liliane, my sister Marion, my brother Lucas, the Mac-Lemire family and many others for their support always.

TABLE OF CONTENTS

INTRODUCTION	11
CHAPTER 1. GENERALITIES	13
PART.1 THE CRYSTALLINE STATE	15
1.1 THE 230 WAYS TO BUILD A CRYSTAL: INTRODUCTION TO SPACE GROUP (SG)	16
1.1.1 Symmetry in Crystal	17
1.1.2 Crystal system, Bravais lattices & Point group (PG)	18
1.1.3 Crystal Lattices	18
1.1.4 Centre of symmetry	20
1.1.5 Asymmetric unit	20
1.1.6 Space groups	20
1.2 SINGLE CRYSTAL VS. POWDERED SAMPLE	21
PART.2 CHARACTERIZATION OF CRYSTAL AND SPACE GROUP DETERMINATION	23
2.1 PRINCIPLE OF X-RAY DIFFRACTION	23
2.2 X-RAY POWDER DIFFRACTION (XRPD)	24
2.3 SINGLE CRYSTAL X-RAY DIFFRACTION (SCXRD)	24
2.4 AVERAGING OF X-RAYS: MOTION AND DISORDER IN CRYSTAL STRUCTURES	25
2.5 SPACE GROUP ASSIGNMENT	26
2.6 MOLECULAR CRYSTAL & SURVEY ON SPACE GROUP OCCURRENCE	26
2.7 POLYMORPHISM AND IMPACT ON THE PHYSICAL PROPERTIES OF CRYSTALS	27
2.8 STRUCTURAL PURITY	28
2.9 SOLVATE	29
PART.3 THERMODYNAMIC AND HETEROGENEOUS EQUILIBRIA.	29
3.1 NOTIONS OF THERMODYNAMIC SYSTEM AND PHASES	30
3.2 PHASE RULE	30
3.3 GIBBS FREE ENERGY	31
3.4 ON THE ORIGIN OF POLYMORPHISM & RELATIVE STABILITY: POLYMORPHIC SPACE	33
3.5 UNARY PHASE DIAGRAM $v = 3 - \phi$	35
3.5.1 Dimorphic solid system	36
3.5.1.1 Monotropic Behavior	36
3.5.1.2 Enantiotropic behavior	37
3.5.1.3 Prediction of thermodynamic relationship	38
3.6 BINARY PHASE DIAGRAM IN ISOBARIC CONDITION ($v=3-\phi$)	38
3.6.1 The Lever Rule	40
3.6.2 Liquidus modeling	40
3.7 SOLID VAPOR EQUILIBRIA: SOLVATE	41
PART.4 PHASE TRANSITIONS	43
4.1 SOLID- SOLID OR POLYMORPHIC TRANSITIONS	43
4.2 THERMODYNAMIC TREATMENT OF POLYMORPHIC PHASE TRANSITIONS	44
4.3 CRYSTALLIZATION MECHANISM	45
4.4 BASIC NOTION OF CRYSTALLIZATION FROM SOLUTION IN BINARY SYSTEM (A-S)	47
4.5 KINETICS OF TRANSITION	48
4.5.1 Arrhenius Behavior	50
4.5.2 Overall transformation rate	51
PART.5 SECOND HARMONIC GENERATION	52
5.1 INTRODUCTION TO NONLINEAR OPTICS	52
5.2 ORIGIN OF NONLINEAR EFFECTS	52
5.2.1 Nonlinear Polarization	53
5.2.1.1 Induced dipole moment	53
5.2.1.2 Linear Polarization	54
5.2.1.3 Nonlinear Polarization	54

5.3 SUSCEPTIBILITY TENSOR $\chi(N)$	56
5.4 SECOND HARMONIC GENERATION (SHG) AND CONVERSION EFFICIENCY	57
5.5 CONDITIONS REQUIRED TO OBSERVE SHG	59
5.5.1 Symmetry Conditions	59
5.5.1.1 Non-centrosymmetry	59
5.5.1.2 Neumann Principle	61
5.5.1.3 Kleinman Symmetry rules (Kleinman 1962)	61
5.5.2 Parameters limiting the conversion efficiency in crystals: Phase-matching conditions (for constructive interferences)	62
5.6 ACHIEVING PHASE-MATCHING CONDITIONS	65
5.6.1 Angle phase-matching	65
5.6.2 Noncritical phase matching (or temperature phase matching)	66
5.7 PHASE-MATCHABLE AND NON-PHASE MATCHABLE MATERIAL	67
5.8 PROPERTIES OF MOLECULES	68

CHAPTER 2. DEVELOPMENT OF A VERSATILE SHG SET-UP AND RELIABILITY OF THE MEASUREMENTS **75**

PART.1 INTRODUCTION	77
PART.2 DEVELOPMENT OF A VERSATILE SHG SET-UP FOR POWDER MEASUREMENTS	78
2.1 AMELIORATIONS TO KURTZ AND PERRY (K&P) SET-UP	78
2.1.1 Spectral analysis	78
2.1.2 Heating-cooling stage	79
2.1.3 Humidity controller	80
2.1.4 Geometry and sample preparation	80
2.1.5 Software development	81
2.2 TEMPERATURE RESOLVED SECOND HARMONIC (TR-SHG) SET-UP	81
2.3 SET-UP FOR MEASUREMENTS AT ROOM TEMPERATURE OR ON “WET” SAMPLES	83
PART.3 DETECTION AND RELIABILITY OF SHG MEASUREMENTS	84
3.1 DETECTION OF THE SHG SIGNAL GENERATED BY DRY POWDERS	84
3.1.1 Measurement duration	84
3.1.2 Incident energy absorption and damage threshold tests	87
3.1.3 Temperature dissipation or time between two measures	88
3.1.4 Fundamental and SHG intensity dependencies	88
3.2 DETECTION OF THE SHG SIGNAL GENERATED BY “WET” POWDER	89
PART.4 USUAL APPLICATIONS OF THE SHG ANALYSIS	90
4.1 A TEST TO CHECK NON-CENTROSYMMETRY IN CRYSTAL	91
4.1.1 On centrosymmetric molecules packed in non-centrosymmetric structures.	92
4.2 NONLINEAR OPTICAL SURVEY: TEST FOR SHG EFFICIENCY	95
PART.5 PROBE THE STRUCTURAL PURITY: THE CASE STUDY OF THE 3-HYDROXYBENZOIC ACID (MHBA)	98
5.1 IMPORTANCE OF IMPURITY DETECTION	98
5.2 STRUCTURAL PURITY OF MHBA	99
5.3 RESULTS AND DISCUSSION	100
5.3.1 Characterization	100
5.3.2 Detection threshold	104
5.3.3 Quantification of structural impurity	106
5.3.4 Structural Purification of MHBA	107
PART.6 CONCLUSION	109

CHAPTER 3. SOLID-SOLID TRANSITIONS INVESTIGATED BY SHG	117
PART.1 INTRODUCTION & LITERATURE REVIEW ON PHASE TRANSITION STUDIED BY SHG METHODS	119
PART.2 MONOTROPIC TRANSITION MECHANISM OF M-HYDROXYBENZOIC ACID (MHBA)	122
2.1 PRESENTATION OF THE POLYMORPHIC SYSTEM	122
2.2 MEASUREMENT OF ACTIVATION ENERGY (E_a) BY MEANS OF TR-SHG	125
2.3 KINETIC STABILITY OF METMHBA	133
2.4 SOLID-SOLID TRANSITION MECHANISM.	134
2.5 CONCLUSION	135
PART.3 DETECTION OF ORDER-DISORDER TRANSITION IN ORGANIC SOLIDS	136
3.1 PRESENTATION OF THE SYSTEM	136
3.2 CRYSTAL STRUCTURE DESCRIPTIONS OF X-TAK DERIVATIVES AND NATURE OF THE DISORDER ON THE T-BU	136
3.3 TR-SHG DETECTION OF THE ORDER-DISORDER TRANSITION	140
3.4 CONCLUSIONS AND POSSIBLE TRANSITION MECHANISM	143
PART.4 GENERAL CONCLUSION ON PHASE TRANSITION INVESTIGATED BY TR-SHG.	145
CHAPTER 4. NOVEL APPLICATIONS OF SHG	151
PART.1 PHASE DIAGRAM DETERMINATION BY MEANS OF TR-SHG	153
1.1 INTRODUCTION & LITERATURE SURVEY	153
1.2 THEORETICAL HYPOTHESIS	155
1.3 PRESENTATION OF THE FORMIC ACID/ WATER SYSTEM	156
1.4 TR-SHG PHASE DIAGRAM INVESTIGATIONS	160
1.5 CONCLUSION AND POSSIBLE EXPLANATION FOR THE SUSPECTED FORMIC ACID PHASE TRANSITION	165
PART.2 SHG MEASUREMENTS VERSUS RELATIVE HUMIDITY	166
2.1 POLYMORPHIC AND HYDRATED FORMS OF STRONTIUM DIFORMATE	166
2.2 DEHYDRATION AND HYDRATION PATHWAYS (FROM LITERATURE)	167
2.3 TR-SHG EXPERIMENTS UNDER DRY ATMOSPHERE	168
2.4 PHASE CHECKING BY XRPD	169
2.5 TR-SHG EXPERIMENTS UNDER VARIOUS RELATIVE HUMIDITY	170
2.5.1 Conclusion and results	175
PART.3 SHG TO STUDY AMORPHOUS SOLIDS	177
3.1 LACTOSE FORMS	177
3.2 SOLID-STATE AMORPHIZATION OF LACTOSE	179
3.2.1 Size reduction by milling and its effect on the SHG signal.	180
3.2.2 Complete amorphization	183
3.3 CRYSTALLIZATION MONITORING BY SHG UNDER VARIOUS RH	184
PART.4 CONCLUSION	186
CHAPTER 5. DIXCUR PROJECT	191
PART.1 INTRODUCTION	193
PART.2 PRINCIPLE	195
PART.3 X-RAY SOURCE AND BEAM SHAPE	196
PART.4 MEASUREMENT CELL: THE CHOICE OF KAPTON	197
PART.5 PRELIMINARY RESULTS	201
5.1 STATIC MODE	202
5.2 DYNAMIC MODE	203
PART.6 CONCLUSION	204
CHAPTER 6. CONCLUSION GÉNÉRALE	207

<u>APPENDICES</u>	215
<u>APPENDIX. I TABLES OF SUSCEPTIBILITY TENSORS</u>	217
<u>APPENDIX. II EXPERIMENTAL DETAILS</u>	220
SINGLE CRYSTAL X-RAY DIFFRACTION (SC-XRD)	220
X-RAY POWDER DIFFRACTION (XRPD)	220
TEMPERATURE RESOLVED X-RAY POWDER DIFFRACTION (TR-XRPD)	221
DETERMINATION OF UNIT CELL PARAMETERS BY (TR-XRPD)	221
DIFFERENTIAL SCANNING CALORIMETRY (DSC)	222
HOT & COLD STAGE MICROSCOPY (HSM, CSM)	223
MULTIPHOTON MICROSCOPY	223
BALL-MILLING	224
LASER GRANULOMETRY	224
CURVE FITTING	224
<u>APPENDIX. III SOFTWARES</u>	226
I.1 DETERMINATION OF THE SHG SIGNAL	226
I.1 LASER CONTROL AND SHG MONITORING	231
<u>APPENDIX IV ADDITIONAL CONSIDERATIONS ON X-RAY DIFFRACTION</u>	235
THEORY OF X-RAY DIFFRACTION	235
SUPERIMPOSITION AND INTERFERENCE BETWEEN ELECTROMAGNETIC WAVES	235
FOURIER TRANSFORM	236
SCATTERING BY A POINT ATOMS, BY AN ASSEMBLAGE OF POINT ATOMS, BY A PERIODIC ARRAY	236
SCATTERING BY AN ASSEMBLAGE OF ATOMS	237
EXTINCTION CONDITIONS	237
<u>APPENDIX. V BASIC NOTIONS OF THERMODYNAMICS</u>	238
DEFINITIONS	238
THE FIRST AND SECOND LAWS OF THERMODYNAMIC AND THE GIBBS FREE ENERGY	238
THE EQUILIBRIUM CONDITION	240
<u>APPENDIX. VI SCIENTIFIC VALORIZATION</u>	241

Introduction

The physicochemical properties of organic solids are intrinsically related to the three-dimensional organization of the constituent molecules. One of the properties of the matter is the possibility to be organized periodically in crystal. This organization can be different according to the crystallization conditions and may evolve to one or another crystal packing according to the surrounding conditions. Solid materials have to withstand a large number of constraints in industry (temperature, pressure, shear, relative humidity changes) that can lead to phase transitions and have a direct impact on the properties of materials. The mechanisms and kinetics involved in these processes are complicated. There is a need to rationalize these processes and it is therefore necessary to develop new analytical methods to meet this challenge.

The primary objective of this work is the development of optical techniques for *in-situ* characterization of crystalline organic compounds. These analytical techniques must be able to probe the state of matter in a very short time in order to meet the monitoring process issues involved in solid-solid phase transitions (including desolvations) or crystallization.

This thesis is mainly focused on the development of a device based on the nonlinear optical principle of second harmonic generation (SHG) by a non-centrosymmetric material when subjected to a laser beam. To a lesser extent, the early stages of development to another device, based on the X-ray diffraction, has also been made (DIXCUR project). The manuscript is divided to reflect the amount of work that has been achieved in the development of these two devices. Consequently, Chapters 2-4 are devoted to the development of SHG apparatus and chapter 5 will be dedicated to the development of DIXCUR project.

This thesis tackles a number of concepts, from the crystallization of organic compounds to their nonlinear optical properties and the various existing heterogeneous equilibrium between the different states of matter and crystalline phases. Thus, Chapter 1 "generalities" will present relevant concepts to the understanding of this manuscript.

In chapter 2, the prototype based on the second harmonic generation and the reliability tests that were performed will be detailed. The installation and improvements to adapt to our problems will be compared with similar existing devices but also with usual characterization

techniques. The sensitivity of the technique will also be proven through the detection of impurities in organic mixtures.

Chapter 3 deals with the relevance of using this technique to the study of phase transitions in organic solids through two studies: the monitoring of a monotropic transition (with a destructive/reconstructive mechanism) and by a order-disorder transition. It will be shown that it is possible to obtain relevant information from the evolution of the SHG signal with temperature.

In Chapter 4, the SHG method will be applied to solve issues such as the monitoring of crystallization of amorphous material or dehydration under controlled humidity. The relevance of using this method will also be demonstrated through the study of liquid / solid equilibrium and the elaboration of a binary system phase diagram.

Chapter 5 is dedicated to the early development of a prototype based on the X-ray diffraction (DIXCUR project) to monitor organic solids precipitation. Due to administrative delays and delivery, access to the device has been greatly reduced during this thesis and, therefore, the stage dedicated to its development as well. Nevertheless, the early stages of development and the first results will be presented all through the study of a precipitating phenomenon.

The general conclusions will summarize the manuscript with a critical analysis of the obtained results with the SHG methods developed during this thesis. The prospects for future works will also be considered.

Chapter 1. GENERALITIES

The Generalities chapter is an overview of relevant notions for the understanding of the manuscript. We will define the notion of crystal and the implication of symmetries on properties of matter. Through the crystallization, we will see that different structure of the same chemical entity can exist and we will describe the relationships between these phases.

Part.1 The Crystalline State

The matter (made of atoms) can exist in the following three main different states: liquid, solid and gas. The properties of the solid state are essentially due to the atoms and their arrangements. In a solid, the particles (ions, atoms or molecules) are closely packed together. The forces between particles are strong so that the particles cannot move as freely as in liquid or gas states. Solids can be divided in two main categories. The atoms constitutive of the matter, can arrange in a strict and periodic array (long range order, LRO) defined as a “*crystal*”. By contrast, if only a short-range order (SRO) is present, the material is *amorphous*. The arrangement of atoms in this two kind of solids are represented Figure 1.1.

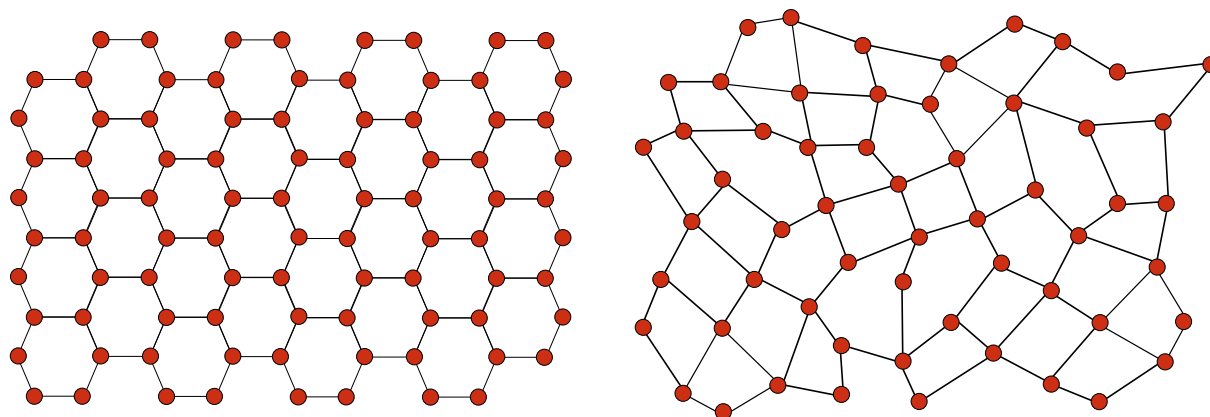


Figure 1.1 (Left) regular arrangement of atom characterized by a Long Range Order and (right) Short-Range Order as existing in amorphous solid. For the same volume, the density is higher in the crystal than in the amorphous solid.

A set of atoms can be linked together by covalent bonds to form a molecule. This work deals principally with the particular class of “molecular” solids crystallizing in non-centrosymmetric space group. The name origin of “crystal” comes from the Ancient Greeks. They identified quartz with the word “crystal” (κρυσταλλος, *crystallos* = cold + drop), according to its characteristics: a very cold stalactite of extraordinary hardness. A crystalline solid is roughly speaking a regular arrangement of molecules or atoms. More precisely, a

crystal is a three-dimensional network¹ (or lattice) in which molecules (or atoms) are stacked and related together by symmetry operators.

An amorphous solid is a liquid-like state exhibiting an infinite viscosity and characterized by a glass transition temperature T_g . Generally, the amorphous solid is less stable than the crystal (only one contrary case exist (Willart et al. 2006)). Above T_g , the diffusion becomes sufficiently high to induce the recrystallization (*i.e.* the solid was a supercooled liquid and recrystallizes to go back to the thermodynamic equilibrium). In contrary, below T_g the molecular arrangements are frozen and the solid remains in the glassy state. The glass transition temperature is not a thermodynamic transition and depends on the heating condition, the solvent content (plastizing effect), and the atmosphere surrounding the sample or the history of the sample.

Crystal is the most ordered manner to pack the matter and is almost always the most stable solid state. Regularity and periodicity impose mathematical laws for the crystal construction, which are summarized below.

1.1 The 230 ways to build a crystal: Introduction to Space Group (SG)

Many contributions in science history, both theoretical and experimental, help us to understand the notion of crystal and how it is built. As early as 1611, one can notice the contributions of the German mathematician, astronomer and astrologer Johannes Kepler amazed by the perfect six-cornered symmetry of the snowflake (see Figure 1.2).

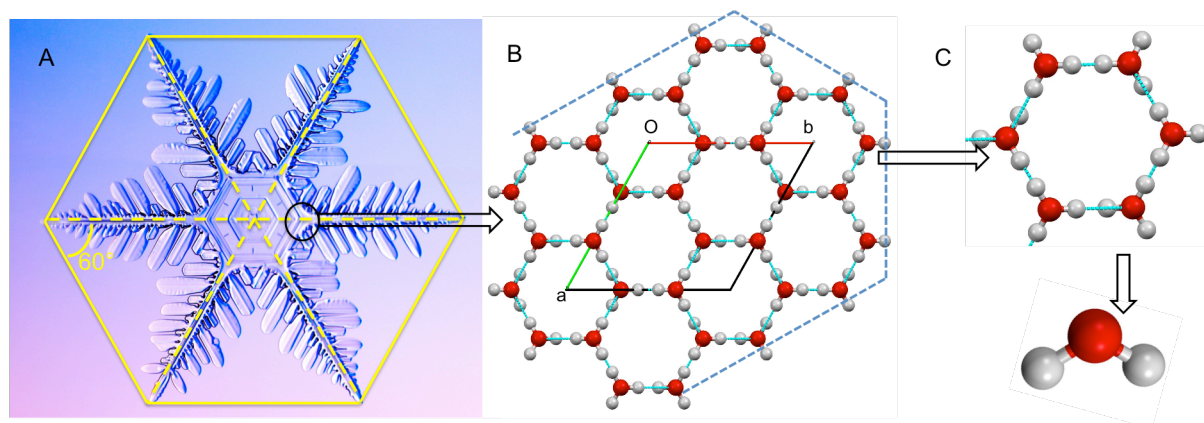


Figure 1.2 (A) Crystal snowflake microscopy picture denotes a 6-fold axis (*i.e.* invariant by rotation of 60°); (B) zoom in, highlighting the crystal packing of the ice; (C) zoom in, highlighting the constituents of the matter: molecules made of oxygen and hydrogen atoms.

¹ One can notice that intermediate situations are also encountered in case of liquid crystals which present LRO in only 2 dimensions, *i.e.* “smectic” or 1 dimension “nematic” solids.

Kepler wrote "Six-cornered Snowflake", (Shafranovskii 1975) the first mathematical description of crystals and work dealing on the problem of crystal structure. He asked the following fundamental question: "*There must be some definite cause why, whenever snow begins to fall, its initial formation invariably displays the shape of a six-cornered starlet. For if it happens by chance, why do they not fall just as well with five corners or seven?*". One of his discoveries was the geometry of the packing of spheres (the well known principle of closest packing in modern structural crystallography). He described the densest cubical packing and two less dense packings for spheres: the hexagonal and the simple cubic. Moreover, starting from the spherical packings, Kepler depicted conclusions about the parallelhedra, the convex polyhedra which can fill space in a regular manner, anticipating the conclusions of R.J. Haüy (1784) (Haüy 1784) and E.S. Fedorov (1885) (Senechal and Galiulin 1984)

In hindsight, its observation includes indirect pointers to the *law of constant angles* in crystals or *Steno law* for a six-sided snow crystal which states that the angles between two corresponding faces on the crystals of any chemical entities are constant and are characteristic of the chemical entity. Therefore, he is regarded as a forerunner of the discoverers of this law: N. Steno (Steno and Winter 1926), M.W. Lomonosov, (Lomonosov 1749) Romé de l'Isle. (De L'Isle 1784) Thenceforward, the connection between an internal order and an external symmetry was established.

Crystal structures result from the convolution of a mathematical lattice with a chemical motif (atoms, ions or molecules). The crystal symmetries fascinated the attention of mathematicians, which contributed to the development of crystallography.

1.1.1 Symmetry in Crystal

We are surrounded by all types of symmetry, regularity and order in Nature, in architecture, in art, etc. By essence a crystal contains symmetries. Imagine a tiller, which must dispose tiles in your house. You want a perfect tiling at the end of the work; all must be ordered, regular, and full without spaces or defects. To accomplish his work, the tiller must follow some rules. It is because there are only some well-defined possibilities to make it. It is true in 2D but in 3D, too.

At the macroscopic scale (*i.e.* for distance higher than the micrometer), a crystal exhibits characteristic forms called morphologies and characterize by point group symmetries.

1.1.2 Crystal system, Bravais lattices & Point group (PG)

A *point group* (PG) or *crystal class* is a set of symmetry operations that leaves at least one point fixed and the appearance of the crystal structure unchanged after application of the set of symmetry. Due to crystallographic restriction, a PG only includes the following symmetry elements²:

Proper rotation that rotates the structure of a specified portion of a circle about a *rotation axis*: 1, 2, 3, 4, and 6.

Improper rotation which consists of a rotation about an axis followed by an inversion (i): $\bar{1}$, $\bar{2}=m$, $\bar{3}$, $\bar{4}$, $\bar{6}$

For instance, the snowflake crystal shape in Figure 1.2. a exhibits a senary symmetry with a 6-fold axis located at the center (*i.e.* the center is fixed, and the shape of the crystal is unchanged by a rotation of $\pi/6 = 60^\circ$). Although objects themselves may appear to have 5-fold, 7-fold, 8-fold, or higher-fold rotation axes, these are not possible in crystals. The reason is that the external shape of a crystal is based on a geometric arrangement of atoms. Note that if we try to combine objects with 5-fold and 8-fold apparent symmetry, we cannot combine them in such a way that they completely fill space.

By combination of these 10 symmetry elements, there are only 32 possible crystal classes. Each one can be classified into one of the seven crystal systems and can be used to describe the 32 types of morphological (external) crystalline symmetries³ derived in 1830 by Johann Friedrich Christian Hessel. (in Gehler et al. 1830)

1.1.3 Crystal Lattices

Let us define a lattice as an infinite array resulting of 3 elementary translations (\vec{a} , \vec{b} and \vec{c}) applied to a chemical motif (set of atoms, ions or molecules). The parallelepiped determined by the basis vectors \vec{a} , \vec{b} and \vec{c} is called a (primitive) *unit cell* of the lattice. The corners of the unit cell are the lattice points. Although the number of primitive unit cell is infinite, it is possible to construct a unit cell exhibiting the smallest volume and the highest number of

² (Hermann–Mauguin notation)

³ Point symmetries are also useful in chemistry to describes molecular symmetries.

symmetry elements. This (conventional) unit cell is defined by the (lattice) parameters: a , b , c (lengths of edge), α , β and γ (angles between edges) and is represented in Figure 1.3. Consequently the system is invariant under translation of the unit cell by \vec{a} , \vec{b} or \vec{c} along the respective directions (and their combinations).

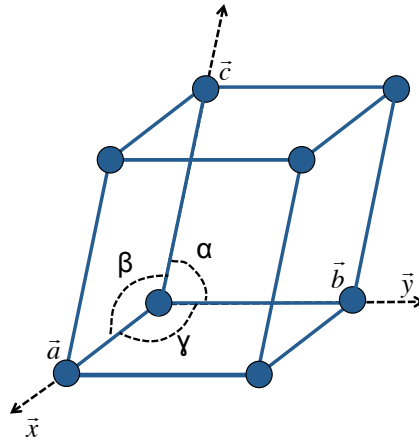


Figure 1.3 Representation of a unit cell defined by crystallographic distances: a , b , c and by angles α , β and γ . Note that unit cell corresponds to a primitive triclinic cell.

The unit cell contains the complete structural information and it is the smallest volume that we must know to fully identify a crystal. The unit cell is called primitive if it has no lattice point inside; otherwise it is centered.

For geometric reasons, lattices compatible with the translation $\vec{r} = u \cdot \vec{a} + v \vec{b} + w \vec{c}$ (with u , v and w integers) conduct only to seven different possible lattices known as the *crystal systems* (Table 1.1) allowing to tile the space periodically.

Nevertheless, the above crystal systems are not sufficient to describe all the possible lattices. The additional points may be regarded as *centering* of the conventional cell. Thus, 4 *centering mode or type of cell* can exist. For a conventional basis, the number of lattice points per cell is 1, 2, 3 or 4. (Hahn 2002)

In three dimensions, the following *centering types* are used:

P: no centering = primitive or simple (*i.e.* corresponds to the seven crystalline systems)

I: body centered

F: all-face centered

A, *B*, or *C*: one-face centered, respectively on faces (\vec{b}, \vec{c}) , (\vec{c}, \vec{a}) , (\vec{a}, \vec{b})

The combination of seven crystal systems with centering types conducts to the classification of the 14 Bravais lattices (see Table 1.1).

1.1.4 Centre of symmetry

Among 32-point groups (PG), 11 are centrosymmetric (*i.e.* with an inversion center). They belong to the Laue Group. A 3-D crystal (or 3-D structure) possesses a center of symmetry if a line passing through the center connects equivalent faces, atoms etc. (see Figure 1.4). A center of symmetry is an imaginary point in the space. The operation of inversion through this point is the same as a rotation by π followed by a reflection about a plane perpendicular to the axis (*i.e.* each point of coordinates (x, y, z) transforms into $(-x, -y, -z)$)

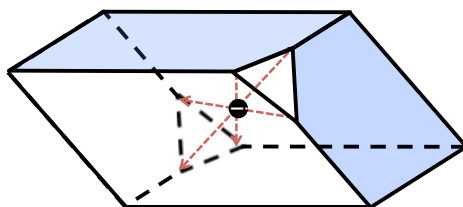


Figure 1.4 Centrosymmetric crystal shape. The black circle symbols the position of the inversion center i

It is interesting to highlight that most crystal properties are correlated to the presence or the lack of an inversion center as, notably, certain optical properties, which will be discussed in the Part.5 of this Chapter.

1.1.5 Asymmetric unit

When internal symmetry is present, the content of the crystal must be specified by a portion of the unit cell called *Asymmetric unit*. This chemical motif is the smallest necessary unit from which can generate the unit cell, and consequently the crystal, by applying the symmetry operations of the space group. Z refers to the number of chemical motif (molecules) in the unit cell and Z' to the number of independent chemical motif (molecules) in the *Asymmetric unit*.

1.1.6 Space groups

Even if all the possible lattices are well defined with the above operators, there are much more symmetries to describe a crystal because the pattern (*i.e.* molecule) can repeat in the unit cell. These include:

- Pure *translations* (displacement of a point along a vector)
- *Screw axes* (combination of a rotation and a translation along the axis of rotation: 2₁, 3₁, 3₂, 4₁, 4₂, 4₃, 6₁, 6₂, 6₃, 6₄, 6₅)
- *Glide planes* (combination of a reflection and a translation parallel with the mirror: a, b, c, n and d)

The combination of all the symmetry elements (point symmetries, translation including centering mode, screw axis and glide plane) leads to 230 space groups⁴ (*i.e.* 230 ways of packing molecules or atoms in a regular manner in 3D) (Hahn 2002). Space groups exhibiting an inversion center are called centrosymmetric, and non-centrosymmetric in the contrary case. Among the 230 SG, 65 are chiral *i.e.* belonging to the Sohncke group.

Symmetry helps us to understand molecular structure and some chemical, and physical properties of the solid. The crystalline state is probably one of the most impressive manifestations of symmetry in Nature. When we think of crystalline symmetry, we are really thinking of a perfectly structured infinite crystal lattice. In fact, all these symmetries are approximate, due to the finite size of a crystal and to naturally occurring defects in the crystal structure.

1.2 Single Crystal vs. Powdered Sample

The crystalline particle that is the most similar to a perfect crystal is a *single crystal*. This particle is made of the repetition of the unit cell in which the chemical nature of the crystal phase is homogeneous. The particle is limited by planar interfaces which correspond to specific reticular plans in the structure.

A powdered sample can be described as a set of randomly oriented single crystals, usually exhibiting small dimensions. Moreover, many particles are made of several crystalline domains separated by boundaries

⁴ See the international Tables for Crystallography for a complete description of SG and symmetry operators (Hahn 2002)

Crystal System	Triclinic	Monoclinic	Orthorhombic	Trigonal	Quadratic	Hexagonal	Cubic
Symmetry	1 (identity)	2	2	3	4	6	3 axes
Dominant axis	-	\vec{b}	$\vec{a}, \vec{b}, \vec{c}$	\vec{c}	\vec{c}	\vec{c}	\vec{v}
Point Group or Crystal Class	1 or $\bar{1}$	2, m ($=\bar{2}$), 2/m	222, mm2, mmm	3, $\bar{3}$, 32, 3m, $\bar{3}m$	4, $\bar{4}$, 4/m, 4mm, 422, 42m, 4/mmm	6, $\bar{6}$, 6/m, 6mm, 622, $\bar{6}m2$, 6/mmm	23, m3, 432, $\bar{4}3m$, m3m
Equivalent Cell parameters	2	4	8	12	16	24	48
Cell parameters	$a \neq b \neq c$ $\alpha \neq \beta \neq \gamma \neq 90^\circ$	$a \neq b \neq c$ $\alpha = \gamma = 90^\circ \neq \beta > 90^\circ$	$a \neq b \neq c$ $\alpha = \beta = \gamma = 90^\circ$	$a = b = c$ $\alpha = \beta = \gamma \neq 90^\circ$	$a \neq b \neq c$ $\alpha = \beta = \gamma = 90^\circ$	$a = b \neq c$ $\alpha = \beta = 90^\circ \neq \gamma = 120^\circ$	$a = b = c$ $\alpha = \beta = \gamma = 90^\circ$
Bravais lattice	Simple P	Simple P Bse-centered C	Simple P Bse-centered C Body-centered I Face-centered F	Simple P	Simple P Body-centered I	Simple P Body-centered I Face-centered F	Simple P Body-centered I Face-centered F

Table 1.1 The 14 Bravais Lattices

Part.2 Characterization of crystal and space group determination

2.1 Principle of X-ray Diffraction

The discovery of X-ray and the first X-ray diffraction by a crystal were both scientific breakthroughs that highlighted two fundamental principles: the structure of crystals is, indeed, tri-periodic and ordered and the light is a wave.

The X-ray diffraction is a powerful technique enables to identify a crystal and to determine the positions of the atoms in crystal structure. In fact, it is possible to determine all the crystallographic parameters (the unit cell metrics and the symmetry elements). Structure determination is essentially an 'imaging' process by means of X-Ray diffraction to produce a picture showing the relative distribution of the atoms in a unit cell.

In 1912, Lauë discovered that a crystal has the ability to diffract the light if the wavelength is of the same order as the interatomic distance. X-Rays provided by usual laboratory sources with wavelength in the range of [0.5-2] angstroms fall in this category. The oscillating electric field associated to the high X-rays frequencies interact with atoms, causing them to oscillate with the same frequency. The protons (much heavier than the electrons) are not really affected and it is much the electron cloud which oscillates and hence becomes a source of secondary X-Rays. This is the main cause of scattering of X-Rays by matter. Interference can occur between two scattered waves in the crystals. Because of the intrinsic periodicity of such edifices, these interferences can be constructive or destructive. In general, heavier atoms (with more electrons) scatter more strongly than lighter atoms, and consequently X-Rays are not successful at locating the position of very light atoms such as hydrogen.

In case of an atomic crystal defined by the lattice translation $\vec{r} = u \cdot \vec{a} + v \vec{b} + w \vec{c}$ (where u, v, w are integers), the periodicity in the atomic distribution results in the diffracted intensity being restricted to certain directions. For a given molecular plan (hkl) with an interplanar distance of d_{hkl} (Figure 1.5), diffraction occurs when θ , the angle of irradiation, satisfies the Bragg relation:

$$2d_{hkl} \sin \theta = n\lambda \quad (1.1)$$

where n is a natural integer, and λ is the wavelength of the incident beam. The meaning of this equation is that all 'scattering units' in a plane (hkl) must be in phase for maxima to occur

and that all scattering in successive (hkl) planes must also be in phase.

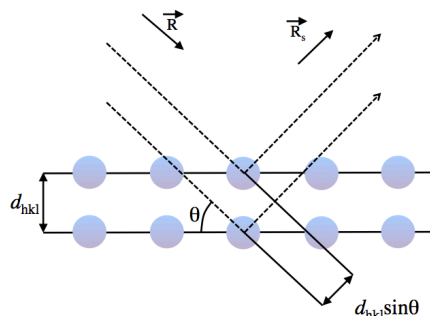


Figure 1.5. Principle of X-ray diffraction

It results from (1.1) that the diffraction phenomenon is only possible in particular direction for particular planes, thus diffraction is a signature of the crystal structure.

2.2 X-ray powder diffraction (XRPD)

For powdered sample, crystals are randomly oriented. In case of Bragg-Brentano geometry, the angle between the incident beam and the plan of the material is progressively increased to perform a measurement of the diffracted intensity versus θ . A diffractogram is thus obtained and can be considered as the signature of the powdered sample. Such diffractograms are commonly used for the identification of polymorphic form.

It is also possible to index the diffraction pattern (*i.e.* assignment of h, k and l for each peak) and thus to calculate lattice metrics and to determine the SG corresponding to the crystal structure.

XRPD patterns can also be used to refine a structural model but this technic requires computational resources and is often time-consuming and less efficient than direct structural determination from a single crystal.

2.3 Single Crystal X-Ray Diffraction (SCXRD)

In this case, the diffraction pattern is obtained by only one single crystal. Typically, it is mounted on a 3-circles goniometer allowing stepwise change in the orientation of the crystal versus the incident X-ray beam. CCD camera detects each diffraction directions. An indexation is used to identify the values h, k and l for each diffraction spot and therefore to determine the SG of the crystal structure via the extinction conditions (see Appendix IV). *In fine*, a Fourier transformation is applied to determine of the electronic density distribution in

the unit cell of the direct lattice. The SC-XRD is considered as the best method to derive unambiguously the chemical structure of molecules.

2.4 Averaging of X-rays: Motion and Disorder in Crystal Structures

The structure obtained by SC-XRD is the result of an average on thousands of billions of unit cells. Punctual or aperiodic defects (impurities, dislocations, vacancies...) are thus not observable, in practice, in SC-XRD experiments.

The aperiodic defects will be however processed as a periodic element in the structural model because of the averaging of X-rays. The significance of the “space occupancy factor” (S.O.F.) refinement parameter in this context is illustrated in Figure 1.6.

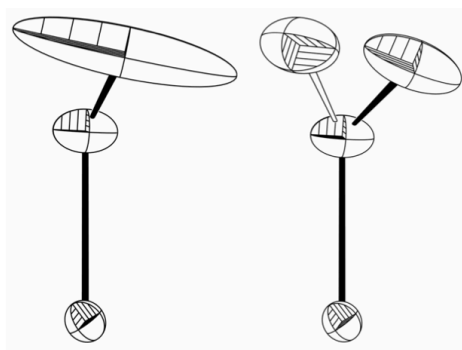


Figure 1.6 Disorder on ethyl group from (Muller et al. 2006). Anisotropic displacement parameters of a disordered ethyl group on the left without and on the right with modeling of the disorder. If the disorder is ignored, the refinement program tries to describe both atom positions with one ellipsoid, giving rise to a cigar-shaped probability ellipsoid. In the contrary case, it is possible to assign a probability of presence of each position: the statistical occupancy factor (S.O.F.)

However, it is important to underline that SOF does not bring any information about the nature of the conformational disorder, *i.e.* “static” or “dynamic” disorder. It means that one atom (or group of atoms) occupies more than a single crystallographic site. If it is distributed among different unit cell, it is a “static disorder” (*i.e.* a statistical occupancy of molecular sites by several conformers without possible conformational changes in the solid state). In contrary, if the atom occupies more than one site in the same unit cell the disorder is called “Dynamic”. The molecular motions are large enough to allow conformational changes in the solid state so that the distribution of conformers in the structure is not static and changes overtime. On average however, the distribution most often remains constant in isothermal conditions and this is why a SC-XRD experiment cannot differentiate a static disorder from a dynamic disorder.

In order to assign the nature of the disorder several methods can be used as spectroscopy techniques (Raman and solid state NMR, in particular). One can mention that dynamic disorder is temperature-dependent contrary to static disorder. It is, thus, possible to assign the nature of the disorder by means of SCXRD at low temperature in order to freeze the motion of the molecules. Since a dynamic disorder, must “vanish” at low temperature.

2.5 Space group assignment

Correct space group assignment of a crystal structure is not always trivial. As a result, many (corrected or uncorrected) errors can be found in the literature and databases (especially, ambiguities between $P1$ and $P-1$, $Pnma$ and $Pna2_1$ or Cc and $C2/c$ (Baur and Kassner 1992) space groups). In fact, most of the assignment errors deal with the problem of centrosymmetry. Discussion on these assignment errors and their occurrences will be given in chapter 2.

2.6 Molecular crystal & survey on space group occurrence

According to the nature of bonds involved in crystal edifice it is possible to classify crystals as ionic, covalent, metallic and molecular. In this manuscript we principally focus on molecular crystals.

Molecule is defined as a group of atoms bound together sufficiently tightly by *directed covalent* forces to retain its individuality when the substance is dissolved, melted, or vaporized.

A molecular crystal is a crystal whose molecules are held together by weak physical bonding (as opposed to chemical bonding involved in molecule). Its properties are related to the weak nature of intermolecular forces. They usually are soft and have low melting points (compare to other kind of crystals).

Small molecules (polymers and proteins are excluded) have the tendency to crystallize in only few Space Groups. Statistic survey on *Cambridge Crystallographic Database* (CSD) shows that roughly 95% of organic molecules crystallize in triclinic, monoclinic or orthorhombic system (see Table 1.2). Up to January 2014, the CSD contains 686 944 entries for 628 684 compounds (292 661 organic structures (42.6%) and 369 682 (53.8%) of organometallic structures).

System	Triclinic	Monoclinic	Orthorhombic	Tetragonal	Trigonal	Hexagonal	Cubic
Structures	171086	357478	121050	14806	11842	3304	3433
%	25.1	52.3	17.7	2.2	1.7	0.5	0.5
%structure in 2002	22.3	53.4	20.4	2.4	1.1	1.2	05

Table 1.2 Crystal system statistic repartition for the 682,999 CSD structures for which the space group is fully defined (January 2014)

According to 2014 CSD statistics, 87.7% of the molecules crystallize in only 10 space groups. Among these, 4 are non-centrosymmetric. The space group frequencies are given Table 1.3.

Space Group	$P2_1/c$	$P\bar{1}$	$C2/c$	$P2_12_12_1$	$P2_1$	$Pbca$	$Pna2_1$	$Pnma$	Cc	$P1$
Frequency (%)	34.8	24.1	8.3	7.4	5.2	3.4	1.4	1.1	1.1	0.9

Table 1.3 Space group frequency ranking for the 682,999 CSD structures for which the space group is fully defined (January 2014.) Non-centrosymmetric (NC) SGs are in bold characters

Statistics for enantiomorphous space groups are also reported in the CSD. In 2014, 78% (532 485) of structures adopt centrosymmetric space groups and 22% (150 514) adopt non-centrosymmetric space groups. In 2002, this proportion was respectively 75.9% and 24.1% (Allen 2002). One can notice that 15.7% (113 908) of structures adopt a Sohncke space groups. Although the number of structure has been triple since 2002, the proportion of centrosymmetric and non-centrosymmetric structures remain quasi the same. For purely organic molecules (organometallic are excluded), circa 13 % crystallize in non-centrosymmetric space groups.

Among non-centrosymmetric space group, 85% of crystals belong to orthorhombic or monoclinic system (see Table 1.4). Less than 1 % crystallizes in cubic system; this is due to a higher symmetry present in this system.

	Orthorhombic	Monoclinic	Tetragonal	Triclinic	Trigonal/hexagonal	rhomboedric	Cubic
Organometallic	28348(19.11)	18454(12.44)	5060(3.41)	2520 (1.7)	2504 (1.82)	1348(0.91)	1234 (0.83)
Organic	46051(31.07)	32839(22.15)	3037(2.05)	3836(2.58)	2003 (1.35)	625(0.42)	244(0.16)
Total	74399(50.18)	51293(34.59)	8097(5.46)	6356(4.28)	4707(3.17)	1973(1.33)	1478(0.99)

Table 1.4 Distribution of non-centrosymmetric structures in organometallic and pure organic compounds in 7 crystalline system. (CCDC Nov 2013) (Percentage values in parentheses)

2.7 Polymorphism and Impact on the physical properties of crystals

The polymorphism is defined as the ability for a chemical entity to crystallize in at least two different crystal packings. (McCrone et al. 1965; Bernstein 2002) The recognition of crystal polymorphism is credited to Mitscherlich, who determined the existence of different crystal structures of the same compound in a number of arsenate and phosphate salts. For a molecule,

this behavior arises from the possibility to adopt different conformations and/or to establish different intermolecular interactions in the solid state. In 2014, the number of polymorphic structures in the CSD is 20753 (3%). Nevertheless, the unexplored polymorphic landscape (in pressure and/or in temperature) lets suppose that polymorphism could concern a greater quantity of compounds.

Since all the properties of a crystalline solid are related to its internal structure, the modification of the crystal packing can greatly change, even drastically, the physicochemical properties of the crystal. Main properties that can be impacted are compiled in the Table 1.5. (Sheth and Grant 2005; Brittain 2009; Lee 2014)

Packing	Mechanical	Thermodynamic	Kinetic	Surface
Molar volume and density	Hardness	Melting and sublimation temperatures	Dissolution rate	Surface free energy
Conductivity, electrical and thermal	Tensile strength	Solubility	Rates of solid state reaction	
Refractive index	Compactibility and tableting	Vapor pressure	Physical/chemical Stability	Interfacial tensions
Particle morphology	Handling, filtration,	Enthalpy, entropy, and heat capacity	Rate of nucleation/crystal	Habit (shape)
Hygroscopicity	Flow and blending	Free energy, chemical potential	Crystal Growth	
Color	Cleavage			

Table 1.5 Properties modified by a change of the crystal structure

The polymorphism is of great importance in the drug development processes since polymorphs have different solubility and bioavailability (Hilfiker 2006). One can mention the drastic case of the Ritonavir® drug (Chemburkar et al. 2000). Many other domains are impacted by this phenomenon as food industry (Kirk et al. 2007) and crystal engineering (*e.g.* opto-electronic and mechanical devices). (Desiraju 2003b; 2003a; Bernstein 2011)

2.8 Structural purity

Polymorphism leads to the notion of structural purity. Contrary to chemical purity (*i.e.* where other chemical entities are involved), a structural impurity is a “self-poisoning” due to the ability of molecules to crystallize in different crystal structures. By definition a “structurally pure” solid is chemically pure and exhibits the same 3D molecular packing for each particle

constitutive of the sample. (Coquerel 2006) As polymorphs have different physicochemical characteristics (solubility, hardness, compressibility, density, melting point, etc., see Table 1.5), not only chemical but also structural impurities have to be considered in the impurity profile. (Coquerel 2006)

This structural purity is temperature and pressure dependent according to the stability domains of the polymorphs involved. This notion will be treated in more details in the chapter 2.

2.9 Solvate

The notion of polymorphism must not to be confused with hydrate or solvate (*i.e.* crystal made of molecules of solvent and solute). In literature, this case is often treated as *pseudopolymorphism* but this notion leads to some misunderstandings (McCrone et al. 1965; Bernstein 2002). Indeed, solvate is a defined compound between two chemical entities (*i.e.* a binary solid). The relationship between a non-solvated crystal and its solvate is not polymorphism even if structural filiations can exist between them. Solvates are of great importance in pharmaceutical and food industries since many compounds are obtained by crystallization from a solvent (leading often to incorporation of solvent molecule in the structure in stoichiometric or non stoichiometric proportion). The stability of solvates is often related to the quantity of solvent moisture in the air and is of particular importance for hydrate. The relative humidity (%RH) in the atmosphere can impact the nature of the phase and drives dehydration or hydration processes. The mechanisms of hydration or dehydration can be complex and depend on many parameters (temperature, pressure, RH, particle size...), (Garnier et al. 2002) and can lead to intermediate phases such as amorphous solid and change drastically the morphology and the particle sizes. The process can be either reversible or irreversible.

Part.3 Thermodynamic and Heterogeneous Equilibria.

This part aims to introduce basic notions of thermodynamics in the treatment of heterogeneous equilibria. The science of phase equilibria is a mathematical tool used to rationalize the equilibria between phases. In the following, the theory will do not treat in exhaustive manner, the large number of possibilities of invariant equilibria between phases but will be limited to few relevant examples in relation with the results presented in the next chapters: unary and binary phase diagram, solid-solid, solid-liquid and solid-gas equilibria.

3.1 Notions of thermodynamic system and phases

A thermodynamic system is a part of the universe separated with real or imaginary boundaries from the outside. The system is *open* if it could exchange matter and/or energy (heat) with the environment; *close*, if it could only exchange energy and *isolated* if neither matter, nor energy can be exchanged. In our case, the systems will be the components, liquid solvents or gaseous atmosphere and will be generally considered as closed.

A phase is a part of the system considered homogeneous in composition and existing in a precisely defined physical state of the matter (e.g. gas, liquid or solid) and that does not evolve with time. (Tschoegl 2000; Findlay 2012) It has specific values of intensive variables and well-defined physicochemical properties. As these parameters are governed, in the solid state, by the nature of the 3D packing, a phase has a single crystallographic form. Consequently, *polymorphs* of molecular crystals are different *crystalline phases* of a molecular entity.

The equilibria between phases can be visualize in a phase diagram in pressure and temperature domains (*i.e.* a geometric representation of the stable and metastable heterogeneous equilibria which fulfills several rules such as Gibbs phase rule). Two phases are separated by an interface. The boundaries between phases are regions in which the properties differ from the properties of one homogeneous phase to those of the other. For instance, in dimorphic systems (*i.e.* involving two polymorphs), this boundary corresponds to a solid-solid transition. We may have several different phases that are identical in composition but different in their physical properties.

In the following, the theory of *heterogeneous equilibria* (*i.e.* involving the three main physical states) is developed, and then applied to specific cases of solid/solid equilibria for polymorphs.

3.2 Phase rule

This rule, due to J.W. Gibbs, is based on thermodynamic principles and gives the *number of degrees of freedom* (*i.e.* connects the possible number of phases in a thermodynamic system with the number of components and thermodynamic variables that characterize it) and can be simply states as:

$$v = C + N - \varphi \quad (1.2)$$

Where, v is the variance, *i.e.* the number of intensive variables that can be changed independently without modifying the state of equilibrium. C the number of independent constituents and ϕ is the number of phases involve in the equilibrium. The term “N” refers to the number of intensive variables considered (the pressure and the temperature).

3.3 Gibbs free energy

The *free enthalpy* G or *Gibb's free energy* (Gibbs 1899; 1906) of the thermodynamic system is given by:

$$G = H - TS \quad (1.3)$$

Where:

H is the enthalpy (H represents the total energy of the system)

S the entropy (at the given pressure and temperature)

T the temperature

TS is the amount of unusable energy, thus G represents the total *free* energy available for the system and is one of the thermodynamic potentials.

The calorific capacity (*i.e.* the necessary amount of energy to increase the crystal temperature of one degree) is defined as the first derivative of the enthalpy (at constant pressure):

$$Cp = \left(\frac{\partial H}{\partial T} \right)_P = T \left(\frac{\partial S}{\partial T} \right)_P \quad (1.4)$$

The entropy is the first derivative of the free enthalpy (at fixed pressure)

$$-S = \left(\frac{\partial G}{\partial T} \right)_P \quad (1.5)$$

It arises, combining (1.4) and (1.5) that the Cp is also the second derivative of the free enthalpy:

$$Cp = -T \left(\frac{\partial^2 G}{\partial T^2} \right)_P \quad (1.6)$$

It is possible to imagine that G varies continuously with the positions of atoms or molecules. A criterion of stability and equilibrium for a thermodynamic state is reached for a minimum value of G (*i.e.* for $dG=0$). The phase diagram is a graphical representation of phases present in equilibrium (*i.e.* with minimum G) as a function of intensive variables (usually the temperature T and/or the pressure P). The equilibrium between two phases is defined for

$\Delta G=0$ (i.e. when the free energy differences of both phases becomes 0). In the following, phase diagrams made of 1 (*unary*) and 2 (*binary*) constituents will be considered.

Energy/temperature diagram $G(T)$ that represents the Gibbs's free energy of two or more pure phases of the same substance versus the temperature was introduced by Buerger in 1951.⁵

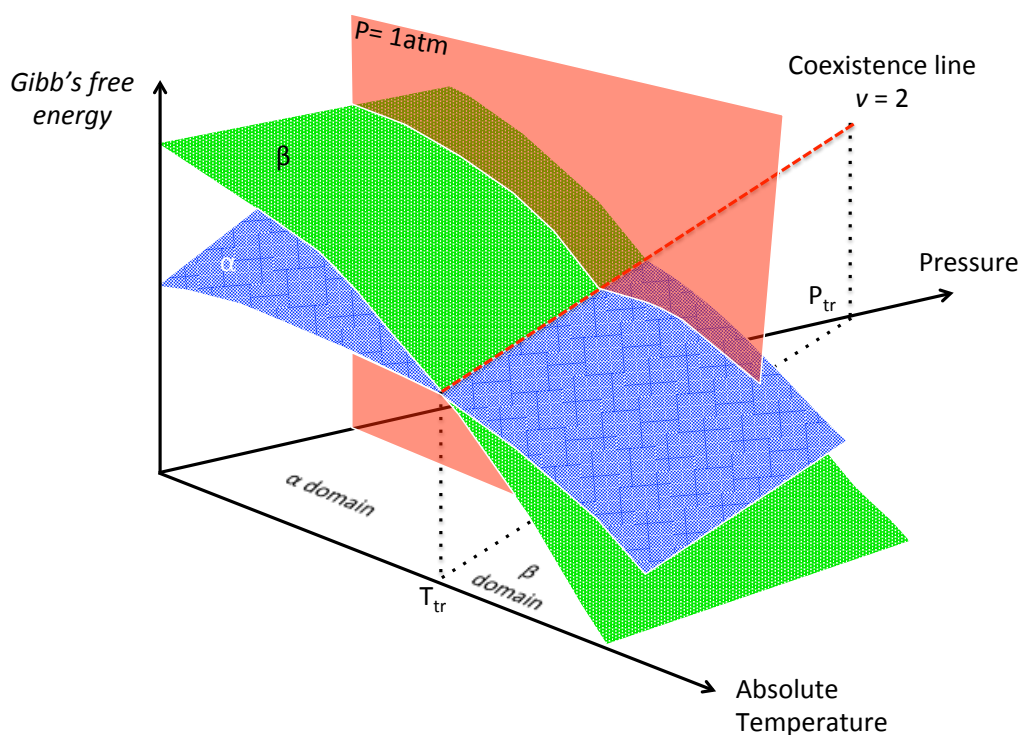


Figure 1.7 $G(T, P)$ diagram of 2 phases (α and β). The blue and green sheets are the Gibbs free energy over pressure and temperature of α and β , respectively. The red dash line corresponds to the coexistence line of both phases. It defines the temperature and pressure transition. The red plane is a section at constant pressure (see Figure 1.8)

These diagrams provide a direct visualization of equilibrium (i.e. when the curves cross) and stability (i.e. the most stable phase has the lower G curve). As their utility is recognized these diagrams becomes more widely used⁶ for the characterization of polymorphic form. (Henck and Kuhnert-Brandstatter 1999; Fischer et al. 2008)

A $G(T, P)$ diagram is plotted in Figure 1.7. The blue and green sheets represent the evolution of the Gibbs free energy of the α and β phases respectively versus pressure and temperature.

⁵ At the origin, Buerger dealt with the Helmholtz free energy. Nevertheless, diagrams based on Gibbs free energy are more commonly in use because of the data required to produce these are more readily accessible experimentally

⁶ Theoretical derivations and practical application of energy/temperature diagram in the field of drug substances (Grunenberg et al. 1996; Upadhyay et al. 2012)

The stable form has the lower free energy; thus it is possible to define the temperature and pressure stability domains of α and β phases. The equilibrium condition between both phases is defined when both sheets cross.

Although pressure could be a relevant parameter, it is often much less relevant than temperature notably in condensed phase (liquid and solid). That is why, for clarity, only the diagrams obtained at constant pressure will be treated in the next part. Under isobaric conditions: $v' = C + 1 - \varphi$. For simplicity we will limit the discussion to dimorphic system, although the extension to a larger number is based on the same principles. For instance the red plane in Figure 1.7 corresponds to the section at constant pressure (e.g. 1 atm) and the corresponding (G,T) diagram is schemed in Figure 1.8.

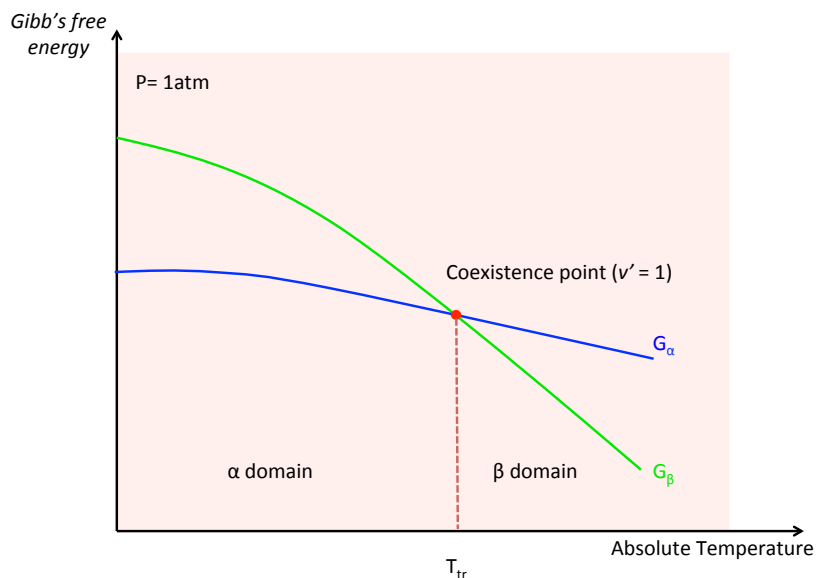


Figure 1.8 The red plane section of the Figure 1.7. It is a (G, T) diagram for 2 phases (α and β) in isobaric conditions. The blue and green lines are the Gibbs free energy versus temperature of α and β , respectively. The red point corresponds to the coexistence point of both phases. It defines the temperature transition.

3.4 On the Origin of polymorphism & relative stability: polymorphic space

Most polymorphic forms are obtained by crystallization pathways that result in an overall decrease in the free energy of the system. This means that, in general, the crystal structures that appear will be those with the lowest free energy (i.e. the greatest lattice energy). (Bernstein et al. 1999) In polymorphic systems there is a number of possible structures with similar lattice energies. The Gibb's free enthalpy difference between lattice energies of two polymorphic forms is generally weak (few kilojoules/mole). (Bernstein 2002; Ouvrard and

Mitchell 2003) As stated by Ostwald, (Ostwald and Taylor 1912) in all processes there is a competition between the minimization of G and the tendency of the system to reach as fast as possible the nearest “stable phase” (i.e. a metastable one). In the case of a crystalline state, the number of polymorphs depends on many parameters such as the nature of the molecule, its versatility to form different bonding networks and the environment (solvents, temperature, pressure, impurities). This can be viewed in a virtual *space phase diagram* at a given pressure and temperature.

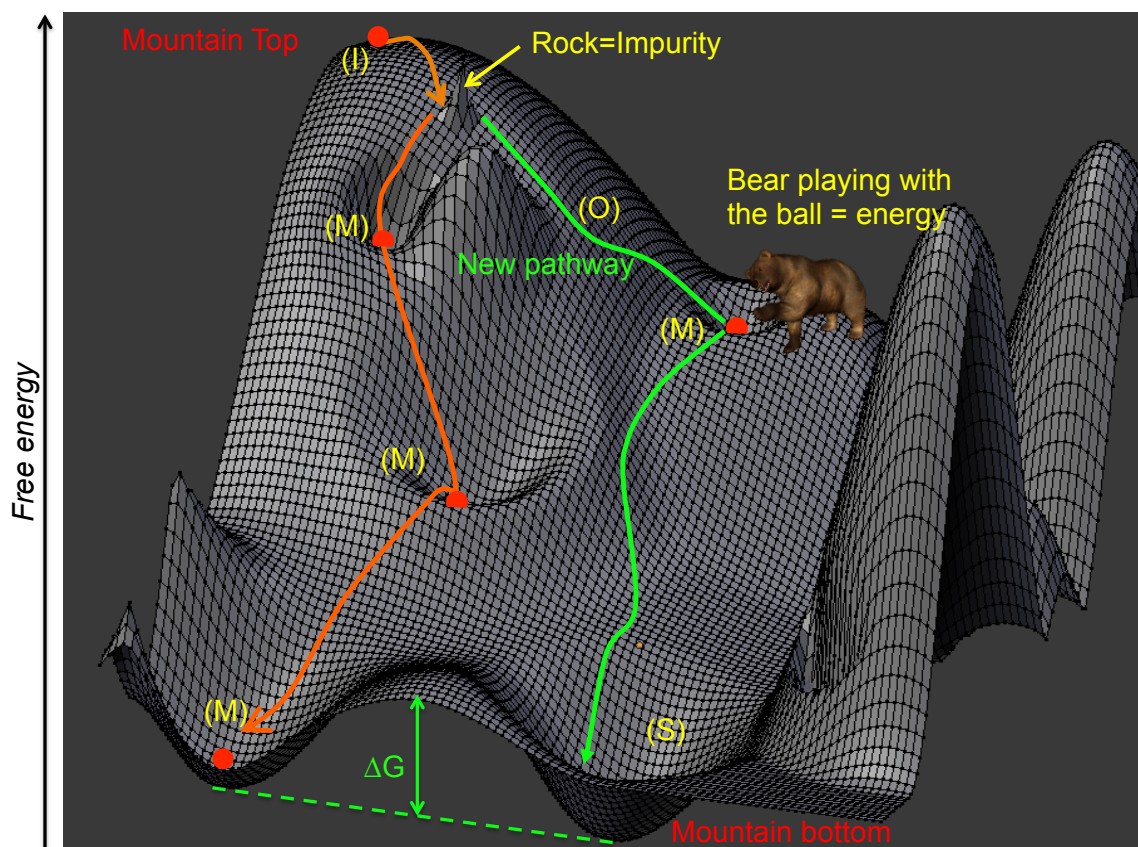


Figure 1.9 Analogy between ball rolling down a mountain and energetic landscape in the case of polymorphism. O , I , M and S points respectively denote the ball Out of equilibrium, Instable, Metastable or in a Stable state. The ball remains (meta)stable if no energy is bring

An analogy could be the image of a ball rolling down a mountain as described in Figure 1.9. Climb a mountain with a ball, at the top, the ball have a quantity of potential energy (as you have). Let the ball fall (not you!). At the beginning the ball is unstable (I) and begins to roll down; the potential energy is transformed in kinetic energy. The ball exchanges energy and is out of equilibrium (O). The ball searches to minimize its gravity potential energy as the molecule its thermodynamic potential (e.g. G free energy) in order to reach the stable equilibrium state (i.e. for the absolute minimum potential).

If its more stable state is definitively at the bottom of the mountain (S), the potential energy of the ball can be stabilized before reaching this state according to Ostwald step rules. (Ostwald and Taylor 1912) It can be stopped by a rock or tree acting as an impurity leading to a different crystallization pathway (green and orange lines in Figure 1.9) (Dunitz and Bernstein 1995) or trapped in cavities on the way.

The ball will be trapped in the cavity and remain in this *metastable state* (M) until a sufficient amount of energy will be brought to get out the ball. Each metastable state could be a polymorph. The necessary amount of energy depends on the depth of this cavity: it corresponds to the energy activation (ΔG). The wind or a bear playing with the ball could be acting forces as pressure or temperature in polymorphic systems. Sometimes the amount of necessary energy is very low and a simple gust of wind is sufficient (as a thermal input energy at room temperature is sufficient to initiate the transition toward another form).

It is not the thermodynamics that tells us in which cavity the ball will be trapped but the kinetics. The times to reach a most stable state depends on kinetic parameters and, often, the rate of transformation follows an Arrhenius law (see 4.5 page 48). The ball will continue to fall and finally, reaches the most stable state for a given pressure and temperature.

A good example of the kinetic stability of a metastable phase is the case of Carbon diamond that is less stable than carbon graphite. Nevertheless, in normal conditions, the energy barrier or activation energy to initiate the transition is so high that, once formed, diamond is kinetically stable although thermodynamically metastable.⁷

3.5 Unary phase diagram ($\nu = 3 - \phi$)

The $H=f(T)$ and $G=f(T)$ (at a given pressure) and the (P, T) phase diagrams of an hypothetical chemical entity is presented Figure 1.10 for a monomorphic system. The purple line represents the Gibbs free energy of the system. At a given pressure, the intercepts between G curves of each phase determine boundaries (*i.e.* temperature of transition) and lead to the construction of the phase diagram (*i.e.* determination of existence phase domains). Each transition is characterized by an enthalpy of transition ΔH . Points 1 and 2 are respectively the melting of the solid phase and the vaporization of the liquid phase.

⁷ do not worry if you own a diamond! Kinetics is in your side.

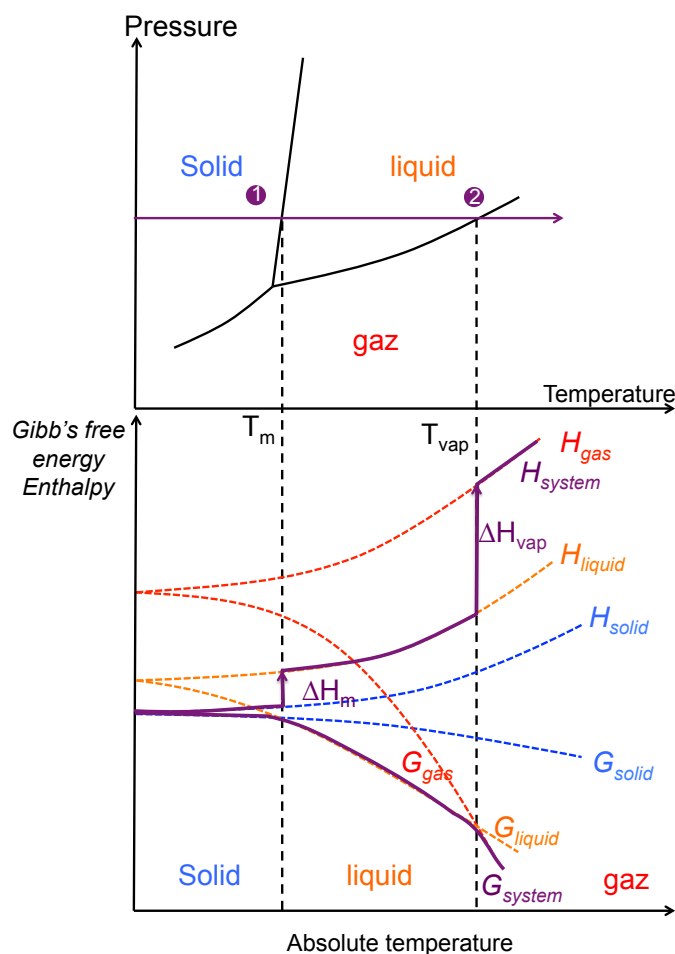


Figure 1.10 (P, T) monomorphic unary phase diagram. (1) denotes the melting and (2) the vaporization

3.5.1 Dimorphic solid system

As polymorphic form can exist, many solid phases can appear. The study will be restrained to only 2 polymorphs (*i.e.* dimorphic system). Two kinds have to be considered: monotropic and enantiotropic systems (Threlfall 2003).

3.5.1.1 Monotropic Behavior

In such system, only one polymorph is stable at all temperature (below the melting point). The other polymorph has no stability domain. Consequently, it is metastable in respect to the stable one. Therefore, if a transformation from one polymorph to another is possible, it is irreversible and always proceeds in the direction of the stable form. Both polymorphs are said to be in a *monotropic* relationship (from the Greek mono: one and tropos: direction). The transition can occur at any temperature and is governed by *kinetic laws* (e.g. Arrhenius law). The unary phase diagram of a compound crystallizing in two polymorphic forms α and β is shown in Figure 1.11a. From the G_{system} curve (in purple), one can see that the α -Form is metastable at all temperature since $G_{\alpha form}$ is higher than $G_{\beta form}$ and G_{liq} from 0 K up to the

melting ($T_m^{\beta\text{-form}}$). If the α -form is obtained and melted without irreversible solid-solid transition into the β -form, the associated heat of fusion should be lower than that of α -form (see Burger-Ramberger rules: Burger and Ramberger 1979).

3.5.1.2 Enantiotropic behavior

The unary phase diagram of an enantiotropic system (from the Greek enantio=reverse and tropos = direction) is described in Figure 1.11b. The α -form and the β -form have their own domain of thermodynamic stability. They are related by a reversible solid-solid transition at defined pressure and temperature.

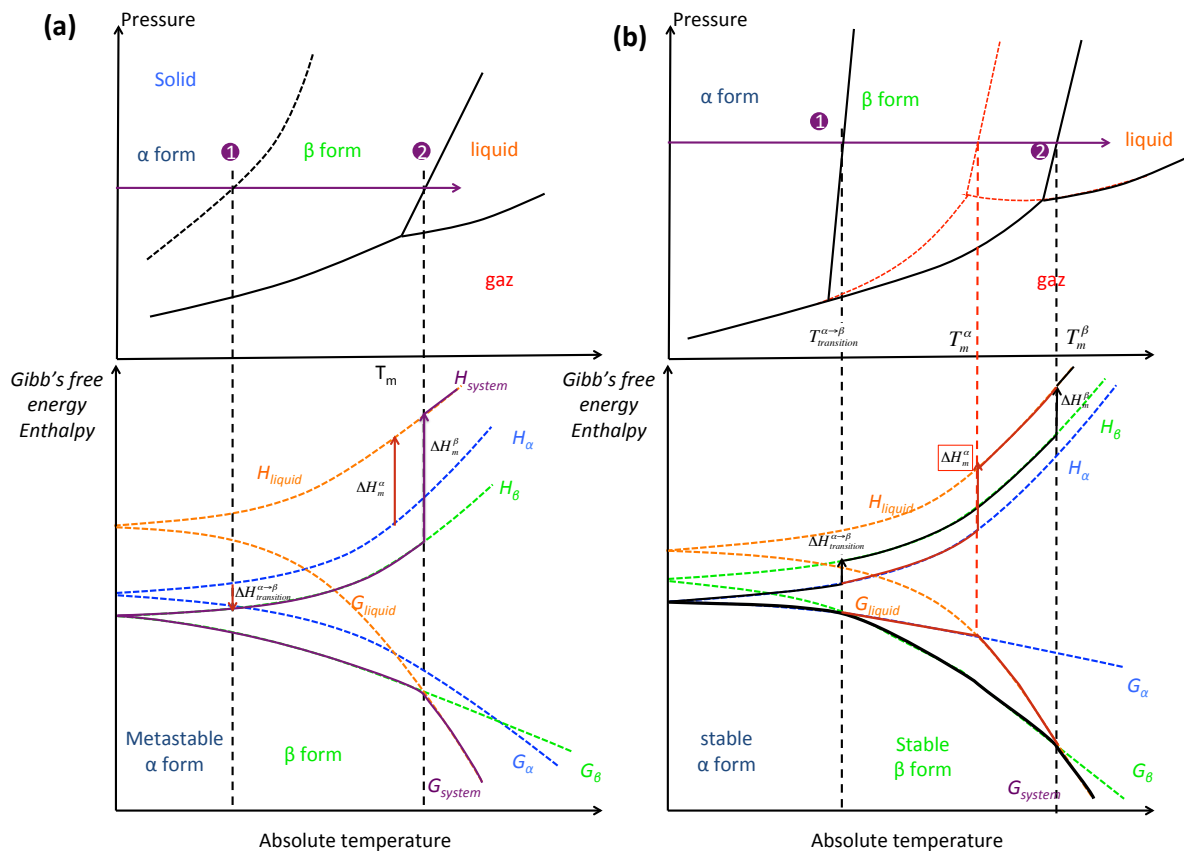


Figure 1.11 Unary dimorphic phase diagram (top) and corresponding (G,T) diagrams in isobaric condition (bottom) for a monotropic (a) and enantiotropic (b) relationship between polymorph α and β . Purple circle labeled (1) denotes the phase transition and (2) the melting point.

G_α and G_β cross at the temperature T_{tr} where both forms have the same free enthalpy. Although that their thermodynamic phase domains are well-defined, it not impossible to observe, for kinetic reason, one form in the existence domain of a other phase (at the same time this phase becomes metastable). It is also possible to observe the melting of the α -form.

Above the transition, the heat of fusion of the stable β -form is lower than that of the metastable α -form.

3.5.1.3 Prediction of thermodynamic relationship

An approach to determine the order of stability among different polymorphs of a compound exists. (Burger and Ramberger 1979; Grunenberg et al. 1996; Bernstein 2011) The Table 1.6 sums up these semi-empirical rules.

	Enantiotropic	Monotropic
Thermodynamic parameters	Transition temperature T_t Reversible transition	Transition at any temperature Irreversible transition
	<u>Below T_t:</u>	
	$G_\alpha > G_\beta$ Solubility of α form is higher	α is the most stable The solubility of α is always lower than the solubility of β
	<u>Above T_t:</u>	
	$G_\beta < G_\alpha$ β -solubility > α -solubility >	
Burger and Ramberger rules	$\Delta H_m(\alpha) < \Delta H_m(\beta)$ α -density < β -density	$\Delta H_m(\alpha) > \Delta H_m(\beta)$ α -density < β -density

Table 1.6 Burger and Ramberger rules on the nature of the relationship between polymorphs α and β

3.6 Binary Phase Diagram in isobaric condition ($v=3-\phi$)

In binary systems, the study focuses on the equilibria between two independent components. The initial physical states of both components are not necessarily the same. The mixture of components A and B can refer to systems such as: two solids, a solid and its crystallization solvents, or its main impurity.

Both constituents A and B can be completely or partially soluble in each other (even in the solid-state). It means that component A, for example, can enter in the crystal structure of the pure compound B without changing it. This solubility in the solid state is described by a free enthalpy of mixing, ΔG_{mix} , in Gibbs free energy depending on the interactions between molecules (attractive or repulsive), the entropy of the different phases, the pressure and the temperature.

For two constituents A and B and for regular solution, the Gibbs free energy of this system is expressed as:

$$G_{mixture} = X_A G_A + X_B G_B + \Delta G_{mix} \quad (1.7)$$

with, X_A and X_B , the molar fractions of A and B, G_A and G_B , the molar Gibbs free energy of A and B and ΔG_{mix} , the Gibbs free energy of mixing.

For fixed pressure, all the equilibria between the different phases can be represented in a temperature/composition diagram. As for unary phase diagram, the phase domains are deduced from the free enthalpy evolution of those phases. This will be explained through the case of *eutectic* phase diagram (see Figure 1.12).

In the graphical representation, the liquidus lines are boundaries between unary liquid phase domains and binary phase domains containing liquid and solid phases. Solidus lines indicate a transition between phase domains containing a liquid phase and another with only solid phase(s).

The eutectic invariant is a reversible heterogeneous equilibrium between a single liquid and two solids (for a binary system). For an overall composition around the eutectic liquid and below the temperature of that invariant, the system is composed of a mixture of solids only. At the eutectic point, one liquid and two solid phases coexist ($v=0$).

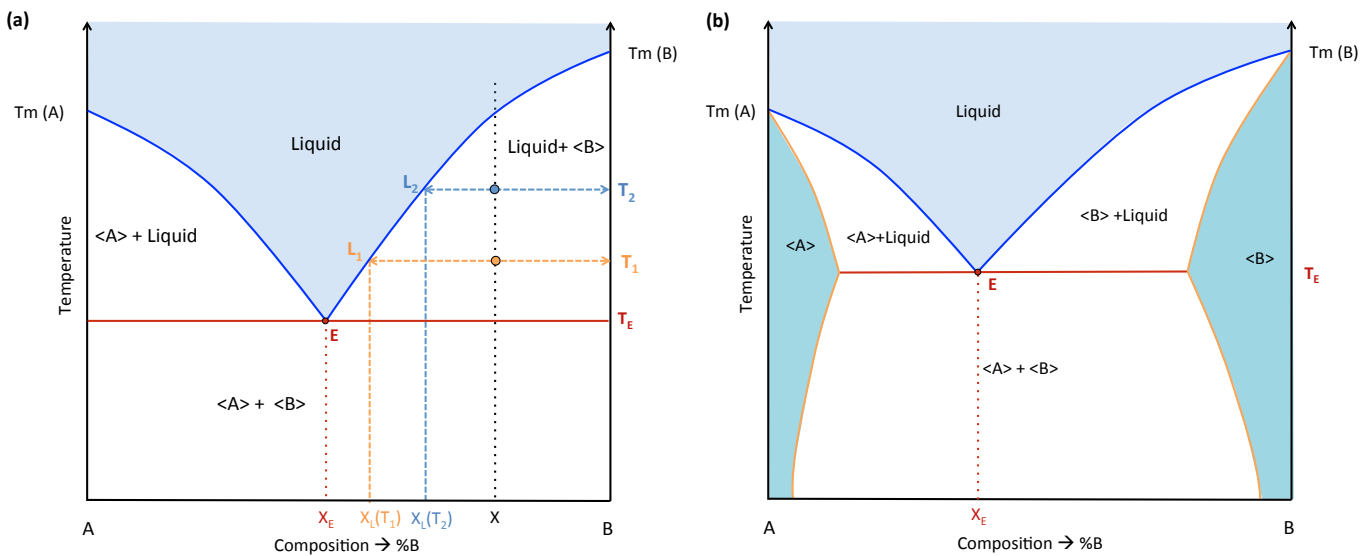


Figure 1.12 (a) eutectic phase diagram without solubility in the solid-state (b) eutectic phase diagram with terminal solid solutions. Blue and orange lines are respectively the liquidus and solidus lines. The red line corresponds to the eutectic invariant (it is also a solidus line). Point E represents the eutectic invariant ($v=0$)

In simple eutectic, the mixtures of A and B melt at lower temperatures than the pure solids. In a binary domain, the liquid and solid are in equilibrium. For instance, in the rich B domain at temperature T_2 , to determine the compositions of the two phases, crystal $\langle B \rangle$ and the liquid, construction lines are drawn. First, an *isotherm* is drawn at temperature T_2 . This is the horizontal blue dashed line that intercepts the *liquidus* at point L_2 representing the liquid that

is present in the mixture at temperature T_2 . The composition of this liquid is obtained by drawing a vertical line or *isopleth* which intersects the composition (horizontal) axis at $X_L(T_2)$. The other phase that is present in the mixture is B, whose composition is fixed, as pure.

3.6.1 The Lever Rule

This rule follows directly the law of mass conservation and is a simple tool to calculate either algebraically or graphically the relative amounts of two phases in a mixture at each temperature.

In a rich B domain, for the overall composition X at a given temperature T, the fractions of liquid and solid, respectively f_{liquid} and f_{solid} , are related by:

$$(f_{\text{liquid}}) * X_L(T) = (f_{\text{solid}}) * X_B \quad (1.8)$$

In a binary domain the law of mass conservation says:

$$f_{\text{liquid}} + f_{\text{crystal}} = 1 \quad (1.9)$$

The lever rule may be used to determine how the compositions of phase mixtures change with temperature.⁸

Combining (1.8) and (1.9), it is possible to express either the fraction of solid or liquid in the mixture:

$$(f_{\text{liquid}}) = \frac{X_B}{B X_T^l} \quad (1.10)$$

$$(f_{\text{solid}}) = \frac{X X_T^l}{B X_T^l} \quad (1.11)$$

Graphically, in Figure 1.12.a, it is easy to see that the fraction of solid decreases with the temperature since $X_L(T_2) < X_L(T_1)$.

3.6.2 Liquidus modeling

For any binary mixture without miscibility in the solid state, the liquidus curve of each constituent can be modeled by using the Schröder-Van Laar equation in its simplified form (for ideal solution):

⁸ Valuable under equilibrium conditions. This usually means that slow rates of heating and, especially, cooling are necessary. Rapid cooling often leads to different results, especially in systems with more complicated phase diagrams.

$$\ln X_B = \frac{\Delta H_{fus B}}{R} \left(\frac{1}{T_{fus 2}} - \frac{1}{T} \right) \quad (1.12)$$

with $\Delta H_{fus B}$ and $T_{fus 2}$, the melting enthalpy and the melting temperature of B. Any deviation to the Schröder-Van Laar model indicates that differences in heat capacity of the solid and the liquid phases have to be taken into account in the model as well as the activity coefficient of B.

3.7 Solid vapor equilibria: solvate

Molecules can exist in the gaseous state; particularly water but also ethanol, methanol, etc., and many usual solvents used in organic chemistry.

The *partial pressure of solvent* is the ratio of the partial vapor pressure of a volatile solvent over the saturating vapor pressure of this solvent. This ratio depends on temperature and defines the concentration of a solvent in the atmosphere. For water, this ratio is called the *Relative Humidity*:

$$RH = \left(\frac{P_{H_2O}}{P_{H_2O}^{sat}} \right)_T \quad (1.13)$$

For instance, the condensation of the first liquid drop correspond to RH=100%. An equivalent relation is valid for all molecules in the gaseous state.

A solid in a given atmosphere is in contact with molecules of solvent and both interact to reach equilibrium. Further phenomena can exist and depend on the nature of the phase, the concentration of gaseous atmosphere (thus on the temperature).

For instance, an hygroscopic solid has the ability to attract and hold water molecule from the surrounding environment. The *adsorption* phenomenon is the ability of solvent molecules (in surrounding atmosphere) to bond on solid phase surfaces. But these equilibria can also lead to a modification of the chemical composition of the solid phase. This can be due to the incorporation of solvent molecules inside the solid structure known as the *absorption*.

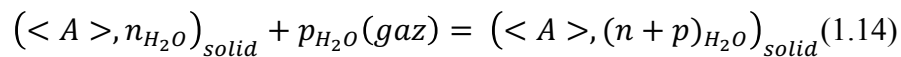
Amorphous materials can absorb relatively large amounts of water compared to their corresponding crystalline phases. This can drastically modify the glass transition temperature. (Šesták et al. 2010)

The stability and existence conditions of some crystalline phases can be strongly affected by

the concentration of solvent in the atmosphere. Deliquescence phenomenon can occur if a substance (mostly salts) has a very strong affinity for moisture that absorbs relatively large amounts of water from the atmosphere forming a liquid solution. This can be problematic, since for an under-saturated solution, a recrystallization towards another phase is not excluded. In contrary, the efflorescence is the complete collapse of a solvated phase due to the loss of solvent molecule in the air. It is often the case for solvent molecules different from water mainly because their concentrations in atmosphere are practically zero. It denotes also weak interactions between solvent and molecules in the solid state. Consequently, such structures are often only stable in saturated solution.

For solids, the reaction of water sorption or desorption can be reversible and conduct to the formation of hydrates phases or anhydrous phases and is drive by the temperature and the RH. The formation of these phases is one main issue for the vapor/solid interactions and can be interpreted by applying the Gibb's Phase rule.

Because the thermodynamic properties of an unsolvated compound are only defined by temperature and pressure, the formation of an hydrate (or solvate) implies the partial pressure of water (P_{H_2O}), at a fixed temperature. The formation of the hydrate is thus described by the following reaction (if the partial pressure of A is neglected):



Where $\left(\langle A \rangle, n_{H_2O} \right)_{solid}$ and $\left(\langle A \rangle, (n + p)_{H_2O} \right)_{solid}$ are two hydrates with n and $n+p$ molecules of water per A molecule ($n=0$ corresponds to the particular case of an anhydrous phase, for even values of p the hydrate is said *stoichiometric* and for odd p *non-stoichiometric*).

For a system in equilibrium, the number of independent components is 2 (water and A molecule), the temperature is fixed thus $N=1$ (only the pressure can vary), the number of phases φ is the vapor phase and the number of differentiable solid phases (n_s). Thus, the variance is expressed as:

$$v' = 2 + 1 - \varphi = 3 - \varphi = 2 - n_s \quad (1.15)$$

For stoichiometric hydrates (i.e. n and p integers), $n_s=2$ and $v' = 0$. In other terms, at a fixed temperature, the water pressure is fixed until the complete transformation from $\left(\langle A \rangle \right)$

, n_{H_2O})_{solid} to ($\langle A \rangle$, $(n + p)_{H_2O}$)_{solid}

It is possible to define an equilibrium constant from the equation (Beckmann 2013):

$$K_H = \frac{a(\langle A \rangle, (n+p)_{H_2O})_{eq}}{a(\langle A \rangle, n_{H_2O})_{eq} \cdot a(H_2O)_{eq}^p} = a(H_2O)_{eq}^{-p} \quad (1.16)$$

It follows that the free energy difference between the two hydrates (or an hydrate and anhydrate phase) is given by:

$$\Delta G_H = \Delta G_H^0 + RT \ln(a(H_2O)^{-p}) \quad (1.17)$$

It exists a precise water activity (associated to the relative humidity) for which the hydrate and the anhydrate are in equilibrium. It means that below this value, the anhydrate is stable and above it is the hydrate that becomes stable.

Part.4 Phase transitions

4.1 Solid- Solid or polymorphic Transitions

As previously said, each polymorphic form has an inherent stability domain of temperature and pressure. By the variation of at least one of these parameters, a transformation of the crystal structure to a different lattice with other symmetry relationships can occur. This structural rearrangement can arise because a thermodynamic system will tend to minimize the Gibbs energy. For instance a pressure increase clearly favors phases of lower volume (more compact packing of constituents). Increasing the temperature clearly favors phases of higher entropy (more disordered). In the following, we will discuss the mechanism involved in the process of transformation from one phase to another known as *phase transition* that is affected by both thermodynamic and kinetic factors.

Numerous classifications of phase transitions exist in literature (Ågren 2002). They are based on microstructural, mechanistic or thermodynamic schemes. It is not the purpose here to give an overall view of all existing classifications but some of them will be considered.

4.2 Thermodynamic treatment of polymorphic phase transitions

The Ehrenfest classification is based on the behavior of the thermodynamic functions (G and its variables) at the transition {Ehrenfest:1933un} for reversible phase transitions. For a given phase in equilibrium conditions (*i.e.* for small temperature changes) the Gibbs free energy is well defined and varies continuously with respect to the temperature. During the transition to another phase (for example going from liquid to solid), the Gibbs function changes “suddenly” from one to another phase. This classification arises from this fact. The nature of the thermodynamic change is often associated to a mechanistic point of view.

In the case of first-order transformation there is a discontinuous change in entropy and enthalpy (*i.e.* experimentally heat of transformation can be measured). The system exchanges energy, but because all the energy cannot be transfer instantaneously, the phase is heterogeneous: it means that, at the transition temperature, the transformation starts and extends progressively to the whole material (*e.g.* existence of a crystallization front). The first order transitions usually present thermal hysteresis: overheating or overcooling is possible (see for example the case of crystallization).

A second-order transformation has a continuous variation in entropy but a discontinuous change in heat capacity (jump is observed in the heat capacity). There is no latent heat and no thermal hysteresis in this case. It means that the phase transition continuously occurs with the temperature and is homogeneous in space. The temperature of transition is thus defined when the new phase is totally present; there is no phase change above this temperature. Often, it is correlated to a molecular cooperative or order-disorder mechanism (see ferromagnetic transition).

The Ehrenfest classification can be extended to higher n th derivatives of Gibbs free energy. This classification is well discussed in literature (Ågren 2002; Christian 2002) but the mechanism involved in these two principal kind of transitions is not described. Based on mechanistic considerations, some have argued (forcibly) that is not possible to observe, experimentally, a second order transition (Mnyukh 2013). Other authors treat a second-order as a degenerate case of a first-order transition (Hurst 1955).

Mechanistic classification is complex due to the versatility of the transition mechanisms (see for example the table I in (Christian 2002) that sums up 14 different phase transition pathways

in metal and alloy, or the 300 mechanisms names listed in the Appendix I in (Mnyukh 2011)). Maybe, the simplest theory is given by Mnyukh: any phase change is a first order transition and occurs by a destructive-reconstructive nucleation and growth mechanism. (Herbstein 2006; Mnyukh 2013). Maybe this mechanism is not the only one, but it is assuredly the most common.

The mechanisms of transition apply to either reversible or irreversible transition. But in the latter case the kinetics is an important factor.

4.3 Crystallization Mechanism

The crystallization is a first-order phase transition from liquid to solid or solid-to-solid. It could happen either from the melt (unary system), from a solution of a compound A in a solvent S (binary system) or from polymorph B to A. In all cases the same theoretical treatment can be applied. In the following polymorphic forms A and B are interchangeable respectively with phases A and B or solution and solid phases.

Most of the first-order phase transitions take place by nucleation and growth of the new phase as described in Figure 1.13. Let us begin with a phase at the thermodynamic equilibrium (e.g. phase A in Figure 1.16 at the temperature T_3).

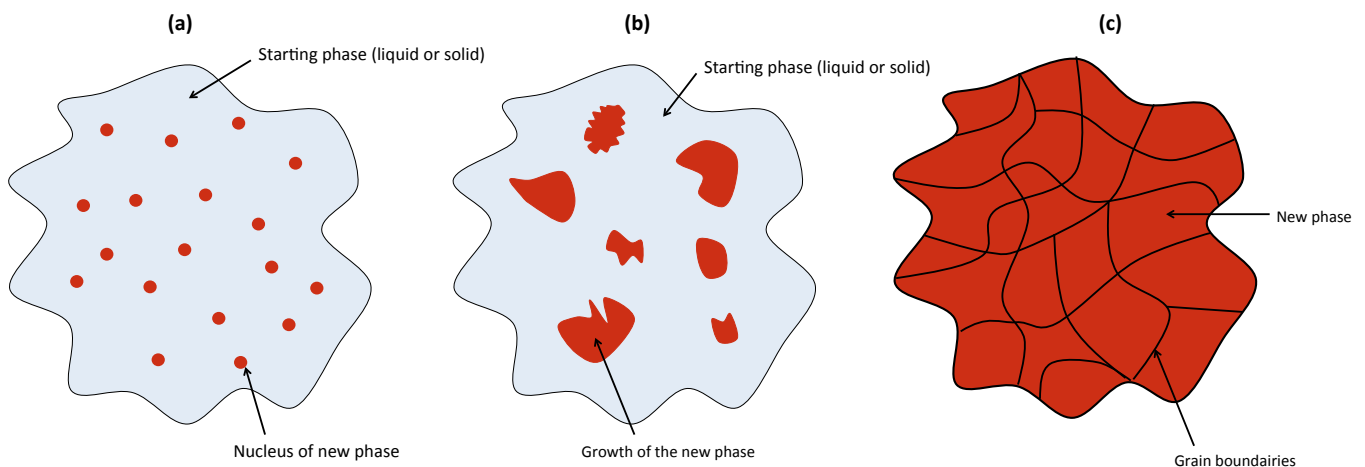


Figure 1.13 Nucleation and growth of a new phase. (a) nuclei appear; (b) nuclei start to grow; (c) often the final material is polycrystalline made of grains separated by grain boundaries.

If the conditions are changed (temperature or pressure) to reach a domain where polymorph A is not the most stable, a phase transition can occur, for example, from A to B (Figure 1.16.a at the temperature T_1). In a nucleation and growth mechanism, small nuclei of the new form (phase) B must appear firstly in the bulk of the original polymorph (form A).

There is a competition between the positive free energy contribution due to A-B interactions at the nucleus surface and the negative contribution due to its creation (minimization of the free energy because of apparition of the thermodynamic stable phase).

Assuming a spherical shape of the nucleus, the total variation of free enthalpy, $\Delta G_{nucleation}$, of the creation of a nucleus is defined as:

$$\Delta G_{nucleation} = -\frac{4}{3}\pi r^3 \Delta g_v + 4\pi r^2 \gamma \quad (1.18)$$

Where Δg_v is the Gibbs free energy variation per unit of volume relative to the starting phase and γ is the surface free energy per unit area of the nucleus. The evolution of $\Delta G_{nucleation}$ is plotted in Figure 1.14 (purple line). The formation of the nucleus is first energetically delaying since the contribution from the created surfaces dominates (red line).

At $r=r^*$, the free energy passes a maximum: $\Delta G_{nucleation} = \Delta G^*$. Then, the growth of the nucleus stabilizes the system. For $r=r_o$, the free energy becomes negative. It implies that any nucleus with $r>r_o$ is thermodynamically stable. However a nucleus with $r^*<r<r_o$, while thermodynamically unstable, should be kinetically stable. Indeed, if it re-dissolves, r decreases and the free energy increases. Therefore, for $r>r^*$, the growth is expected because it minimizes the free energy.

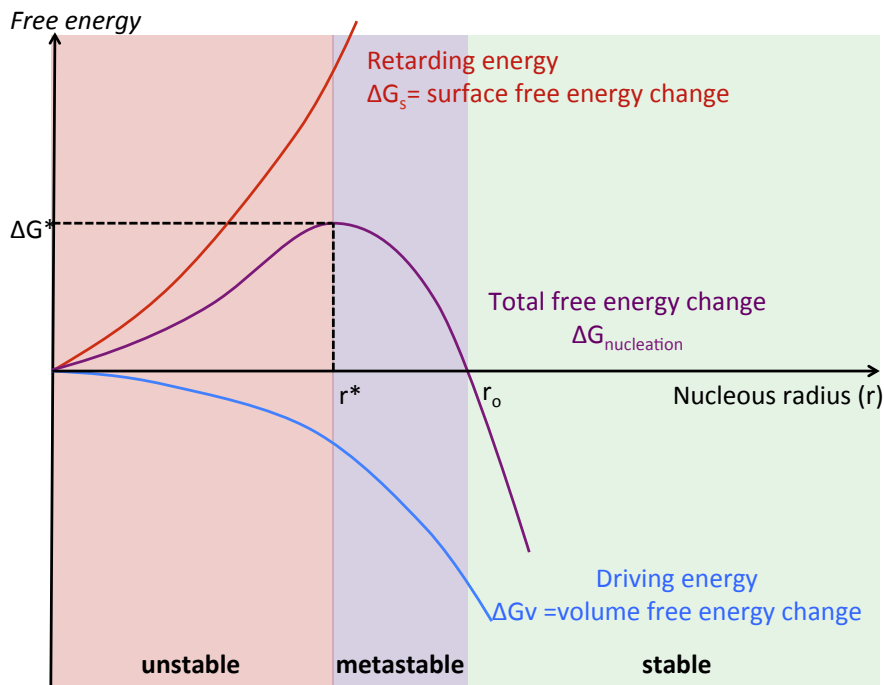


Figure 1.14 The free energy change associated with homogeneous nucleation of a sphere of radius r (purple curve)

In the Classical Nucleation Theory, r^* and ΔG^* can be easily derived:

$$r^* = \frac{2\gamma}{\Delta g_v} \quad (1.19)$$

$$\Delta G^* = \frac{16\pi\gamma^3}{3(\Delta g_v)^2} \quad (1.20)$$

The nucleation rate J can be expressed as:

$$J(T) = A \exp\left(\frac{-\Delta G^*}{k_B T}\right) \quad (1.21)$$

Where ΔG^* corresponds to an energy barrier that nuclei must overcome to start their growth. However, (1.18), (1.19) and (1.20) are only valid when homogeneous nucleation occurs, *i.e.* when nuclei are formed in the bulk of the initial phase. In most processes, the heterogeneous nucleation is involved and takes place preferentially on defects, impurities (structural or chemical), foreign surfaces (side of the crystallizer, stirrer, dust...). In heterogeneous nucleation, the ΔG^* value is lowered, thus it occurs more likely than homogeneous nucleation.

4.4 Basic notion of crystallization from solution in binary system (A-S)

The “solubility” C_s is the maximum concentration of compound A in solvent S at a given temperature. Generally, the solubility increases with the temperature.

The crystallization of A molecules can be achieved by a decrease of temperature or an evaporation in order to established a supersaturation β acting as a driving force.

The supersaturation ratio β can be defined as

$$\beta = \frac{C_A(T)}{C_s(T)}$$

with C_A , the concentration (molar) of A molecule in the solvent.

 $\beta=1$, the solution is saturated since $C_A = C_s$.

 $\beta < 1$, the system is undersaturated and crystallization cannot occur

 $\beta > 1$, the system is supersaturated and a driving force is established

In solution, the process of nucleation is mainly driven by kinetics and the energy barrier ΔG^* would be locally overcome by stochastic aggregation of solvated molecules. During crystallization, nucleation is usually the rate-limiting step. This fact leads to the possibility for the system to be supersaturated or supercooled and maintained in the Ostwald metastable zone. As a matter of fact, when an undersaturated solution is linearly cooled (or evaporated)

from the blue to the orange zone in Figure 1.15. The system enters in a metastable zone where ΔG^* is hardly overcome: the Ostwald zone. The nucleation occurs spontaneously below the Ostwald limit (*i.e.* in the white zone). In the metastable zone, crystallization can be observed only after more or less long induction time under isothermal conditions and usually stirring. The metastable zone width is dependent on kinetic factors: the cooling rate or the rate of evaporation of the solution, stirring speed, impurities, etc.

In the metastable zone, the nucleation rate is much smaller than in the domain of spontaneous crystallization. It is possible, but difficult, to measure nucleation rates and it requires a perfect control of experimental conditions (temperature, supersaturation, stirring rate, impurities concentration...).

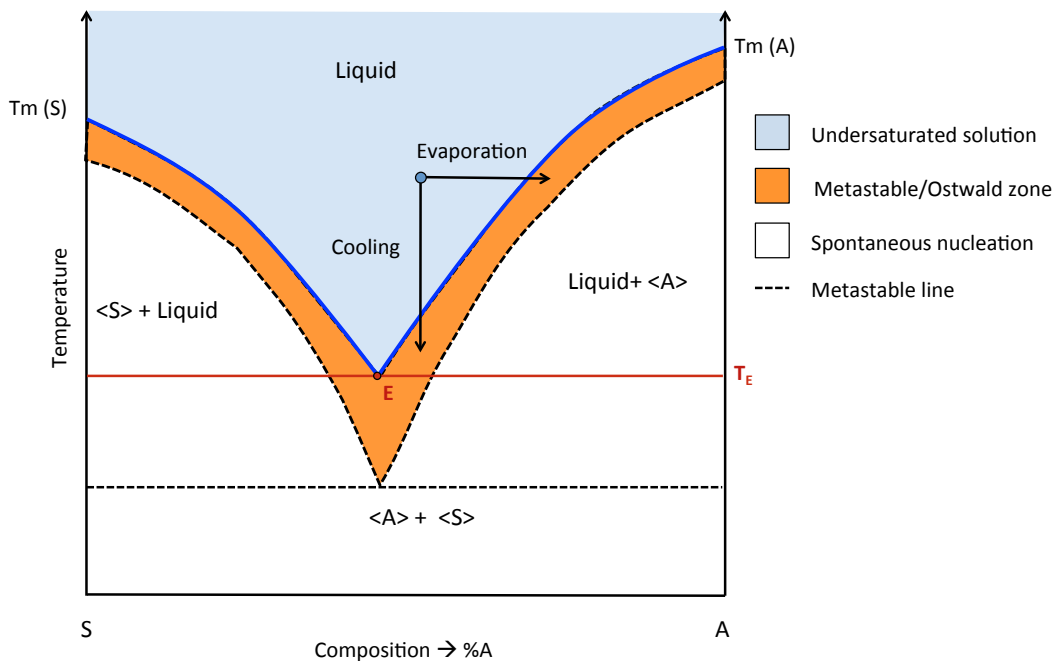


Figure 1.15. Schematic representation of the Ostwald zone in eutectic phase diagram that can occur during the cooling or the change in composition (e.g. the evaporation of the solvent)

4.5 Kinetics of transition

If the thermodynamics indicates if it is possible to observe a transition from one state to another (*i.e.* if the driving force $\Delta G < 0$), the kinetics informs on how the transition occurs. Kinetic treatments are applicable to transition from nonequilibrium to equilibrium, or between two equilibrium states. Kinetics of a process generally informs on how to overcome the energy barrier to finish the transformation from the initial state (A) to the final state (B).

The following part is largely inspired of the book “Kinetic processes” from K.A. Jackson (Jackson 2010) and “Phase transformation in metal” (Porter and Easterling 1992).

In the polymorphic space, it is possible to imagine a pathway between two stable polymorphic states (A and B) as illustrated in Figure 1.16.

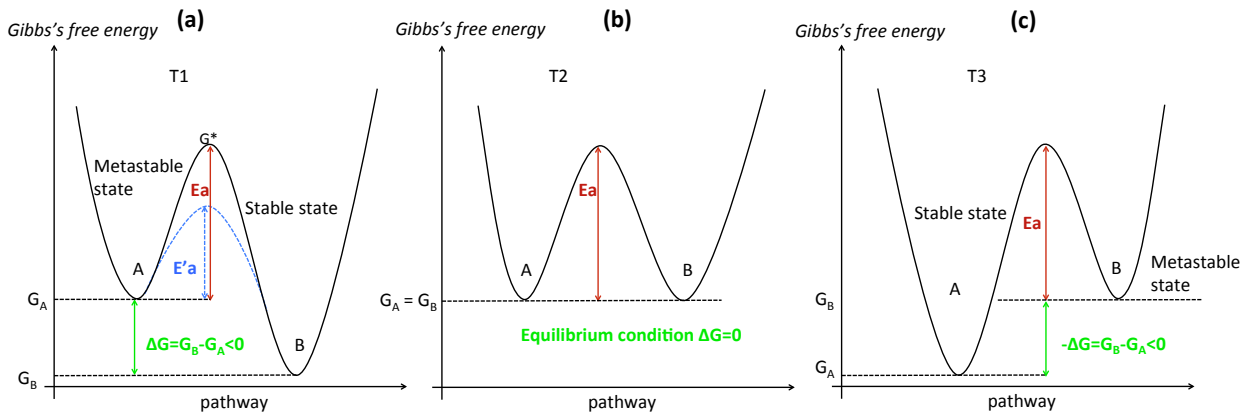


Figure 1.16 Gibbs free energy of A and B states at temperature T1, T2 and T3 respectively in (a), (b) and (c).

G_A and G_B are the free energies in the initial and final states, A and B respectively. These two minima in free energy are separated by a maximum G^* that is the highest free energy along the pathway. It depends on the reaction path and can change for different conditions (for example, when an impurity either chemical or structural is present). G_A and G_B can be easily compute but this is not the case for G^* that do not depend on the structure of A or B. The energy barrier that molecules in A-state must overcome to go in B-state is the activation energy $E_a = G^* - G_A$. The larger the energy barrier, the harder is the transition to occur and the slower is the rate. Due to a random thermal motion of molecules, the energy of one molecule will vary with time and can be sufficient to reach the thermal activated state G^* . Intuitively we guess that the number of molecules exhibiting enough energy to overcome the barrier will increase with the temperature. In all processes of materials transformation, molecular rearrangement takes place. The rate for the transition is thus proportional to the number of molecules per unit volume times the probability that they will have enough energy to get over the barrier of transition. Basically, the higher the temperature, the stronger the mobility of atoms or molecules, resulting in a greater probability for them to overcome the energy barrier, increasing the rate of a reaction or process.

In phase transitions either polymorphic or between two matter states (crystallization), most of the rate processes are described by Boltzmann statistics. Population analysis according to Boltzmann distribution and probability for the system to go from A to B and the contrary

defines the rate of transition, k , as: .

$$k = A_0 \left(e^{-\frac{G^* - G_A(T)}{k_B T}} \right) \left(1 - e^{-\frac{G_A(T) - G_B(T)}{k_B T}} \right) \quad (1.22)$$

One can notice that to have $k > 0$ it is necessary to have $\left(1 - e^{-\frac{G_A - G_B}{k_B T}} \right) > 0$, thus $\Delta G = G_B - G_A < 0$ (i.e. the thermodynamic criterion of stability). It is the case in Figure 1.16.a. In the equation the rate of reaction is thus defined by a kinetic term (implying the activation energy) and a thermodynamic term (depending on the driving force). For polymorphic system, notably enantiotropic, the driving force as defined in (1.22) can be reversed when G curves cross at the transition temperature (i.e. there is a driving force for the transition to occur in either direction). This evolution is described for temperature T2 and T3 in Figure 1.16. For monotropic relationships, the driving force cannot reverse its sign (State B is always the most stable) and the transition rate only depends on the kinetic factor. It simplifies the equation⁹:

$$k = A_0 e^{-\frac{E_a}{RT}} \quad (1.23)$$

The exponential term is known as the Boltzmann factor, R is the gas constant and E_a is the activation energy. The Boltzmann factor gives the fraction of atoms or molecules with energy exceed E_a at temperature T . So the rate at which the process occurs depends on a prefactor, A_0 , and the number of atoms or molecules that have enough energy to cross the path.

4.5.1 Arrhenius Behavior

Taking the logarithm of both sides of (1.23):

$$\ln(X) = \ln(A_0) - \frac{E_a}{kT} \quad (1.24)$$

Plotting $\ln(X)$ vs. $\frac{1}{T}$ gives a straight line with slope $-\frac{E_a}{kT}$. This kind of plot is known as an Arrhenius plot. A practical example is detailed in chapter 3.

If the rate process has single activation energy, E_a , over the range of the measurement, this suggests strongly that the mechanism controlling the rate is the same over that range.

⁹ The Boltzmann constant in the expression of rate means that we express the number of atoms undergoing a phase transition. It is also possible to refer to the quantity of mol; in this case k_B is replaced by R , the gas constant.

There is a simple relationship between the rate equation above and thermodynamics, which can be written:

$$G = -kT \ln X = E_a - kT \ln(A_0) \quad (1.25)$$

This implies that the rate at which atoms leave a state depends on their properties in that state. Comparing with $G = H - TS$, it is evident that E_a is related to the enthalpy, and the entropy, S , is $k \ln A_0$.

If two states or phases are in equilibrium, their free energies are equal, which is equivalent to the statement that rates of transition back and forth between the two states are the same.

4.5.2 Overall transformation rate

In powder, it is easier to measure the overall transformation rate (often treated by a Avrami-Johnson-Mehl-Erofeev equation) than the nucleation rate. The volume fraction x of the new phase can be thus described by:

$$x = 1 - e^{(-kt)^n} \quad (1.26)$$

with k the rate constant, n is called the Avrami constant that depends on the nature of the nucleation and growth and t the time of transformation. The method to obtain the Avrami and rate constants will be described through a experimental case study in chapter 3.

Many factors can change the kinetic of phase transition as:

- the nature of the sample (e.g. single crystal, powder, size: surface area)
- the activation energy, strength of intermolecular bonds broken during the transition
- temperature, pressure, change in volume, humidity
- transition mechanism (destructive-reconstructive, order-disorder...)
- nucleation is often the rate-limiting step in many transition and depends on the nature of the sample, the crystal defect concentration (vacancies, dislocation, impurities either structural or chemical)
- difference of crystal structure between both phases (e.g. it is intuitive that the kinetics will be higher if a low structural reorganization is necessary (this is most probable if both structures are similar))

Part.5 Second Harmonic Generation

5.1 Introduction to nonlinear optics

Nonlinear optics is the field that describes the interaction of electromagnetic radiations and matter in which the matter responds in a nonlinear manner to the incident radiation fields. As nonlinear effects and nonlinear interactions can only be obtained in a material when it is illuminated with a sufficiently energetic radiation, nonlinear optical effects became observable only after the invention of the ruby laser by Maiman in 1960, (Maiman 1960). In 1961, Franken (Franken et al. 1961) reported, for the first time, the generation of optical harmonics in a quartz crystal illuminated by a laser and signed with this successful experiment the very beginning of a new field of research.

Among the various nonlinear effects that have been observed and studied since the Franken's experiment, Second Harmonic Generation (SHG) is certainly the most popular and still generates an intense research activity. SHG can simply be viewed as the interaction of two electromagnetic waves (of same frequency) in a material that gives rise to a third wave at twice the initial frequency. The Figure 1.17 illustrates this phenomenon in the case of a Lithium triBorate (LBO) crystal illuminated by an infrared laser source and generating light in the optical region (green light).

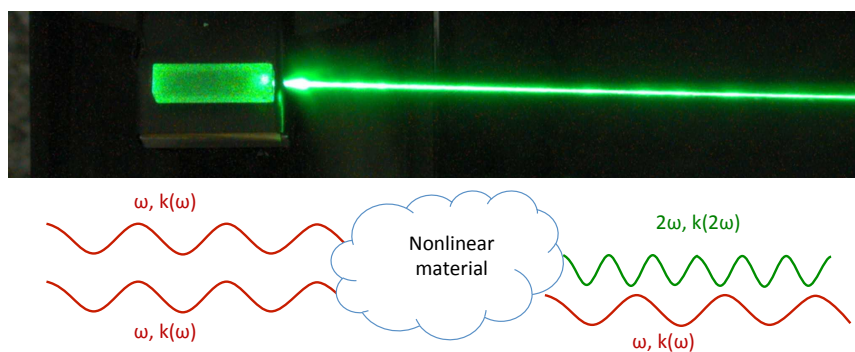


Figure 1.17 Top: Frequency doubling (i.e. Second Harmonic Generation) from 1064 nm laser source through LBO crystal. Photographic credits©: Sébastien Forget (http://www-lpl.univ-paris13.fr:8090/rech_laser.htm). Bottom: schematic representation of the SHG principle in term of waves interactions.

5.2 Origin of nonlinear effects

It is not the purpose here to go deeply in the theory of nonlinear optics which is based on quantum mechanics. However, some classical models can be used with relevancy for the description, the understanding and the mathematical modeling of the nonlinear effects.

5.2.1 Nonlinear Polarization

As previously mentioned, nonlinear optical effects arise from the interaction of an energetic electromagnetic field with a material. As atoms and electron can interact with electromagnetic field, its propagation through the material produces changes in the spatial and temporal distribution of electrical charges.

5.2.1.1 Induced dipole moment

At this point, we can consider the simple case of a one dimension, time independent electric field applied to an atom or a molecule.

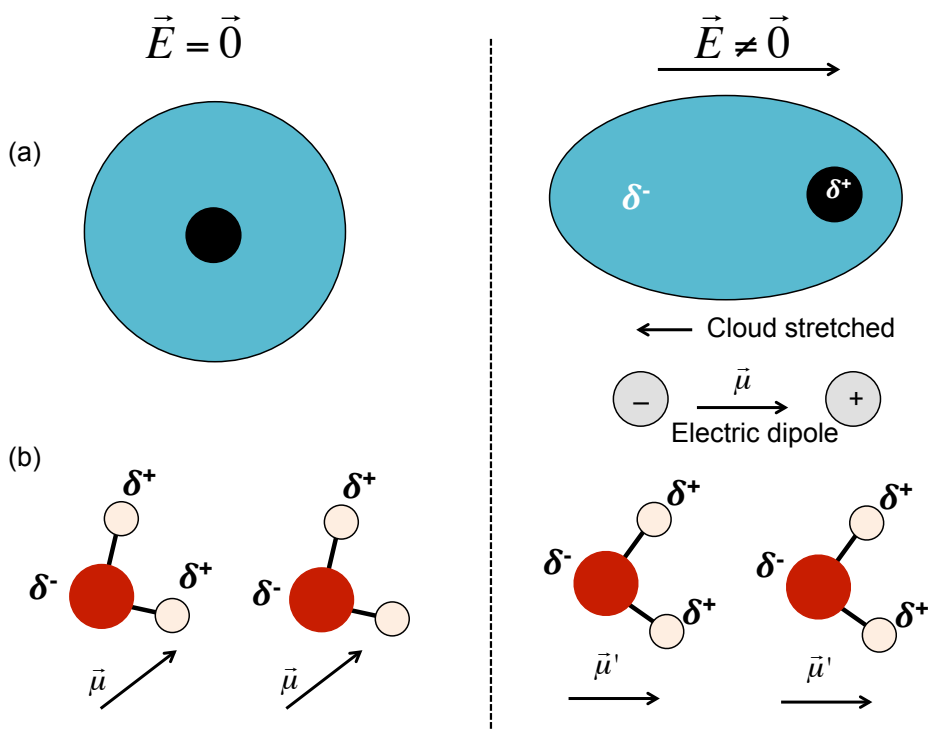


Figure 1.18 Effect of electric field applies on solid. (a) Simple model of nucleus surrounding by a spherical electron cloud in absence of electronic field. If an electronic field is applied, it displaces the electron cloud with respect to the nucleus. This distortion produces a dipole $\vec{\mu}$. (b) Molecules having a permanent dipole $\vec{\mu}$. It tends to align in the field (in crystal structure, the degree of alignment depends on surrounding molecules)

This static electric field \vec{E} acts on positive and negative charges of the atom (positive charges are pulled in the direction of the field while negative charges are pulled in the opposite direction). This main effect is to disturb and distort the electronic cloud of atom or molecule from its normal equilibrium states. The material is, consequently, polarized (i.e. each molecules or atoms acquire a induce dipole moment).

5.2.1.2 Linear Polarization

Light is commonly described as an oscillating and progressive electromagnetic wave; the electric field is then not static but oscillating. Therefore, the material illuminated by an optical wave can be viewed as a set of oscillating electric dipoles.

At the macroscopic scale, the addition of all the radiations emitted by a set of oscillating dipoles recreates instantaneously (~ 1 attosec) a new electromagnetic wave at the same frequency: this phenomenon is known as the diffusion of light and the response of the material can be described by the polarization \vec{P} .

In the linear case (e.g. sunlight, for which the amplitude of the electric field is in the order of $E_0 \approx 10^{-2} \text{Vm}^{-1}$) (Tilley 2010), the dipoles oscillate proportionally to the electric field amplitude, thus at the same frequency ω than the incident wave. The polarization \vec{P} of the material is then proportional to the incident electric field \vec{E} and can be written as

$$\overrightarrow{P(\omega)}_L = \varepsilon_0 \chi^{(1)} \overrightarrow{E(\omega)} \quad (1.27)$$

With $\chi^{(1)}$ the tensor of electric susceptibility and ε_0 the vacuum permittivity.

5.2.1.3 Nonlinear Polarization

In the nonlinear case, the attractive strength between the electronic cloud and the nucleus is not proportional to the displacement of the electronic cloud. The atom behaves as an anharmonic oscillator. Nonlinearities can be graphically understood through the variation of the electron potential (see Figure 1.19). Under irradiation the electronic cloud is disturbed and the electrons (bonds in atoms and molecules) oscillate about their equilibrium positions r_0 . When the intensity of the incident field is small the oscillation of each dipole can be viewed as harmonic (blue dash line Figure 1.19). But if the incident field is strong enough, the response of the material becomes anharmonic. If the perturbation is periodic, it has for consequence the appearance of new frequencies whose values are multiples of the initial frequency and are called *harmonics* (e.g. 2ω , 3ω , $4\omega, \dots$).

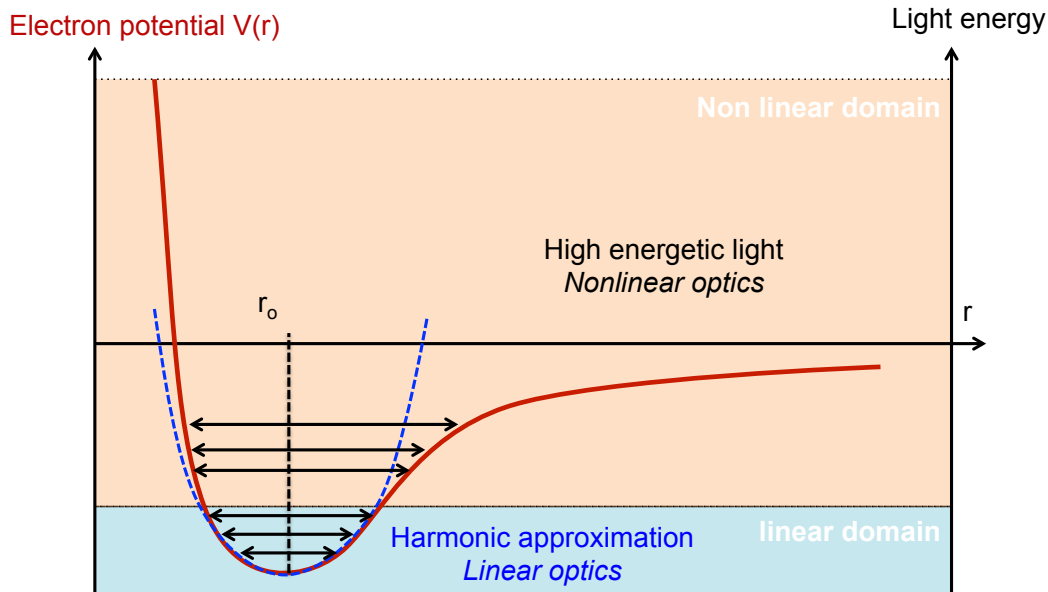


Figure 1.19 Electron potential. The sharp increase of the potential at the origin acts as a wall that keeps the charge from reaching the origin. The minimum represents the equilibrium position r_0 of dipole distance. In linear (blue) domain, oscillation of charge can be approximate by harmonic potential (blue dash-line). For high energetic electric field, the response becomes anharmonic., we enter in (brown) nonlinear domain.

The nonlinear response of the material to a strong incident field can be described using nonlinear susceptibility tensors (Shen 1984; Boyd 2003; Bloembergen 2008) and the macroscopic polarization can then be expressed as a power series expansion of the macroscopic electric field :

$$\vec{P} = \epsilon_0 \left(\chi^{(1)} \vec{E} + \chi^{(2)} \vec{E} \cdot \vec{E} + \chi^{(3)} \vec{E} \cdot \vec{E} \cdot \vec{E} + \dots \right) = \vec{P}_L + \vec{P}_{NL} \quad (1.28)$$

where, $\chi^{(n)}$ corresponds to the linear susceptibility ($n=1$) and the susceptibility tensors of n^{th} ($n=2,3,\dots$) order.

For example, $\chi^{(2)}$ and $\chi^{(3)}$ are, respectively, the nonlinear electric susceptibility tensor of second and third order. In this case, the resulting wave (emitted by the matter) can have a frequency different of the fundamental one.

The polarization evolutions versus the input electric field strength for linear, quadratic and cubic expansions (of equation 2.28) are plotted in Figure 1.20.

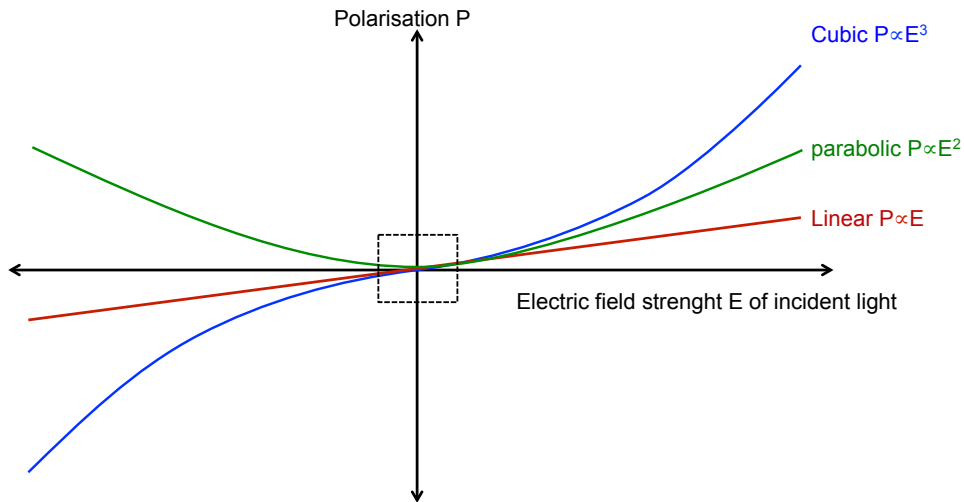


Figure 1.20 Variation of the polarization with the electric field strength for linear, second and third order effects. Dash square at the center denotes the area where all approximate to the linear case (i.e. for low incident energy)

The electric charges in matter are held in equilibrium by atomic fields of the order of 10^8 - 10^9 V/cm, and anharmonicity in their motion (at the origin of harmonic generation) can only be observed by using perturbing fields that are not negligible compared to these values. To enter in the nonlinear response domain of the material, we should use energetic light reaching the order of the characteristic atomic electric field strength: $E_{at}=2 \cdot 10^7$ esu (for hydrogen atom in Bohr approximation). In fact, in crystal, nonlinear phenomena can appear with lower incident energy and it is not necessary to reach energy corresponding at the interatomic bonds (i.e. a rate $E_{at}/E_{light} = 10^{-4}$ will be sufficient). It is because of the coherent oscillation of each dipole, which can interfere constructively and therefore enhanced the nonlinear response of material (intensity of the resulting field is greater than the sum of individual dipole oscillating in incoherent manner).

5.3 Susceptibility tensor $\chi^{(n)}$

The susceptibility tensors link the polarization vector to the electric field vector and govern the optical properties of the material. They are composed of $3^{(n+1)}$ components; for example $\chi^{(1)}$, $\chi^{(2)}$ and $\chi^{(3)}$ are respectively described by 9, 27 and 81 coefficients. It can be noticed that second and subsequent term in the development of the polarization are progressively much smaller than the first term: $\chi^{(1)} > \chi^{(2)} > \chi^{(3)} > \dots > \chi^{(n)}$

This means that only first nonlinear processes could occur in the low optical intensity. To observe a n th order nonlinearity, the material must exhibit either $\chi^{(n)}$ or either E large enough. The magnitude of E depends on the intensity of the light used and $\chi^{(n)}$ is a property

of the material. Lasers are suitable optical sources for the purpose (high power, good monochromaticity, good directivity, good polarization, large coherence length, and further, ultra-short pulses can be realized). The Table 1.7 sums up the main nonlinear effects associated to each susceptibility tensor.

Tensor (unit)	$\chi^{(1)}$	$\chi^{(2)}$ (m.V ⁻¹)	$\chi^{(3)}$ (m.V ⁻²)
Rank	2	3	4
Coefficients	9	27	81
Effects	Refraction Birefringence Absorption Diffraction	SHG $\chi^{(2)}$ (-2 ω , ω , ω) Sum frequency generation $\chi^{(2)}$ (- ω_3 , ω_2 , $\pm\omega_1$) Optical rectification $\chi^{(2)}$ (0, ω , - ω) Linear electro-optic effect (Pockels effect) $\chi^{(2)}$ (- ω , 0, ω)	THG $\chi^{(3)}$ (-3 ω , ω , ω , ω) Degenerate four wave mixing (DFWM) $\chi^{(3)}$ (- ω , ω , - ω , ω) Nonlinear refractive index two-photon absorption (TPA) $\chi^{(3)}$ (- ω , ω , - ω , ω) Cross-phase modulation non degenerate TPA $\chi^{(3)}$ (- ω_1 , ω_1 , - ω_2 , ω_2) General four wave mixing $\chi^{(3)}$ (- ω_4 , ω_3 , ω_2 , ω_1) Electric field induced SHG (EFISH) $\chi^{(3)}$ (-2 ω , 0, ω , ω) Quadratic electro-optic Kerr effect $\chi^{(3)}$ (- ω , 0, 0, ω)
Applications	Glasses, lens, microscope	Laser pointer Tunable laser source Biology marker	Tunable laser source

Table 1.7 Linear, first and second order nonlinear effects and its applications.

A table of $\chi^{(2)}$ tensor coefficients for the noncentrosymmetric crystal classes is given in appendix I (page 217)

5.4 Second harmonic generation (SHG) and conversion efficiency

The susceptibility coefficients decrease rapidly with increasing order. Consequently, in most cases, the nonlinear polarization P_{NL} can be approximated by the quadratic term of equation (1.27): $\epsilon_0 \chi^{(2)} \vec{E} \cdot \vec{E}$

Considering the case of a monochromatic wave of frequency ω , the electric field E can be written using the complex notation as:

$$\vec{E}(\omega) = \frac{1}{2} \left(\vec{E}_0 e^{i(\omega t - \vec{k} \cdot \vec{r})} + \vec{E}_0 e^{-i(\omega t - \vec{k} \cdot \vec{r})} \right) \quad (1.29)$$

then

$$\overrightarrow{E}(\omega) \cdot \overrightarrow{E}(\omega) = \frac{1}{4} \left(2E_0^2 + E_0^2 e^{2i(\omega t - \vec{k} \cdot \vec{r})} + E_0^2 e^{2i(\omega t - \vec{k} \cdot \vec{r})} \right) \quad (1.30)$$

Neglecting terms higher than 2 in equation (1.27), the applied electric field gives rise to the a polarization expressed as:

$$\vec{P} = \varepsilon_0 \chi^{(1)} \overrightarrow{E}(\omega) + 2\varepsilon_0 \chi^{(2)} \overrightarrow{E}_0^2 + \varepsilon_0 \chi^{(2)} \overrightarrow{E}(2\omega) \quad (1.31)$$

The first term of equation (1.31) (at frequency ω) corresponds to the optical polarizability. The second term describes a constant polarization and does not participate to the emission of new frequencies. It is responsible of the optical rectification phenomena (Bass et al. 1962). The third term (at frequency 2ω), is responsible of the phenomenon of second harmonic generation.

In SHG, a fundamental wave of angular frequency ω (wavelength λ), electric field amplitude $E(\omega)$ and wave vector k_ω passing through a material generates a second harmonic wave of angular frequency 2ω (wavelength $\lambda/2$) and wave vector $k_{2\omega}$. The amplitude of the second harmonic electric field $E(2\omega)$ varies with the distance travelled through the medium due to the continuous exchange of energy between the fundamental and the harmonic wave.

The mathematical expression of the light intensity carried by the second harmonic wave through the medium can be obtained by solving the propagation equation given by:

$$\nabla^2 \vec{E} - \mu_0 \varepsilon_0 \frac{\partial^2 \vec{E}}{\partial t^2} = \mu_0 \frac{\partial^2 \vec{P}}{\partial t^2} \quad (1.32)$$

with μ_0 and ε_0 the permeability and the permittivity of the free space respectively.

Armstrong (Armstrong et al. 1962) performed a complete resolution of the propagation equation for waves travelling in the same direction z and assuming that the conversion of the fundamental wave into the SH wave was sufficiently low to consider that the amplitude corresponding to the fundamental wave remains almost unchanged.

This led to the following relation between the incident intensity I_ω sent to the medium and the intensity of the second harmonic $I_{2\omega}(l)$ after a distance l travelled through the medium:

$$I_{2\omega}(l) = \frac{(\omega I_{\omega} \chi^{(2)})^2 l^2 \sin^2\left(\frac{l\Delta k}{2}\right)}{2\varepsilon_0 c^3 n_{\omega}^2 n_{2\omega}} = I_{2\omega}^{max} l^2 \text{sinc}^2\left(\frac{\Delta k l}{2}\right) \quad (1.33)$$

with

$$I_{2\omega}^{max} = \frac{(\omega I_{\omega} \chi^{(2)})^2}{2\varepsilon_0 c^3 n_{\omega}^2 n_{2\omega}}$$

n_{ω} , the refractive index of the material at frequency ω

$n_{2\omega}$, the refractive index of the material at frequency 2ω

l , the distance travelled through the medium

c , the speed of light in vacuum

Δk is the *phase mismatch* expressed as:

$$\Delta k = \left| \overrightarrow{k(2\omega)} - 2\overrightarrow{k(\omega)} \right| = \frac{2\omega}{c} (n_{2\omega} - n_{\omega})$$

The influence of these various parameters on the second harmonic intensity will be detailed in the part 5.5.2, but one can already notice that $I_{2\omega}$ varies as the square of both the nonlinear coefficients and the fundamental intensity.

As the intensity associated to the fundamental and the harmonic waves is the only directly measurable parameter to evaluate the quadratic nonlinear response of a given material, we can introduce here the notion of second harmonic conversion efficiency.

Second harmonic conversion efficiency is defined as the converted intensity with respect to the incident intensity sent through the material. That is to say:

$$\eta(l) = \frac{I_{2\omega}(l)}{I_{\omega}}$$

5.5 Conditions required to observe SHG

5.5.1 Symmetry Conditions

5.5.1.1 Non-centrosymmetry

The observation of second harmonic generation requires the emitting dipoles to be periodically organized with the aim of producing coherent waves. Moreover, periodically organized structures exhibiting inversion symmetry are not supposed to produce SHG since

the presence of an inversion center implies all the coefficients of the third rank tensor $\chi^{(2)}$ to be equal to zero.

Actually, in centrosymmetric media (with inversion center) the sign of the polarization changes when the electric field sign changes (invariant by parity). It can be simply demonstrated with respect to the polarization vector. If an inversion center is present, the polarization must reverse the sign for a reversal of the applied electric field, regardless the complexity of the tensor relationship between them (cf. Figure 1.21). But, as simply demonstrated in the equation (1.34), for the even n order, $(-E)^n$ remains E^n and it results in that $P=-P$.

$$-\vec{P}_{NL} = \epsilon_0 \chi^{(2)} (-\vec{E}(\omega)) \cdot (-\vec{E}(\omega)) = \epsilon_0 \chi^{(2)} \vec{E}(\omega) \cdot \vec{E}(\omega) = \vec{P}_{NL} \quad (1.34)$$

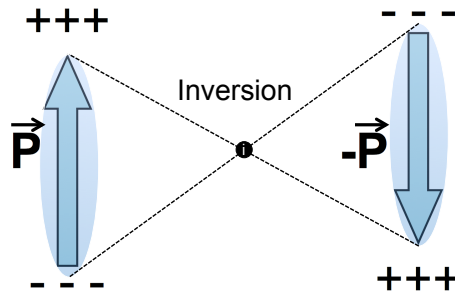


Figure 1.21 Inversion center operator symmetry on polarization vector.

As a consequence, all the coefficients of the susceptibility tensors of even order ($\chi^{(2)}, \chi^{(4)}, \dots$) vanish in centrosymmetric media (conventional liquid, gases, amorphous solids, centrosymmetric crystals) in absence of an external DC field (Armstrong et al. 1962; Franken and Ward 1963).

Thus, only non-centrosymmetric crystals and macromolecular assemblies which are fairly ordered to form large noncentrosymmetric structures (e.g. collagen or myosin) can generate SHG. There is no restriction for the odd-power terms of the susceptibility tensors and phenomena associated to $\chi^{(1)}$ and $\chi^{(3)}$ can appear in all materials.

In crystalline material in particular, the intrinsic symmetry of the crystal governs the tensor properties and imposes supplementary restrictions in relation with on one hand the Neumann principle (Nye 1986) and on the other hand, the Kleinman permutation rules (Kleinman 1962).

5.5.1.2 Neumann Principle

The Neumann principle (Nye 1986) asserts that macroscopic physical properties of a crystal must exhibit, at least, the symmetry of the point group to which the crystal belongs. In other term, if the crystal has symmetry thus the property must also exhibit this symmetry. The property is expected to exhibit the symmetry of the point group or more but not less. This assertion can be understood by looking, for example, to the snowflake, which has a 6-fold symmetry about an axis perpendicular at the sheet. Rotating the crystal through the angle of 60° about that axis would generate a new crystal but with atomic arrangement identical to the crystal before the rotation. The crystal is said invariant under the 6-fold symmetry operation and this must be true for every symmetry elements belongs to the crystal class of the crystal.

Based on the Neumann principle, it is possible to reduce the number of independent coefficients of the susceptibility tensor. In the same manner than for the inversion center, it is possible, by application of the symmetry elements of the point group to find relation that simplify the susceptibility tensor coefficients (see reference Nye 1986)

One of the major results is that SHG is not possible in **432** point group.

5.5.1.3 Kleinman Symmetry rules (Kleinman 1962)

To produce SHG, there is a particular interest in using wavelengths far from the resonance frequencies of the material mainly because the medium is then only dispersive without loss of energy but also because the nonlinear susceptibilities are independent of the frequency. These “non resonant” conditions studied by Kleinman (Kleinman 1962) lead to reduce to 10 (instead of 27) the number of independent coefficients in $\chi^{(2)}$. The most important consequence of Kleinman symmetry is that, in combination with the above symmetry restrictions due to “Neumann” principle, it requires that all the $\chi^{(2)}$ coefficients in the point groups 422 and 622 vanish. Thus SHG should not be observable for crystals belonging to this two space groups which reduces the number of possible analyzable crystals.

A statistical survey of molecular structures crystallizing in such point group is sum-up in Table 1.8. It was found that it represents only 2.41% of non-centrosymmetric structures. This limits this drawback. Moreover, it is quite unusual that no absorption at all occurs in a material. In fact, many compounds crystallizing in these system classes have proved to exhibit a positive SHG signal and it seems that this restriction is the exception rather than the rule for

organic solids at the incident wavelength of 1064 nm. (Dailey et al. 2004; Zhao et al. 2012).

	422		432		622	
Space group	<i>P</i> 422	7	<i>P</i> 432	5	<i>P</i> 622	5
	<i>P</i> 42 ₁ 2	46	<i>P</i> 4 ₁ 32	36	<i>P</i> 6 ₁ 22	186
	<i>P</i> 4 ₁ 22	56	<i>P</i> 4 ₂ 32	5	<i>P</i> 6 ₂ 22	45
	<i>P</i> 4 ₁ 2 ₁ 2	1377	<i>P</i> 4 ₃ 32	27	<i>P</i> 6 ₃ 22	86
	<i>P</i> 4 ₂ 22	6	<i>F</i> 432	22	<i>P</i> 6 ₄ 22	30
	<i>P</i> 4 ₂ 2 ₁ 2	120	<i>F</i> 4 ₁ 32	24	<i>P</i> 6 ₅ 22	141
	<i>P</i> 4 ₃ 22	47	<i>I</i> 432	21		
	<i>P</i> 4 ₃ 2 ₁ 2	1156	<i>I</i> 4 ₁ 32	20		
	<i>I</i> 422	43				
	<i>I</i> 4 ₁ 2 ₁ 2	70				
Total/% NC CSD	2922/1.97		160/0.11		493/0.33	

Table 1.8 Statistical survey of structures crystallizing in point group 422, 622 and 432. (CCDC database Nov 2013)

5.5.2 Parameters limiting the conversion efficiency in crystals: Phase-matching conditions (for constructive interferences)

The energy conversion efficiency from fundamental to harmonic is about 1 part in 10^8 (New 2012). The reason of this small efficiency is due to the spatial dependence of the field through the material. (Maker et al. 1962)

As previously mentioned, during the propagation along the crystal, there is a continuous exchange of energy between the fundamental and the second harmonic waves (Armstrong et al. 1962; Boyd 2003). The Manley-Rowe relation (Manley and Rowe 1956) states that the rate at which a photon at frequency 2ω is created is equal to the rate at which two photons at frequency ω are destroyed. In general, the newly created waves and fundamental phase are not in phase which generates interferences. Consequently, the intensity of the SHG wave emerging from the crystal can be very low due to destructive interferences. Destructive interferences can only be prevented if all of the beams remain in phase. This condition is called *phase-matching* condition. When conditions for phase-matching are fulfilled the generated wave maintains a fixed phase relation with respect to the nonlinear polarization and is able to extract energy most efficiently from the incident wave. (i.e. all microscopic dipole are phased and fields emitted by each dipole add coherently).

In paragraph 5.4 (page 57) we show that the SHG intensity obtained after a distance l travelled through the material is given by

$$I_{2\omega}(l) = \frac{(\omega I_{\omega} \chi^{(2)})^2 l^2 \sin^2\left(\frac{l\Delta k}{2}\right)}{2\epsilon_0 c^3 n_{\omega}^2 n_{2\omega} \left(\frac{l\Delta k}{2}\right)^2} = I_{2\omega}^{max} l^2 \text{sinc}^2\left(\frac{\Delta k l}{2}\right) \quad (1.35)$$

Δk is the *phase mismatch* expressed as:

$$\Delta k = \left| \vec{k}(2\omega) - 2\vec{k}(\omega) \right| = \frac{2\omega}{c} (n_{2\omega} - n_{\omega})$$

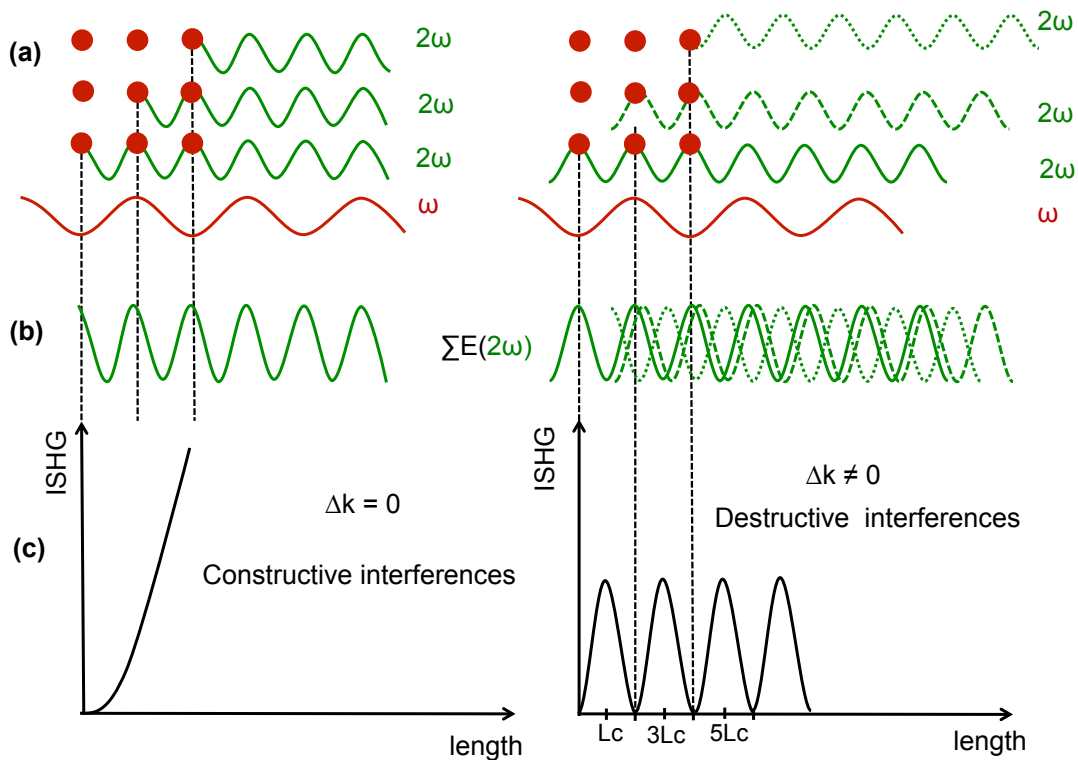


Figure 1.22 As the nonlinear susceptibilities are weak quantities, all electric dipoles must oscillate in phase in order to produce an amplified waves. (a) fundamental wave induced second-harmonic polarization $P(2)$, and second-harmonic waves generated at different positions in a nonlinear material for two different cases. Left: second-harmonic waves travel at the same velocity as the fundamental wave, all are in-phase. Right: different velocities, the usual case, mismatch between the phases of the second-harmonic waves. (b) Consequently, the SHG waves add up coherently (left) or destructively (right). (c) Finally the SHG intensity grows quadratically with the distance l travelled by the light in the crystal for achieved phase-matching (left) and varies sinusoidally with a maxima every odd coherence length multiples.

Second-order processes have to satisfy the energy conservation condition:

$$\omega + \omega = 2\omega$$

And for an efficient conversion phase-matching is also required that:

$$2k(\omega) = k(2\omega) \text{ (momentum conservation)}$$

where

$$k(\omega) = \frac{\omega n(\omega)}{c}$$

If $\Delta k \neq 0$ then the SH intensity reaches a maximum value for $l = nL_c$ where $n = 1, 3, 5, \dots$ with L_c expressed as :

$$L_c = \frac{\pi}{|\Delta k|} = \frac{\lambda}{4|n_{2\omega} - n_{\omega}|}$$

L_c is called the *coherence length*, and is defined as the distance in the crystal for which both waves are in phase. During the first L_c distance travelled inside the crystal, the SHG signal grows to reach a maximum. For $L_c < l < 2L_c$ the energy is back-converted from the harmonic wave to the fundamental wave. For $l = 2L_c$, the two waves are out of phase and the SHG signal is minimum. In numerous materials (organic and inorganic), the coherence length has been evaluated to few μm (Kurtz and Perry 1968; New 2012).

If $\Delta k = 0$, the two waves remain in phase and the intensity of the SH signal is maximum, growing as the square of the distance l . This particular case called phase-matching conditions is obtained if the refractive indices at ω and 2ω are equal :

$$n(\omega) = n(2\omega)$$

However, materials are usually dispersive which means that the refractive index varies with frequency. For normal dispersion, the refractive indices increase with frequency (i.e. $n(2\omega) > n(\omega)$). This obviously makes it difficult to achieve the phase-matching condition. Nevertheless, it is possible to use the birefringence properties of certain crystals (Franken et al. 1961).

5.6 Achieving Phase-matching conditions

5.6.1 Angle phase-matching

The dependence of refractive index versus crystalline systems is summarized in Table 1.9.

System	Linear optical property	Number of refractive index
Triclinic, monoclinic, orthorhombic	Biaxial	3
Trigonal, tetragonal, hexagonal	Uniaxial	2
Cubic	Isotropic	1

Table 1.9 Crystalline system and dependency of refractive index

Cubic crystals are isotropic (i.e. exhibit no birefringence); the condition of phase matching can not be achieved. Cubic crystals are consequently classified as not phase-matchable crystals and will usually exhibit only a very weak SHG signal.

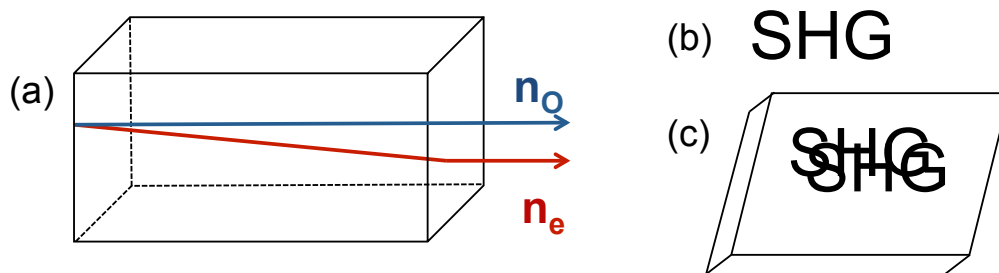


Figure 1.23 (a) Light beam entering in birefringent uniaxial crystal (not along the optical axis). The fundamental beam is split into an ordinary (blue line) and an extraordinary (red line) beams. (b) a image (SHG letters) (c) the same image see through a birefringent crystal appears doubled.

Crystal refractive indices can be described by an ellipsoid. This ellipsoid is derived from the linear susceptibility tensor, thus must be compatible with the point group symmetry. For uniaxial crystals, there are two different principal refractive indices: along the optical axis (e.g. c axis) is the extraordinary n_e index and the ordinary n_o along a and b axis. The ellipsoid for a uniaxial crystal is rotationally symmetric and is described Figure 1.24. In birefringent uniaxial crystals, the refractive index depends on the incident direction of the fundamental beam (Figure 1.24). This refractive ellipsoid depends on the wavelength, too. It is then possible to find propagation directions for which the velocities of fundamental and harmonic waves are identical (Figure 1.25).

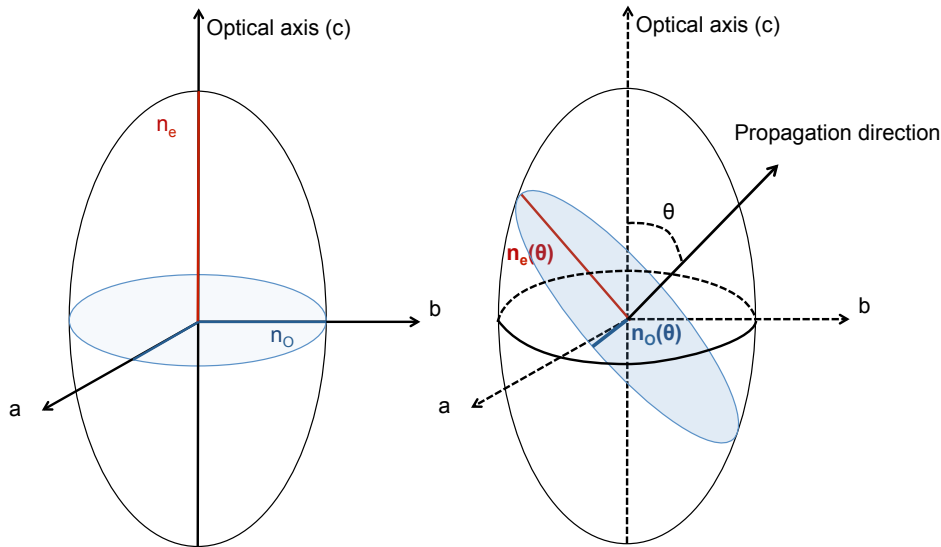


Figure 1.24 Refractive index ellipsoid for uniaxial crystal

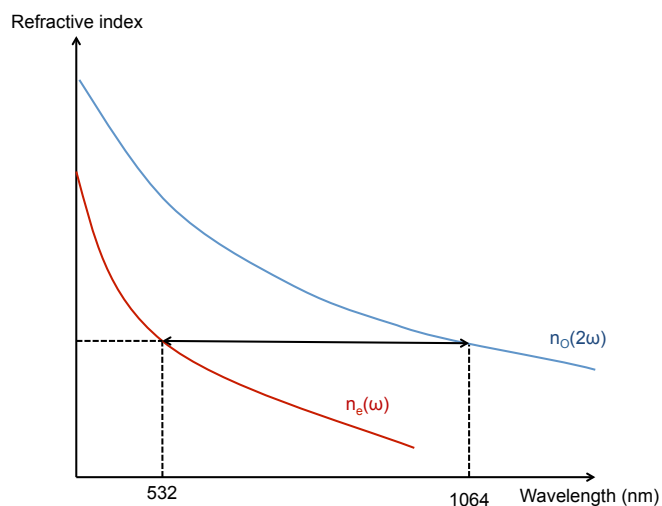


Figure 1.25 achievement of phase-matching condition. Refractive index at ω is the same of the ordinary refractive index at 2ω . In this condition, phase-matching is achieved.

5.6.2 Noncritical phase matching (or temperature phase matching)

The refractive index of a material is also a function of the temperature. The Sellmeier relation (Sellmeier 1871) can be used to describe the dependence of refractive index with respect to the temperature. Consequently, it is also possible to achieve phase-matching conditions by increasing or decreasing the temperature. This technique is often used in optical devices (Ghosh 1998; Regelskis et al. 2012). Another way to achieve phase-matching is a spatial modulation of the nonlinear susceptibility (e.g. by inverting the crystal axis every coherence length) known as *quasi-phase-matching*. (Armstrong et al. 1962; Miller 1964)

Nevertheless the calculation of the phase-matching direction and/or temperature remains difficult because of a lack of reliable and available optical parameters notably in organic solids.

Moreover, achieving the phase-matching conditions is not sufficient to obtain a detectable SHG signal. Crystals must be transparent to wavelength 2ω and ω ; exhibit a low absorption energy (the local temperature could drastically increase with a possible destruction of the sample). This latter condition is linked to the damage threshold of the crystal (maximal tolerate time of exposure and laser intensity). Obviously, the crystal must exhibit a large enough effective nonlinear coefficient $\chi^{(2)}$. Other considerations exist as the optical molecular properties.

5.7 Phase-matchable and non-phase matchable material

In powder sample, crystals are randomly oriented and assure that a proportion of the sample is in phase-matching condition. Due to the random orientation, the SHG intensities of different particles add up incoherently. The Laser illuminates a volume V (containing N particles). The SHG intensity is modified by the length r of the crystal and two kinds of behavior described the evolution of the SHG intensity versus the crystal size of powdered samples.

For a *non-phase-matchable material* the SHG intensity for each particle of size r will increase quadratically with r for particle size lower than the coherence length L_c . Then, it reaches a constant value I_{\max} (proportional at L_c^2). The total SHG intensity is described as:

$$I_{SHG} = Nr^2I_p \approx \begin{cases} r, r < L_c \\ \frac{L_c^2}{r}, r \geq L_c \end{cases}$$

For a *phase-matchable material*, results are similar for particles lower than L_c and for larger particles the signal must increase quadratically too but only for properly oriented particles (i.e. in phase-matching condition). This leads to a SHG intensity plateau for larger particles.

The evolution of SHG intensity versus particles size for both material behaviors is described in Figure 1.26

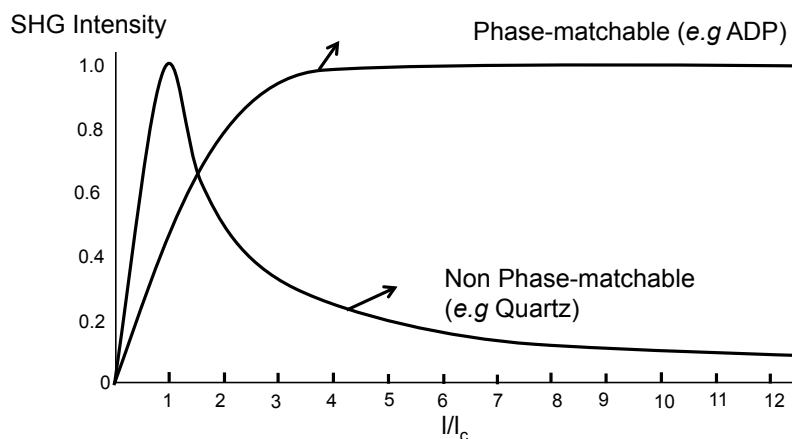


Figure 1.26 SHG intensity evolution with travelled distance in crystal for phase matchable and non phase matchable material

5.8 Properties of molecules

From the beginning, the non-centrosymmetry of the crystal is described as the principal prerequisite of the SHG. Although the noncentrosymmetric symmetry of the crystal packing allow the possibility to detect a SHG signal, it is not the origin of the 2ω wavelength by itself. Attention must be paid to the properties of the constitutive matter of the crystal: the molecules. The macroscopic changes in polarization are caused by microscopic changes in the dipoles moment of the molecules. Under local static electric field, the molecular dipole moment \vec{p} is given as:

$$\vec{p} = \vec{\mu} + \overline{\alpha}\vec{E} + \beta\vec{E}\cdot\vec{E} + \gamma\vec{E}\cdot\vec{E}\cdot\vec{E} + \dots$$

At the molecular level, this relation is equivalent to the macroscopic polarization where α is the linear molecular polarizability, β the first and γ the second molecular hyperpolarizabilities. $\vec{\mu}$ is the permanent electric dipole, if any, of the molecule without applied electric field.

The polarizability of a chemical entity reflects how easy it is to distort the electron density within a molecule (or atom). The relation between polarizability and polarization is dynamic, because the oscillating field causes dipole oscillation *and* the dipole oscillation induces light emission.

Macroscopic crystalline susceptibilities $\chi^{(n)}$ can be related to the molecular polarizabilities described above, it is usually assumed that the molecules are independently polarized by the light with no interatomic or intermolecular coupling. Within this approximation $\chi^{(n)}$ is then given by the sum of all the individual polarizabilities (Vogt and Happ 1971; Singer et al. 1987) (note that more sophisticated approaches including molecular interaction exist(Munn

1988)):

$$\chi^{(1)} = \frac{1}{V} \sum \alpha$$

$$\chi^{(2)} = \frac{1}{V} \sum \beta$$

Consequently, α and β are tensors with, respectively, the same dimension and properties than $\chi^{(1)}$ and $\chi^{(2)}$. The β hyperpolarizability causes second harmonic frequency doubling (SHG).

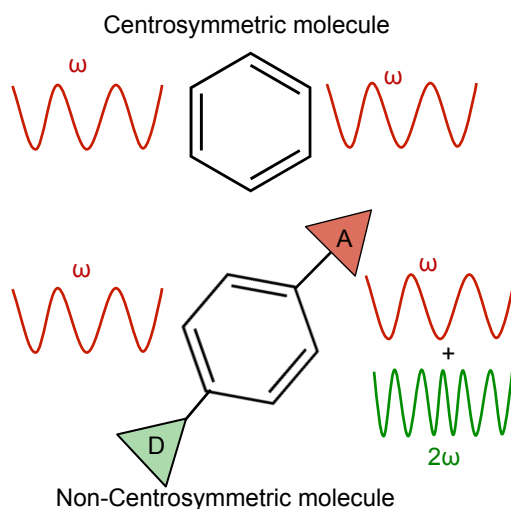


Figure 1.27. No SHG for centrosymmetric molecule. Generation of second harmonic by non centrosymmetric molecule

Researches conducted in nonlinear optics showed that electron donor-acceptor-systems exhibit the greatest anharmonicity (Chemla 2012) with organic compounds reaching SHG intensity several orders of magnitude higher than usual inorganic noncentrosymmetric crystals (Kaino and Tomaru 1993). Nevertheless, for applications, frequency doubling is a bulk property in the solid state. This means that the dipoles of neighboring molecules can either reinforce or negate each other's effects with a total cancellation of 2ω contributions in centrosymmetric packing.

Second-order effects can only occur in non-centrosymmetric crystals and until now, it has been assumed that the smallest building block, the molecule, should satisfy this requirement. Subsequently, no SHG can occur within centrosymmetric molecules (i.e. where $\beta=0$). This could be a great restriction to the number of analyzable crystals. Fortunately, the molecular conformational versatility and supramolecular forces, such as hydrogen bonding or

coordination bonds (Desiraju 2003a), can ensure that the molecules pack into non-centrosymmetric space groups (i.e. the molecules becomes non-centrosymmetric in the solid state).

However, the question of SHG emitted by centrosymmetric molecules packed in noncentrosymmetric space group arises. In fact, it seems that such arrangements are not possible. Based on Kitajgorodskij considerations (see Wilson 1993), the centrosymmetry in crystal structures seems the rule followed by the Nature (see statistics 2.6 page 26.) He has shown that the molecules should not be centrosymmetric when packed in a non-centrosymmetric space group (at least in triclinic, monoclinic and orthorhombic spaces groups which notwithstanding represent the majority of SG for organic molecules) (Pidcock 2005). Rare and unexpected examples exist in literature and will be discussed in a part of the next chapter that deals on the elaboration of the SHG device, its reliability and several usual uses of the SHG method to compare our apparatus with literature results.

References

- Allen FH. The Cambridge Structural Database: a quarter of a million crystal structures and rising. *Acta Crystallogr B Struct Sci. International Union of Crystallography*; 2002 May 29;58(3):380–8.
- Armstrong J, Bloembergen N, Ducuing J, Pershan P. Interactions between Light Waves in a Nonlinear Dielectric. *Phys. Rev.* 1962 Sep;127(6):1918–39.
- Ågren J. On the classification of phase transformations. *Scripta materialia*. Elsevier; 2002;46(12):893–8.
- Bass M, Franken P, Hill A, Peters C, Weinreich G. Optical Mixing. *Physical Review Letters*. 1962 Jan;8(1):18–8.
- Baur WH, Kassner D. The perils of Cc: comparing the frequencies of falsely assigned space groups with their general population. *Acta Cryst* (1992). B48, 356-369 [doi:10.1107/S0108768191014726]. *International Union of Crystallography*; 1992 Aug 1;:1–14.
- Beckmann W. *Crystallization: Basic Concepts and Industrial Applications*. John Wiley & Sons; 2013.
- Bernstein J. *Polymorphism in molecular crystals*. Clarendon Press/International Union of Crystallography; 2002.
- Bernstein J. Polymorphism – A Perspective. *Crystal Growth & Design*. 2011 Mar 2;11(3):632–50.
- Bernstein J, Davey RJ, Henck J-O. Concomitant Polymorphs. *Angew. Chem. Int. Ed.* 1999 Nov 30;38(23):3440–61.
- Bloembergen N. *Nonlinear Optics*. 2008. pp. 1–45.
- Boyd RW. *Nonlinear Optics (Second Edition)*. Elsevier, editor. *Optic Communications*; 2003.
- Brittain HG. *Polymorphism in pharmaceutical solids*. Informa HealthCare; 2009.

- Burger A, Ramberger R. On the polymorphism of pharmaceuticals and other molecular crystals. II. *Microchimica Acta*. Springer; 1979;72(3):273–316.
- Chemburkar SR, Bauer J, Deming K, Spiwek H, Patel K, Morris J, et al. Dealing with the Impact of Ritonavir Polymorphs on the Late Stages of Bulk Drug Process Development. *Org. Process Res. Dev.* 2000 Sep;4(5):413–7.
- Chemla DS. *Nonlinear Optical Properties of Organic Molecules and Crystals*. Elsevier; 2012.
- Christian J. *The Theory of Transformations in Metals and Alloys: Part I+ II*. Elsevier; 2002.
- Coquerel G. The “structural purity” of molecular solids—An elusive concept? *Chemical Engineering and Processing*. 2006 Oct;45(10):857–62.
- Dailey CA, Burke BJ, Simpson GJ. The general failure of Kleinman symmetry in practical nonlinear optical applications. *Chemical Physics Letters*. 2004 May;390(1-3):8–13.
- De L'Isle J-B-LR. *Des caractères extérieurs des minéraux*. 1784.
- Desiraju GR. *Crystal Design*. Wiley; 2003a.
- Desiraju GR. Crystal engineering. From molecules to materials. *Journal of Molecular Structure*. Elsevier; 2003b;656(1):5–15.
- Dunitz JD, Bernstein J. Disappearing polymorphs. *Acc. Chem. Res.* ACS Publications; 1995;28(4):193–200.
- Fedorov ES. An Introduction to the Theory of figures. *Notices of the Imperial Petersburg Mineralogical Society*; pp. 1–279.
- Findlay A. *The Phase Rule and Its Applications...* 2012.
- Fischer PJ, Hanson RM, Riley P, Schweinfus J. Using Graphs of Gibbs Energy versus Temperature in General Chemistry Discussions of Phase Changes and Colligative Properties. *J. Chem. Educ.* 2008 Aug;85(8):1142.
- Franken P, Ward J. Optical Harmonics and Nonlinear Phenomena. *Rev. Mod. Phys.* 1963 Jan;35(1):23–39.
- Franken PA, Hill AE, Peters CW, Weinreich G. Generation of Optical Harmonics. *Phys. Rev. Lett.* American Physical Society; 1961 Aug;7:118–9.
- Garnier S, Petit S, Coquerel G. Dehydration mechanism and crystallisation behaviour of lactose. *Journal of Thermal Analysis and Calorimetry*. Akadémiai Kiadó, co-published with Springer Science+ Business Media BV, Formerly Kluwer Academic Publishers BV; 2002;68(2):489–502.
- Gehler JST, Littrow KL, Brandes HW, Gmelin L, Horner JC, Muncke GW, et al. *Johann Samuel Traugott Gehler's Physikalisches wörterbunch*. 1825.
- Ghosh G. *Handbook of Optical Constants of Solids*. Academic Press; 1998.
- Gibbs JW. *Equilibre des systemes chimiques* translated by H. Le Chatelier. Le Chatelier. 1899.
- Gibbs JW. On the Equilibrium of Heterogeneous Substances" reprinted in *The Scientific Papers of J. Willard Gibbs, Vol. I*. Longmans, Green & Co; 1906.
- Grunenberg A, Henck J-O, Siesler HW. Theoretical derivation and practical application of energy/temperature diagrams as an instrument in preformulation studies of polymorphic drug substances. *International Journal of Pharmaceutics*. Elsevier; 1996;129(1):147–58.
- Hahn T. *International Tables for Crystallography, Brief Teaching Edition of Volume A*. Springer; 2002.

Haüy RJ. Essai d'une théorie sur la structure des cristaux, appliquée à plusieurs genres de substances cristallisées. Chez Gogué & Née de la Rochelle; 1784.

Henck J-O, Kuhnert-Brandstatter M. Demonstration of the terms enantiotropy and monotropy in polymorphism research exemplified by flurbiprofen. *J. Pharm. Sci.* 1999 Jan;88(1):103–8.

Herbstein FH. On the mechanism of some first-order enantiotropic solid-state phase transitions: from Simon through Ubbelohde to Mnyukh. *Acta Crystallogr B Struct Sci. International Union of Crystallography*; 2006 May 15;62(3):341–83.

Hilfiker R. *Polymorphism: in the pharmaceutical industry.* John Wiley & Sons; 2006.

Hurst C. Phase Transitions of the First and Second Orders. *Proc. Phys. Soc. B.* 1955 Dec 18;68(8):521–5.

Jackson KA. *Kinetic Processes.* Wiley-VCH; 2010.

Kaino T, Tomaru S. Organic materials for nonlinear optics. *Adv. Mater.* 1993 Mar;5(3):172–8.

KIRK J, DANN S, BLATCHFORD C. Lactose: A definitive guide to polymorph determination. *International Journal of Pharmaceutics.* 2007 Apr 4;334(1-2):103–14.

Kleinman DA. Theory of Second Harmonic Generation Light. *Physical Review.* 1962 Nov 15;128(4):1–15.

Kurtz SK, Perry TT. A Powder Technique for the Evaluation of Nonlinear Optical Materials. *J. Appl. Phys. AIP*; 1968;39(8):3798–813.

Lee EH. A practical guide to pharmaceutical polymorph screening & selection. *Asian Journal of Pharmaceutical Sciences.* 2014 May.

Lomonosov MV. On the Genesis and Nature of Saltpeter. *Academy of Sciences, St. Petersburg.* 1749 Jul 27.

Maiman T. Optical and Microwave-Optical Experiments in Ruby. *Physical Review Letters.* 1960 Jun;4(11):564–6.

Manley J, Rowe H. Some General Properties of Nonlinear Elements-Part I. General Energy Relations. *Proc. IRE.* 1956 Jul 20;44(7):904–13.

Maker P, Terhune R, Nisenoff M, Savage C. Effects of Dispersion and Focusing on the Production of Optical Harmonics. *Physical Review Letters.* 1962 Jan;8(1):21–2.

McCrone WC, Fox D, Labes MM, Weissberger A, Rice SA. *Physics and Chemistry of the Organic Solid State. Volume 2.* *Phys. Today.* 1965;18(8):59.

Miller RC. OPTICAL SECOND HARMONIC GENERATION IN PIEZOELECTRIC CRYSTALS. *APPLIED PHYSICS LETTERS.* 1964;5(1):17.

Mnyukh Y. Mechanism and kinetics of phase transitions and other reactions in solids. 2011 Oct 7.

Mnyukh Y. On the Phase Transitions That Cannot Materialize. *arXiv preprint arXiv:1310.5009.* 2013.

Muller P, Herbst-Irmer R, Spek A, Schneider T, Sawaya M. Crystal structure refinement. *International Union of Crystallography*; 2006. pp. 1–95.

Munn RW. Electric dipole interactions in molecular crystals. *Molecular Physics.* Taylor & Francis Group; 1988 May;64(1):1–20.

New G. *Introduction to Nonlinear Optics.* Cambridge University Press; 2012. pp. 1–276.

Nye JF. *Physical properties of crystals : their representation by tensors and matrices.* 1986.

- Ostwald W, Taylor WW. *Outlines of General Chemistry*. Nabu Press; 1912.
- Ouvrard C, Mitchell JBO. Can we predict lattice energy from molecular structure? *Acta Crystallogr B Struct Sci*. 2003 Oct;59(Pt 5):676–85.
- Pidcock E. Achiral molecules in non-centrosymmetric space groups. *Chem. Commun. The Royal Society of Chemistry*; 2005;(27):3457–9.
- Porter DA, Easterling KE. *Phase Transformations in Metals and Alloys, (Revised Reprint)*. CRC press; 1992.
- Regelskis K, Želudevičius J, Gavrilin N, Račiukaitis G. Efficient second-harmonic generation of a broadband radiation by control of the temperature distribution along a nonlinear crystal. *Opt Express. Optical Society of America*; 2012;20(27):28544–56.
- Sellmeier W. Zur Erklärung der abnormen Farbenfolge im Spectrum einiger Substanzen. *Annalen der Physik und Chemie*. 1871 Feb 18;219:272–82.
- Senechal M, Galiulin RV. An introduction to the theory of figures: The geometry of ES Fedorov. *Structural Topology* 1984 núm 10. 1984.
- Shafrafovskii II. 14.10. Kepler's crystallographic ideas and his tract 'The six-cornered snowflake'. *Vistas in Astronomy. Elsevier*; 1975;18:861–76.
- Shen YR. *Principles Of Nonlinear Optics*. 1984. pp. 1–553.
- Sheth A, Grant D. Relationship between the structure and properties of pharmaceutical crystals. *Kona*. 2005;23:36–48.
- Singer KD, Kuzyk MG, Sohn JE. Second-order nonlinear-optical processes in orientationally ordered materials: relationship between molecular and macroscopic properties. *J. Opt. Soc. Am. B. Optical Society of America*; 1987;4(6):968–76.
- Steno N, Winter JG. *The Prodrum of Nicolaus Steno's Dissertation Concerning a Solid Body Enclosed by Process of Nature Within a Solid; an English Version with an Introduction and Explanatory Notes by John Garret Winter, with a Foreword by William H. Hobbs*. 1926.
- Šesták J, Mareš JJ, Hubík P. *Glassy, amorphous and nano-crystalline materials: thermal physics, analysis, structure and properties*. Springer; 2010;8.
- Threlfall T. Structural and Thermodynamic Explanations of Ostwald's Rule. *Org. Process Res. Dev. American Chemical Society*; 2003 Nov;7(6):1017–27.
- Tilley RJD. *Colour and The Optical Properties of Materials*. Wiley; 2010.
- Tschoegl NW. *Fundamentals of Equilibrium and Steady-State Thermodynamics*. Elsevier; 2000.
- Upadhyay P, Dantuluri AK, Kumar L, Bansal AK. Estimating relative stability of polymorphs by generation of configurational free energy phase diagram. *J. Pharm. Sci.* 2012 Feb 17;101(5):1843–51.
- Vogt H, Happ H. The temperature dependence of the optical nonlinear susceptibility of sodium nitrite. *Phys. Stat. Sol. (b)*. 1971 Mar 1;44(1):207–16.
- Willart JF, Hédoux A, Guinet Y, Danède F, Paccou L, Capet F, et al. Metastability release of the form alpha of trehalose by isothermal solid state vitrification. *J. Phys. Chem. B*. 2006 Jun 15;110(23):11040–3.
- Wilson AJC. Kitajgorodskij's categories. *Acta Crystallogr A Found Crystallogr*. 1993 Jan;49(1):210–2.
- Zhao H-J, Zhang Y-F, Chen L. Strong Kleinman-Forbidden Second Harmonic Generation in Chiral Sulfide: La₄InSbS₉. *J. Am. Chem. Soc.* 2012 Feb;134(4):1993–5.

Chapter 2. Development of a versatile SHG set-up and reliability of the measurements

Part.1 Introduction

The majority of compounds of interest for the SMS laboratory and broadly in material science are synthesized in powder form. DSC and XRPD are commonly used to characterize these compounds and especially to obtain information on the thermal behavior and crystal structure. However, these techniques suffer limitations (notably a low detection threshold).

Consequently, there is a particular interest in developing novel and more sensitive characterization technique (e.g. exhibiting high detection thresholds of impurities in the crystalline state either chemical or structural). To this purpose, technique based on SHG could be of relevance.

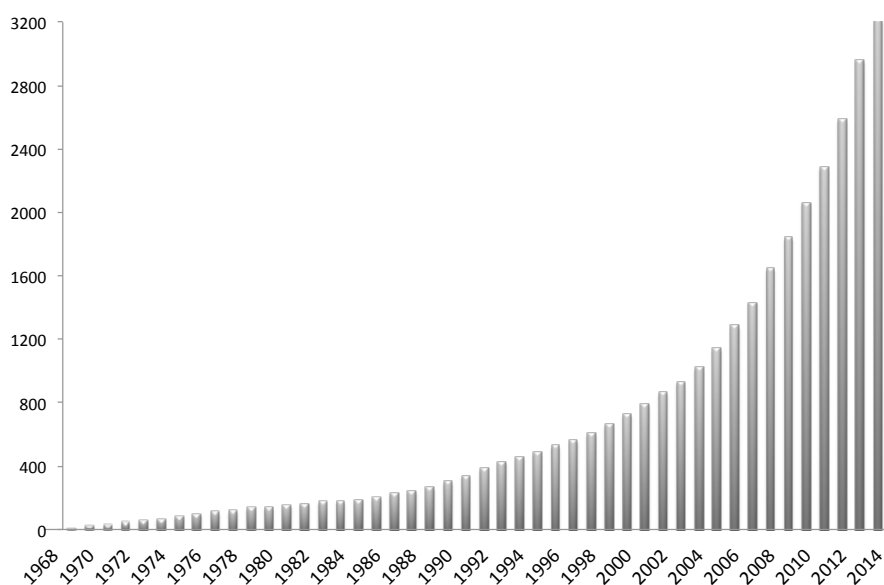


Figure 2.1 Number of citations since 1968 of the S. K. Kurtz and T. T. Perry, “A Powder Technique for the Evaluation of Nonlinear Optical Materials,” *J. Appl. Phys.*, vol. 39, no. 8, pp. 3798–3813.

One of the main interests of SHG measurements is the possibility to conduct experiments either on single crystal or on powdered sample. Large single crystals are, in general, necessary to characterize the *linear and nonlinear* optical properties such as spectral transmission range, refractive indices, coefficients of the susceptibility tensors (Maker et al. 1962). But relevant information can also be extracted from the SHG signal emitted by powdered samples (Aramburu et al. 2011; 2013; 2014).

The powder measurement technique has been developed by Kurtz and Perry (K&P) (Kurtz and Perry 1968) in the 60’s and is extremely popular for evaluating or surveying new nonlinear optical materials (total amount of citations is close to 3300 in 2014; see Figure 2.1).

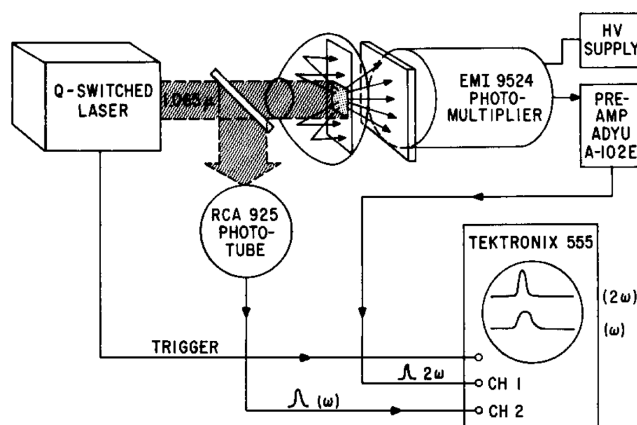


Figure 2.2 Initial set-up developed in 1968 (from: Kurtz and Perry 1968). A laser beam irradiated a sample and the SHG signal, if any, was detected using a photomultiplier and quantified with an oscilloscope.

The principal goal of this thesis work was to evaluate the potential of SHG measurements for the fine characterization of organic solids (in the crystalline state). This led us to adapt the existing set up developed by Kurtz and Perry (see Figure 2.2) in order to fit our experimental requirements (spectral analysis, study of efflorescent compounds in equilibrium with their mother liquor, regulation of temperature, gas flow and hygrometry control, etc.). In following, the improvements incorporated into the initial K&P set-up and numerous tests performed in order to assess the reliability and the sensitivity of the device are reported.

Part.2 Development of a versatile SHG set-up for powder measurements

2.1 Ameliorations to Kurtz and Perry (K&P) set-up

2.1.1 Spectral analysis

Compared to the set-up developed by K&P, a major difference is the use for the signal detection of a spectrometer that allows direct spectral analysis of the light emitted by the sample. K&P used a photo-multiplier (PM) to detect the SHG signal. Although, the detection threshold of PM is better than a spectrometer, in counter-part, it is a technical and expensive complications. Indeed, it is necessary and time consuming to check the wavelength of detected photons and to determine if the recorded signal is only composed of the SHG contribution. The use of a spectrometer avoids this problem (*i.e.* the system detects only photon at 2ω) and allows to perform SHG measurements in short time (typically 3sec). A typical spectrum obtained for α -quartz reference is show in Figure 2.3. It is suitable to monitor the evolution with respect to time or temperature of a powdered sample

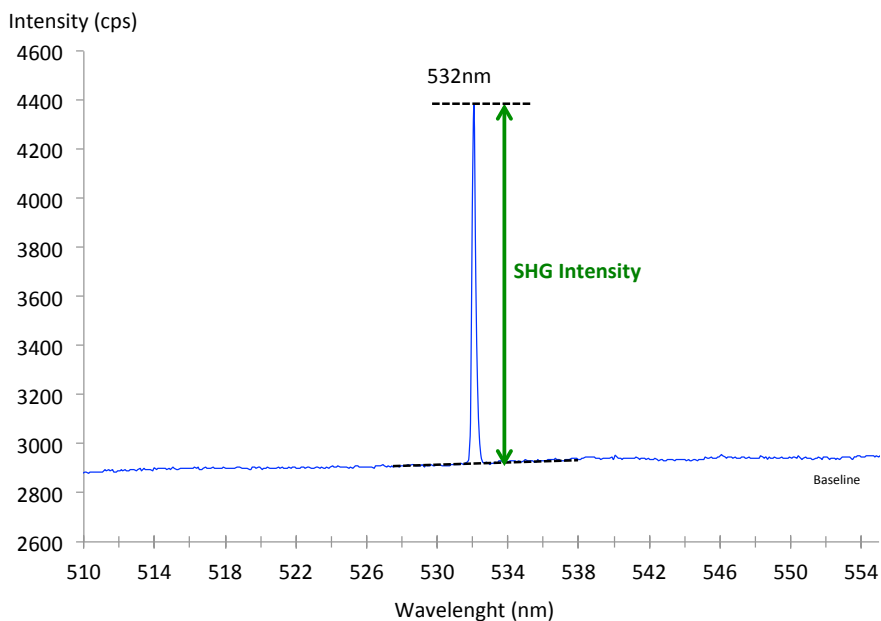


Figure 2.3 SHG spectrum typically obtained for the α -quartz sample reference.

2.1.2 Heating-cooling stage

An heating-cooling stage (Linkam® TMS 600 see Figure 2.4) was coupled to the SHG set-up in order to perform measurements on large temperature range (-196°C to 600°C). The measurements of the evolution of the SHG signal versus the temperature was denominated *Temperature-Resolved Second Harmonic Generation (TR-SHG)*. A continuous dinitrogen flow was also sent in the heating/cooling stage to limit oxidation processes or to avoid vapor deposition on the windows of the heating/cooling stage.

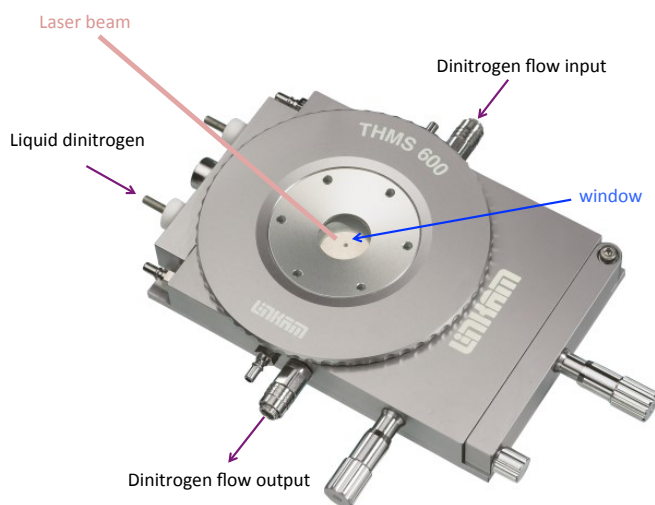


Figure 2.4 Picture of the Heating/cooling stage (Linkam THMS600®)

2.1.3 Humidity controller

A Humidity controller (Seratam® Wetsys apparatus) is another option added to the set-up in order to control the concentration of water (RH) in the heating/cooling stage atmosphere. Typically, it consists in sending a dinitrogen flow (50mL/min) with a known concentration of water. The RH dependency with respect to the temperature is not linear and thus difficult to control. For numerous measurements, the RH was fixed at 0 or was changed only in isothermal condition to assure a good control.

2.1.4 Geometry and sample preparation

In the apparatus of K&P the measurements were performed in transmission geometry. The sample was put on a microscope slide and held in place with a transparent tape, or, for more sophisticated measurements was load in a quartz cell. For a powder, all crystallites have random orientations with respect to the incident laser beam. The strong scattering in all directions due to the refractive index mismatch between the crystallites and air causes a substantial loss of SHG signal due to the finite solid angle collected by the optical fiber probe. In order to minimize the loss of SHG signal, K&P immersed the powder in a refractive index matching liquid in order to concentrate the SHG signal in the direction of the detector.

Due to the design of the heating/cooling stage, measurements in our set-up are performed in reflection geometry. It was recently demonstrated that this geometry could be as reliable as the one used by K&P. (Aramburu et al. 2014) The sample is the put uniformly in a SHG negative crucible and then is slightly packed using a microscope coverslide (see Figure 2.5). The height of the sample is estimated lower than 0.5mm.

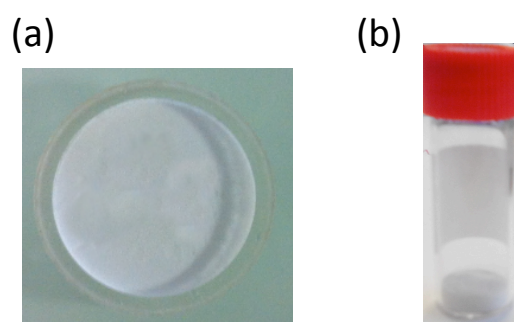


Figure 2.5 (a) Sample in the crucible for TR-SHG or SHG measurements versus relative humidity. (b) Sample in vial for measurements at room temperature or in solution.

For the measurements conducted during this thesis, the samples were not immersed in a refractive index phase matching liquid for several reasons. Firstly, it is necessary to know the

refractive index of the sample analyzed that is not always easy and often time consuming to obtain (necessity to have a single crystal). Secondly, even if the refractive index of the sample is known, the corresponding liquid is expensive. Moreover, some chemical reactions or dissolution could occur during the analysis especially if the temperature is increased. In this latter case, the dilatation or contraction of the liquid during the change of temperature could also modify the SHG scattering and thus conduct to a misinterpretation of the SHG signal evolution. In addition, the immersion of the sample in a liquid makes impossible to monitor all equilibria between gas and solid (e.g. dehydration).

2.1.5 Software development

Several programs were developed during this thesis in order to control the device and treat the data. To determine SHG intensity and treat a large set of spectra at once, a software based on the free scientific programming language Scilab[®] was written. The laser, the energy adjustment device and the spectrometer were controlled by a software based on graphical Labview[®] language. All program codes are described and available in appendix III.

2.2 Temperature Resolved Second Harmonic (TR-SHG) set-up

Fig. 2.6 is a scheme of the experimental setup developed during this thesis for the TR-SHG measurements. A Nd:YAG Q-switched laser (Quantel) operating at 1.06 μm was used to deliver up to 360 mJ pulses of 5 ns duration with a repetition rate of 10 Hz.

An energy adjustment device made up of two polarizers (P) and a half-wave plate ($\lambda/2$) allowed the incident energy to vary from 30 to ca. 330 mJ per pulse. A RG1000 filter was used after the energy adjustment device to remove light from laser flash lamps or other parasites.

The samples (100 mg of powder in a crucible) were placed in a computer controlled Heating-Cooling stage (Linkam THMS-600) and were irradiated with a beam (4 mm in diameter).

The signal generated by the sample (diffused light) was collected into an optical fiber (500 μm of core diameter) and directed onto the entrance slit of a spectrometer (Ocean Optics QE 65000). A boxcar integrator allowed an average spectrum (spectral range 490-590 nm) with a resolution of 0.1 nm to be recorded over, generally, 3 s (30 pulses).

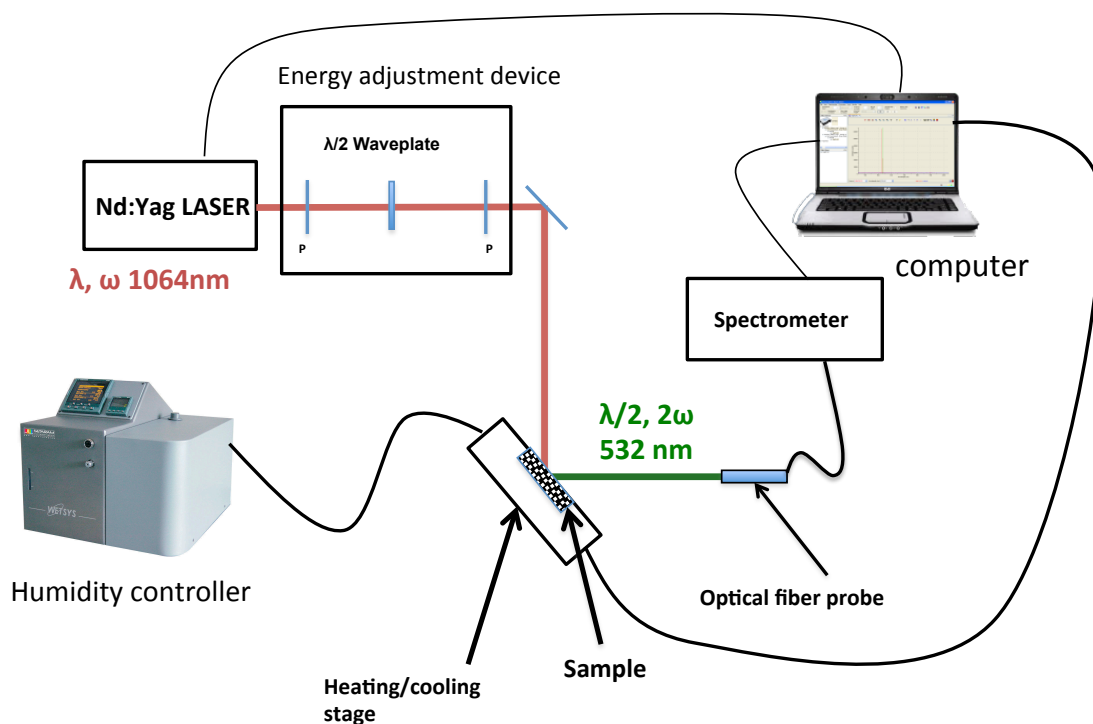


Fig. 2.6: Experimental setup Second Harmonic Generation Apparatus constituted of Nd:YAG Q-switched laser operating at 1064 nm.

For the laser beam, an incident angle of circa 45° was used to illuminate the sample as show in Figure 2.7.

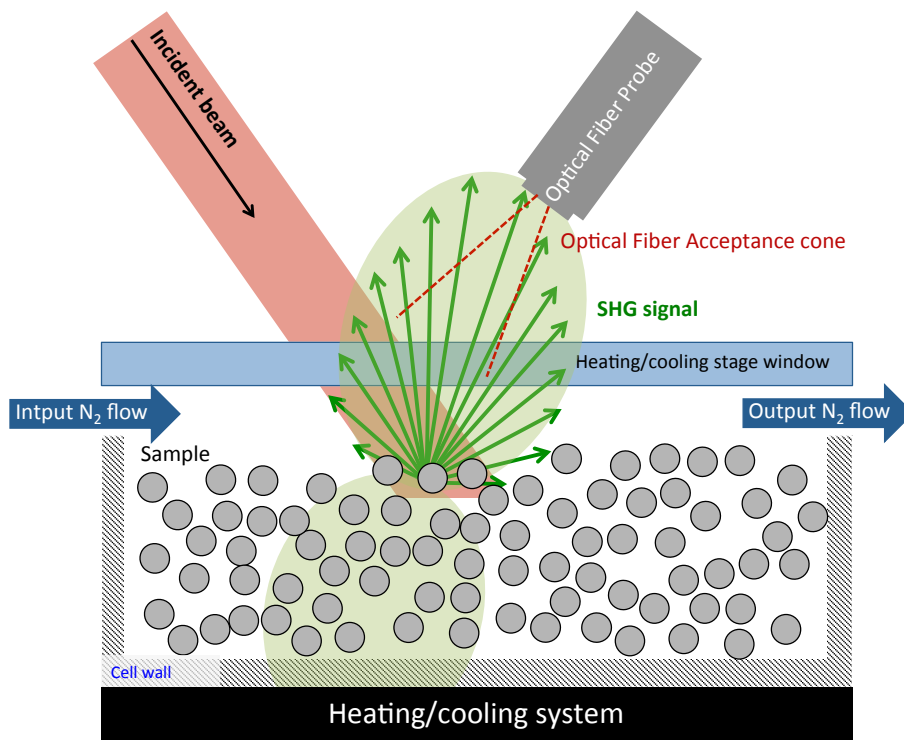


Figure 2.7 Sample in crucible place in the heating/cooling stage irradiated by the laser. The SHG is scattered in all direction. Only one part is detected.

In the particular case of powder samples, each particle, which can be considered spherical, diffuses the SHG emitted light in all directions. Consequently, only the fraction of the light emitted in the acceptance cone of the optical fiber is collected. The main consequence is the impossibility to determine in a reliable manner the nonlinear optical coefficients of the nonlinear susceptibility tensor. Nevertheless, the evolution of the SHG signal (even if only one part of the whole SHG signal is detected) is directly correlated to the crystalline structure and the molecular packing.

2.3 Set-up for measurements at room temperature or on “wet” samples

For measurement at room temperature or in solution (e.g. for the measurement of efflorescent compounds) the set-up described in Figure 2.8 was developed. To measure the SHG signal on “wet” sample (e.g. in saturated solution), the laser beam is sent to the bottom of the vial. If, the geometry of the set-up is modified; the principle remains the same.

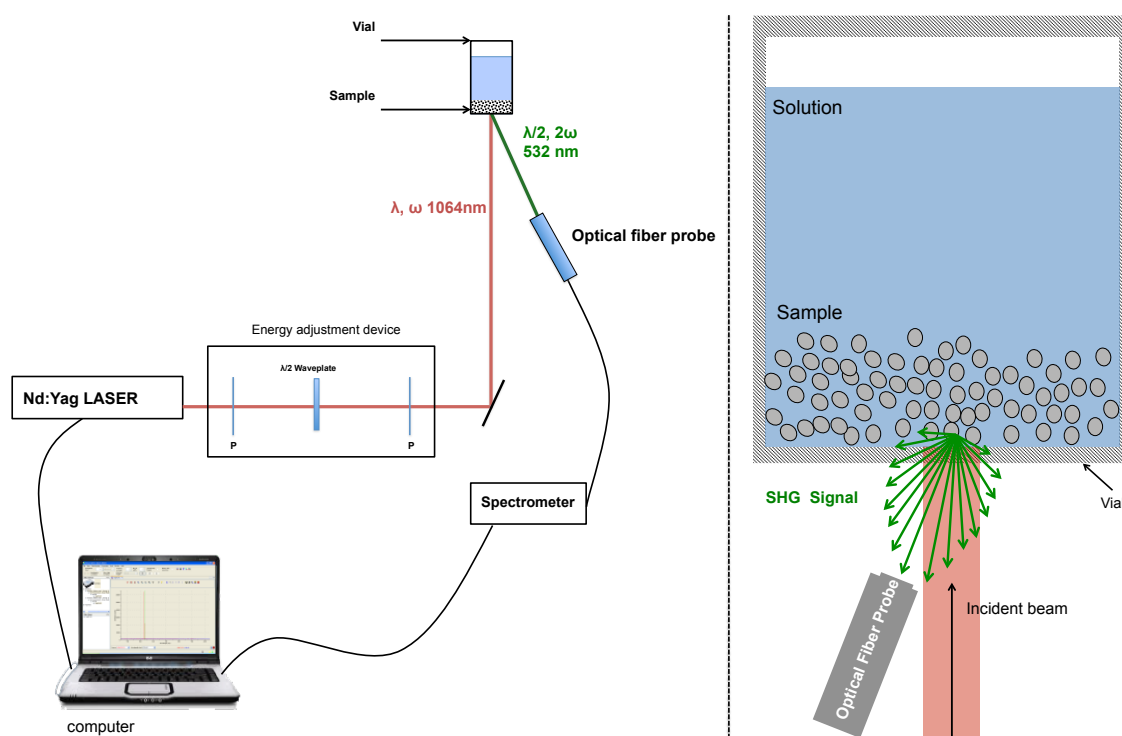


Figure 2.8 SHG set-up for measurement of powder in vial. It is possible to measure sample in liquid (e.g. for efflorescent sample)

According to Kurtz and Perry SHG powder method (Kurtz and Perry 1968), SHG signal intensities were usually compared to the signal of a reference compound (α -quartz powder- 45 μm average size).

Part.3 Detection and Reliability of SHG measurements

In order to establish the reliability of the developed SHG set-up several tests have been carried out. In the following, these tests are described and, finally, detection possibilities of the setup are exemplified through the case study of the structural purity of the 3-hydroxybenzoic acid.

The crystalline structure of α -quartz is non-centrosymmetric. It is the first crystal in which the second harmonic generation was observed (Franken et al. 1961). That is why, often in the literature, nonlinear optical surveys usually compare values of crystal efficiency relatively to the SHG signal given by the α -quartz (Delfino 1978). This standard material generates a relatively low SHG signal compared to other nonlinear optical (NLO) compounds (Nikogosyan 2006). Consequently the α -quartz is a good candidate to test the detection threshold and the reliability of our set-up. This aspect is developed in the following through several tests in order to define the better measurement parameters.

3.1 Detection of the SHG signal generated by dry powders

3.1.1 Measurement duration

The SHG measurement duration is one of the main parameters to assure a good reliability of the measurement. To find the better ratio between the measurement duration, the SHG signal intensity and to assure a non-destructive analysis (e.g. for crystal exhibiting low damage threshold), it is necessary to understand how the signal is measured.

The SHG signal emitted by the sample is collected into an optical fiber probe and the detection is performed thanks to a CCD detector in the spectrometer. The spectrometer allows an integration time in the range of 8ms to 15min. The typical time duration of communication with PC is 8ms. The laser sends pulses at a frequency of 10Hz (*i.e.* one pulse every 100ms) and is relatively stable in energy but some fluctuations can occur (typically 1-3% depending on the incident intensity). The fluctuations of the incident beam are determined thanks to a detector placed behind the first mirror and that allows the detection of a small part (0.06%) of the incident beam intensity. The detected intensity was plotted in Figure 2.9. If it can be noticed that the absolute standard deviation of the laser beam energy increases with the

energy, the relative standard deviation in % with respect to the mean energy value (Figure 2.10) does not.

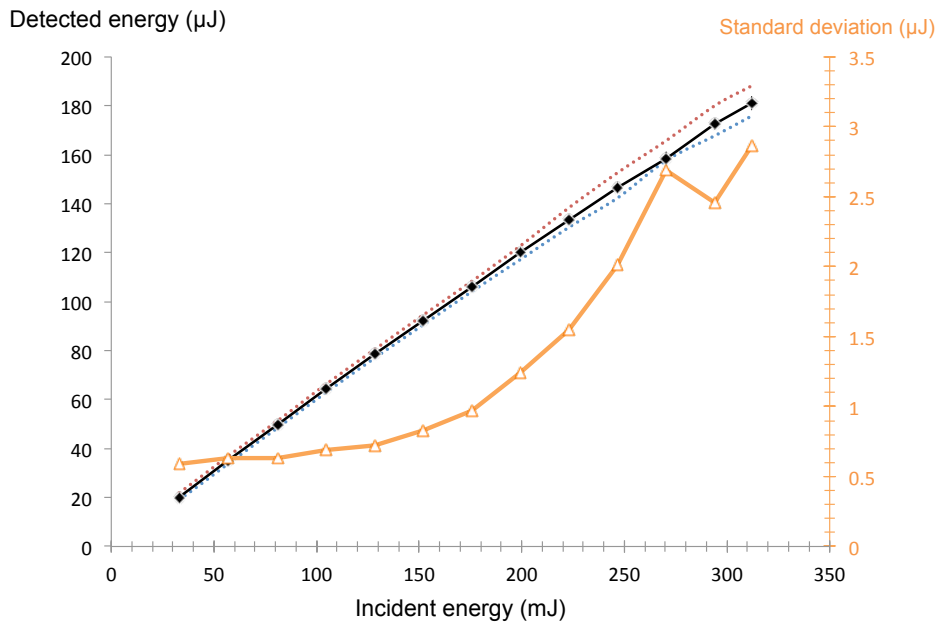


Figure 2.9 Detected intensity on the detector located behind the first mirror of the SHG set-up and standard deviation curves. Results are averaged over 100 laser pulses. The red and blue dash-lines are, respectively, the maximum and minimum intensities observed.

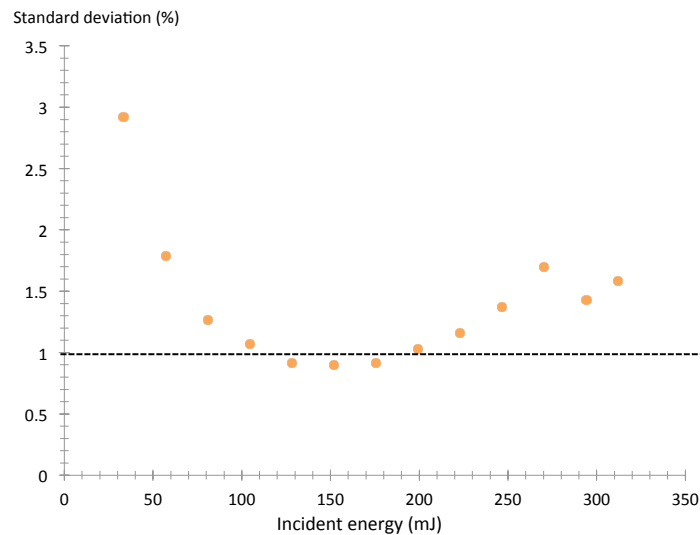


Figure 2.10 Standard deviation (in %) of the incident beam. energy

The fluctuations are lower (limited at circa 1%) if the laser is used with an energy in the range of 30-60% of the maximal energy available. These fluctuations can create dispersion in data and lead to non-reliable results. They are all the more important that the SHG intensity as function of the input energy is supposed to follow a square-law relationship (see chapter 1

page 57). This problem can be easily solved by averaging the measured signal over a sufficient period of time.

A supplementary parameter that must be taken into account is the saturation of the detector that can lead to wrong SHG intensity calculations (*i.e.* to avoid it, the integration time is set at 100 ms.)

A set of SHG intensities emitted by a quartz sample ($44\mu\text{m}$) obtained with the same incident intensity for 0.1s and 3 sec of measurement are plotted, respectively, in Figure 2.11 and Figure 2.12.

For the set of measures of 0.1 sec (*i.e.* 1 pulse) duration, the mean SHG signal is 2444 counts and the fluctuations with respect to the mean value reaches circa 10%.

For the set of measures of 3 sec (30 pulses) duration, the stability of the SHG signal is highly improves. The mean SHG signal is 2545 counts and the standard deviation with respect to the mean value is only 1.6%.

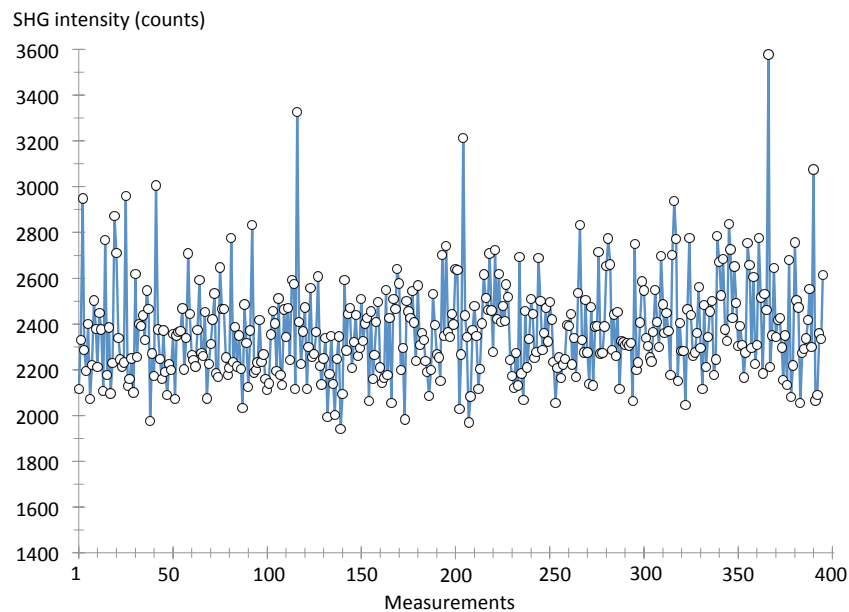


Figure 2.11 Set of 400 measures of 0.1s on α -quartz ($44\mu\text{m}$). Mean value: 2244 counts and standard deviation: 10%

Finally, for reproducibility reason, the SHG signal must be collected over 3 seconds.

The signal-to-noise ratio is 1000:1 (at full signal). The dark noise is of 2 counts (1 counts=26 photons). Therefore, in the common case, calculated SHG signal (program in appendix III)

lower than 6 counts are considered as noise and experimental error (notice that it depends on the spectrum and notably of the shape of the baseline; in the case of particular flat baseline clear SHG signal of only 3 counts can be detected).

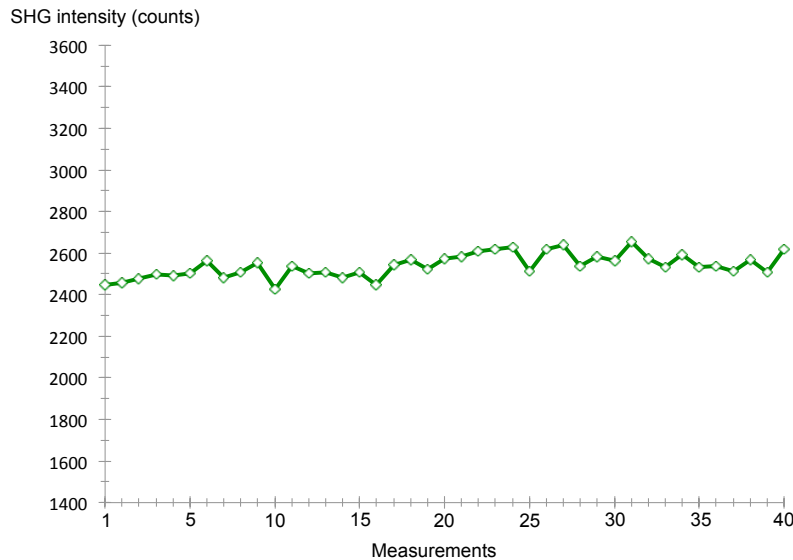


Figure 2.12 Set of 40 measures of 3 sec on α -quartz ($44\mu\text{m}$). Mean value: 2545 cps and standard deviation: 1.6%

3.1.2 Incident energy absorption and damage threshold tests

Another parameter to take seriously into account during the SHG measurements is the possible absorption of the sample at the incident wavelength (1064 nm) and/or at the 2nd harmonic wavelength (532 nm). Of course the absorption is compound-dependent and is hardly predictable since the absorption spectrum of powdered samples are rarely available. Absorption can degrade (even destroy, see Figure 2.13) the sample. A same behavior can also be observed in the case of a low thermal dissipation.

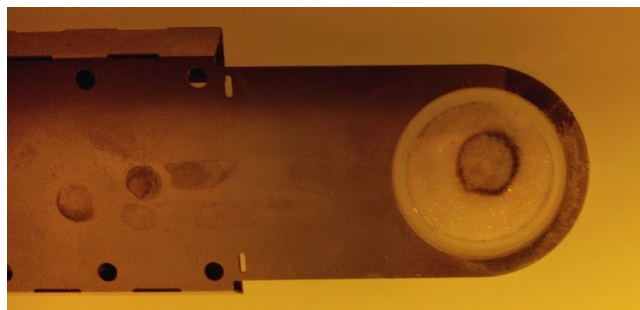


Figure 2.13 Sample of NaCl in the crucible after irradiation of few seconds

This problem can be partly overcome by decreasing the incident laser intensity. However, it is important to recall that decreasing the laser power decreases the SHG signal (absolute value).

Shorter measurement duration can also be used but with the above mentioned consequence of increasing the experimental error.

Since the actual device does not give access to alternative wavelength (to work under non-resonant conditions), “stability” tests for the sample under laser irradiation are required prior to other measurements (TR-SHG, RHR-SHG...).

During a SHG analysis, many laser pulses hit the sample. In order to ensure that any SHG signal changes are not related to an absorption effect or destruction of the sample (e.g. during a thermal treatment), tests of damage threshold can be performed. It consists in irradiating continuously (during 10 or 20 min at room temperature) the sample and to monitor the SHG signal versus the time. This continuous irradiation constitute much more extreme conditions compared to a ‘real’ TR-SHG analysis for which the laser is shut down between two consecutives measurements of 3s durations (performed every x degrees).

Consequently, we assumed that, if at a given energy the SHG signal remains stable no effect of destruction or absorption of the sample will occur during the TR or RH-SHG analysis.

3.1.3 Temperature dissipation or time between two measures

The hit of the laser can increase locally the temperature of the sample. This increase is sample-dependent because various thermal behaviors. The temperature increase of the sample is difficult to measure. But an irradiation of 3sec with an energy set at circa 200mJ/pulse (commonly used in this thesis) on a metallic thermal probe leads to an increase of 0.2°C. The energy provided by the laser can slightly change the kinetic processes but its effect seems limited.

3.1.4 Fundamental and SHG intensity dependencies

As shown in equation (1.33), the SHG intensity depends on the square of the fundamental beam intensity. If only one part of the total SHG signal emitted by the sample is detected, it could be interesting to check if the square law is respected. The evolution of the detected SHG signal emitted by a quartz sample versus the incident energy is plotted in Figure 2.14. The equation used to fit this evolution (by a least square method) is a simplified equation:

$$I_{2\omega} = A(I_{\omega})^2 \quad (1.36)$$

As show in Figure 2.14, the SHG signal follows the square law. It highlights that the photons emitted at 532 nm originate only from the second harmonic process. Thus, this law remains valuable even if only one part of the total SHG emission is detected.

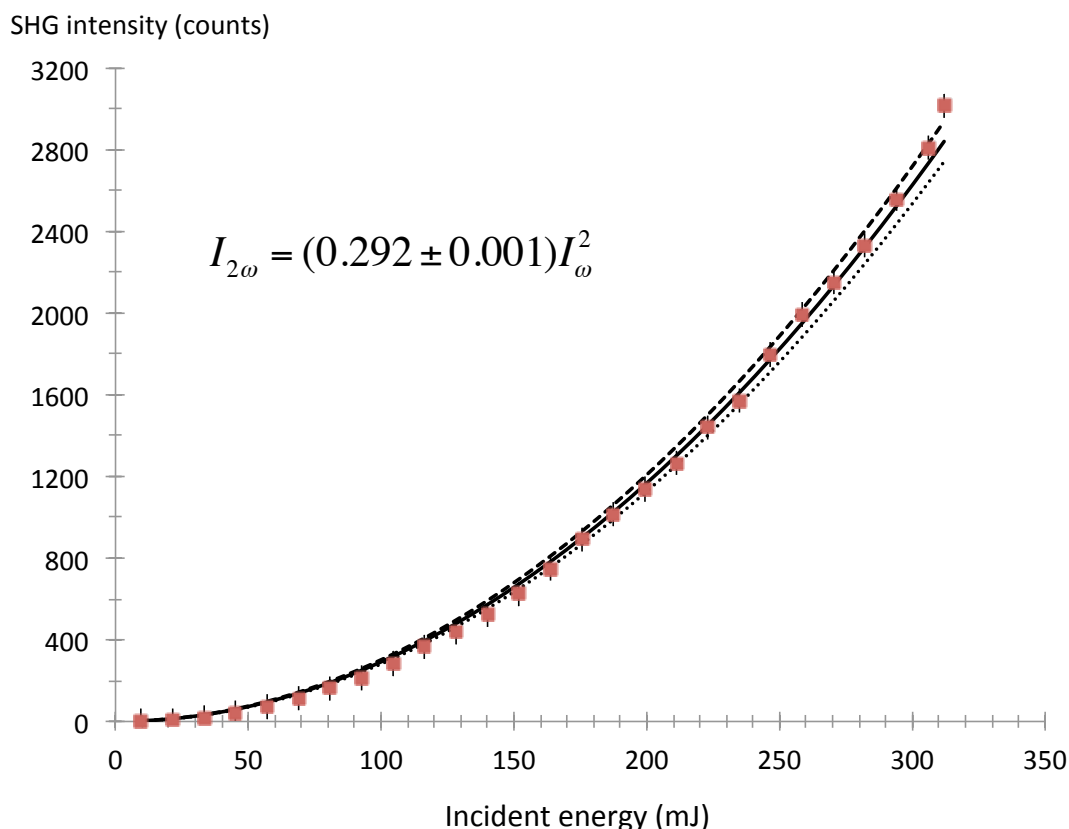


Figure 2.14 SHG intensity of a α -quartz sample for different incident energies. SHG signal evolution fit a square law with respect to the incident energy

Note that the SHG measurement duration in this experiment was 3 seconds which demonstrates also the relevance of this characteristic measure duration.

3.2 Detection of the SHG signal generated by “wet “ powder

The SHG apparatus described in Figure 2.8 gives the possibility to probe crystals inside a liquid. It is of particular interest since certain crystalline substances are highly instable in room conditions and since exist only in solution. It is the case, for example, of efflorescent compounds.

Nevertheless, this kind of measurement suffers from limitations in term of detection threshold due to absorption and/or scattering of the fundamental and second harmonic beam by the liquid. For instance, α -quartz SHG intensities measured without and with solvent (ethanol) are presented Figure 2.15. The SHG intensity is smaller in an homogenized suspension with a loss of circa 66% compare to the dry sample.

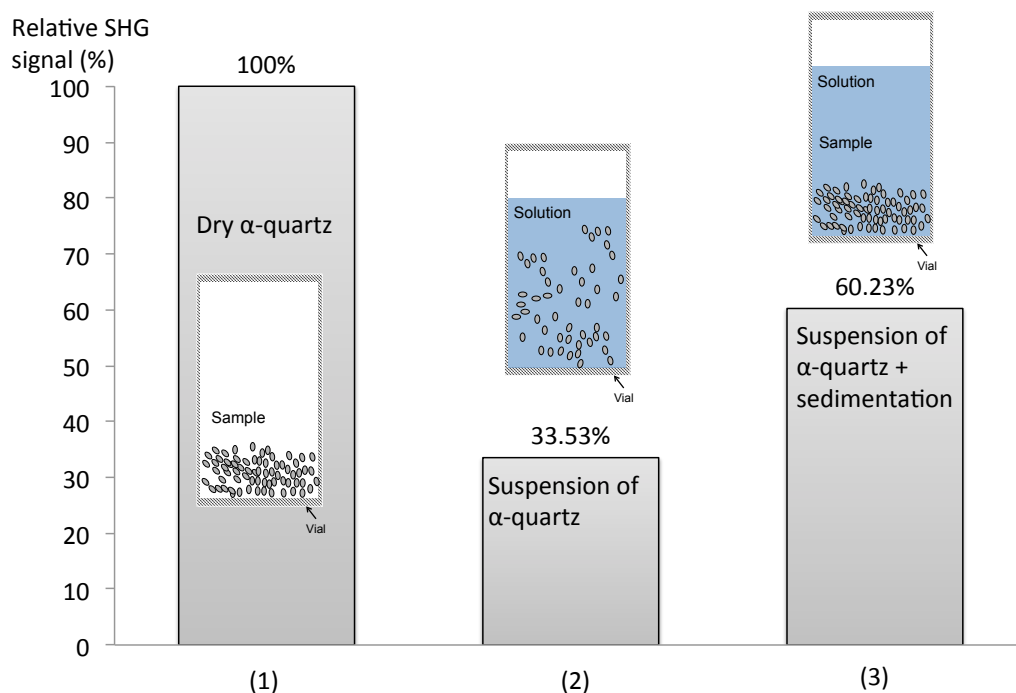


Figure 2.15 comparison of SHG intensity for (1): dry α -quartz powder, (2) suspension of α -quartz in ethanol, (3) the same suspension than in (2) but with a sedimentation time.

Although a drastic decrease of the SHG signal is observed for wet samples, it is nevertheless possible to detect a signal with a loss of 40% in ethanol, after sedimentation, compared to the dry α -quartz powder. Note that it is not possible to predict the loss in the SHG intensity because it is both sample and solvent dependent.

Part.4 Usual Applications of the SHG analysis

Nonlinear optical materials are important for many applications in optics. An intensive and continuous search for new materials is in progress in many research domains. These materials must belong to a non-centrosymmetric point group. Thus, a test of non-centrosymmetry is usually performed at a very early stage of the development of new compounds. The powder SHG measurement technique has been intensively used for this purpose as all other investigation methods require larger crystals that are more difficult and time-consuming to obtain.

4.1 A test to check non-centrosymmetry in crystal

Recent studies (Galland et al. 2009) conducted in the SMS laboratory have demonstrated that the measurement of the SHG signal is a very sensitive probe to detect the noncentrosymmetry of crystal lattices such as conglomerates. Since, this technique was applied routinely for pre-screening of conglomerate and demonstrated its rapidity contrary to time-consuming usual method of detection. (Dupray, 2012)

SHG could also be a relevant technique in the space group assignment. Structure resolution by means of X-ray diffraction implies, in numerous cases, the irksome problem of centrosymmetry (Watkin 1994; Marsh 1995; Watkin 2008). The considerable increase of entries in the Cambridge Crystal Database (CSD) also leads to an increase of wrong assignment. Note that the number of wrong structures was estimated at circa 3% of published crystal structures (Baur and Tillmanns 1986). It was demonstrated that the lack or presence of an inversion center is a source of problem for a correct crystal structure resolution (dilemma between centrosymmetric or non centrosymmetric SG). Clemente et al (Clemente 2005) have highlighted the fact that the determination of the proper space group is of capital importance to science theory of space group occurrence, second order nonlinear optic, IR and NMR in the solid state and the correct attribution of polymorphism. They, also determined in 2004 and 2005, based on the treatment of crystallographic data, 52 wrong space group assignments; among them, 20 (ca. 38%) were related to problems of centrosymmetry. In 2007, they corrected 138 structures among them 93 (ca. 49%) concerned centrosymmetry and finally in 2003 26 space group were revisited (with 70% of addition of inversion centers). Among 60 space group corrections by Marsh *et al* (Marsh et al. 2001), 31 (52%) concerns a problem of centrosymmetry. In this paper « Centrosymmetric and pseudo-centrosymmetric structures are refined as non-centrosymmetric ». Flack has reacted and gave some advises in the structure determinations by means of X-Ray (Flack and Bernardinelli 2006). Nevertheless, no characterization test of non-centrosymmetry was indicated.

It can be considered that circa 50% of the space group assignment problems are related to the presence or not of the inversion center.

Crystal class	Enantiomorphism	Optical activity	Pyroelectricity	Piezoelectricity, SHG
1 2 3 4 6	(+)	(+)	(+)	(+)
222 422 ^a 32 622 ^a 23	(+)	(+)	(-)	(+)
432	(+)	(+)	(-)	(-)
m mm2	(-)	(+)	(+)	(+)
4mm 3m 6mm	(-)	(-)	(+)	(+)
$\bar{4}$ 42m	(-)	(+)	(-)	(+)
6 62m 43m	(-)	(-)	(-)	(+)

Table 2.1 Division of non-centrosymmetric classes according to its physical properties. (+) denotes a positive effect and (-) a negative. ^aIf Kleinman symmetry applies 422 and 622 PGs are SHG (-)

One must recall that crystal structure must reflect the real (macroscopic) properties of the crystal. If a doubt subsists in the space group, a physical test of the non-centrosymmetry by means of piezo- and pyro-electricity or SHG could prevent numerous debate in literature (Glazer and Stadnicka 1989) and give evidence of the real symmetry of 3D packing (Point group characteristic tests are summarized in Table 2.1). As early as in 1972, in his letter to the editor of the *Journal of Applied Crystallography* (Abrahams 1972), Abrahams aware of Kurtz&Perry's works on SHG, proposed the use of this technique ("higher in sensitivity", "rapid" and "simple" than the others) for determination of space group. This technique has enabled to resolved some literature ambiguities. (Cummins 1968; Bass 1969; Newnham et al. 1971; Wolfe et al. 1972; Abrahams et al. 1973; Dougherty and Kurtz 1976; Abrahams et al. 1998). In 1976, Coda et al (Coda and Pandarese 1976) tested 90 crystalline substances and concluded to the real attractiveness of the SHG technique as a test of non-centrosymmetry. "Resolution of space group ambiguities in mineral" published in 1982 (Loiacono et al. 1982), is a direct application of the Kurtz and Perry method. Furthermore, the method is referenced in the International Tables for Crystallography (Hahn 2002) and is described as a "powerful method of testing crystalline materials for the absence of a symmetry center. With an appropriate experimental device, very small amounts (less than 10mg) of powder are sufficient to detect the second-harmonic signals, even for crystals with small deviations from centrosymmetry (Dougherty and Kurtz 1976) .

4.1.1 On centrosymmetric molecules packed in non-centrosymmetric structures.

Let us remember that the SHG efficiency is directly related to the acentricity of the molecules. A centrosymmetric molecule thus cannot generate a SHG signal. Rare and unexpected cases of centrosymmetric molecules packed in NC SG are referenced in literature and are submitted to debate(Zorkii and Lazareva 1967). The first occurrence survey was performed in 1957 by Herbstein (Herbstein and Schoening 1957)(who find only 5 potential molecules crystallizing

in NC SG in the literature (only 2 cases were confirmed in the paper)); Since, this result was faulted for one molecule. (van Niekerk and Boonstra 1961; Boonstra 1963). A more important statistical survey of 594 centrosymmetric molecules has been performed in 1977 (Muller 1978). It indicates that, among these, only 5 (0.8%) crystallize in non-centrosymmetric space groups. These examples are of particular interest that from Kitajgorodskij theory, it is only possible if a small molecular acentricity appears in the solid state (i.e. the molecule becomes acentric; see for example KAPNIZ structure in CSD: Meng et al. 2005) or can be obtained with two independent molecules ($Z'=2$, see examples in Table 2.4).

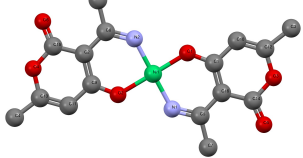
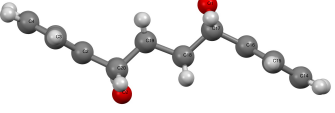
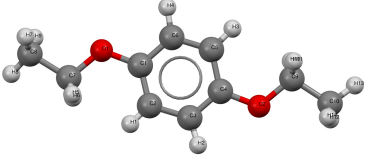
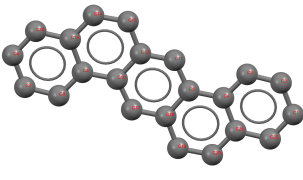
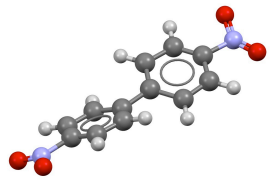
Molecule	nickel(II)-dehydroacetic acid monoimide	1,4-epoxy-1,4-dihydronaphthalene	1,4-Diethoxybenzène
CCDC Code	NDHAIM(Kiryu 1967)	EPNPHD10(Bordner et al. 1970)	DEXBEN(Haisa and Kashino 1977)
Asymmetric unit			
SG	P212121	Pca21	P21
Z, Z'	4, 1	4, 1	2, 1
R factor(%)	10.3	2.7	6.9
Remarks	-	-	Give positive SHG signal at circa 0.1 relative to α -quartz
Molecule	C30 H42 Ni3 O12	<i>dibenz[a,h]-anthracene</i>	4,4'-dinitrobiphenyl
CCDC code (authors, date)	ACACNI(Hursthouse et al. 1982)	DBNTHR10(Robertson and White 1956)	DNTDPH(van Niekerk and Boonstra 1961)
Asymmetric unit			
SG	<i>Pca2₁</i>	<i>P2₁</i>	<i>Pc</i>
Z,Z'	4, 1	2, 1	2, 1
R factor (%)	7.87	14.8	15
Remarks	<i>No impurity detected by XRPD. The sample gives a positive SHG signal at 0.004 relative to the α-quartz SHG signal)</i>	<i>Notice that another polymorphic form exists and was refined as centrosymmetric in Pcab space group R=3.5 %: (Iball et al. 1975). The commercial product is a mixture of both polymorphs and gives a positive SHG signal (0.003 relative to α-quartz SHG signal)</i>	<i>Structure firstly resolved with centrosymmetric molecule by Herbstein et al. The molecule is in fact non-centrosymmetric. No impurity detected by XRPD. Positive SHG signal (0.024 relative to the α-quartz SHG signal)</i>

Table 2.2 Structures found to be non-centrosymmetric with centrosymmetric asymmetric unit and $Z'=1$

Asymmetric unit and some crystallographic data of these NC structures with centrosymmetric molecules are summarized in Table 2.2 and Table 2.3. Available marketed products (highlighted in green in the tables) were ordered in order to determine the SHG efficiency, if any, of these compounds and results are also summarized in these tables.

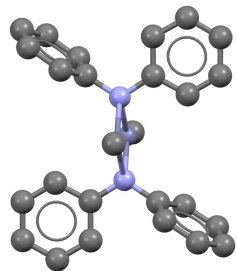
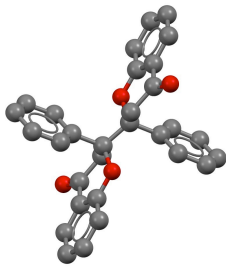
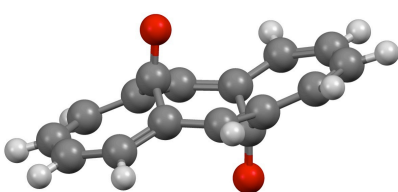
Molecule	bis(m2-Diphenylamido)-bis(methyl-zinc)	$C_{30}H_{22}O_4$	$C_{16}H_{10}O_2$
CCDC code	CADCEP (Bell et al. 1983)	LELSEA (Li et al. 1992)	COANUL (Destro et al. 1980)
Asymmetric unit			
SG	$P2_12_12_1$	$Pna2_1$	$Pca2_1$
Z, Z'	4, 1	4, 1	4, 1
R factor (%)	8.6	4.1	4.6
Remarks	-	-	Some partial crystal disorder might be present.

Table 2.3 Structures found to be non-centrosymmetric with centrosymmetric asymmetric unit and $Z'=1$

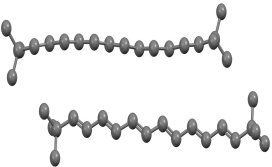
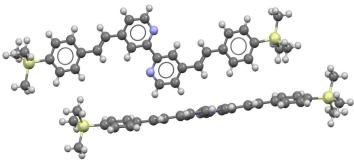
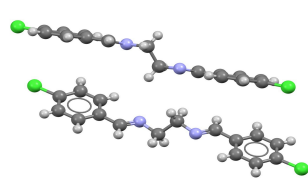
Molecule	1,2-Di-t-butyl-dodeca-1,3,5,7,9,11-hexaene	4,4'-bis(4-(Trimethylsilyl)styryl)-2,2'-bipyridine	(E,E)-N,N'-bis(4-Chlorophenyl)ethylenediamine
CCDC code	PATNUT (Kiehl et al. 1992)	RASVIR (264290) (Haberecht et al. 2005)	REWCUS (636855) (Bahron et al. 2007)
Asymmetric unit			
SG	Cc	Cc	Cc
Z, Z'	8, 2	8, 2	8, 2
R factor (%)	5.6	3.21	2.82
Remark(s)	none	none	Acquisition at 100K The SHG is 0.016 relative to the α -quartz SHG signal

Table 2.4 Examples of non-centrosymmetric structures made of centrosymmetric molecules with $Z'=2$

For compounds with $Z'=1$, one can notice that SHG signal is relatively low (maximum 10% of α -quartz). It could be in agreement with a small deviation from centrosymmetric molecules. It is important to remark that the reliability factor (R) of these structures is also relatively high (6.9-15% range)¹⁰: it can cast doubt on the centrosymmetry of these molecules in the crystal structure. For the structure REWCUS with $Z'=2$, a very low SHG signal is also detected at 1.6% of α -quartz SHG signal. It should be noticed that SHG has also been detected on monolayer of centrosymmetric molecules because of intermolecular charge transfer effects (Ashwell 1996) and thus could explain these results.

¹⁰ Only circa 8% of CCDC crystal structures exhibit a Rfactor higher than 7% (CCDC January 2014)

The particular case of the phase transition of the 4,4'-biphenyl is interesting because it is in accordance with Kitajgorodskij statements. Indeed, at room temperature the crystal structure is centrosymmetric ($P2_1/a$ SG with no SHG signal detected) and the molecular conformations too. At circa 40K, a new crystal phase (Pa SG) appears wherein the molecular conformation is non-centrosymmetric. Molecular conformations in both phases are represented in Figure 2.16.

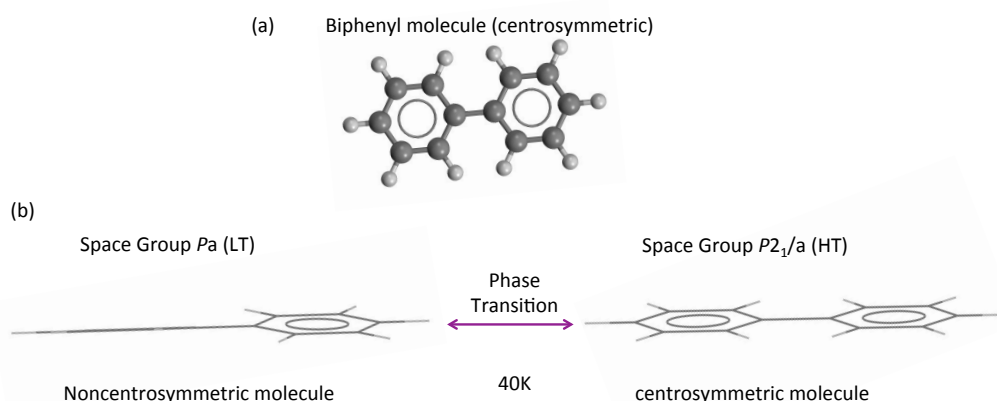


Figure 2.16 Biphenyl molecule in planar centrosymmetric conformation (a) and molecular conformations in both polymorphs (noncentrosymmetric for the low temperature form and centrosymmetric for the high temperature form)(b)

It has also been shown, based on a statistical study from Pidcock et al (Pidcock 2005), that the propensity to crystallize in Sohncke space group was more marked for achiral molecule exhibiting a rigid body. This result could be of interest for the design of non-linear optical material made of organic molecules. Moreover, almost 75 % of the achiral molecules crystallizing in noncentrosymmetric space group crystallize in $P2_1$ (35%) or $P2_12_12_1$ (40.5%) space groups.

4.2 Nonlinear optical survey: test for SHG efficiency

The K&P method is also widely used to determine in a qualitative manner the SHG efficiency of novel compounds. Nevertheless, many people didn't mention the size of the sample, which leads to incomparable results. One can mentioned the study of Delfino (Delfino 1978) on amino acid compounds who indicated the particle sizes when available. Delfino used the K&P method with the refractive index phase-matching liquid contrary to our case, thus a

comparison between both methods seems interesting in order to highlight possible errors. These comparisons are summarized in the Table 2.5. The known crystallographic data also figure in this table.

Compound	Known Crystallographic data			Particle size Delfino/our study (μm)	ISHG relative to α -quartz from	
	CCDC Code	SP	Rfactor (%)		Delfino	This study
L-Alanine	LALNIN24	$P2_12_12_1$	1.59	212-300/568	0.80 +30%	2.542
DL Alanine	DLALNI01(Subha Nandhini et al. 2001)	$Pna2_1$	2.52	212-300/113	0.35	4.786
L-Arginine	Not resolved			-	-	0.633
D-Arginine	(XRPD resolution Courvoisier et al. 2001; Thomas 2012)			-	-	0.857
L-Asparagine.H ₂ O	ASPARM09(Flaig et al. 2002)	$P2_12_12_1$	2.66	106-125/293	0.006	0.036
L-Aspartic Acid	LASPR03(Bendeif and Jelsch 2007)	$P2_1$	1.9	106-150/162	0.52	11.247
L-Cysteine	LCYSTN04(Görbitz and Dalhus 1996a)	$P2_1$	3.11	UG/178	0.02	0.194
	LCYSTN28(Kolesov et al. 2008)	$P2_12_12_1$	1.62			
L-Cystine	LCYSTI11(Chaney and Steinrauf 1974)	$P41$	9.7	106-125/441	0.04	0.080
	LCYSTI14(Dahaoui et al. 1999)	$P6122$	1.4			
L-Glutamic Acid	LGLUAC03(Lehmann and Nunes 1980)	$P2_12_12_1$	2.1	212-300 237/	0.15	8.252
	LGLUAC11(Lehmann et al. 1972)	$P2_12_12_1$	2.6			
DL-Glutamic Acid. H ₂ O	CADVUY01(Flaig et al. 2002)	$Pbca$	3.47	UG/103	0	0.139
L-Glutamine	GLUTAM02(Wagner and Luger 2001)	$P2_12_12_1$	1.4	106-150/187	0.5	8.440
L-Histidine	LHISTD04(Averbuch-Pouchot 1993)	$P2_1$	3.9	106-125//229	0.02	7.428
	LHISTD10(Madden et al. 1972)	$P2_12_12_1$	3.4			
DL Histidine	DLHIST01(Coppens et al. 1999)	$P21/c$	2.96	UG/106	0	0.022
L(-) Isoleucine	LISLEU02(Görbitz and Dalhus 1996b)	$P2_1$	5.24	212-300/174	0.8	4.693
L(-) Leucine	LEUCIN02(Görbitz and Dalhus 1996c)	$P2_1$	4.35	150-212/37	0.2	10.339
DL Leucine	DLLEUC02(Iwama et al. 2010)	$P-1$	3.89	106-150/81	0	0
L-Lysine	Unknown, probably C_2 (Dogan et al. 2000)			UG/204	0.36	0.890
L-Methionine	LMETON02(Dalhus and Görbitz 1996)	$P2_1$	3.7	UG/171	0.25	6.429
D-Methionine	Unresolved see FAZHAP(Khawas 1986)		$P2_1$	UG/298	0.25	0.946
DL-Methionine	DLMETA02(Taniguchi et al. 1980)	$P21/a$	11.8	UG/469	0	0
	DLMETA05(Alagar et al. 2005)	$I2/a$	4.08			
DL-Norleucine	DLNLUA03(Coles et al. 2009)	$P21/c$	6.01	UG/113	0.015	0
L-Phenylalanine	SIMPEJ(Weissbuch et al. 1990)	$C2$	14.72	106/125/291	0.15	0.36
D-Phenylalanine	QQQAUJ(Khawas 1970)	$P2_1$?	106-125/149	0.11	0.37
DL Phenylalanine	Unresolved (Khawas 1971)		$P2$ or $Pnmm$	UG/52	0	0.0846
L-Proline	PROLIN (Kayushina and Vainshtein 1965)	$P2_12_12_1$	16.9	UG/81	0.23	5.16
L-Serine	LSERIN01(Kistenmacher et al. 1974)	$P2_12_12_1$	5.9	150-300/544	1.6	1.98
D-Serine				150-300/197	1.7	3.4
L-Tryptophan	VIXQOK(Görbitz et al. 2012)	$P1$	8.5	UG/172	0.54	18.65
DL-Tryptophan	QQQBTP02(Hübschle et al. 2004)	$P21/c$	4.03	UG/78	0	0.020
L-Threonine	LTHREO03(Janczak et al. 1997)	$P2_12_12_1$	2.6	UG/135	1.8	12.80
L-Tyrosine	LTYROS11(Frey 1973)	$P2_12_12_1$	4	45-106/49	0.007	0.094
DL-Tyrosine	DLTYRS(Mostad and Romming 1973)	$Pna21$	3.7	45-106/42	0	2.04
L-Valine	LVALIN01(Dalhus and Görbitz 1996)	$P2_1$	3.4	212-300/759	6.7	13.83

Table 2.5 SHG efficiency comparison between Delfino survey on several amino acids or derivative and our results. Lines highlighted in red indicate differences. UG means unknown granulometry

The crystal size distribution of each sample was determined by laser granulometry. XRPD was performed for all samples and pattern were compared to available structures in order to assess the structural purity. Except for the DL-glutamic acid.H₂O and the DL-phenylalanine that contains either an unknown polymorphic form or impurities all other samples are structurally pure in the limit of detection of the XRPD method.

Lines highlighted in red in the Table 2.5 denote incoherent results either related to the Delfino SHG values or to the known crystal structures. These inconsistent results and their possible explanation(s) are summarized in the Table 2.6.

Problem (s)	Sample	Reason(s)
SHG signal detected in our study and not consistent with known crystal structure(s) and Delfino' results	DL-glutamic acid monohydrate	Impurity detected and identify as L-Glutamic acid that is NC
	DL-Histidine	Unknown (possible undetected impurity by XRPD, e.g. the L-Histidine)
	DL-Tryptophan	Unknown (possible partial solid-solution, XRPD of 12h has revealed no additional peak on the XRPD pattern compare to the calculated)
SHG signal detected in the Delfino study and not consistent with known crystal structure(s) and our results	DL-Norleucine	Unknown: possible impurity in Delfino sample, but he mentioned that single crystals exhibit positive SHG signal thus possible polymorphic form involved
SHG signal detected in our study and not in Delfino work that could be explain by known crystal structure(s).	DL-Phenylalanine	Possible polymorph: Our sample does not correspond to known X-ray patterns. The known structures are not totally resolved but indexation of powder pattern leads to both centro or NC space groups.

Table 2.6 Summarize of identified problems between our and Delfino's results.

One can also notice that, in all cases, our SHG values are at least 1.25 higher than those found by Delfino even for similar granulometries. For instance, our SHG value obtained for the L-Histidine (7.428 higher than the α -quartz) is circa 370 higher than Delfino value. This high value must be related to the inconsistent result observed in DL-Histidine that thus could be explained by a really small amount of L-Histidine acting as an impurity (not detected by XRPD) in the sample.

In following work, the SHG potential for structural impurity detection is compared with those of usual DSC and XRPD techniques in the case of the 3-hydroxybenzoic acid.

Part.5 Probe the structural purity: the case study of the 3-hydroxybenzoic acid (MHBA)

5.1 Importance of impurity detection

The detection, identification and quantification of impurities are of fundamental importance in material science and most of all for compounds involved in the production of active pharmaceutical ingredients (APIs). Impurities can originate from starting materials, by-products, intermediates, reagents, degradation products, ligands, catalysts, etc. Pharmaceutical compounds are often administered in the form of crystalline powders and impurities can, for example, be present as liquid inclusions inside the solid phase (Couvrat et al. 2009; Waldschmidt et al. 2011a; 2011b). Pharmaceutical compounds can also exist in various solid phases including: polymorphs, hydrates, solvates, co-crystals, host-guest associations, salts and hybrids of all sorts of these phases. As polymorphs have different physicochemical and physical characteristics (solubility, hardness, compressibility, density, melting point, etc.), not only chemical but also structural impurities have to be considered in the impurity profile (Coquerel 2006). Notably, if the marketed form of a compound is not the most stable form, storage conditions (temperature, hygrometry...) can induce phase transitions. Then, the structural purity assessment of products all along their formation processes (from the production to the formulation) is nowadays a necessity.

A standard value of 0.1 % has been fixed by regulatory authorities as the threshold above which impurities have to be properly identified (Ahuja 2007). Several analytical methods are commonly used to probe the purity of products. Concerning chemical impurities, HPLC with UV detection and LC-MS are the most common analytical methodologies used to monitor impurities at very low levels. Structural impurities are often more difficult to identify and to quantify as they are constituted of the same molecules as the original compound. Spectroscopic techniques such as Infrared or Raman spectroscopy are frequently used to characterize contaminated samples with reported limits of detection in the range of 3 to 5 % wt. (Helmy et al. 2003). XRPD certainly constitutes the most direct way to identify the presence of a polymorph but suffers limitations as long as the mass fraction remains below 5% in the physical mixture. Differential scanning calorimetry and differential thermal analysis are also widely used to reveal phase transitions in solids with a usual reported detection threshold of 1% wt. (McGregor et al. 2004). Consequently, the detection of a structural

impurity at a threshold below 1% wt. seems to constitute the actual limit for usual analytical methods. Nonlinear optics and second harmonic generation (SHG) can be precisely a way to overcome this limit. However, to our knowledge, SHG has never been used to probe the structural purity and to tackle the structural purification of organic products.

5.2 Structural purity of MHBA

In this study, a thermal induced structural purification of m-hydroxybenzoic acid (hereafter MHBA, see Figure 2.17) was monitored with SHG. MHBA is an intermediate in the production of pharmaceuticals, plasticizer, germicides and preservatives. Its sodium salt is claimed to promote the discharge of bile {Thomas:2000gt}.

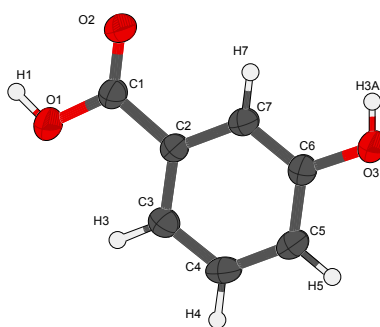


Figure 2.17. ORTEP view-like of MHBA molecule with labeled atoms. Both polymorphs comprise the same conformer .

Two polymorphic forms of MHBA are reported in literature and referenced in the Cambridge Structural Database (CSD) as BIDLOP for the centrosymmetric $P2_1/c$ form and BIDLOP01 for the noncentrosymmetric $Pna2_1$ form {Gridunova:1982up}. This noncentrosymmetric form is metastable at all temperature investigated and as a consequence the polymorphic system is of monotropic character under usual pressure. Under normal pressure, a known irreversible solid-solid phase transition from the metastable form to the stable form occurs associated to an exothermic event {Nordstrom:2006km}. A more detailed description on this polymorphic system is given in the next chapter through the study of the monotropic transition by TR-SHG.

Preparation of pure polymorphic forms

m-hydroxybenzoic acid (MHBA) was purchased from Acros Organic (CAS registry number 99-06-9) with a chemical purity better than 99%. Different samples were prepared:

- (1) StabMHBA: Stable MHBA (Commercial MHBA annealed at 145°C during 1 hour)
- (2) MetMHBA: Metastable MHBA (recrystallization in acetone by evaporation under normal pressure and room temperature)
- (3) ComMHBA: Commercial MHBA without further purification

In the following we will demonstrate how second harmonic generation and TR-SHG can be used to detect and quantify structural impurities in commercial *m*-hydroxybenzoic acid and together with the structural purification monitoring of this product. The sensitivity of SHG is also compared with other usual techniques such as X-Ray Powder Diffraction (XRPD) and Differential Scanning Calorimetry (DSC).

5.3 Results and discussion

In order to evaluate the potential of the SHG technique for probing the structural purity of MHBA, samples of StabMHBA, MetMHBA and ComMHBA were first characterized by XRPD, DSC and SHG.

5.3.1 Characterization

XRPD analyses were performed on StabMHBA, MetMHBA and ComMHBA samples in the 2θ range from 3° to 30° at room temperature¹¹ and diffractograms are depicted in Figure 2.19, Figure 2.18 and Figure 2.21, respectively. The diffractogram of StabMHBA matches with the diffractogram of the centrosymmetric polymorph obtained from the CSD database (P2₁/c BIDLOP (Gridunova et al. 1982)). The diffractogram of MetMHBA fits with the diffractogram of the noncentrosymmetric polymorph (Pna2₁) (BIDLOP01 (Gridunova et al. 1982)).

¹¹ Experimental details in Appendix II

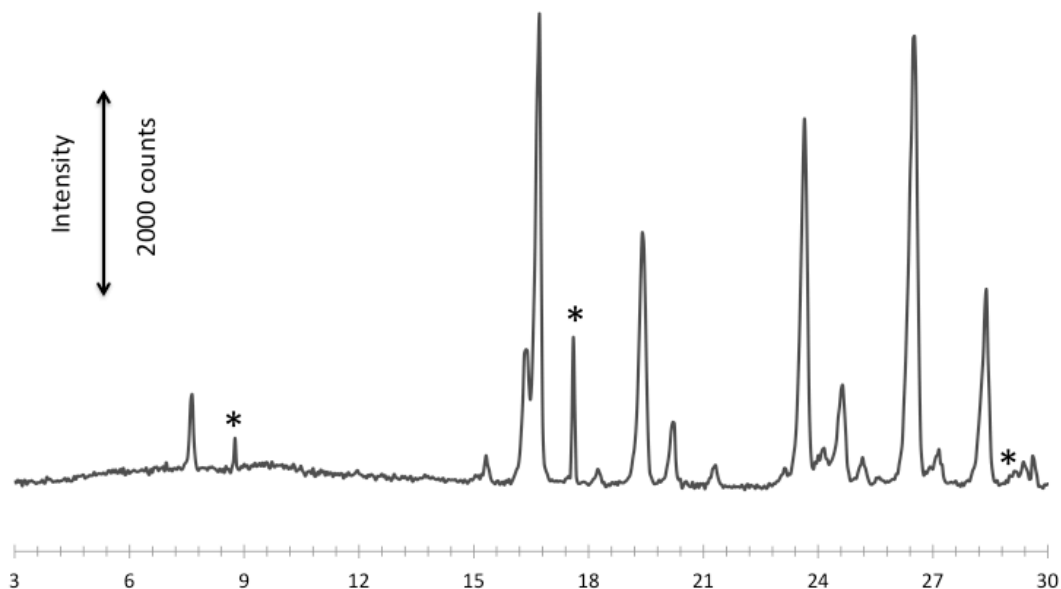


Figure 2.18 ComMHBA XRPD pattern (full line). Asterisk highlights peak diffraction of the metastable phase.

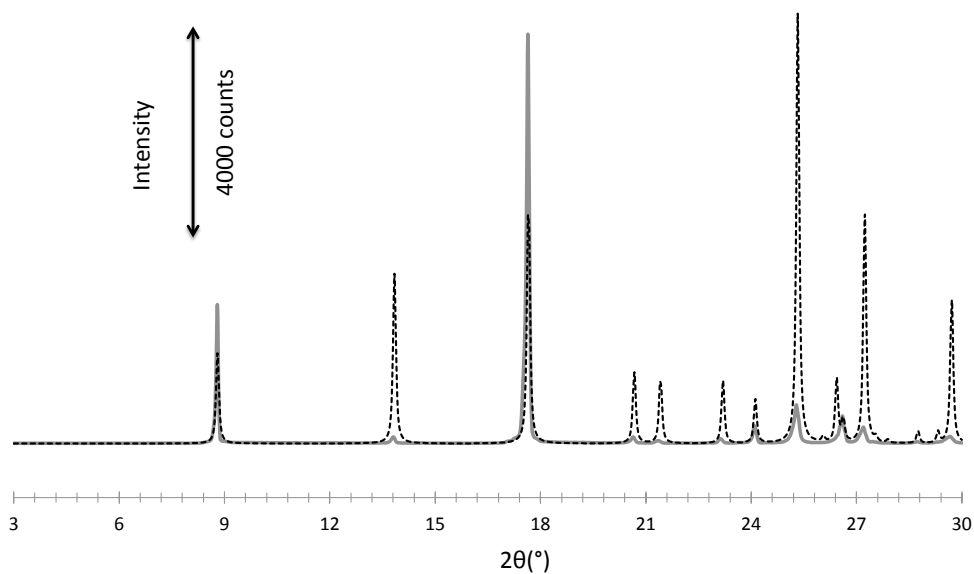


Figure 2.19 MetMHBA XRPD pattern (full line) and calculated pattern (dash line)

The diffractogram of ComMHBA exhibits 3 supplementary peaks by comparison to the diffractogram of the centric phase. These three peaks are also present on the diffractogram of MetMHBA. Two peaks (8.79° - 17.66°) correspond to a same lattice plane set ($h00$) with $h=2n$ and $n=1, 2$ and the latter peak (29.70°) corresponds to the (410) lattice interspace.

Consequently, XRPD results show that the commercial product (mainly centrosymmetric) is not structurally pure and contains a detectable amount of metastable Pna2₁ phase (with preferred orientation).

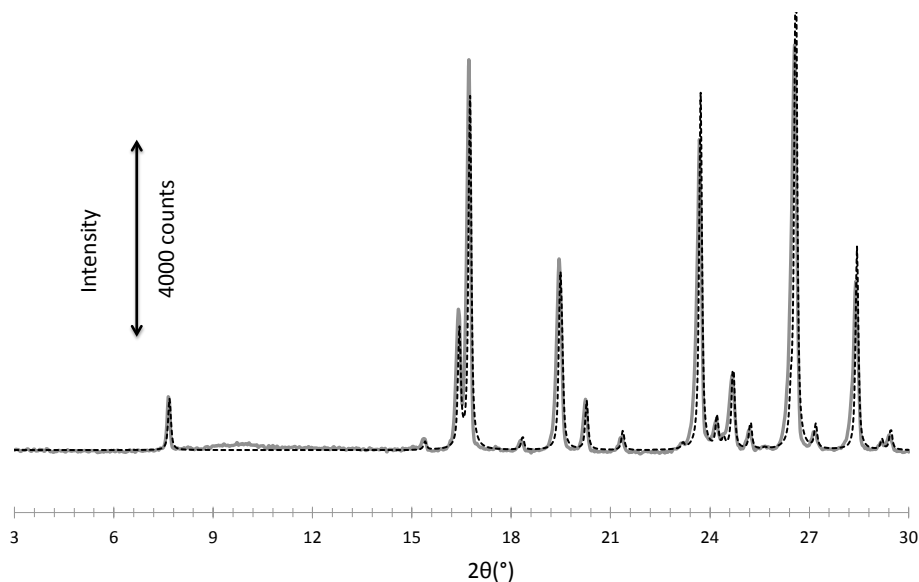


Figure 2.20 StabMHBA XRPD pattern (full line) and calculated pattern (dash line).

DSC analyses¹² were performed on StabMHBA, MetMHBA and ComMHBA samples for a heating rate of 16 K.min⁻¹ (Figure 2.21). This heating rate was chosen as the optimal rate for the detection of the exothermic event in the case of the solid-solid phase transition of MHBA. As expected, StabMHBA thermogram (a) exhibits a single thermic event (endothermic) corresponding to the melting. The melting enthalpy of StabMHBA derived from the DSC curves is 32.7 kJ.mol⁻¹. This value is in fairly good agreement with the enthalpy reported by Nordström (35.9 kJ.mol⁻¹) (Nordström and Rasmuson 2006). However, a lower value of 26.2 kJ.mol⁻¹ has also been reported (Sabbah and Le 1993).

¹² Experimental details in Appendix II

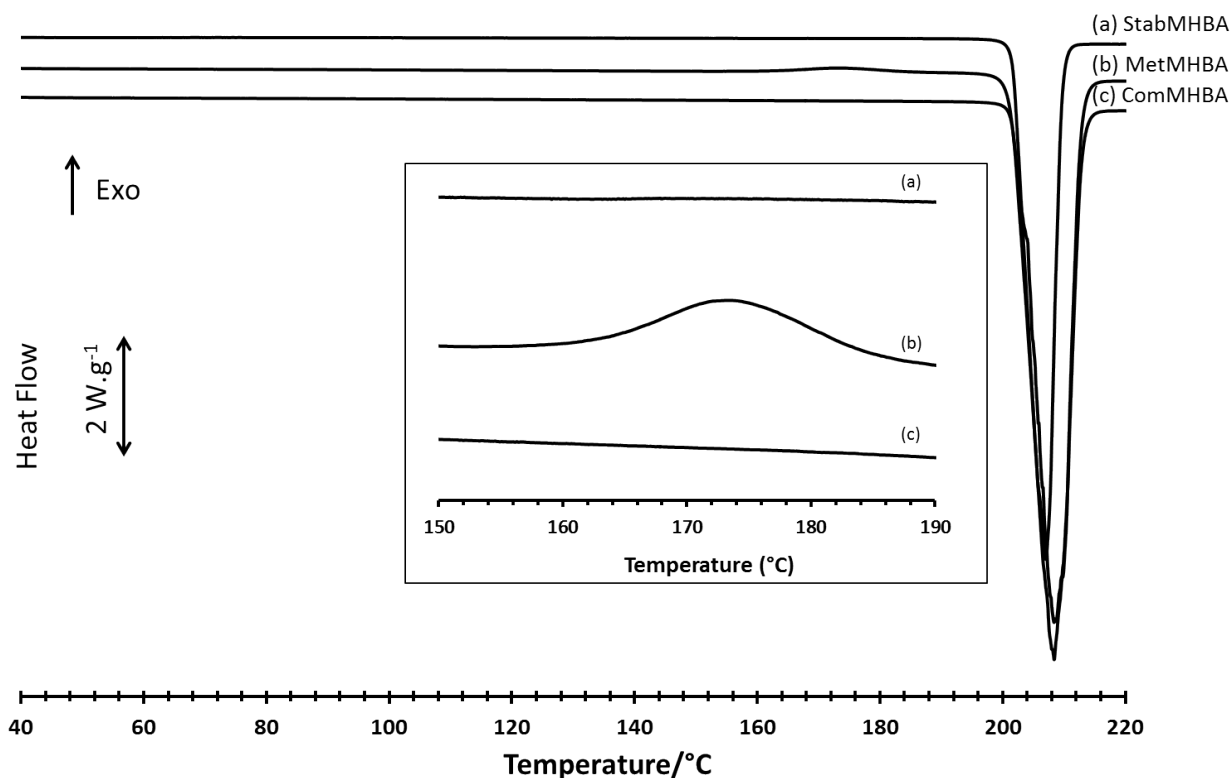


Figure 2.21 DSC curves from 40°C to 220°C and magnification between 150°C and 190°C for StabMHBA (a), MetMHBA (b) and ComMHBA (c) (heating rate: 16K.min⁻¹). The masses used to obtain thermograms were respectively 15.00, 14.98, and 15.05 mg. The exothermic event (conversion of the metastable form into the stable form) is visible only for MetMHBA.

MetMHBA thermogram (b) exhibits a weak exothermic event at circa 175°C in addition to the fusion peak already observed for StabMHBA (see magnification of the DSC traces on Figure 2.21). This exothermic event corresponds to the irreversible conversion of the metastable (Pna2₁) form into the stable form (monoclinic P2₁/c). Note that the solid-solid phase transition was also confirmed by polarized thermomicroscopy (results not shown). ComMHBA thermogram (c) does not exhibit any detectable exothermic event and is superimposable to the StabMHBA thermogram.

Consequently, DSC, contrary to XRPD, does not detect the presence of the metastable phase in the commercial product.

SHG analyses were performed on StabMHBA, MetMHBA and ComMHBA samples at room temperature. StabMHBA did not show any measurable SHG signal (as expected for this centrosymmetric structure). Thus the surface related SHG signal can be neglected. Contrary to StabMHBA, MetMHBA exhibited a high SHG value (3000 % of α -quartz). ComMHBA exhibited a weak SHG signal (28% of quartz), indicating the presence of a noncentrosymmetric impurity (here the metastable polymorph of MHBA) that is also confirmed by SHG microscopy. SHG microscopy picture (Figure 2.22) illustrates the

presence of MetMHBA in commercial product. Only few parts of the sample give a positive signal (metastable crystals emit green light)¹³.

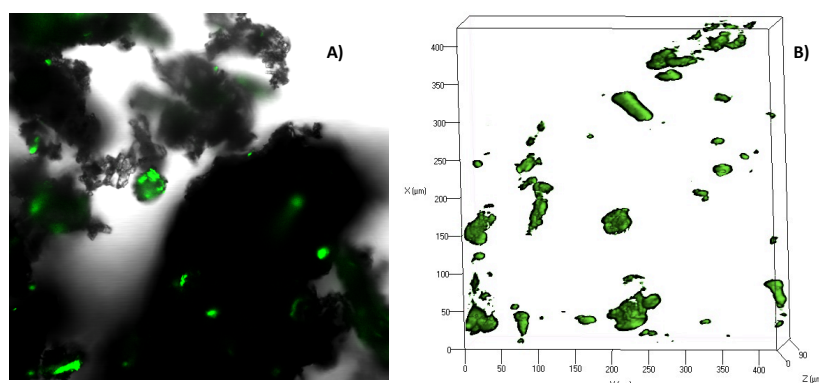


Figure 2.22 SHG-microscopy on ComMHBA (A) and 3D reconstruction (B). Only few particles give a positive signal (green light)

Finally, only SHG and XRPD detected the presence of the metastable form (structural impurity) into the commercial product whereas DSC did not.

5.3.2 Detection threshold

In order to compare the sensitivity of the three techniques, their detection thresholds were assessed. The detection threshold is defined here as the minimum mass fraction of metastable MHBA (in a physical mixture of MetMHBA and StabMHBA) measurable by the experimental device.

Several calibration standards containing mass fraction of metastable MHBA comprised between 2ppm and 50% were then prepared and submitted to XRPD, DSC and SHG analyses.

XRPD exhibits a good detection threshold with 1% wt. of metastable form detected. This value is significantly better than the commonly accepted value of 5%. It is probably due to a relatively high intensity of the diffraction peak of the metastable form. It is known that parameters such as preferential orientation, crystal size, crystallinity or low absorption coefficient can positively affect the response of the sample. It is also worth noting that some detection thresholds lower than 1% wt. have already been reported in favorable cases (Varasteh et al. 2009).

By comparison, DSC presents a poor detection threshold of 17% wt. (on Figure 2.23, the exothermic event is no more visible for compositions below this value). This low sensitivity is

¹³ Experimental details in Appendix II

mainly due to the weakness of the thermodynamic exothermic event associated with the irreversible transformation from the Pna2₁ form (SHG positive) to the P2₁/c form (SHG negative).

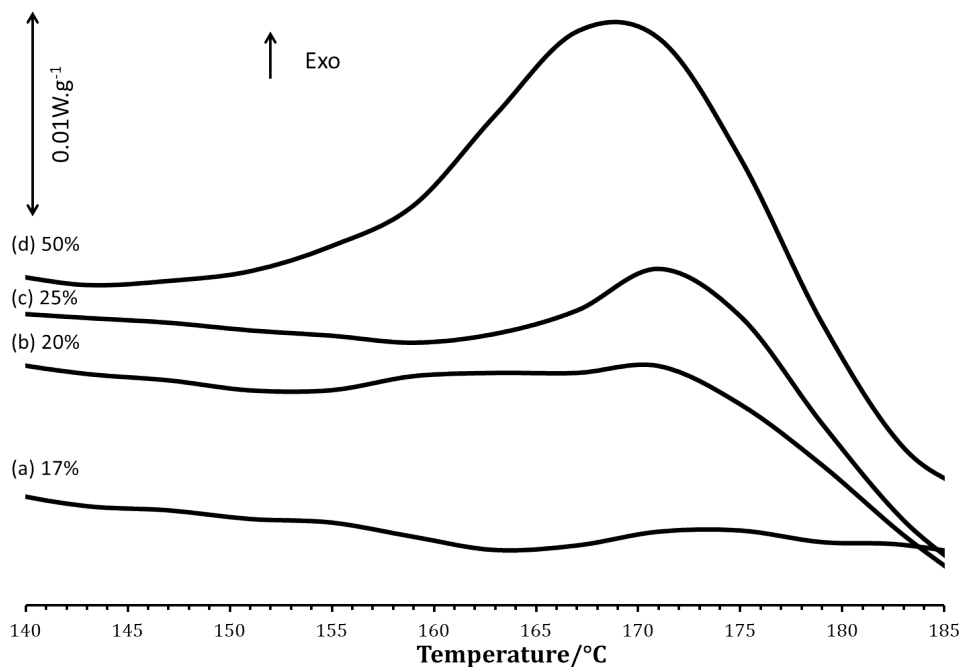


Figure 2.23 DSC curves for physical mixture of 17, 20, 25 and 50 % wt. of Metastable MHBA. The weak exothermic event attributed to the solid-solid phase transition is no more visible for fraction of metastable MHBA below 17% wt.

Most interesting is the 2 ppm threshold exhibited by the SHG technique which underlines the high sensitivity of SHG for the detection of very small quantities of structural impurities. However, this threshold value cannot be considered as a universal detection threshold for SHG as it highly depends on the sample studied. Indeed, the intensity of the SHG signal is related to various parameters such as the susceptibility tensor $\chi^{(2)}$, the shape and the size of the particles, the crystallinity, etc. It is also worth mentioning that SHG can only originate from noncentrosymmetric crystals, which limits the technique to non-centrosymmetric polymorphic phases or noncentrosymmetric impurities. From this point of view, m-hydroxybenzoic acid constitutes a favorable case as the structural impurity (here the metastable MHBA) crystallizes in a non-centrosymmetric structure and exhibits a high nonlinear response (the intensity of the SHG signal of the pure metastable phase is 30 times that of the alpha Quartz).

Nevertheless, provided a sufficient SHG activity of the impurity, SHG can be used to probe the structural purity of a sample at the level of few ppms. It should be noticed that similar works dealing on the detection of impurity using SHG microscopy (SHGM) demonstrate the high SHG sensitivity and selectivity with reported detection level of 0.04% (volume fraction)

of crystallinity in amorphous matrix (Wanapun et al. 2011) or of 1 part in 10 billion by volume (Wanapun et al. 2010). Nevertheless, these works imply the use of recent photomultipliers.

5.3.3 Quantification of structural impurity

Another challenging issue is to evaluate the proportion of structural impurity with a good accuracy. To find out if the mass fraction of metastable MHBA in the commercial product can be determined precisely by SHG, the SHG signal of mixtures of known compositions (prepared from the same batches of MetMHBA and StabMHBA) was measured and the SHG intensity was plotted versus the mass fraction of metastable MHBA. Results of Figure 2.24 show that the SHG intensity can be considered as linear with the mass fraction (determination coefficient of the regression line equal to 0.997). At first glance, this result could seem surprising because the *SHG signal is theoretically quadratic with the number of molecules within a crystal*. Nevertheless, signals arising from different crystals are not correlated so the SHG signal scales linearly with the number of non-centrosymmetric crystals in powders (Andrews et al. 1995). As a consequence, for powders SHG measurements, the dependence of the SHG signal with the mass fraction has often been reported to be linear or between linear or quadratic depending on the sample. (Vidal and Martorell 2006; Smilowitz et al. 2009) Consequently, from the slope of the regression line and the SHG intensity measured for the commercial product, the mass fraction of metastable MHBA in the commercial product can be evaluated to circa 1% wt.

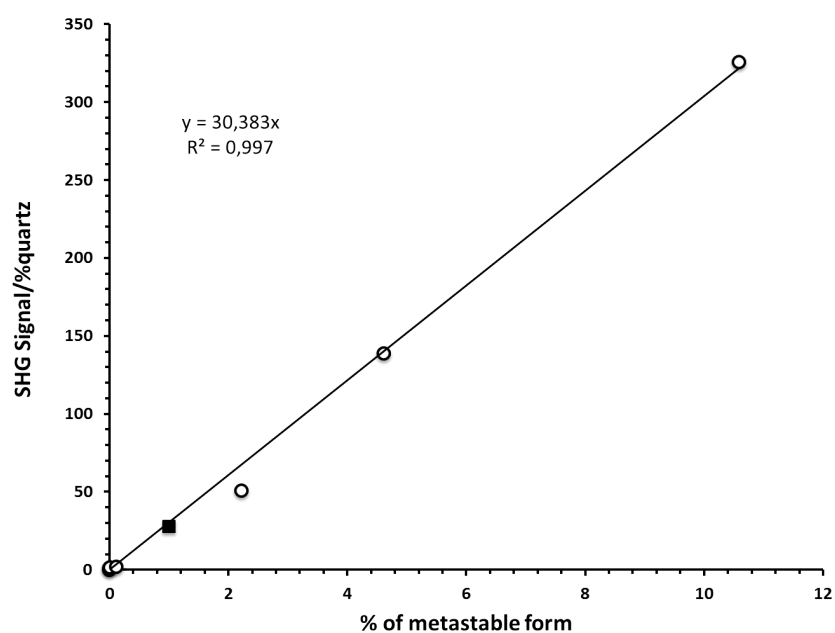


Figure 2.24 SHG signal (%quartz) versus fraction of metastable form inside the mixture (o). The fraction of metastable form in the commercial product estimated from the curve is 1% (■)

However, the accuracy of this result is difficult to evaluate. Indeed, the intensity of the SHG signal depends on the particle size. So, samples with different crystal size distribution but same mass fraction of impurity will not exhibit exactly the same SHG response. As a consequence, a certain variability of the results can be observed if non-calibrated samples are analyzed. Nonetheless, when the crystal size exceeds the coherence length, the SHG signal is independent of the crystal size for phase matchable materials. According to reference (Kurtz and Perry 1968), phase matchable materials of average size greater than 100 μm are not likely to exhibit a dependence of the SHG intensity with the crystal size. MetMHBA is phase matchable and the average crystal size of the crystals has been measured to circa 150 μm . then the SHG signal should not be strongly affected if samples from different batches have to be analyzed. Finally, if SHG can detect structural impurity at a very low level, it is not the preferred option in terms of precise quantification of impurity. Nevertheless, we show in the following, that due to its exceptional sensitivity, SHG coupled with a temperature control (TR-SHG) can be used with a significant relevancy to follow in-situ the structural purification of “contaminated” products.

5.3.4 Structural Purification of MHBA

The SHG signals emitted by MetMHBA and ComMHBA were measured versus temperature during heating at a rate of $5\text{K}\cdot\text{min}^{-1}$. The evolution of the mass fraction x of metastable MHBA converted to stable MHBA versus temperature is plotted on Figure 2.25 for each sample. A converted mass fraction x equal to 0% corresponds to the maximum SHG signal measured and a value of x equal to 100% is obtained when the SHG signal has totally vanished. So, x can be considered as the degree of completion of the solid-solid phase transition (i.e. of the structural purification process).

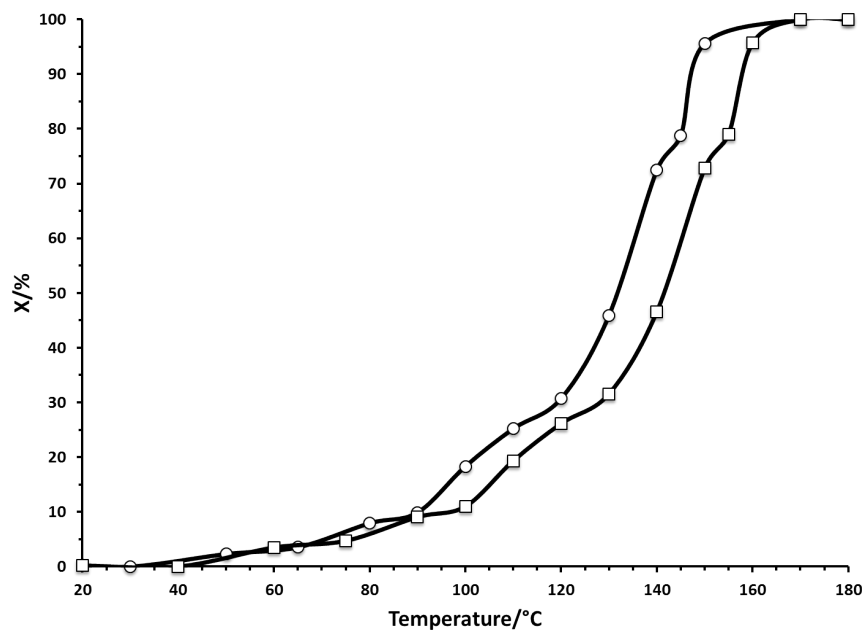


Figure 2.25 Evolution of the converted mass fraction x during heating at $5K.min^{-1}$ for (o) ComMHBA and (\square) MetMHBA

Results for MetMHBA show that the structural purity of the sample starts to increase at $40^{\circ}C$ but the phenomenon becomes really significant after circa $100^{\circ}C$. Above $160^{\circ}C$, the purification is completed (i.e. the material is constituted of the stable form ($P2_1/c$) only).

Results for ComMHBA show that despite the low mass fraction of metastable polymorph in the commercial product (previously evaluated at circa 1% wt), TR-SHG measurements allow to monitor with a high accuracy the solid-solid phase transition and thus the structural purification of the sample. Moreover, the conversion starts and is completed at slightly lower temperatures compared to MetMHBA which underlines the promoting effect of stable MHBA in the solid-solid phase transition.

In both cases, the curves are not perfectly smooth as some cut-off segments can be observed. This could be due to the crystal size distribution of the sample. Indeed, the solid-solid phase transition between MetMHBA and StabMHBA is monotropic. Thus the solid-solid phase transition can occur at any temperature once the energy barrier is overcome. The increase of the temperature enhances the molecular motion and helps to overcome this energy barrier. The crystal size acts as a kinetic barrier. As a consequence, in a polydisperse sample, most of the crystals of equivalent size will experience the transition simultaneously. In other terms, once the activation energy corresponding to a given crystal size class is reached, the

transformation starts and the SHG signal decreases (x increases) until the transformation is completed. Afterwards, the SHG intensity remains stable awaiting the energy barrier for a larger size class to be reached. This behavior seems consistent with a mechanism of nucleation and growth. A more detailed study of this transition will be presented in the next chapter.

Part.6 Conclusion

The developed SHG apparatus has been well tested and appears as reliable technique to detect very small amount of non-centrosymmetric sample. Generally, SHG signal at 0.1% of the α -quartz SHG intensity can be detected without ambiguity. This level of detection allows to be sure at 99% that a structure is centrosymmetric when no SHG signal is detected. (Kurtz and Perry 1968; Dougherty and Kurtz 1976)

Moreover, through the investigation of MHBA structural purity by SHG, the developed set-up reveals its high sensitivity and the following conclusions can be drawn:

- (1) SHG can be used to detect the presence of structural impurities provided that the contaminant exhibits a non-centrosymmetric structure in a centrosymmetric matrix.
- (2) SHG can show in favorable cases a detection threshold of few ppm. Such sensitivity can be reached neither by XRPD nor DSC techniques (i.e. in StabMHBA matrix, the detection of the percentage of metastable form is 17% by DSC, 1% by XRPD and only 2ppm by SHG)
- (3) SHG can be used to measure the fraction of structural impurity in a contaminated sample. However, quantification with SHG has to be considered with care when non-calibrated samples are used since the SHG intensity can vary upon the particle size distribution.
- (4) SHG and TR-SHG can be used at various stage of the process to control the structural purity with a particular relevance when polymorphs are in a monotropic relationship.
- (5) TR-SHG can be used to monitor, in situ, the purification of a contaminated sample even if the fraction of impurity in the starting product is far below 1% wt.

This latter point highlights the possibility to use this technique in order to monitor solid-solid transition. This aspect is developed in the following chapter.

References

- Abrahams SC. Letter to the Editor. *J Appl Crystallogr. International Union of Crystallography*; 1972;5(2):143–3.
- Abrahams SC, Schmalte HW, Williams T, Reller A, Lichtenberg F, Widmer D, et al. Centrosymmetric or Noncentrosymmetric? Case Study, Generalization and Structural Redetermination of Sr₅Nb₅O₁₇. *Acta Crystallogr B Struct Sci. International Union of Crystallography*; 1998 Aug 1;54(4):399–416.
- Abrahams SC, Sherwood RC, Bernstein JL, Nassau K. Transition metal iodates. II. Crystallographic, magnetic, and nonlinear optic survey of the 3d iodates. *Journal of Solid State Chemistry*. 1973 Jun;7(2):205–12.
- Ahuja SS. Assuring quality of drugs by monitoring impurities. *Advanced Drug Delivery Reviews. Elsevier*; 2007;59(1):3–11.
- Alagar M, Krishnakumar RV, Mostad A, Natarajan S. β - DL-Methionine at 105 K. *Acta Crystallogr Sect E Struct Rep Online. International Union of Crystallography*; 2005 Apr;61(4):o1165–7.
- Andrews DL, Allcock P, Demidov AA. Theory of second harmonic generation in randomly oriented species. *Chemical Physics*. 1995 Jan;190(1):1–9.
- Aramburu I, Ortega J, Folcia CL, Etxebarria J. Second harmonic generation by micropowders: a revision of the Kurtz–Perry method and its practical application. *Appl. Phys. B. Springer Berlin Heidelberg*; 2013 Dec 6;:1–23.
- Aramburu I, Ortega J, Folcia CL, Etxebarria J. Second-harmonic generation in dry powders: A simple experimental method to determine nonlinear efficiencies under strong light scattering. *APPLIED PHYSICS LETTERS*. 2014 Feb 17;104(7):071107.
- Aramburu I, Ortega J, Folcia CL, Etxebarria J, Illarramendi MA, Brezowski T. Accurate determination of second order nonlinear optical coefficients from powder crystal monolayers. *J. Appl. Phys. American Institute of Physics*; 2011;109(11):113105–113105–6.
- Ashwell GJ. Centrosymmetric molecules for second harmonic generation. *Adv. Mater*. 1996 Mar;8(3):248–50.
- Averbuch-Pouchot MT. Crystal structure of l-histidinium phosphite and a structure reinvestigation of the monoclinic form of l-histidine. *Zeitschrift für Kristallographie*. 1993 Jan;207(Part-1):111–20.
- Bahron H, Kassim K, Omar SRS, Rashid SH, Fun H-K, Chantrapomma S. (E, E)- N, N'-Bis(4-chlorophenyl)ethylenediamine. *Acta Crystallogr Sect E Struct Rep Online*. 2007 Feb;63(2):o558–60.
- Bass M. optical second-harmonic generation in crystals of organic dyes. *applied physics letters*. 1969;15(12):393.
- Baur WH, Tillmanns E. How to avoid unnecessarily low symmetry in crystal structure determinations. *Acta Crystallogr B Struct Sci. International Union of Crystallography*; 1986;42(1):95–111.
- Bell NA, Shearer HMM, Spencer CB. Dimeric methyl(diphenylamino)zinc, C₂₆H₂₆N₂Zn₂. *Acta Crystallogr C Cryst Struct Commun. International Union of Crystallography*; 1983 Sep 15;39(9):1182–5.
- Bendeif E-E, Jelsch C. The experimental library multipolar atom model refinement of L-aspartic acid. *Acta Crystallogr C Cryst Struct Commun. International Union of Crystallography*; 2007 May 24;63(6):o361–4.
- Boonstra EG. The crystal and molecular structure of 4,4'-dinitrodiphenyl. *Acta Cryst*. 1963 Aug;16(8):816–23.
- Bordner J, Stanford Jnr RH, Dickerson RE. The crystal structure of a photodimer of 1,4-epoxy-1,4-dihydronaphthalene. *Acta Crystallogr B Struct Crystallogr Cryst Chem*. 1970 Aug 15;26(8):1166–72.
- Chaney MO, Steinrauf LK. The crystal and molecular structure of tetragonal L-cystine. *Acta Crystallogr B Struct Crystallogr Cryst Chem*. 1974 Mar 15;30(3):711–6.

- Clemente DA. A study of the 8466 structures reported in *Inorganica Chimica Acta*: 52 space group changes and their chemical consequences. *Inorganica Chimica Acta*. 2005 Mar;358(6):1725–48.
- Clevers S, Simon F, Dupray V, Coquerel G. Temperature resolved second harmonic generation to probe the structural purity of m-hydroxybenzoic acid. *Journal of Thermal Analysis and Calorimetry*. Springer; 2013;(112):1–7.
- Coda A, Pandarese F. Reliability of second-harmonic generation in crystalline powders at optical frequencies as a test of absence of centrosymmetry. *J Appl Crystallogr*. 1976 Jun;9(3):193–8.
- Coles SJ, Gelbrich T, Griesser UJ, Hursthouse MB, Pitak M, Threlfall T. The Elusive High Temperature Solid-State Structure of d, l-Norleucine. *Crystal Growth & Design*. 2009 Nov 4;9(11):4610–2.
- Coppens P, Abramov Y, Carducci M, Korjov B, Novozhilova I, Alhambra C, et al. Experimental Charge Densities and Intermolecular Interactions: Electrostatic and Topological Analysis of dl-Histidine. *J. Am. Chem. Soc*. 1999 Mar;121(11):2585–93.
- Coquerel G. The “structural purity” of molecular solids—An elusive concept? *Chemical Engineering and Processing*. 2006 Oct;45(10):857–62.
- Courvoisier L, Gervais C, Mignot L, Petit MN, Coquerel G. Effect of the polymorphic form of the seeds on the preferential crystallisation. *J. Phys. IV France*. 2001 Dec;11(PR10):Pr10–71–Pr10–77.
- Couvrat N, Blier AS, Berton B, Cartigny Y, Dupray V, Coquerel G. Characterization of Defects Inside Single Crystals of Ciclopirox. *Crystal Growth & Design*. 2009 Jun 3;9(6):2719–24.
- Cummins SE. Electrical and Optical Properties of Ferroelectric Bi₄Ti₃O₁₂ Single Crystals. *J. Appl. Phys.* AIP Publishing; 1968;39(5):2268–74.
- Dahaoui S, Pichon-Pesme V, Howard JAK, Lecomte C. CCD Charge Density Study on Crystals with Large Unit Cell Parameters: The Case of Hexagonal l-Cystine. *J. Phys. Chem. A. American Chemical Society*; 1999 Aug;103(31):6240–50.
- Dalhus B, Görbitz CH. Crystal structures of hydrophobic amino acids I. Redeterminations of L-Methionine and L-Valine at 120 K. *Acta Chemica Scandinavica*. Copenhagen: Munksgaard, c1989-c1999; 1996;50(6):544–8.
- Delfino M. A comprehensive optical second harmonic generation study of the non-centrosymmetric character of biological structures. *J Biol Phys*. 1978 Sep;6(3-4):105–17.
- Destro R, Pilati T, Simonetta M. Another aromaticity vs non-aromaticity dilemma. *Tetrahedron*. 1980 Jan;36(22):3301–4.
- Dogan A, Uchino K, Newnham RE, Galassi C, Dinescu M, Uchino K, et al. *Piezoelectric Materials: Advances in Science, Technology and Applications*. 2000;:357–74.
- Dougherty JP, Kurtz SK. A second harmonic analyzer for the detection of non-centrosymmetry. *J Appl Crystallogr*. 1976 Apr;9(2):145–58.
- Dupray V. *Recrystallization of Enantiomers from Conglomerates*. intechopen.com. InTech; 2012.
- Flack H, Bernardinelli G. Centrosymmetric crystal structures described as non-centrosymmetric: An analysis of reports in *Inorganica Chimica Acta*. *Inorganica Chimica Acta*. Elsevier; 2006;359(1):383–7.
- Flaig R, Koritsanszky T, Dittrich B, Wagner A, Luger P. Intra- and Intermolecular Topological Properties of Amino Acids: A Comparative Study of Experimental and Theoretical Results. *J. Am. Chem. Soc. American Chemical Society*; 2002 Apr;124(13):3407–17.
- Franken PA, Hill AE, Peters CW, Weinreich G. Generation of Optical Harmonics. *Phys. Rev. Lett. American Physical Society*; 1961 Aug;7:118–9.

- Frey MN. Precision neutron diffraction structure determination of protein and nucleic acid components. X. A comparison between the crystal and molecular structures of L-tyrosine and L-tyrosine hydrochloride. *J. Chem. Phys.* 1973;58(6):2547.
- Galland A, Dupray V, Berton B, Morin-Grognet S, Sanselme M, Atmani H, et al. Spotting Conglomerates by Second Harmonic Generation. *Crystal Growth & Design.* 2009 Jun 3;9(6):2713–8.
- Glazer AM, Stadnicka K. On the use of the term 'absolute' in crystallography. *Acta Cryst* (1989). A45, 234-238 [doi:10.1107/S0108767388011055]. *International Union of Crystallography*; 1989 Mar 1;:1–5.
- Görbitz CH, Dalhus B. L-Cysteine, Monoclinic Form, Redetermination at 120K. *Acta Crystallogr C Cryst Struct Commun. International Union of Crystallography*; 1996a Jul 15;52(7):1756–9.
- Görbitz CH, Dalhus B. L-Isoleucine, Redetermination at 120K. *Acta Crystallogr C Cryst Struct Commun. International Union of Crystallography*; 1996b Jun 15;52(6):1464–6.
- Görbitz CH, Dalhus B. Redetermination of L-Leucine at 120K. *Acta Crystallogr C Cryst Struct Commun.* 1996c Jul 15;52(7):1754–6.
- Görbitz CH, Törnroos KW, Day GM. Single-crystal investigation of L-tryptophan with $Z' = 16$. *Acta Crystallogr B Struct Sci.* 2012 Sep 13;68(5):549–57.
- Gridunova GV, Furmunova NG, Struchkov YT, Ezhkova ZI, Grigoreva L.P, Chayanov BA. BIDLOP&BIDLOP01. *Kristallografiya.* 1982 Feb 17;27:267.
- Haberecht MC, Bolte M, Bats JW, Lerner H-W, Wagner M. 4, 4'-Disubstituted 2, 2'-bipyridines for the design of push-pull ligands. *Zeitschrift für Naturforschung B-Journal of Chemical Sciences.* Tubingen: Verlag der Zeitschrift für Naturforschung, 1987; 2005;60(7):745–52.
- Hahn T. *International Tables for Crystallography, Brief Teaching Edition of Volume A.* Springer; 2002.
- Haisa M, Kashino S. The crystal and molecular structure of 1, 4-diethoxybenzene. *Acta Crystallogr B Struct Crystallogr Cryst Chem. International Union of Crystallography*; 1977;33(2):485–90.
- Helmy R, Zhou GX, Chen YW, Crocker L, Wang T, Wenslow RM, et al. Characterization and Quantitation of Aprepitant Drug Substance Polymorphs by Attenuated Total Reflectance Fourier Transform Infrared Spectroscopy. *Anal. Chem.* 2003 Feb;75(3):605–11.
- Herbstein FH, Schoening F. On centrosymmetric molecules in non-centrosymmetric space groups. *Acta Cryst. International Union of Crystallography*; 1957;10(10):657–63.
- Hursthouse MB, Laffey MA, Moore PT, New DB, Raithby PR, Thornton P. Crystal and molecular structures of some binuclear complexes of cobalt(II) and nickel(II) acetylacetonates with pyridines and piperidine and a refinement of the crystal and molecular structure of hexakis-(acetylacetonato)trinickel(II). *J. Chem. Soc., Dalton Trans. The Royal Society of Chemistry*; 1982;(2):307–12.
- Hübschle CB, Messerschmidt M, Luger P. Crystal structure of DL-Tryptophan at 173K. *Cryst. Res. Technol. Wiley Online Library*; 2004;39(3):274–8.
- Iball J, Morgan CH, Zacharias DE. Refinement of the crystal structure of orthorhombic dibenz[a,h]-anthracene. *J. Chem. Soc., Perkin Trans. 2. The Royal Society of Chemistry*; 1975;(12):1271–2.
- Iwama S, Horiguchi M, Sato H, Uchida Y, Takahashi H, Tsue H, et al. Observation of the Preferential Enrichment Phenomenon for Essential α -Amino Acids with a Racemic Crystal Structure. *Crystal Growth & Design. American Chemical Society*; 2010 Jun 2;10(6):2668–75.
- Janczak J, Zobel D, Luger P. L-Threonine at 12 K. *Acta Crystallogr C Cryst Struct Commun.* 1997 Dec;53(12):1901–4.

- John Wiley & Sons, Inc., editor. Kirk-Othmer Encyclopedia of Chemical Technology. Hoboken, NJ, USA: John Wiley & Sons, Inc; 2000.
- Kayushina RL, Vainshtein BK. Kristallografiya(Russ.)(Crystallogr.Rep.). 1965 Sep 22;10:833
- Khawas B. The unit cells and space groups of L-methionine, L- β -phenylalanine and DL-tyrosine. Acta Crystallogr B Struct Crystallogr Cryst Chem. International Union of Crystallography; 1970 Dec 15;26(12):1919–22.
- Khawas B. X-ray study of l-arginine HCl, l-cysteine, dl-lysine and dl-phenylalanine. Acta Crystallogr B Struct Crystallogr Cryst Chem [Internet]. International Union of Crystallography; 1971 Aug 15;27(8):1517–20. Available from: <http://journals.iucr.org/b/issues/1971/08/00/a08270/a08270.pdf>
- Khawas B. Crystal data for D-methionine $\text{CH}_3\text{SCH}_2\text{CH}_2\text{CH}(\text{NH}_2)\text{COOH}$ and D-tyrosine $\text{HOCH}_2\text{CH}_2\text{CH}(\text{NH}_2)\text{COOH}$. J Appl Crystallogr. International Union of Crystallography; 1986 Oct;19(5):410–0.
- Kiehl A, Eberhardt A, Adam M, Enkelmann V, Müllen K. A Homologous Series of Stable Polyenes: Synthesis, Structure, and Redox Behavior. Angew. Chem. Int. Ed. 1992 Dec;31(12):1588–91.
- Kiryu S. The crystal structure of nickel(II)-dehydroacetic acid monoimide complex. Acta Cryst. 1967 Sep 10;23(3):392–7.
- Kistenmacher TJ, Rand GA, Marsh RE. Refinements of the crystal structures of DL-serine and anhydrous L-serine. Acta Crystallogr B Struct Crystallogr Cryst Chem. 1974 Nov 15;30(11):2573–8.
- Kolesov BA, Minkov VS, Boldyreva EV, Drebushchak TN. Phase Transitions in the Crystals of l- and dl-Cysteine on Cooling: Intermolecular Hydrogen Bonds Distortions and the Side-Chain Motions of Thiol-Groups. 1. l-Cysteine. J. Phys. Chem. B. 2008 Oct 9;112(40):12827–39.
- Kurtz SK, Perry TT. A Powder Technique for the Evaluation of Nonlinear Optical Materials. J. Appl. Phys. AIP; 1968;39(8):3798–813.
- Lehmann MS, Koetzle TF, Hamilton WC. Precision neutron diffraction structure determination of protein and nucleic acid components. VIII: the crystal and molecular structure of the β -form of the amino acid l-glutamic acid. J Chem Crystallogr. 1972 Dec;2(5-6):225–33.
- Lehmann MS, Nunes AC. A short hydrogen bond between near identical carboxyl groups in the α -modification of L-glutamic acid. Acta Crystallogr B Struct Crystallogr Cryst Chem. 1980 Jul 15;36(7):1621–5.
- Li Y-L, Zhang F-J, Wang Q-G. Studies on the synthesis of some new biflavanoids VII. Synthesis and structures of 2,2"-biflavanones. Chin. J. Chem. 1992 Aug 27;10(4):359–64.
- Loiacono G, Kostecky G, White J. Resolution of space group ambiguities in minerals. American Mineralogist. Mineral Soc America; 1982;67(7-8):846–7.
- Madden JJ, McGandy EL, Seeman NC. The crystal structure of the orthorhombic form of L-(+)-histidine. Acta Crystallogr B Struct Crystallogr Cryst Chem. International Union of Crystallography; 1972 Aug 15;28(8):2377–82.
- Maker P, Terhune R, Nisenoff M, Savage C. Effects of Dispersion and Focusing on the Production of Optical Harmonics. Physical Review Letters. 1962 Jan;8(1):21–2.
- Marsh RE. Some thoughts on choosing the correct space group. Acta Crystallogr B Struct Sci. 1995 Dec 1;51(6):897–907.
- Marsh RE, Kapon M, Hu S, Herstein FH. Some 60 new space-group corrections. Acta Crystallogr B Struct Sci. International Union of Crystallography; 2001 Jan 24;58(1):62–77.
- McGregor C, Saunders MH, Buckton G, Saklatvala RD. The use of high-speed differential scanning calorimetry (Hyper-DSC™) to study the thermal properties of carbamazepine polymorphs. Thermochemica Acta. 2004

- Jul;417(2):231–7.
- Meng Q, Zhang W, Yu J, Huang D. Crystal structure of anthraquinone-1,5-dithiol. *Dyes and Pigments*. 2005 Jun;65(3):281–3.
- Mostad A, Romming C. Crystal-structure of DL-tyrosine. *Acta Chem. Scand*. 1973;27:401–10.
- Muller U. Kristallisieren zentrosymmetrische Moleküle immer in zentrosymmetrischen Raumgruppen?-Eine statistische Übersicht. *Acta Crystallogr B Struct Crystallogr Cryst Chem. International Union of Crystallography*; 1978;34(3):1044–6.
- Newnham RE, Wolfe RW, Dorrian JF. Structural basis of ferroelectricity in the bismuth titanate family. *Materials Research Bulletin*. 1971 Oct;6(10):1029–39.
- Nikogosyan DN. *Nonlinear Optical Crystals: A Complete Survey*. Springer; 2006.
- Nordström FL, Rasmuson ÅC. Polymorphism and thermodynamics of m-hydroxybenzoic acid. *European Journal of Pharmaceutical Sciences*. 2006 Aug;28(5):377–84.
- Pidcock E. Achiral molecules in non-centrosymmetric space groups. *Chem. Commun. The Royal Society of Chemistry*; 2005;(27):3457–9.
- Robertson JM, White JG. 195. The crystal structure of the monoclinic modification of 1 : 2-5 : 6-dibenzanthracene. A quantitative X-ray investigation. *J. Chem. Soc. The Royal Society of Chemistry*; 1956;(0):925–31.
- Sabbah R, Le THD. Étude thermodynamique des trois isomères de l'acide hydroxybenzoïque. *Can J Chem. NRC Research Press*; 1993;71(9):1378–83.
- Smilowitz LB, Henson BF, Romero JJ. A comparison of observables for solid-solid phase transitions. Los Alamos National Laboratory (LANL); 2009.
- Subha Nandhini M, Krishnakumar RV, Natarajan S. DL-Alanine. *Acta Crystallogr C Cryst Struct Commun*. 2001 May 15;57(5):614–5.
- Taniguchi T, Takaki Y, Sakurai K. The crystal structures of the .ALPHA. and .BETA. forms of DL-methionine. *Bull. Chem. Soc. Jpn*. 1980;53(3):803–4.
- Thomas JM. Determining the Structure of L-Arginine and Other Organic Molecules. *ChemPhysChem*. 2012 Jun 11;13(11):2637–8.
- van Niekerk JN, Boonstra EG. Evidence from 4:4'-dinitrodiphenyl on the improbability of non-centrosymmetric crystals containing centrosymmetric molecules. *Acta Cryst*. 1961 Nov 10;14(11):1186–7.
- Varasteh M, Deng Z, Hwang H, Kim YJ, Wong GB. Quantitative determination of polymorphic impurity by X-ray powder diffractometry in an OROS® formulation. *International Journal of Pharmaceutics*. 2009 Jan;366(1-2):74–81.
- Vidal X, Martorell J. Generation of Light in Media with a Random Distribution of Nonlinear Domains. *Phys. Rev. Lett*. 2006 Jul;97(1).
- Wagner A, Luger P. Charge density and topological analysis of l-glutamine. *Journal of Molecular Structure*. 2001 Sep;595(1-3):39–46.
- Waldschmidt A, Couvrat N, Berton B, Dupray V, Morin S, Petit S, et al. Impact of Gas Composition in the Mother Liquor on the Formation of Macroscopic Inclusions and Crystal Growth Rates. Case Study with Ciclopirox Crystals. *Crystal Growth & Design. American Chemical Society*; 2011a Jun;11(6):2463–70.
- Waldschmidt A, Rietveld I, Couvrat N, Dupray V, Sanselme M, Berton B, et al. About Aged Heterogeneous

- Liquid Inclusions Inside Organic Crystals in Relation to Crystal Formation, Structure, and Morphology. *Crystal Growth & Design*. 2011b Jun;11(6):2580–7.
- Wanapun D, Kestur US, Kissick DJ, Simpson GJ, Taylor LS. Selective Detection and Quantitation of Organic Molecule Crystallization by Second Harmonic Generation Microscopy. *Anal. Chem. American Chemical Society*; 2010 Jul;82(13):5425–32.
- Wanapun D, Kestur US, Taylor LS, Simpson GJ. Single Particle Nonlinear Optical Imaging of Trace Crystallinity in an Organic Powder. *Anal. Chem.* 2011 Jun 15;83(12):4745–51.
- Watkin D. The control of difficult refinements. *Acta Crystallogr A Found Crystallogr.* 1994 Jul;50(4):411–37.
- Watkin D. Structure refinement: some background theory and practical strategies. *J Appl Crystallogr.* 2008 Apr 19;41(3):491–522.
- Weissbuch I, Frolow F, Addadi L, Lahav M, Leiserowitz L. Oriented crystallization as a tool for detecting ordered aggregates of water-soluble hydrophobic α -amino acids at the air-solution interface. *J. Am. Chem. Soc.* 1990 Oct;112(21):7718–24.
- Wolfe RW, Newnham RE, Smithf DK, Kay MI. Crystal structure of Bi₃tinbo₉. *Ferroelectrics*. Taylor & Francis Group; 1972 Feb;3(1):1–7.
- Zorkii PM, Lazareva SG. Crystal-chemical analysis of structures with asymmetric congruently-similar molecules. *J Struct Chem*. Kluwer Academic Publishers-Plenum Publishers; 1967 Jul;8(4):597–601.

Chapter 3. Solid-solid transitions investigated by SHG

Part.1 Introduction & Literature review on phase transition studied by SHG methods

Understanding and tracking phase transition (mechanisms) constitute an important topic for researchers in various fields and especially in pharmaceuticals. As we previously mentioned, new polymorphic forms can arise during the production processes (consecutive to temperature, pressure or humidity changes) with drastic consequences in many domains (e.g. Napoleon Bonaparte Russian campaign disaster (Monk 2008), appearance of new phase drug (Chemburkar et al. 2000)...).

	Molecule	References
First-order transition	$\text{NH}_4\text{Cl}^{14}$	(Bartis 1971; Herbststein 2006; Monk 2008)
	$\text{NH}_4\text{Cl}_{(1-x)}\text{Br}_x$ (for $x=0.11$)	(Hirsch and Stühmer 1976)
	2,3-dichloroquinizarin	(Hall et al. 1988)
	HMX	(Henson et al. 1999; Saw et al. 2001)
	TATB	(Son et al. 1999; Saw et al. 2001)
	BaTi_2O_5	(Masuno et al. 2011)
	SrTiO_3	(Betzler 1980)
	Squaric acid	(Betzler and Bäuerle 1979)
	$\text{Ba}_2\text{NaNb}_5\text{O}_{15}$	(Schneck et al. 1977)
	Colemanite	(Dougherty and Kurtz 1976)
	$\text{Ca}_9\text{Fe}(\text{PO}_4)_7$	(Lazoryak et al. 2004)
	$\alpha\text{-(H}_3\text{N(CH}_2)_2\text{-S(CH}_2)_2\text{NH}_3\text{)BiI}_5$	(Bi et al. 2008)
	$[\text{C}(\text{NH}_2)_3]_4\text{Cl}_2\text{SO}_4$	(Bragiel et al. 2007)
	$[(\text{H}_2\text{cys})\text{PbI}_6]\cdot 2\text{H}_2\text{O}$	(Louvain et al. 2008)
	KNbO_3	(Gopalan and Raj 1996)
	$\text{Na}_{0.5}\text{Bi}_{0.5}\text{TiO}_3$	(Jones and Thomas 2002)
TiNbWO_6 & RbNbWO_6	(Sleight et al. 1978)	
${}^6\text{LiRbSO}_4$ & ${}^7\text{LiRbSO}_4$	(Kim et al. 1996; Henson et al. 1999; Saw et al. 2001)	
KNO_3	(Son et al. 1999; Saw et al. 2001; Kidyarov et al. 2013)	
Order-disorder transition	BaTiO_3	(Vogt 1974; Dougherty and Kurtz 1976; Fox et al. 1990; Masuno et al. 2011; Kovalevskii et al. 2012)
	NaNO_2	(Vogt et al. 1970; Iio and Yanagi 1973; Betzler 1980; Fleury and Lyons 1981)
	Quartz	(Dolino 1975; Betzler and Bäuerle 1979)
	LiTaO_3 & LiNbO_3	(Miller 1966, Bergman 1976)
	PbHPO_4	(Dougherty and Kurtz 1976; Keens and Happ 2000)
	Triglycine sulphate (Hdabco ⁺)(CF ₃ COO ⁻)	(Lazoryak et al. 2004; Xiong 2013) (Bi et al. 2008; Sun et al. 2013)
Conformation changes	Collagen	(Theodossiou et al. 2002)

Table 3.1 TR-SHG studies found in literature and using a K&P apparatus or similar.

¹⁴ See (Herbststein 2006) for clarification between first and second-order phase transition

In chapter 2, we already demonstrated that our TR-SHG set up can be used to check the structure purity and to track purification processes in the case of MHBA. This was our first step in the study of solid-solid transitions by TR-SHG. Several authors have already reported the use of SHG to characterized temperature-induced phase transitions in polymorphic systems. The most relevant studies are summarized in Table 3.1. It should be also noted that the evolution of SHG signal with pressure (Bayarjargal et al. 2012; Bayarjargal and Winkler 2013) and magnetic field (Fiebig et al. 2005; Sampaio et al. 2005) were also recently studied. Several data can be obtained from TR-SHG experiments. For instance, the structural phase transitions of BaTiO₃ are an interesting case because highlighting the potential of SHG to monitor phase transitions between NC and NC or C and NC phases (see TR-SHG curves in Figure 3.1).

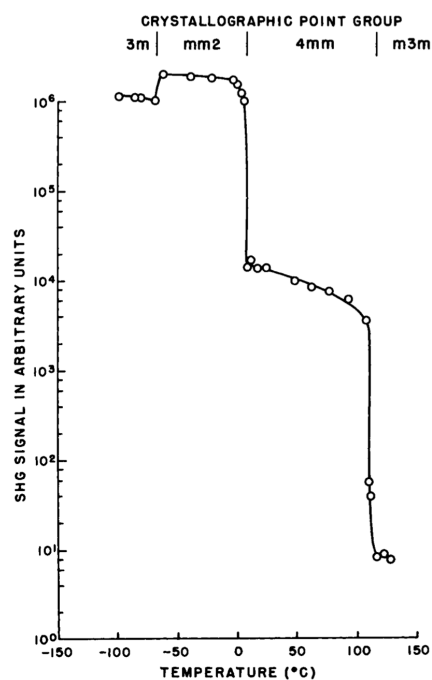


Figure 3.1 TR-SHG¹⁵ in BaTiO₃ showing the sensitivity to both centric \leftrightarrow acentric ($m3m \leftrightarrow 4mm$ at 130°C) and acentric \leftrightarrow acentric ($4mm \leftrightarrow mm2$ at 4°C and $mm2 \leftrightarrow 3m$ at -75°C) phase transition. Since the equilibrium structure above T_c is cubic, $Pm3m$, a plausible hypothesis for the high-temperature anomalous SHG is dynamic disorder, possibly coupled with local polarization fluctuations.

Another interesting example is the observation of a SHG signal for the high-temperature phase of (Na⁺:NO₂⁻) having a “time-averaged” point group symmetry mmm (thus centrosymmetric). In fact, SHG activity is due to the flipping motion (see Figure 3.2) of Na⁺ and NO₂⁻ ions about the (010) plane (Vogt et al. 1970; Vogt 1973; 1974).

¹⁵ (Reprint from Dougherty and Kurtz 1976)

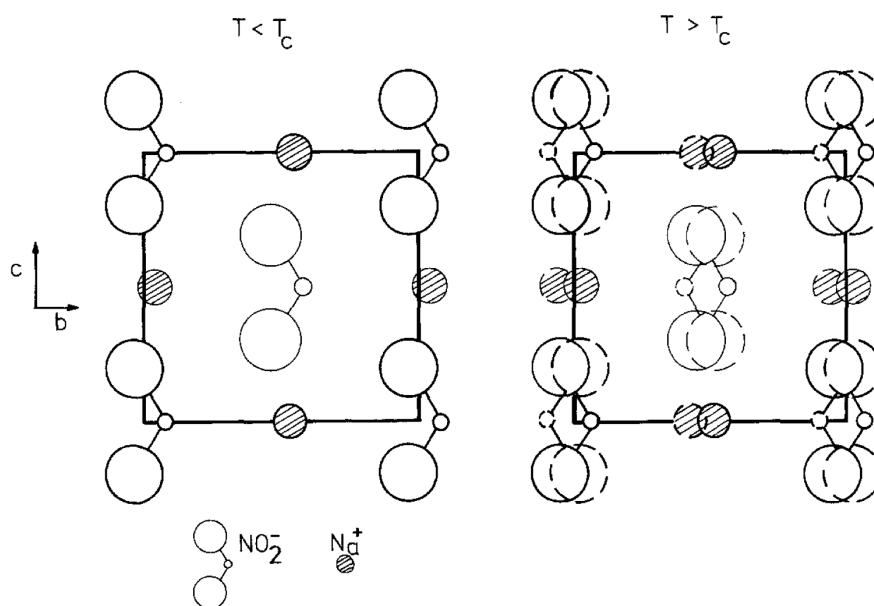


Figure 3.2 Scheme of the order-disorder transition in NaNO_2 from (Vogt 1974). Projections of the orthorhombic unit cell of NaNO_2 above and below T_c . Above T_c , the long-range order is destroyed by flipping motion of the ions. Macroscopically, the crystal structures possess an inversion center due to the average on the positions and orientations taken by the ions (statistical occupancy factor (S.O.F) = 50/50).

This reported case illustrates the potential of the SHG technique to probe short-range order in nominally centric phases and could be applied to the detection of molecular disorder in organic solids. The nonlinear susceptibility tensor is proportional to the average molecular polarizability $\langle\beta\rangle$ of the unit cell, thus it is proportional to the mean position and orientation of molecular units with respect to crystallographic axes. Consequently, the SHG signal can be used as a probe revealing the molecular and crystal symmetry changes.

One can notice that the majority of compounds studied by TR-SHG (in Table 3.1) belongs to inorganic or organo-metallic although the proportion of NC structures are lower than in purely organic solids. This fact can be attributed to a lack of “cross-fertilization” between nonlinear optics and solid-state organic chemistry communities.

In this chapter the relevancy of TR-SHG to monitor phase transitions in organic solids will be discussed through two main studies: a monotropic transition with a destructive/reconstructive mechanism and a second-order like transition. We will demonstrate that SHG is all the more interesting than further data can be extracted from SHG measurements versus temperature.

Part.2 Monotropic transition mechanism of m-hydroxybenzoic acid (MHBA)

The main characteristics of MHBA such as the experimental used to obtain the various polymorphic forms have already been described in chapter 2. Let us just recall that MHBA exhibits two polymorphic forms in a monotropic relationship: the metastable $Pna2_1$ (MetMHBA) and the stable $P2_1/n$ (StabMHBA). Hereafter a more precise description of the two crystalline structures is given in order to support the discussion arising from TR-SHG experiments.

2.1 Presentation of the polymorphic system

The two unsolvated polymorphic forms of MHBA are referenced in Crystal Structure Database as BIDLOP01 (metastable $Pna2_1$ form) and BIDLOP (stable $P2_1/n$ form). Crystallographic data from CSD are reported in Table 3.2. Single Crystal X-Ray Diffraction (SC-XRD)¹⁶ was performed for MetMHBA in order to detect a potential disorder in the crystal packing. The corresponding crystallographic data (reported on Table 3.2) are in good agreement with the data from CSD (with a slightly better reliability factor) and did not give any argument in favor of a disordered structure. Unfortunately, single crystal of StabMHBA with sufficient good quality to perform SC-XRD could not be isolated due to concomitant crystallization of stable and metastable polymorphs.(Nordstrom et al. 2012; Svard and Rasmuson 2013)

¹⁶ Experimental details in Appendix II, MHBA large crystals of good optical quality (several microns size) were obtained by cooling of a saturated solution of ComMHBA in acetone from 45°C to 20°C with a rate of 1K.h⁻¹. The solution was kept at 20°C for 24h before drying.

Ref Code	BIDLOP	BILOP01	This work CCDC 933474
Crystal system	Monoclinic	Orthorhombic	Orthorhombic
Space group	$P2_1/n$	$Pna2_1$	$Pna2_1$
a	5.493(2)	20.075(5)	20.085(2)
b	4.943(0)	3.751(2)	3.7591(4)
c	23.022(1)	8.291(2)	8.293(1)
β (°)	92.421(1)	90	90
Volume (Å ³)	624.536	624.323	626.1(1)
Z	4	4	4
Analysis Temperature (K)	283-303K	283-303K	293(2) K
wR (F ²)	0.055	0.047	0.0319
Measured data	-	-	4530 / 1283
Unique data (I>2sig)	-	-	1224
Number of restraints/parameters	-	-	1/93
Goodness Of Fit	-	-	1.052
Density	1.469	1.469	1.465

Table 3.2. Crystal data and refinement parameters obtained from CCSD and SC-XRD for stable and metastable MHBA

The crystal structures of the two polymorphs are represented in Figure 3.3 and Figure 3.4. The hydrogen bonds involving the carboxylic moieties i.e. the formation of dimers are represented in dashed blue lines; the hydrogen bonds involving the hydroxyl moieties and linking the dimers along c axis are represented in dashed green lines. These interactions build F faces parallel to *bc* plan. The corresponding H-bonds are listed in Table 3.3.

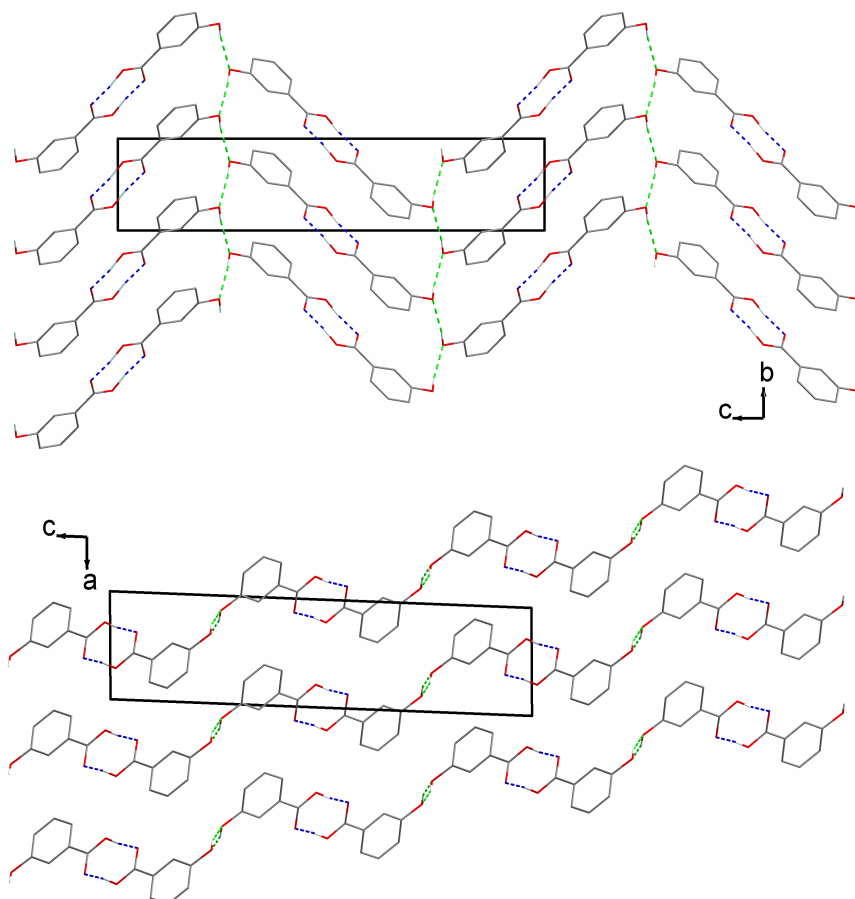


Figure 3.3. Packing of the stable form of MHBA. In dashed blue lines: hydrogen bonds involving carboxylic moieties and in dashed green lines: the hydrogen bonds involving the hydroxyl moieties. Top view: Projection along *a*: dimers are linked along *c* axis. Bottom view: Projection along *b*.

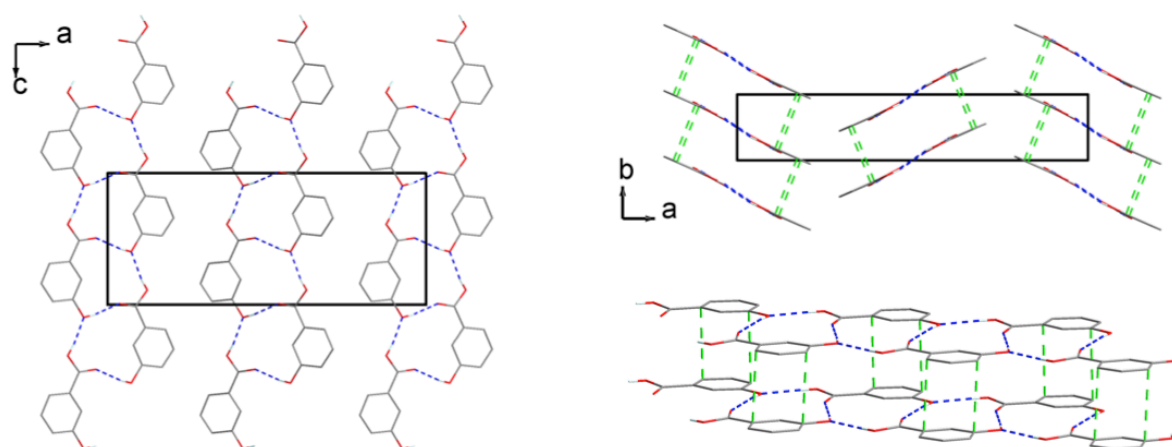


Figure 3.4. Packing of the metastable form: On the left : view along *b* axis (hydrogen bonds are represented in dashed blue lines), Top right: view along *c* axis: consecutive ribbons are stacked through π interactions ($d \sim 3.4 \text{ \AA}$, dashed green lines). Bottom right: two consecutive molecular ribbons stacked through π interactions.

Structure	Interaction	d(H...A) (Å)	d(D...A)(Å)	Angle (°)
<i>P</i> ₂₁ / <i>n</i>	O1H1-O2	1.473	2.617	172.16
	O3H3A-O3	1.976	2.796	164.12
	C5H5-O2	2.626	3.455	148.16
<i>P</i> _{na} 2 ₁	O1H1-O3	1.874	2.687	170.86
	C4H4-O1	2.673	3.601	176.10

Table 3.3. Hydrogen bond parameters of both polymorphs (*D* = donor and *A*=Acceptor)

In both polymorphs, the molecule of MHBA adopts a low-energy stable conformer form as shown on Figure 3.3 and Figure 3.4 (coplanarity of the phenyl ring (C2, C3, C4, C5, C6, C7) and the carboxyl group, and C1=O2 carboxyl directed toward the O3-H3A).(Aarset et al. 2008) The structure of the stable form is based on the usual carboxylic acid dimers (intermolecular hydrogen bonds between opposite carboxylic groups). Each dimer is linked to two other dimers by two H-bonds (O3H3A---O3). The structure of the metastable form consists of molecular ribbons spreading along *c* stacked through $\pi\pi$ interactions along *b*. Indeed, MHBA molecule creates intermolecular hydrogen bond network with four other molecules using the -OH and -COOH groups that leads to ribbons. Consecutive ribbons along *b*, establish π - π interactions (phenyl rings are distant of 3.4Å and parallel), this stacking gives rise to molecular layers in *bc*.

There is no structural filiation between the hydrogen bond networks of the both polymorphic forms.

At this points, we would like to report the work performed in order to extract from the TR-SHG data collected on MHBA a relevant parameter: the activation energy of the monotropic solid-solid transition. We will also see that TR-SHG measurements are of particular interest to gather information about the kinetics of this polymorphic transition.

2.2 Measurement of activation energy (E_a) by means of TR-SHG

In the previous chapter, we demonstrated that SHG could be used with relevancy to detect a small amount of metastable MHBA in a matrix of stable MHBA. A common approach to determine the activation energy, E_a , is to track the conversion of the metastable form (toward the stable form) by means of isothermal experiments at various temperatures. Isothermal transformation of MetMHBA was then studied by monitoring the time dependence of the SHG signal for four different temperatures: 85°C, 115°C, 130°C and 145°C. The evolution of the transformed fraction *x* versus time is plotted in Figure 3.5 (*x* is defined as the volume

fraction of stable form into the sample). Assuming that the SHG intensity depends linearly on x , (Clevers et al. 2013) it is calculated as follows:

$$x = 100 \left(1 - \frac{I_{SHG}(T)}{I_{SHG}^0} \right)$$

I_{SHG}^0 is the initial SHG intensity (at room temperature) and $I_{SHG}(T)$, the SHG intensity measured at temperature T . Isothermal curves depicted in Figure 3.5 exhibit a classical “S” shape for transformation profile (for each isothermal temperature, the origin corresponds to the beginning of the solid-solid transition). It can be noticed that for the lower temperatures (85°C and 115°C) the curves are stepped. This feature will be discussed later.

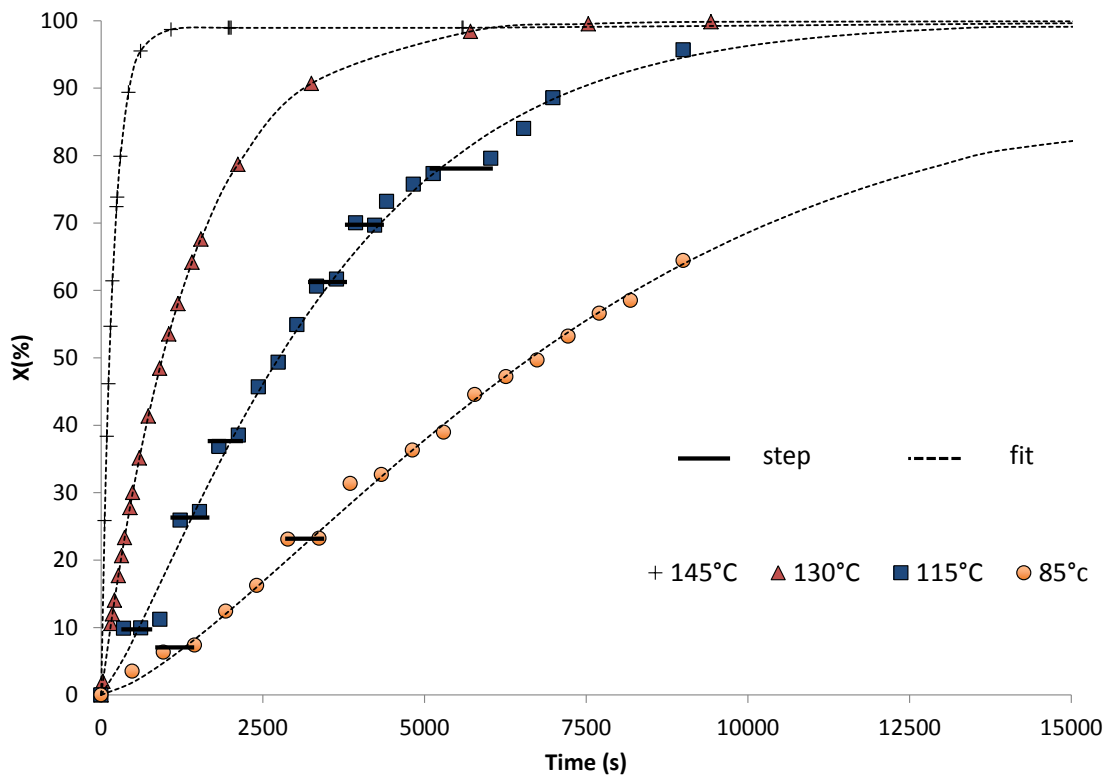


Figure 3.5. Isothermal SHG measurements on pure MetMHBA for 85°C (circle), 115°C (square), 130°C (triangle) and 145°C (plus symbol). Dash-lines are fit curves obtained by least squares method.

The evolution of the volume fraction x of the stable form can be described by the Avrami equation: (Avrami 1939; 1940; 1941; Fanfoni and Tomellini 1998)

$$x = 1 - e^{-k(T)t^n} \quad (2)$$

with t the time of reaction, n the Avrami exponent and $k(T)$ the Avrami constant. Avrami constant $k(T)$ depends on temperature and can be expressed with an Arrhenius law as follows:

$$k(T) = Ae^{\frac{-Ea}{RT}} \quad (3)$$

Constant A is a pre-exponential factor, E_a the activation energy of the transition, R the universal gas constant and T the temperature.

A standard method to calculate the activation energy E_a is to use the natural logarithms of equation (2) that leads to the following equation:

$$\ln[-\ln(1-x)] = \ln[k(T)] + n \ln(t) \quad (4)$$

A linear regression is then applied to the plot of $\ln[-\ln(1-x)]$ versus $\ln(t)$ to obtain n as the slope and $\ln(k(T))$ as the intercept.

A natural logarithm of $\ln(k(T))$ leads to:

$$\ln[k(T)] = \ln(A) + \frac{E_a}{RT} \quad (5)$$

Finally, the activation energy E_a is obtained from the slope of the plot of $\ln(k(T))$ versus $\frac{1000}{T}$ (Figure 3.7). Usually, the extreme experimental values are not taken into account (because of logarithm divergence).

Figure 3.6 shows the plot of $\ln(-\ln(1-x))$ versus $\ln(t)$ for isothermal experiments (values of n and $k(T)$ are determined from the slopes and the intercepts). For 85, 115, 130 and 145°C, n values are respectively 1.35; 1.21; 1.03; 1.07 and $k(T)$ values are $4.64e-6$; $5.12e-5$; $5.77e-4$; $3.97e-3$, respectively.

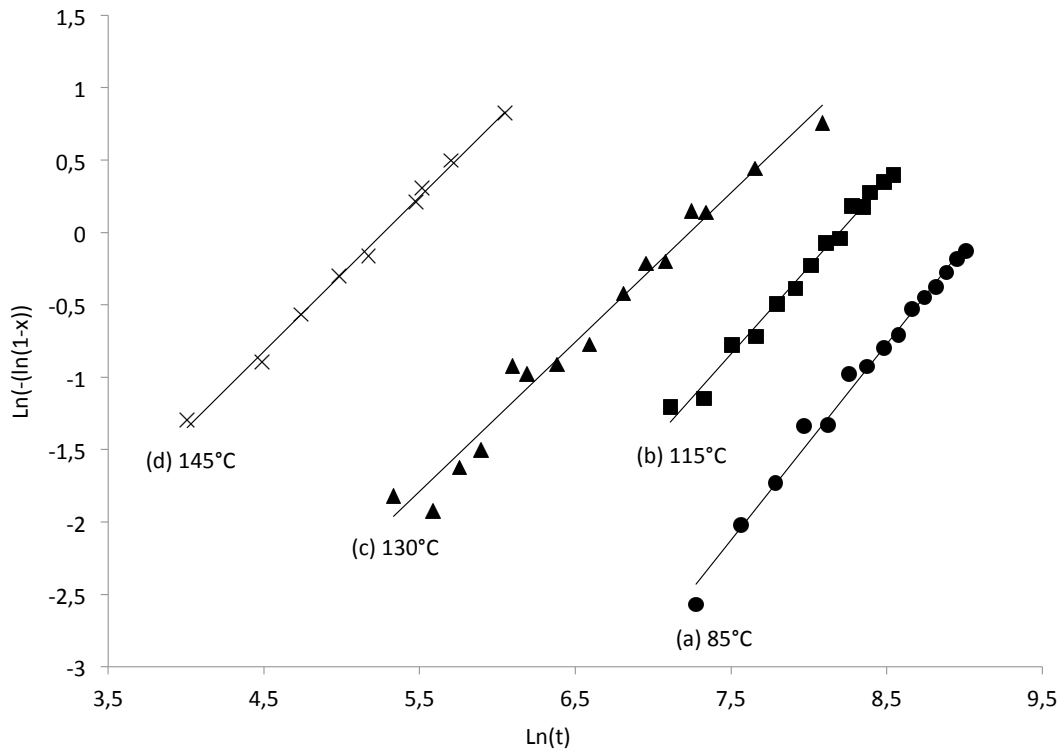


Figure 3.6 $\ln(-\ln(1-x))$ versus $\ln(t)$ plot at 85°C, 115°C, 130°C and 145°C . Slopes give n (respectively 1.35 ; 1.21 ; 1.03 ; 1.07) and intercept $\ln(k(T))$ (respectively $k(T) = 4.64e-6$; $5.12e-5$; $5.77e-4$; $3.97e-3$)

An alternative to this method can be to proceed to a direct fit of the experimental data using least squares method, with the Avrami equation set in the program and all parameters let free for the fit. In this last case, the whole range of data is used. These two different approaches lead to the results summarized in Table 3.4.

Temperature (°C)	Direct Fit of experimental data using least square method			Linear Regression of the Ln(-ln(1-x)) versus ln(t) plot		
	Avrami exponent n	$k(T)$	rms	Avrami exponent n	$k(T)$	R ²
85	1.399 ± 0.003	3,64e-06 ± 9.063e-08	1.324	1.354 ± 0.036	4.64e-6 ± 1.151e-07	0.991
115	1.223 ± 0.047	4.37e-05 ± 1.304e-6	2.412	1.205 ± 0.038	5.12e-5 ± 1.581e-5	0.988
130	1.004 ± 0.006	7.06e-04 ± 2.86e-5	1.874	1.025 ± 0.043	5.77e-4 ± 2.234e-5	0.977
145	1.070 ± 0.002	3.55e-03 ± 3.559e-5	3.109	1.068 ± 0.024	3.97e-3 ± 8.659e-5	0.997

Table 3.4. Fit parameters of isothermal SHG measurements at 85°C, 115°C, 130°C and 145°C

The classical method leads to an activation energy E_a equal to 137 kJ.mol⁻¹ with regression coefficient R^2 of 0.963. With the direct fit method, activation energy value equals 144 kJ.mol⁻¹ with a regression coefficient R^2 of 0.962.

Results from the direct fit of experimental data are in good agreement with results obtained by linear regression from the plot of $\ln[-\ln(1-x)]$ versus $\ln(t)$. The deviation between the two methods is more pronounced at 85°C and 115°C than at 130°C and 145°C. This is certainly due to the steps observed on the isothermal curves, which limits the fit accuracy.

These steps or “plateau effect” are probably related to the crystal size distribution of the powder sample. Assuming that every crystal contains an evenly distribution of defects concentration and/or identical mosaicity, the larger the crystal, the higher the thermal energy (or time) required to initiate the transition. Consequently, the phase transition occurs progressively by domains or by particles size. Therefore, the “plateau effect” is more pronounced at lower temperature. For higher isothermal temperatures, this size effect is no more visible due to the increase of the conversion rate. Indeed, the kinetic of the phase transition increases exponentially with temperature (the calculated Avrami constant $k(T)$ at 145°C is three orders of magnitude higher than 85°C).

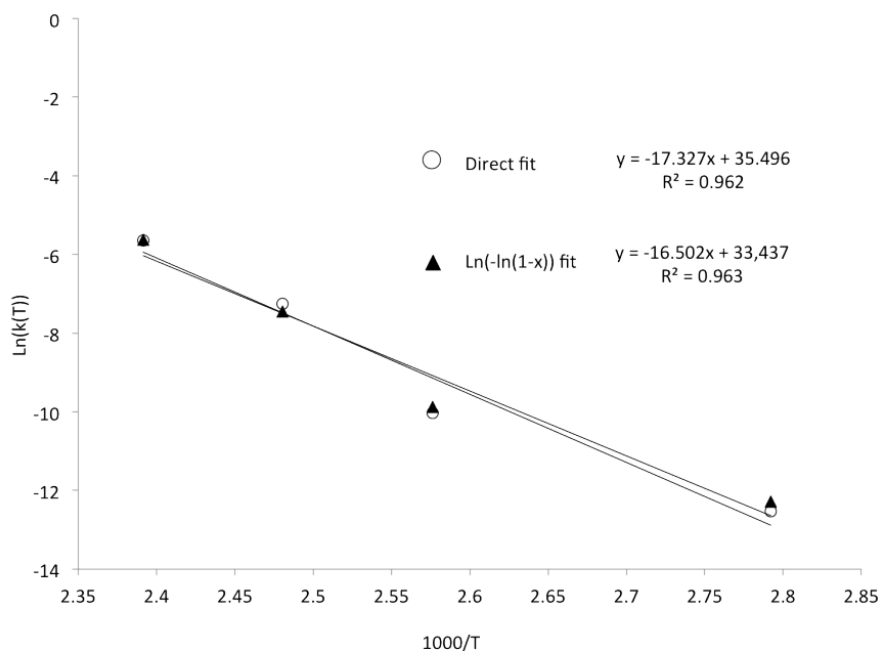


Figure 3.7. $\ln(k(T))$ versus $1000/T$ plots for isothermal transformation of MetMHBA to StabMHBA. E_a from the slope is $144\text{kJ}\cdot\text{mol}^{-1}$ for the direct method and $137\text{kJ}\cdot\text{mol}^{-1}$ for the classical method.

In order to evaluate the accuracy of TR-SHG measurements for the determination of the activation energy, results obtained by DSC and TR-SHG were compared.

In the particular case of MHBA, differential isothermal calorimetric measurements cannot be used because of the weakness of the exothermic event associated to the transformation of the metastable form into the stable form. Indeed, the limit of detection of the metastable form by DSC has been evaluated to 17% wt. (for a $16\text{K}/\text{min}$ heating rate). (Clevers et al. 2013) Therefore only dynamic DSC measurements are possible.

The solid-solid transition of MetMHBA towards StabMHBA was studied at five different heating rates (φ): $1\text{K}\cdot\text{min}^{-1}$, $2\text{K}\cdot\text{min}^{-1}$, $4\text{K}\cdot\text{min}^{-1}$, $8\text{K}\cdot\text{min}^{-1}$ and $16\text{K}\cdot\text{min}^{-1}$ from 35°C to 220°C and thermograms are presented on Figure 3.8. The corresponding thermal data are listed on Table 3.5.

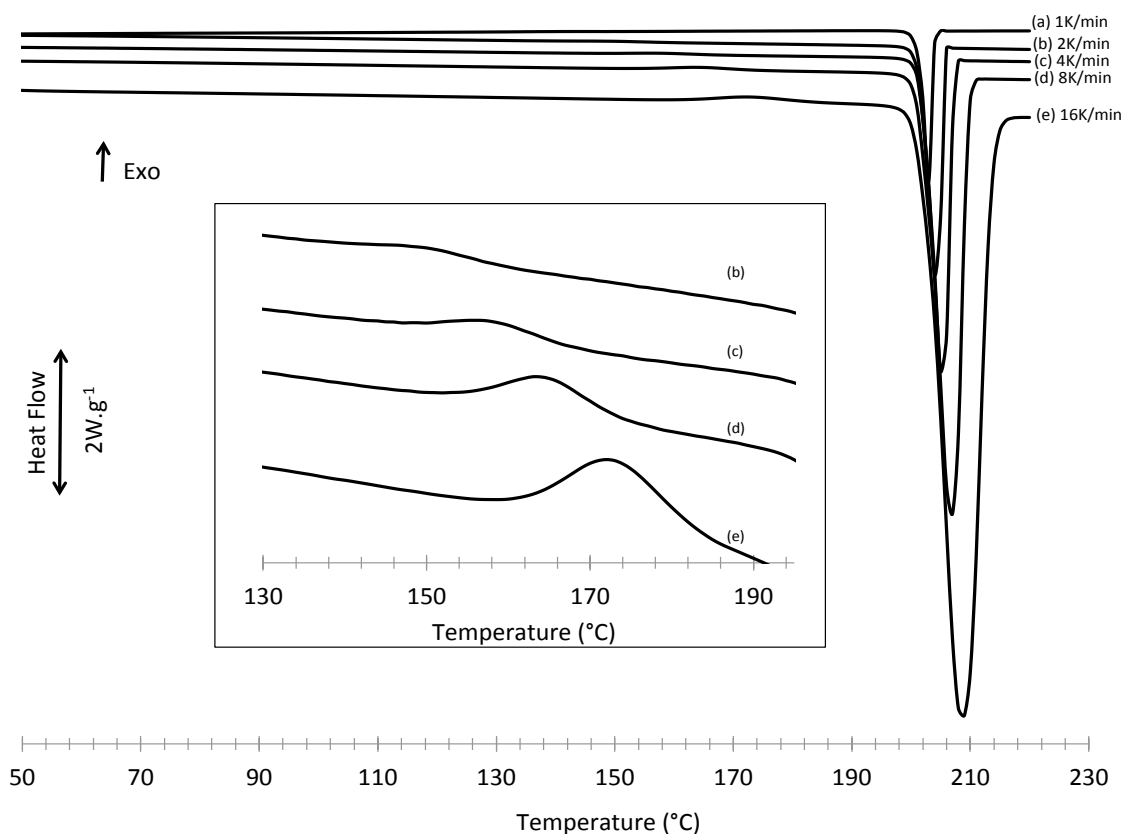


Figure 3.8. DSC curves for 1, 2, 4, 8 and 16 K.min⁻¹ heating rates. The inset is a zoom of DSC scan from 130°C to 195°C starting from pure MetMHBA. Weak exothermic event is visible and attributed to the transformation of the metastable form. The peak temperature, T_p , increases with the heating rate.

Heating rate ϕ (K/min)	Solid-solid transition			Fusion	
	T_p (°C)	Enthalpy of transformation (kJ/mol)(exothermic)	T_m^{onset} (°C)	T_m^{peak} (°C)	Melting Enthalpy (kJ/mol)
1	-	-	201.8±0.4	203.5±0.3	31.19±1.75
2	150.0±0.3	0.592±0.118	201.9±0.3	204±0.5	32.93±1.05
4	156.4±0.7	0.567±0.108	202±0.8	205.1±0.3	33.04±0.44
8	163.1±0.6	0.600±0.131	202±0.3	207±0.8	32.62±0.39
16	172.4±0.8	0.523±0.110	202.5±1	208.3±1.4	33.70±0.71

Table 3.5. Thermal data for MetMHBA for five different heating rates (average of two set of measurements).

The average onset fusion temperature T_m^{onset} is 202.04°C. Data processing leads to an average melting enthalpy of 32.7 kJ.mol⁻¹ for the stable MHBA. This value fits with the enthalpy reported by Nordstrom et al (35.9 kJ.mol⁻¹) (Nordström and Rasmuson 2006) and Perlovich et al 34.9 kJ.mol⁻¹. (Perlovich et al. 2006) Note that a lower value of 26.2 kJ.mol⁻¹ was also reported. (Sabbah and Le 1993)

In addition to the endothermic peak corresponding to the fusion of the stable MHBA, all thermograms (except for 1K/min heating rate) exhibit a weak exothermic event at circa 160°C (see enlargement of the DSC traces on Figure 3.8). It corresponds to the solid-solid transition of the metastable (P_{na2_1}) form toward the stable form ($P_{2_1/n}$).

The exothermic transformation heat presents an average value of $0.57\text{kJ}\cdot\text{mol}^{-1}$ which is in good agreement with the value of $0.51\text{kJ}\cdot\text{mol}^{-1}$ reported by Nordstrom et al. (Nordström and Rasmuson 2006)

The peak temperature T_p of the solid-solid transition increases with the heating rate. The dependence of the peak temperature T_p on the heating rate ϕ can be used to determine the activation energy E_a of the solid-solid transition on the basis of the Kissinger relation written as:

$$\ln\left(\frac{\phi}{T_p^2}\right) = -\frac{E_a}{RT_p} + \ln\left[\frac{AR}{E_a}\right] \quad (6)$$

where R is the universal gas constant and A a constant.

Figure 3.9 shows the plot of $\ln\left(\frac{\phi}{T_p^2}\right)$ versus $\frac{1000}{T_p}$. The slope of the resulting straight line (linear regression with regression coefficient $R^2=0.993$) gives calculated activation energy of $139\text{kJ}\cdot\text{mol}^{-1}$.

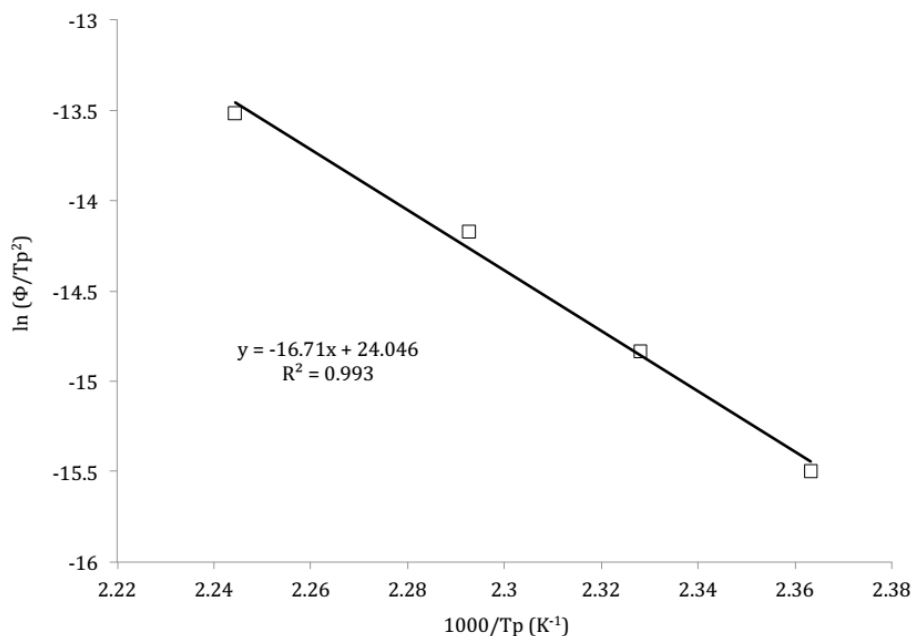


Figure 3.9. Kissinger plot of $\ln\left(\frac{\phi}{T_p^2}\right)$ versus $\frac{1000}{T_p}$. The activation energy E_a is $139\text{kJ}\cdot\text{mol}^{-1}$

The Ozawa-Flynn-Wall Method based on Doyle's approximation can also be used and is expressed in a simple form as follows:

$$\ln(\phi) \approx -1.052 \frac{E_a}{RT_p} + cst$$

Figure 3.10 shows the plot of $\ln(\phi)$ versus $\frac{1}{T_p}$. The activation energy (obtained from the slope) is $139 \text{ kJ}\cdot\text{mol}^{-1}$.

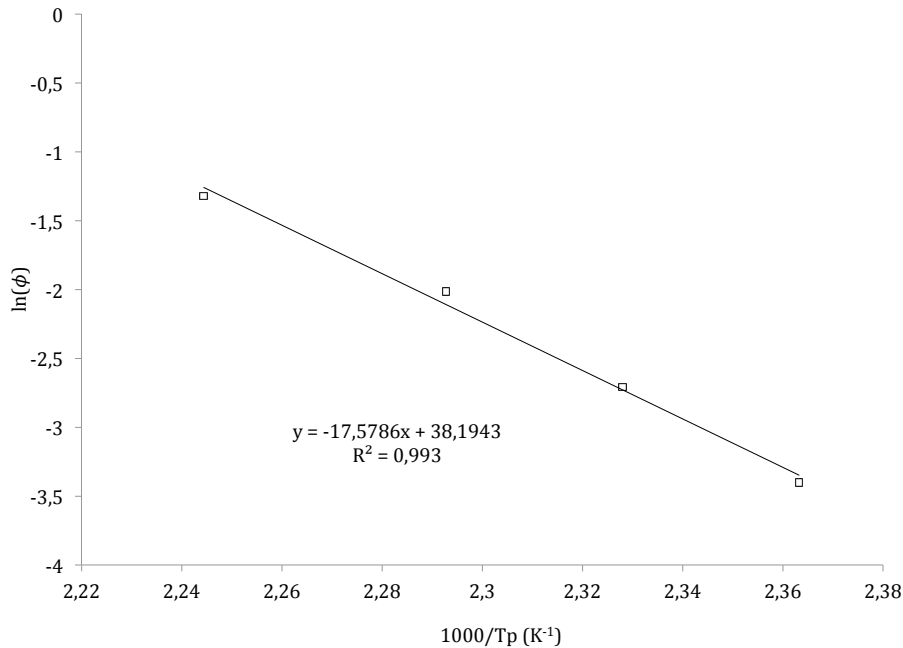


Figure 3.10 Ozawa Plot: $\ln(\phi)$ versus $\frac{1000}{T_p}$. The activation energy E_a is $139 \text{ kJ}\cdot\text{mol}^{-1}$

The same value is thus obtained by application of the Ozawa model.

Activation energy, E_a , determined by isothermal TR-SHG measurements using Avrami model (range $137\text{-}144 \text{ kJ}\cdot\text{mol}^{-1}$ depending of the data processing used) is in good agreement with values found by DSC using Kissinger and Ozawa methods ($139 \text{ kJ}\cdot\text{mol}^{-1}$). However in order to avoid any bias related to step effect, it is suitable to limit the dispersion in the crystal size distribution. Another point to consider is the possibility of a local heating induced by the laser beam, which could modify kinetics by energy input. In the present case, this effect was limited by choosing the minimum of incident energy in order to keep the better SHG signal/noise ratio. During isothermal experiment, laser strikes always the same part of the powder. SHG measurements at other parts of the powder were performed and values found were similar (maximum deviation of 0.5%). Thus energy brought by the laser has no significant effect on the global result of the experiments.

2.3 Kinetic stability of MetMHBA

An accurate monitoring of the evolution of transformed fraction x by TR-XRPD is difficult because of analysis duration and the low vapor pressure of MHBA. DSC cannot be used with relevancy in this case due to the low detection threshold of MetMHBA (e.g. 17% wt). In contrast, a Time Temperature Transformation diagram (TTT) giving the relative stability of metastable form versus temperature and necessary time to complete the phase transition of the MHBA polymorphic system can be established from isothermal SHG measurements (Figure 3.11).

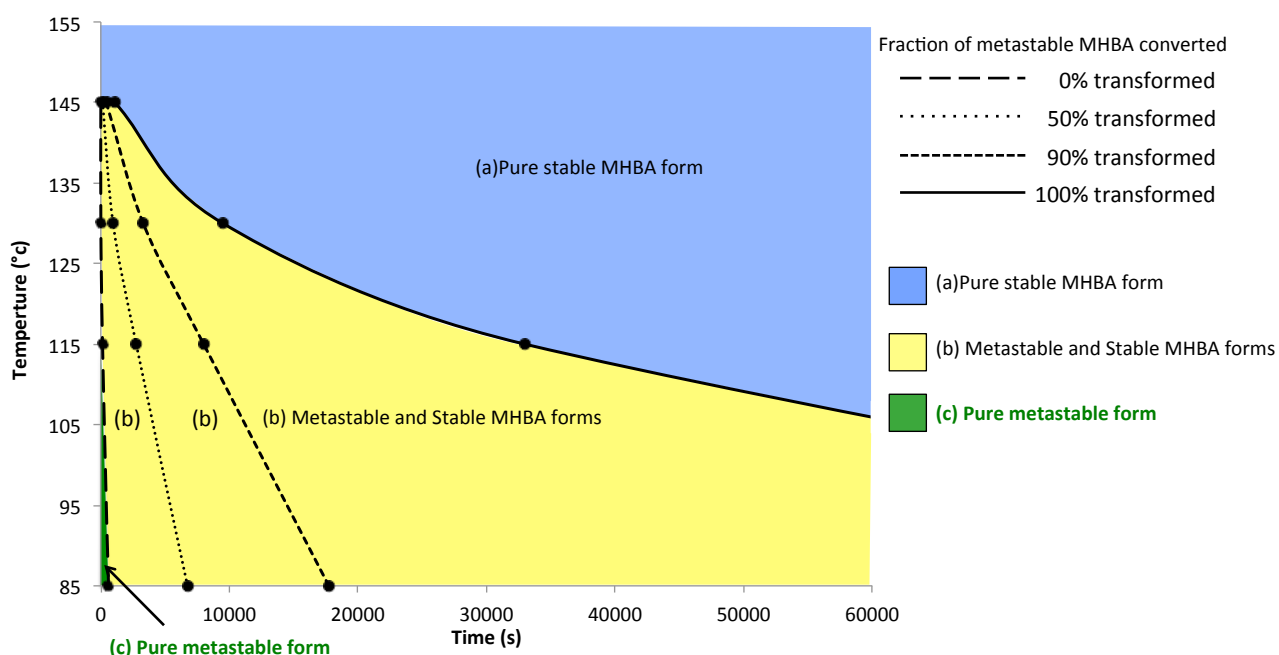


Figure 3.11. TTT diagram of MHBA metastable form for 85°C-145°C temperature range; Three domains can be determined: a) pure stable form (in blue); b) mixture of stable and metastable forms (in yellow), c) pure metastable form (in green). Lines represent the converted fraction of MetMHBA.

Figure 3.11 shows that the kinetic stability of MetMHBA decreases with temperature and that kinetics of the solid-solid transition becomes predominant from 85°C to higher temperature where the metastable phase could survive only for few minutes. Of course, the higher the temperature, the shorter the necessary period of time to complete the transition toward the stable form: more than 2 days are necessary to complete the solid-solid transition at 85°C instead of 20 minutes at 145°C and MetMHBA still exhibits a high SHG signal after a storage of several months at room temperature. Therefore, according to the exponential dependency of $k(t)$ with the temperature, a complete conversion of the metastable form could take several years at room temperature (a SHG signal, corresponding at circa 1 %wt of metastable form, was detected in a commercial sample produced in 2011).

If the study of the metastable equilibrium is of particular interest regarding the relative stability of the phase, it does not provide information about the molecular reorganization of the solid along the transition. In order to gather information about the transition mechanism, and the possible similarities between the two polymorphic forms such as hydrogen bonds network, packing, cell parameters), the study of the crystalline structure of both phases was performed.

2.4 Solid-solid transition mechanism.

The similarity between crystal lattice volumes of both polymorphs and the efficient crystal packing of the metastable form associated to high activation energy E_a of the solid-solid transition can explain the kinetic stability of the metastable phase.

As mentioned at the end of the paragraph 2.1 page 125, there is no structural filiation between the hydrogen bond networks of the two polymorphic forms. This excludes the possibility of a smooth and continuous transition via a concerted movement of molecules. Thus, it is likely that the irreversible solid-solid transition from the metastable to the stable form proceeds through a destructive/reconstructive mechanism.

To confirm a destructive/reconstructive mechanism, hot-stage polarized light microscopy can be used. This is a relevant technique to gather information on solid-solid transition mechanisms. Therefore, isothermal Temperature-Resolved microscopy was performed on large metastable single crystals (few millimeters) of MHBA at 85°C, 115°C, 130°C and 145°C (the sublimation induced by an isolated crystal is limited and allows to keep the heating stage closed along the whole experiment). At 85°C, a crystallization front became visible and started to move after an annealing of 20 hours. Then it propagated through the single crystal, which kept its shape integrity in agreement with the very close volumes of the two forms. Solid-solid transition was completed within 2 days and 14 hours in good agreement with the value obtain by isothermal treatment of the powder¹⁷. For higher isothermal temperatures, observations were similar but the time required to complete the solid-solid transition decreased dramatically with increasing temperature. Displacement of a

¹⁷ Optical microscopy movies of isothermal treatment at 85°C (Movie 2) and of a single crystal of MetMHBA (Movie 1) undergoing a solid-solid transition are available free of charge via the Internet at http://pubs.acs.org/doi/suppl/10.1021/cg400712s/suppl_file/cg400712s_si_005.zip

crystallization front is another argument in favor of destructive/reconstructive solid phase transition mechanism.(Mnyukh 2011)

Since the metastable phase is non-centrosymmetric, SHG microscopy is particularly appropriate to differentiate the polymorphs and to image the crystallization front. Therefore, SHG microscopy was performed at room temperature on a single crystal of MetMHBA annealed at 100°C for 20min. A 3D reconstruction of the metastable part of the crystal is shown in Figure 3.12. Results show that nucleation of the stable form (white part) occurred at different location in the metastable crystal (green part) and was followed by the growth of the stable form. The step shape observed on the $x = f(\text{time})$ curves (Figure 3.5) is also consistent with a destructive/reconstructive mechanism as described by Mnyukh. (Mnyukh 2011)

Another fact that supports this mechanism is the value of Avrami exponent, n , close to 1 (1.070-1.399 range) that corresponds, in metal and alloy compounds, to solid-solid transition initiated at a grain boundary.(Christian 2002) This could be correlated, in molecular crystal, to the nucleation on crystal defects and/or on boundaries of mosaic blocks.

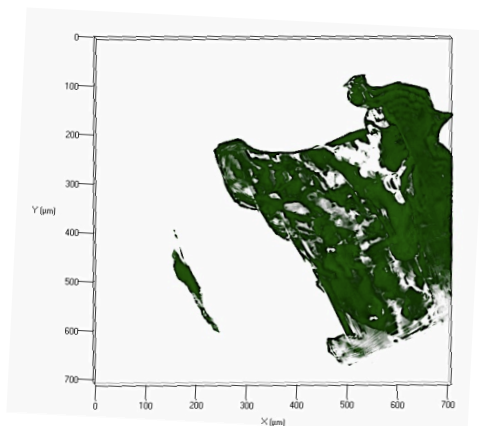


Figure 3.12. SHG microscopy of a MHBA metastable single crystal in transition toward the stable form. Green volume corresponds to the metastable form and white volume to the stable form.

2.5 Conclusion

Results demonstrate that TR-SHG can be considered as an interesting alternative to usual methods (DSC, XRPD, RAMAN) for the determination of the activation energy and the kinetic stability of MetMHBA with the establishment of a TTT diagram obtained from isothermal TR-SHG measurements. This kind of diagram could be helpful for the determination of storage conditions of metastable polymorphs. TR-SHG, Optical and SHG microscopy experiments highlighted the presence of a crystallization front consistent with the crystal structures analyses that reveal no structural filiation between the polymorphs. These observations led us to propose a destructive/reconstructive mechanism for the irreversible MHBA solid-solid transition.

Part.3 Detection of order-disorder transition in organic solids

In this part, we report the work performed in order to extend the TR-SHG studies of phase transitions to the case of second-order like transition observed in a series of derivatives of 1-(4-X-phenyl)-4,4-dimethyl-2-(1H-1,2,4-triazol-1-yl) pentan-3-one hereafter X-TAK (X = H, Methyl (Me), Ethyl (Et) or Cl).

3.1 Presentation of the system

Recent investigations in the series of triazolyl ketone X-TAK derivatives depicted Figure 3.13 revealed several deracemizable conglomerates (Levilain et al. 2009), that is to say SHG positive crystalline racemic mixtures. Furthermore, a main feature of these chiral compounds is to exhibit a disorder of the *tert*-butyl group (*t*-Bu, hereafter) at room temperature. In this study, we demonstrate that some order-disorder transitions and molecular configurations of X-TAK compounds can be investigated by TR-SHG.

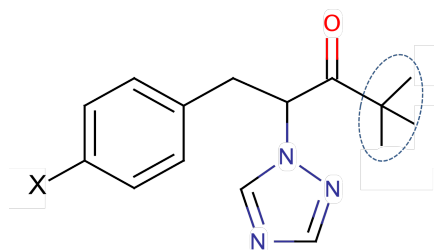


Figure. 3.13: X-TAK molecules. X = H, Me, Et, Cl. The *t*-Bu group is encircled by a dash-line

3.2 Crystal structure descriptions of X-TAK derivatives and nature of the disorder on the *t*-Bu

The main crystallographic data are summarized in Tab. 1. The crystal structures of X-TAK (X= Cl, Me, Et) derivatives are isomorphous so only the Cl-TAK crystal packing is presented. The asymmetric unit is built from one molecule of Cl-TAK (Figure. 3.14). The *t*-Bu extremity is split into two positions with statistical occupancy factor (*S.O.F.*) of 78%/22%.

	H-TAK	Me-TAK	Et-TAK	Cl-TAK	Cl-TAK
CCDC number	973150	973151	973153	973152	973149
Chemical Formula	C ₁₅ H ₁₉ N ₃ O	C ₁₆ H ₂₁ N ₃ O	C ₁₇ H ₂₃ N ₃ O	C ₁₅ H ₁₈ ClN ₃ O	C ₁₅ H ₁₈ ClN ₃ O
Molecular Weight (g.mol ⁻¹)	257.33	271.36	285.38	291.77	291.77
Temperature (K)	293	293	293	293	200
Crystal System	Monoclinic			Orthorhombic	
Space group	P2 ₁			P2 ₁ 2 ₁ 2 ₁	
Z, Z'	4, 2			4, 1	
a / Å	5.747(1)	5.808(1)	5.678(2)	5.8076(5)	5.7843(7)
b / Å	19.183(1)	13.641(1)	13.848(5)	13.553(1)	13.4537(16)
c / Å	13.437(1)	19.789(1)	21.308(8)	19.661(2)	19.464(2)
β / °	96.561(1)			90	
V / Å ³	1471.8(2)	1567.9(2)	1675.43(1)	1547.5(2)	1514.7(3)
d _{calc}	1.161	1.150	1.131	1.252	1.279
R factor (with >2σ)	R1 = 0.0623 wR2 = 0.1142	R1 = 0.0483 wR2 = 0.0938	R1 = 0.0600 wR2 = 0.1578	R1 = 0.0367 wR2 = 0.0871	R1=0.0280 wR2=0.0756
Goodness of Fit	1.024	0.965	1.020	1.024	1.077
S.O.F. on t-Bu	No disorder	69/31	25/75	78/22	No disorder

Table 3.6 Crystallographic data of HTAK, Me-TAK, Et-TAK, Cl-TAK.

The crystal packing of Cl-TAK is depicted Figure. 3.15. The aromatic rings are interacting with their adjacent equivalents along b axis, and by means of π interactions in T shape, generate infinite chains of molecules in [100] direction. The angle between two consecutive aromatic rings involved into the interaction is at circa 60°. The distance between two consecutive rings is 3.7Å from centroid to carbon. The chains are stacked along c and give rise to slices. The cohesion within slices is ensured through Van der Waals interactions ($d \sim 3.7\text{Å}$ t-Bu to t-Bu from carbon to carbon). Along b direction a d002 shift is observed between two consecutive slices of chains.

Furthermore, except for H-TAK, all the compounds (X= Me, Et, Cl) exhibit a statistical disorder on the t-Bu group. In these three cases, two positions exist for this group with S.O.F. at circa 70% and 30%. However, the resolution of Cl-TAK crystal structure at low temperature (200K) reveals no disorder of the t-Bu group and the unique conformation being that prevailing at room temperature (see Table 3.6 and fig. 3).

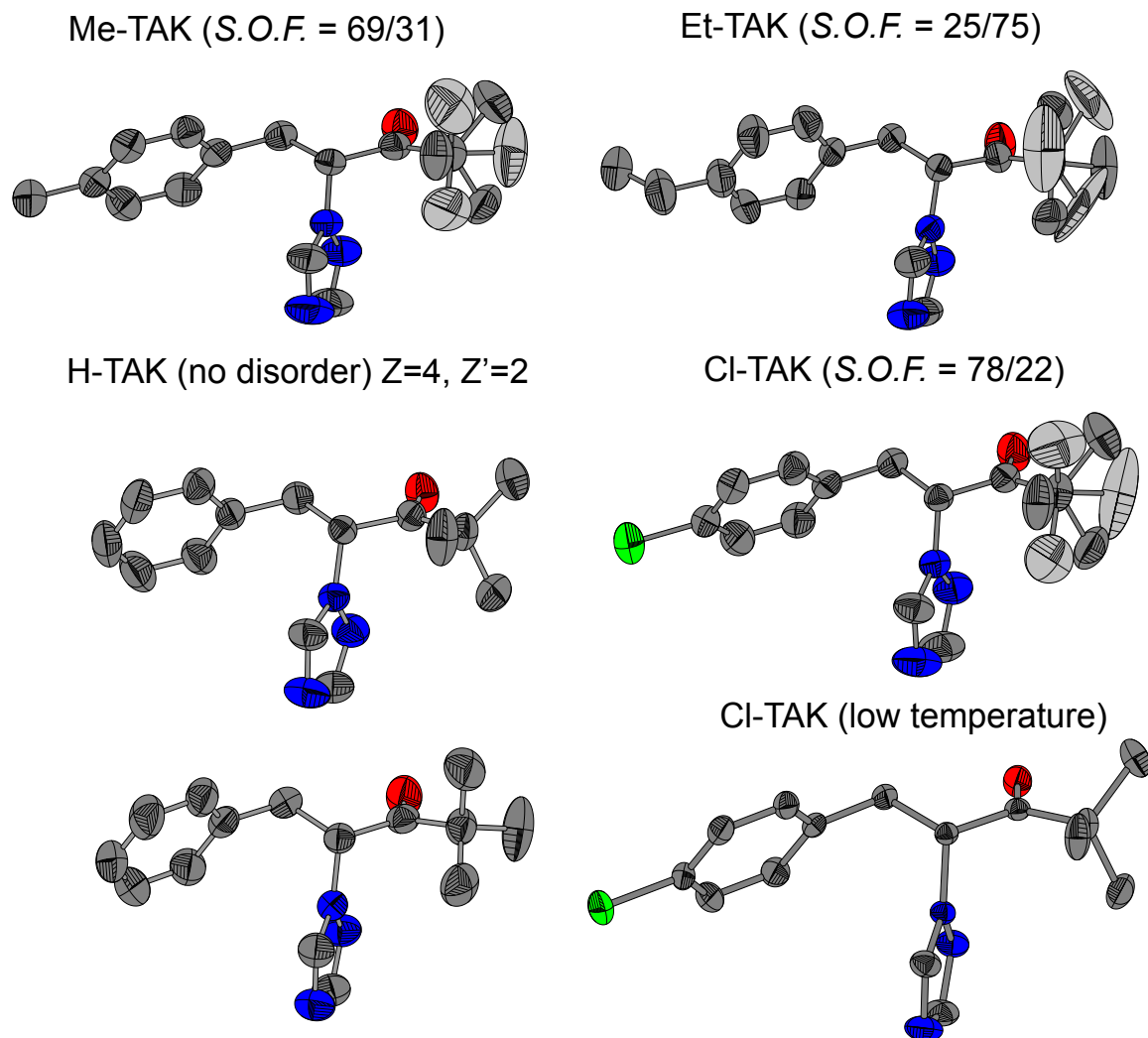


Figure 3.14: Asymmetric units of Me-TAK, Et-TAK, H-TAK and Cl-TAK at room temperature and at 200K for the Cl-TAK. The major positions of the *t*-Bu group are represented in dark grey and the minor in light grey with corresponding statistical occupancy factor (S.O.F.) at RT.

The H-TAK compound crystallizes as a conglomerate in the $P2_1$ space group. The asymmetric unit is composed of two molecules of H-TAK and their *t*-Bu moieties are not disordered. However, the two molecules of the asymmetric unit differ mainly by the position of the *t*-Bu group (Figure. 3.16). Therefore, it is possible to consider a fifty/fifty statistical orientation for the *t*-Bu group.

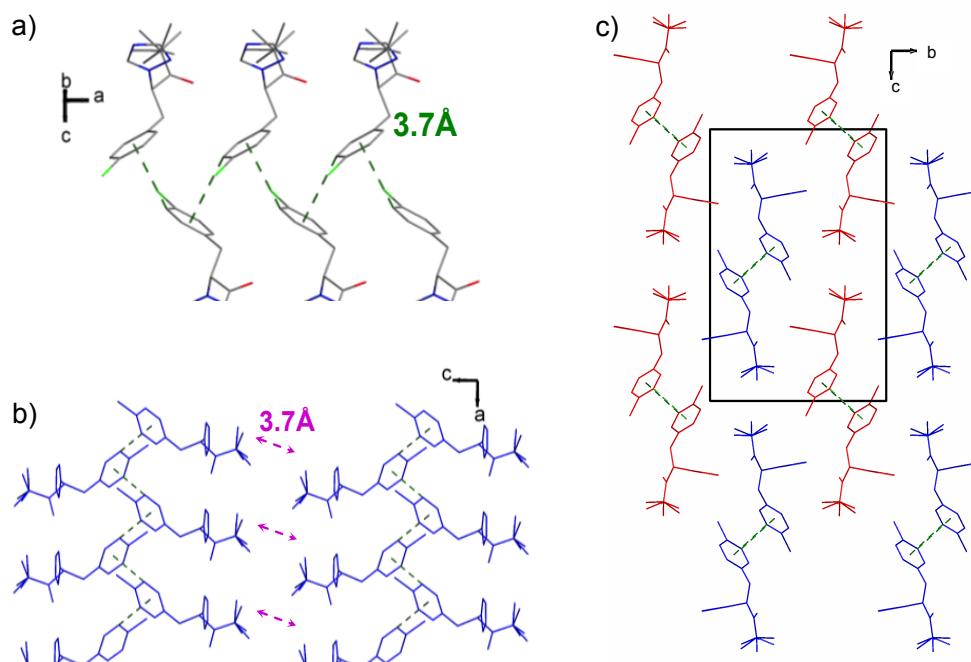


Figure. 3.15: Packing of Cl-TAK: a) π stacking in T shape (dashed green lines). b) Double chains that are spreading along the [100] direction. c) Projections along a axis, one chain is circled in black. The chains are stacked along c direction and give rise to slices (blue and red).

Cohesion of molecules in the crystal packing (Figure. 3.17) is ensured by means of π interactions in T shape, generating infinite chains of molecules along a. The angle between two consecutive aromatic rings involved into the interaction is circa 60° . The distance between two consecutive rings is 3.9\AA . Moreover, the triazolyl moieties are oriented towards the interior (endo position) of the chains and not towards the exterior (exo position) like in the three other derivatives crystallizing in the $P2_12_12_1$ space group.

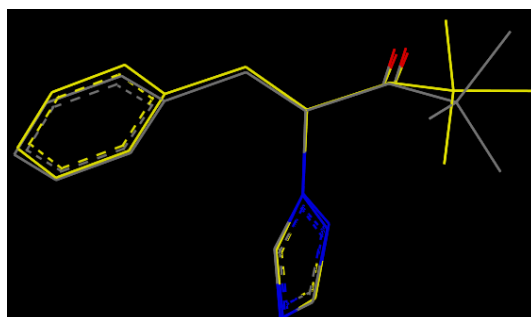


Figure. 3.16: Superimposition of both molecules of the H-TAK asymmetric unit

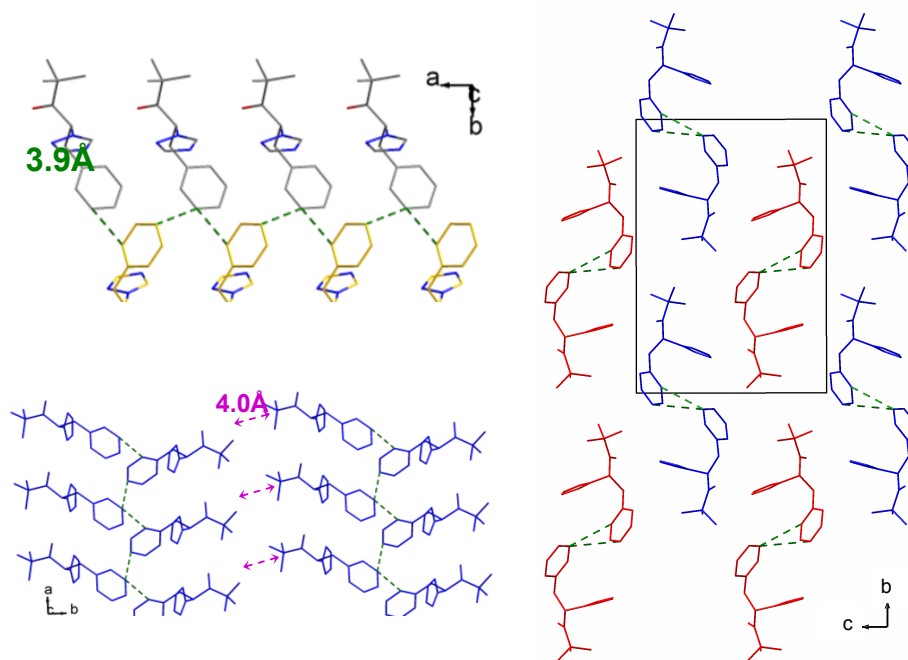


Figure. 3.17: Packing of H-TAK a) π stacking in T shape (dashed green lines). b) Double chains that are spreading along the [100] direction. c) Projections along a axis, one chain is circled in black and asymmetric unit in red.

As observed with the Cl-TAK compound, the disorder of the *t*-Bu moiety can be stopped by decreasing the temperature. That is to say, the disorder is most probably of a dynamic nature. The SHG signal can be strongly affected due to a slight modification of the crystal packing (contraction of lattice, thermal motion of molecules, disorder, etc.) (Seyidov et al. 2012). Thus, temperature resolved second harmonic generation (TR-SHG) analyses were performed on the TAK-derivatives in order to study the order-disorder transition and to detect the freezing temperature of the *t*-Bu motion in the solid state.

3.3 TR-SHG Detection of the order-disorder transition

TR-SHG measurements were carried out on H-TAK and X-TAK derivatives. First, the samples were cooled from 20°C to -70°C and then heated back to 20°C. Both heating and cooling were performed at a 5K.min⁻¹ rate. The number and the duration of the TR-SHG analyses were chosen in order to ensure the best stability of the compound under the laser irradiation along both heating and cooling.

TR-SHG curves plotting the evolution of the relative SHG intensity defined as $\frac{I_{SHG}(T)}{I_{SHG}(20^{\circ}\text{C})}$ for H-TAK, Cl-TAK, Me-TAK and Et-TAK are presented Figure. 3.18. For all these X-TAK compounds, the SHG signal increases when the temperature decreases. For the H-TAK compound the intensity variation of the SHG signal is weak and linear. By contrast, TR-SHG

curves for the other X-TAK derivatives exhibit a clear slope disruption at circa -30°C . Moreover, after cooling from 20°C to -70°C , the value of SHG signal is at least doubled. Similarities in the thermal behavior can be explained by the isomorphism of Me-TAK, Et-TAK and Cl-TAK crystal structures. This thermal behavior is completely reversible with very small hysteresis effect (if any): it suggests a second-order like transition. (Dougherty and Kurtz 1976)

Vogt (Vogt 1974), and Dougherty and Kurtz (Dougherty and Kurtz 1976) mentioned that dynamic disorder can induce a second harmonic generation signal (even in cubic phases) because of the modifications of the optical properties due to local polarization fluctuations (temperature dependent). Therefore, the disruption observed on the TR-SHG curves could result from the freeze of the *t*-Bu group motion. However, disruption could also arise from a particular lattice contraction during the cooling.

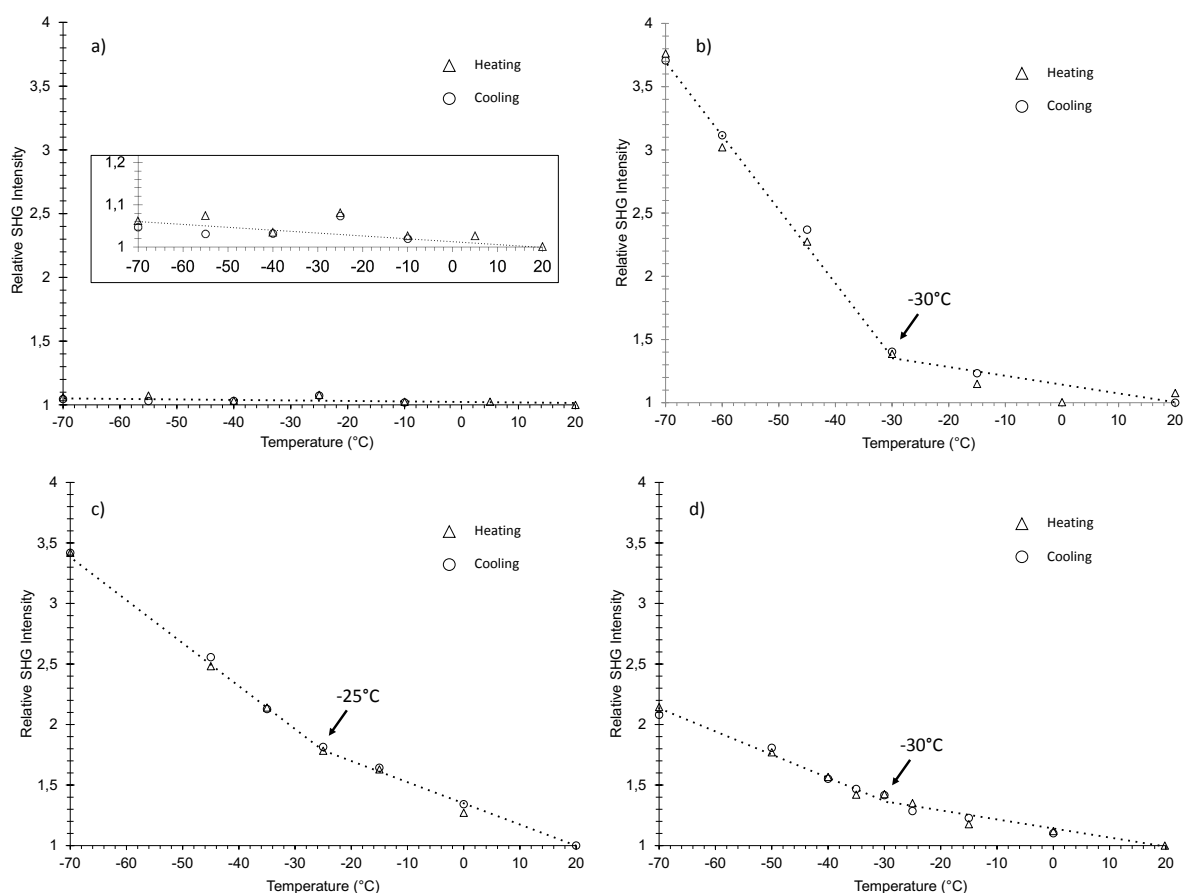


Figure 3.18 TR-SHG curves of H-TAK with an enlargement (a), Cl-TAK (b), Me-TAK (c) and Et-TAK (d) and at 5 K min^{-1} . A disruption of the curve is observed at circa -25°C for Me-TAK (c) and circa -30°C for Cl-TAK (b) and Et-TAK (d). No disruption of the curve is observed for H-TAK (a).

Therefore, in order to decouple the influence on the SHG signal of (i) the lattice contraction (or expansion) and (ii) the *t*-Bu group motion, TR-XRPD was performed from 20°C to -50°C and lattice parameters were refined each 2 °C for the Me-TAK.

Lattice parameters contraction¹⁸ compared to the values found at 20°C are presented Figure 3.19. The evolution of the lattice volume versus temperature is presented Figure 3.20. Values obtained at 20°C by the refinement of X-ray powder pattern are consistent with those obtained by SC-XRD. The contraction of the lattice is anisotropic with a major contraction along the c-axis.

The results clearly show that all the crystallographic parameters evolve linearly with temperature. Thus, there is no crystallographic reason for the disruption observed on the TR-SHG curve. Consequently, assuming an identical crystallographic behavior for all the isomorphous TAK derivatives, the disruption on the TR-SHG curves can be attributed to the contribution of the *t*-Bu group motion. Finally, it confirms the dynamic nature of the disorder observed by structural resolution on single crystal.

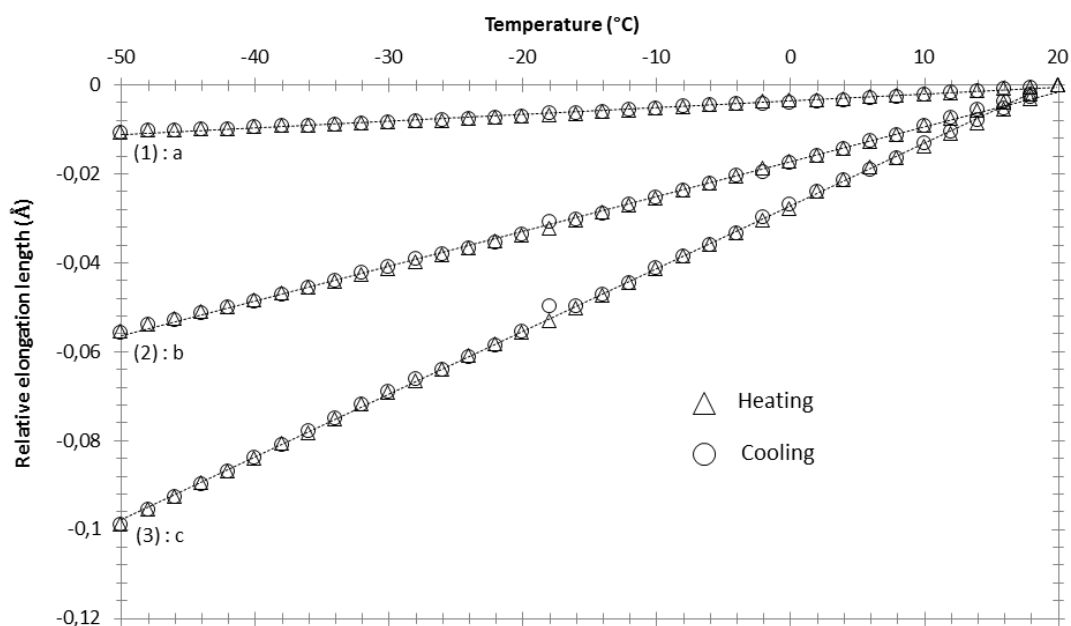


Figure 3.19 Elongation of lattice parameters versus temperature compare to the reference values at 20°C. Dash line corresponds to a linear regression curve: (1): *a* parameter with $y = 1.503E-04x - 3.584E-03$ and $R^2 = 0.9905$; (2): *b* parameter with $y = 7.872E-04x - 1.716E-02$ and $R^2 = 0.9988$; (3): *c* parameter with $y = 1.408E-03x - 2.722E-02$ and $R^2 = 0.9995$

¹⁸ Details on the experimental procedure are available in Appendix II page 219

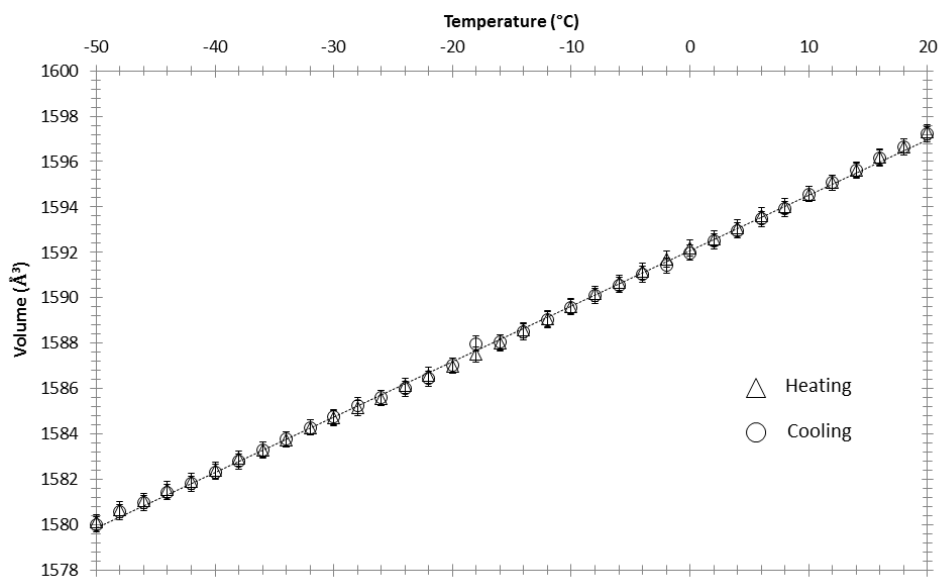


Figure 3.20 Linear evolution of the lattice volume versus temperature in the -50°C - 20°C temperature range for Me-TAK ($y = 0.2442x + 1592.1$ $R^2 = 0.9993$)

3.4 Conclusions and possible transition mechanism

The crystallographic studies of Me-TAK, Et-TAK and Cl-TAK revealed a dynamic disorder on the *tert*-Butyl group at room temperature (SC-XRD confirmed that the *t*-Bu group is no more disordered at 200K for Cl-TAK). Moreover, TR-SHG results clearly showed a slope disruption at circa -30°C with no hysteresis effect. Measurements performed on H-TAK showed that there is no disorder on the *t*-Bu group and no slope disruption on the TR-SHG curve. These results suggest that the disorder at room temperature associated to the *t*-Bu group in the $P2_12_12_1$ structures could be frozen by thermal treatment in agreement with the linear evolution of the lattice parameters.

That could indicate a progressive freezing of the *t*-Bu group motion down to circa -30°C (temperature of the disruption on the TR-SHG curves). However, the pathway between the disordered and ordered structure remains unclear. Further investigations are in progress (in particular solid-state NMR (see Figure 3.21) and heat capacity measurements in order to establish if the transition mechanism consists in:

- (i) a progressive evolution of the *S.O.F.* toward 100/0 at the transition temperature
- (ii) a *S.O.F.* that remains constant down to the transition temperature and then shows a sharp change upon further cooling (i.e. *t*-Bu groups remained in minor conformation suddenly evolve into the most stable conformation).
- (iii) a more complex mechanism combining (i) and (ii) and possibly a coupling between the rotation of the three methyl groups and the rotation of the *t*-Bu group.

The first results of ss-NMR (for measurements around the temperature of the disruption on SHG curves) on H-TAK and CI-TAK are plotted in Figure 3.21. For the H-TAK, no change on the NMR spectra is visible that suggests no temperature-induced phase transition.

For the CI-TAK, the peak located around 30 ppm in the methyl expansion region starts to exhibit a shoulder at -32°C . The split of the methyl peak continues to increase for lower temperature and at -60°C , a split of this peak in two parts is clearly visible.

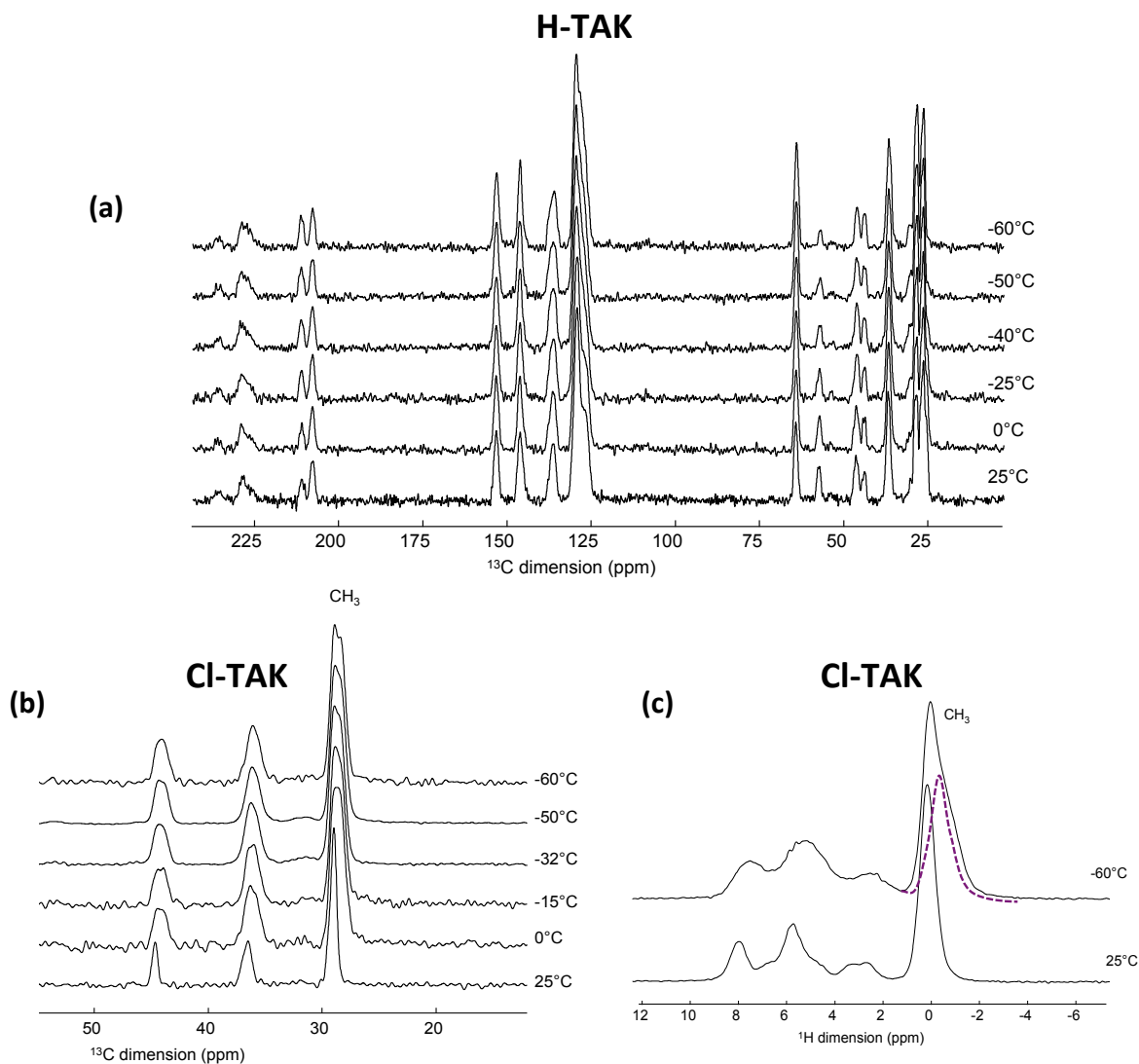


Figure 3.21 Variable Temperature solid-state NMR (VT-ssNMR)¹⁹ on H-TAK (a) and CI-TAK (b) and (c). Expansion methyl region

These suggest a complex mechanism as describe in point (iii) with a molecular conformation, which continues to change with the temperature below the disruption temperature detected by TR-SHG. A schematic view is given in Figure 3.22.

¹⁹ Acknowledgements: Francis Taulelle, Charlotte Martineau, Fadila Saïdi from the Tectospin, Institut Lavoisier de Versailles, Université de Versailles Saint Quentin en Yvelines, France & Jürgen Senker, Renée Siegel from the University of Bayreuth, Department for Inorganic Chemistry III, Germany

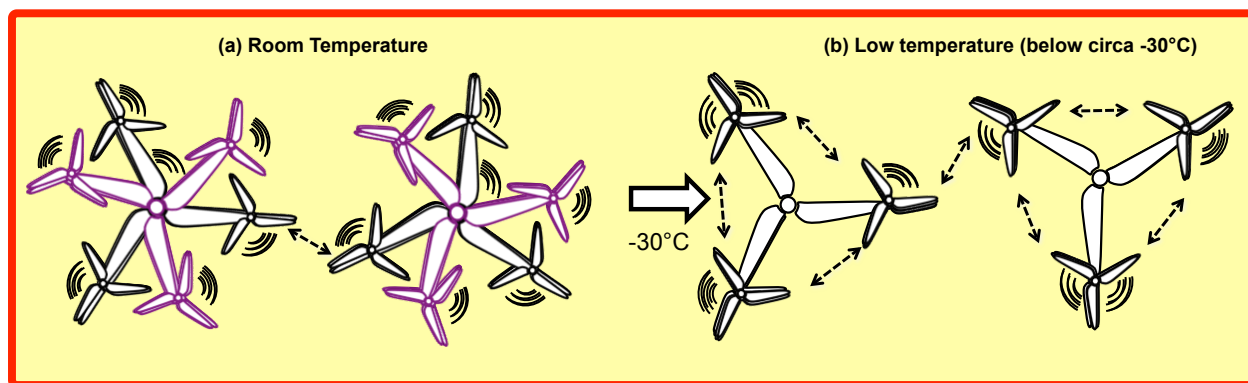


Figure 3.22 Possible “Click and stop transition mechanism”: (a) *t*Bu and Me rotate freely between two major conformations (black and purple), (b) At circa -30°C *t*Bu adopts only the major conformation (freeze of *t*Bu motion) but the Me of the *t*Bu group continue to rotate.

The complementary analyses, in particular TR-ss-NMR and Cp vs. temperature, showed that there is, prior to the complete freezing of the *t*-Bu moiety, a progressive slow down in the rotations of its methyl groups which behave like cogwheels (starting from circa 0°C and intensifying their spinning correlation as temperature decreases). This order-disorder transition is therefore a complex mixture of correlated rotations between methyl groups and the entire *t*-Bu group.

Part.4 General conclusion on phase transition investigated by TR-SHG.

Through two examples of solid-solid transitions in organic solid, the TR-SHG appears as an interesting method to probe the crystal structure, monitor its evolution with respect to temperature and detect molecular changes in the solid-state. Relevant parameter such as the activation energy and the kinetics of the MHBA monotropic transition has been extracted from TR-SHG data. Especially in the case of TAK derivatives, TR-SHG results together with the lack of hysteresis effect confirm the dynamic nature of the disorder – with a freezing temperature (of the *t*Bu) at circa -30°C – likewise the second order like transition for the $P2_12_12_1$ X-TAK family (X= Me, Et, Cl). It underlines the potential of second harmonic generation as a reliable and rapid method for the investigation of difficult to detect solid-solid transformations.

It underlines the potential of TR-SHG as a reliable and rapid method for the investigation of difficult to detect solid-solid transformations.

References

- Aarset K, Page EM, Rice DA. Molecular Structures of 3-Hydroxybenzoic Acid and 4-Hydroxybenzoic Acid, Obtained by Gas-Phase Electron Diffraction and Theoretical Calculations. *J. Phys. Chem. A. American Chemical Society*; 2008 Oct 9;112(40):10040–5.
- Avrami M. Kinetics of Phase Change. I General Theory. *J. Chem. Phys.*; 1939;7(12):1103–12.
- Avrami M. Kinetics of Phase Change. II Transformation-Time Relations for Random Distribution of Nuclei. *J. Chem. Phys.*; 1940;8(2):212–24.
- Avrami M. Granulation, Phase Change, and Microstructure Kinetics of Phase Change. III. *J. Chem. Phys.* 1941;9(2):177.
- Bartis FJ. Second-Harmonic Generation and the Ordering Reaction in NH₄Cl. *Phys. Stat. Sol. (b)*. 1971 Feb 1;43(2):665–8.
- Bayarjargal L, Wiehl L, Friedrich A, Winkler B, Juarez-Arellano EA, Morgenroth W, et al. Phase transitions in KIO₃. *J. Phys.: Condens. Matter. IOP Publishing*; 2012 Jul 12;24(32):325401.
- Bayarjargal L, Winkler B. Pressure-induced magnetic phase transition in Cr₂O₃ determined by second harmonic generation measurements. *APPLIED PHYSICS LETTERS. AIP Publishing*; 2013;102(18):182403.
- Bayarjargal, Winkler. Second harmonic generation measurements at high pressures on powder samples. *Zeitschrift für Kristallographie – Crystalline Materials*. 229(2).
- Bergman JG. Molecular mechanics of the ferroelectric to paraelectric phase transition in lithium tantalate via optical second harmonic generation. *J. Am. Chem. Soc.* 1976 Feb;98(4):1054–5.
- Bergman JG. Molecular mechanics of the ferroelectric to paraelectric phase transition in LiNbO₃ via optical second harmonic generation. *Chemical Physics Letters*. 1976 Mar;38(2):230–3.
- Betzler K. Second harmonic generation near the phase transition of SrTiO₃. *Ferroelectrics. Taylor & Francis*; 1980;26(1):819–22.
- Betzler K, Bäuerle D. Second harmonic generation in squaric acid. *Physics Letters A. Elsevier*; 1979;70(2):153–4.
- Bi W, Louvain N, Mercier N, Luc J, Rau I, Kajzar F, et al. A Switchable NLO Organic-Inorganic Compound Based on Conformationally Chiral Disulfide Molecules and Bi(III)I₅ Iodobismuthate Networks. *Adv. Mater.* 2008 Mar 5;20(5):1013–7.
- Bragiel P, Piasecki M, Kityk I. Optical and thermal tools for the phase transitions detection in the guanidine compounds. *IOP Publishing*; 2007;79(1):012044.
- Chemburkar SR, Bauer J, Deming K, Spiwek H, Patel K, Morris J, et al. Dealing with the Impact of Ritonavir Polymorphs on the Late Stages of Bulk Drug Process Development. *Org. Process Res. Dev.* 2000 Sep;4(5):413–7.
- Christian J. *The Theory of Transformations in Metals and Alloys: Part I+ II.* Elsevier; 2002.
- Clevers S, Simon F, Dupray V, Coquerel G. Temperature resolved second harmonic generation to probe the structural purity of m-hydroxybenzoic acid. *Journal of Thermal Analysis and Calorimetry. Springer*; 2013;(112):1–7.
- Dolino JP, BAG. Measurement of the order parameter of α-quartz by second-harmonic generation of light. 1975 Sep 8;:1–11.
- Dougherty JP, Kurtz SK. A second harmonic analyzer for the detection of non-centrosymmetry. *J Appl*

- Crystallogr. 1976 Apr;9(2):145–58.
- Fanfoni M, Tomellini M. The Johnson-Mehl- Avrami-Kohnogorov model: A brief review. *Nouv Cim D*. 1998 Jul;20(7-8):1171–82.
- Fiebig M, Pavlov VV, Pisarev RV. Second-harmonic generation as a tool for studying electronic and magnetic structures of crystals: review. *J. Opt. Soc. Am. B. Optical Society of America*; 2005;22(1):96–118.
- Fleury PA, Lyons K. *Optical Studies of Structural Phase Transitions*. link.springer.com. Berlin, Heidelberg: Springer Berlin Heidelberg; 1981. pp. 9–92.
- Fox GR, Yamamoto JK, Miller DV, Cross LE, Kurtz SK. Thermal hysteresis of optical second harmonic in paraelectric BaTiO₃. *Materials Letters*. 1990 Apr;9(7-8):284–8.
- Gopalan V, Raj R. Domain structure and phase transitions in epitaxial KNbO₃ thin films studied by insitu second harmonic generation measurements. *APPLIED PHYSICS LETTERS*. AIP Publishing; 1996;68(10):1323–5.
- Hall RC, Paul IC, Curtin DY. Structures and interconversion of polymorphs of 2, 3-dichloroquinizarin. Use of second harmonic generation to follow the change of a centrosymmetric to a polar structure. *J. Am. Chem. Soc. ACS Publications*; 1988;110(9):2848–54.
- Henson B, Asay B, Sander R, Son S, Robinson J, Dickson P. Dynamic Measurement of the HMX β - δ Phase Transition by Second Harmonic Generation. *Phys. Rev. Lett*. 1999 Feb;82(6):1213–6.
- Herbstein FH. On the mechanism of some first-order enantiotropic solid-state phase transitions: from Simon through Ubbelohde to Mnyukh. *Acta Crystallogr B Struct Sci. International Union of Crystallography*; 2006 May 15;62(3):341–83.
- Hirsch R, Stühmer G. A simple technique to measure optical SHG in powder samples by means of electronic integration. *Phys. Stat. Sol. (a)*. 1976 Sep 16;37(1):105–8.
- Iio K, Yanagi T. Nonlinear Optical Property of Sodium Nitrite. II. Temperature Dependence of Second Harmonic Generation. *J. Phys. Soc. Jpn*. 1973 May;35(5):1465–71.
- Jones GO, Thomas PA. Investigation of the structure and phase transitions in the novel A-site substituted distorted perovskite compound Na_{0.5}Bi_{0.5}TiO₃. *Acta Crystallogr B Struct Sci. International Union of Crystallography*; 2002 Mar 25;58(2):168–78.
- Keens A, Happ H. A study of the ferroelectric phase transition in PbHPO₄ by optical second-harmonic generation. *J. Phys. C: Solid State Phys. IOP Publishing*; 2000 Nov 21;21(8):1661–71.
- Kidyarov BI, Kovalevskii VI, Malinovsky VK, Pugachev AM, Rozhkov AF. Generation of the second harmonic of laser radiation in powders of pure and doped potassium nitrate in the temperature interval of 25–160 °C. *Optoelectron.Instrument.Proc. Springer US*; 2013 Jul 24;49(3):293–7.
- Kim JH, Kim M, Kim SB, Hahn JH. Temperature-dependent second harmonic generation in 6LiRbSO₄ and 7LiRbSO₄. *Solid State Communications*. 1996 Apr;98(3):241–4.
- Kovalevskii VI, Malinovskii VK, Pugachev AM, Raevskii IP, Raevskaya SI, Rudych PD, et al. Second harmonic generation in the paraelectric phase in powders and ceramics of BaTiO₃. *Phys. Solid State. SP MAIK Nauka/Interperiodica*; 2012 May 22;54(5):920–3.
- Lazoryak BI, Morozov VA, Belik AA, Stefanovich SY, Grebenev VV, Leonidov IA, et al. Ferroelectric phase transition in the whitlockite-type Ca₉Fe(PO₄)₇; crystal structure of the paraelectric phase at 923 K. *Solid State Sciences. Elsevier*; 2004;6(2):185–95.
- Levilain G, Rougeot C, Guillen F, Plaquevent J-C, Coquerel G. Attrition-enhanced preferential crystallization combined with racemization leading to redissolution of the antipode nuclei. *Tetrahedron: Asymmetry*.

- Elsevier; 2009;20(24):2769–71.
- Louvain N, Mercier N, Luc J, Sahraoui B. Example of Disulfide Conformational Change in the Solid State: Preparation, Optical Properties, and X-ray Studies of a Cystamine-Based Iodoplombate Hybrid. *Eur. J. Inorg. Chem.* 2008 Aug;2008(23):3592–6.
- Masuno A, Kikuchi Y, Inoue H, Yu J, Arai Y. Giant Second Harmonic Generation from Metastable BaTi₂O₅. *Appl. Phys. Express.* 2011;4:042601.
- Miller RC. Temperature Dependence of the Optical Properties of Ferroelectric LiNbO₃ and LiTaO₃. *APPLIED PHYSICS LETTERS.* AIP Publishing; 1966;9(4):169–71.
- Mnyukh Y. Mechanism and kinetics of phase transitions and other reactions in solids. 2011 Oct 7.
- Monk PM. *Physical chemistry: understanding our chemical world.* John Wiley and Sons; 2008.
- Nordstrom FL, Svard M, Malmberg B, Rasmuson ÅC. Influence of Solution Thermal and Structural History on the Nucleation of m-Hydroxybenzoic Acid Polymorphs. *Crystal Growth & Design.* American Chemical Society; 2012 Jul 13;:120713102601007.
- Nordström FL, Rasmuson ÅC. Polymorphism and thermodynamics of m-hydroxybenzoic acid. *European Journal of Pharmaceutical Sciences.* 2006 Aug;28(5):377–84.
- Perlovich GL, Volkova TV, Bauer-Brandl A. Towards an understanding of the molecular mechanism of solvation of drug molecules: A thermodynamic approach by crystal lattice energy, sublimation, and solubility exemplified by hydroxybenzoic acids. *J. Pharm. Sci.* 2006;95(7):1448–58.
- Sabbah R, Le THD. Étude thermodynamique des trois isomères de l'acide hydroxybenzoïque. *Can J Chem.* NRC Research Press; 1993;71(9):1378–83.
- Sampaio LC, Hamrle J, Pavlov VV, Ferré J, Georges P, Brun A, et al. Magnetization-induced second-harmonic generation of light by exchange-coupled magnetic layers. *J. Opt. Soc. Am. B. Optical Society of America;* 2005;22(1):119–27.
- Saw C, Zauh J, Farber D, Ruddle C. Using Simultaneous SHG and XRD Capabilities to Examine Phase. 2001.
- Schneck J, Primot J, Mühl Von der R, Ravez J. New phase transition with increasing symmetry on cooling in barium sodium niobate. *Solid State Communications.* 1977 Jan;21(1):57–60.
- Seyidov MY, Suleymanov RA, Salehli F. Phase-matched second-harmonic generation due to thermal expansion of TiGaSe₂ layered crystal. *Physics Letters A.* Elsevier B.V; 2012 Jan 9;376(4):643–5.
- Sleight AW, Zumsteg FC, Barkley JR, Gulley JE. Acentricity and phase transitions for some AM₂X₆ compounds. *Materials Research Bulletin.* 1978 Nov;13(11):1247–50.
- Son SF, Asay BW, Henson BF, Sander RK, Ali AN, Zielinski PM, et al. Dynamic Observation of a Thermally Activated Structure Change in 1,3,5-Triamino-2,4,6-trinitrobenzene (TATB) by Second Harmonic Generation. *J. Phys. Chem. B.* 1999 Jul;103(26):5434–40.
- Sun Z, Luo J, Zhang S, Ji C, Zhou L, Li S, et al. Solid-State Reversible Quadratic Nonlinear Optical Molecular Switch with an Exceptionally Large Contrast. *Adv. Mater.* 2013 Jun 27;25(30):4159–63.
- Svard M, Rasmuson ÅC. m-Hydroxybenzoic Acid: Quantifying Thermodynamic Stability and Influence of Solvent on the Nucleation of a Polymorphic System. *Crystal Growth & Design.* 2013 Mar 6;13(3):1140–52.
- Theodossiou T, Rapti GS, Hovhannisyan V, Georgiou E, Politopoulos K, Yova D. Thermally induced irreversible conformational changes in collagen probed by optical second harmonic generation and laser-induced fluorescence. *Lasers Med Sci.* 2002;17(1):34–41.

Vogt H. Study of Disordered Crystals by Optical Second Harmonic Generation. *Phys. Stat. Sol. (b)*. 1973 Aug 1;58(2):705–14.

Vogt H. Study of structural phase transitions by techniques of nonlinear optics. *Applied Physics A: Materials Science & Processing*. Springer; 1974;5(2):85–96.

Vogt H, Happ H, Häfele HG. Optical second harmonic generation in sodium nitrite. *Phys. Stat. Sol. (a)*. 1970 Mar 16;1(3):439–50.

Xiong R-G. The temperature-dependent domains, SHG effect and piezoelectric coefficient of TGS. *Chinese Chemical Letters*. Chinese Chemical Society; 2013 Jun 7;:1–4.

Chapter 4. Novel Applications of SHG

In this chapter, we report the use of the SHG method for novel applications in material science. In the first part, we describe how TR-SHG can be used for the determination of phase diagrams. In the second part, we explain how we performed SHG measurements versus relative humidity (RH) in order to monitor processes such as desolvation or recrystallization from the amorphous state. In the last part some prospective works are discussed.

Part.1 Phase Diagram Determination by Means of TR-SHG

1.1 Introduction & literature survey

In a mixture of two molecules A and B, new solids phases can appear such as an intermediate compounds or polymorphs of either A, B or defined compounds. Moreover, phase transitions can occur with the temperature or the pressure changes imposed to the system.

Although the SHG has been commonly used to determine if a new phase is NC or not (e.g. SHG test of the new defined compounds or the polymorphic forms) they are, to our knowledge, only two reported cases for which SHG was directly used to plot a phase diagram and notably the phase domain boundaries (transition lines).

The first example (taken from Richardson:1978vc and reprinted from Schulze 1973) is a study of the $\text{PbZrO}_3\text{:PbTiO}_3\text{:La}_2\text{O}_3$ ternary system. The corresponding phase diagram is plotted Figure 4.1. It demonstrates the usefulness of SHG in rapidly delineating the phase boundaries in this complex ceramic system exhibiting solid solutions of PbZrO_3 , PbTiO_3 , and La_2O_3 . There is an abrupt change in intensity of the SHG signal at the phase boundaries. Kurtz and Dougherty in (Richardson 1978) noticed the presence of a weak SHG signal in the paraelectric cubic phase ($m3m$ centrosymmetric crystal class, see Figure 4.1) and conclude that is probably due to trace amounts of residual lead titanate which exhibit a very strong SHG signal (i.e. 2400 times stronger than quartz, Kurtz and Perry 1968). One can notice that the SHG measurements in Schulze's work were made using reflection geometry. If this example highlights the high potential of the technique for phase diagram investigations, the SHG measurements were made on different compositions but only at room temperature. Other temperatures were not investigated; consequently “real time” measurements versus the temperature were not performed.

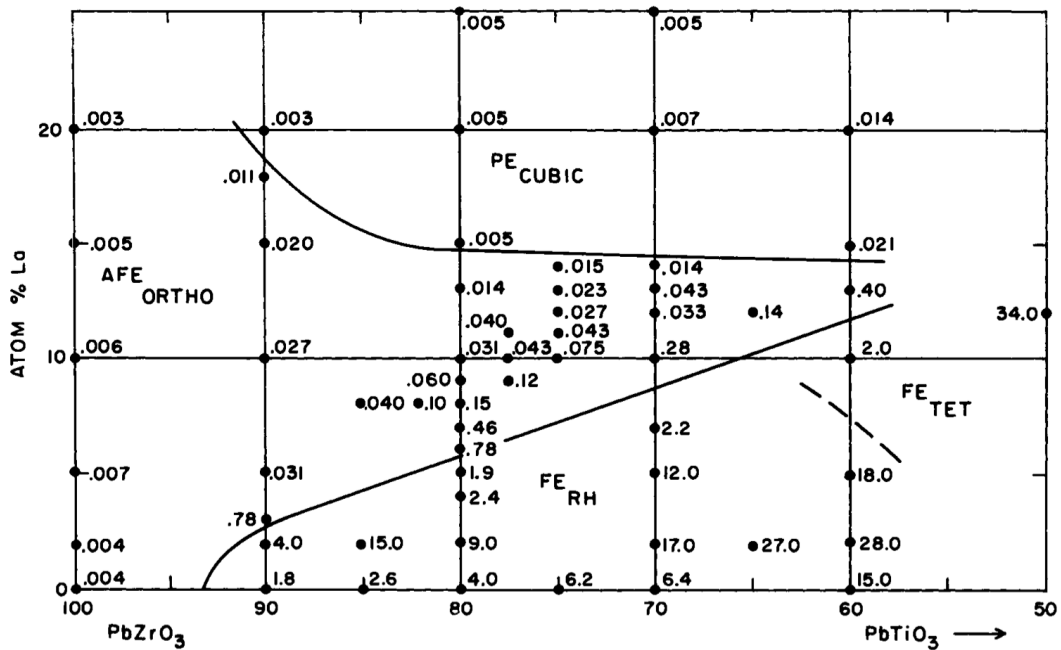


Figure 4.1 “Application of SHG by Schulze (1973)²⁰ to study phase diagram for the complex system $PbZrO_3:PbTiO_3:La_2O_3$. Relative SHG intensity for each composition tested is indicated next to the corresponding closed circle. The sharp change in the signal at a phase boundary permits a rapid mapping of the phase diagram, providing an alternative to differential thermal analysis”

In the second work, SHG was used on ZnO and AlN (nitride of Aluminium) in order to plot their unary (P, T) phase diagrams. (Bayarjargal et al. 2009; Bayarjargal and Winkler 2012; Bayarjargal et al. 2013). In these works, SHG measurements were performed versus temperature (at RT and 900K) and pressure (from 1 atm to 30 GPa). Results show that the onset of the phase transition causes a decrease in the SHG signal, and the transition is completed once the SHG signal has vanished (transition from NC toward centrosymmetric phase). Due to their large experimental error, the transition pressure was taken as the pressure, where the SHG intensity had decreased by 50%. Then, the Bayarjargal *et al.* experiments serve (at least) to semi quantitatively monitor the change of the SHG intensity as a function of pressure

TR-SHG has already been employed to monitor in situ the crystallization of a non-centrosymmetric phase from a supersaturated solution (LeCaptain and Berglund 1999) and is thus suitable for monitoring the crystallization either in solid state (as described in chapter 3) or when a liquid phase is involved such as in phase diagram (liquid \Leftrightarrow solid phase boundaries or in binary domains with liquid). Consequently, we decided to investigate by real-time measurements several mixtures by means of TR-SHG in order to investigate phase diagrams.

²⁰ Reprint in (Richardson 1978) from « Dielectric properties of $PbZrO_3:PbTiO_3 La_2O_3$ ceramics » thesis Schulze 1973

Before performing numerous experiments, it was important to develop some theoretical hypothesis on the evolution of the SHG signal in binary mixtures.

1.2 Theoretical hypothesis

Possibly, several cases are imaginable depending on the nature of pure A and B crystals and of their equilibria. In the following, we assume that the compound A crystallizes in a non-centrosymmetric space group and B in a centrosymmetric one. Moreover, it is supposed that no solid-solid phase transition occurs during the heating. In addition, the theory is developed here only for simple eutectic phase diagram.

The theoretical evolution for the SHG signal in a binary eutectic mixture of A and B at given composition (rich in A) during the heating is plotted on Figure 4.2.

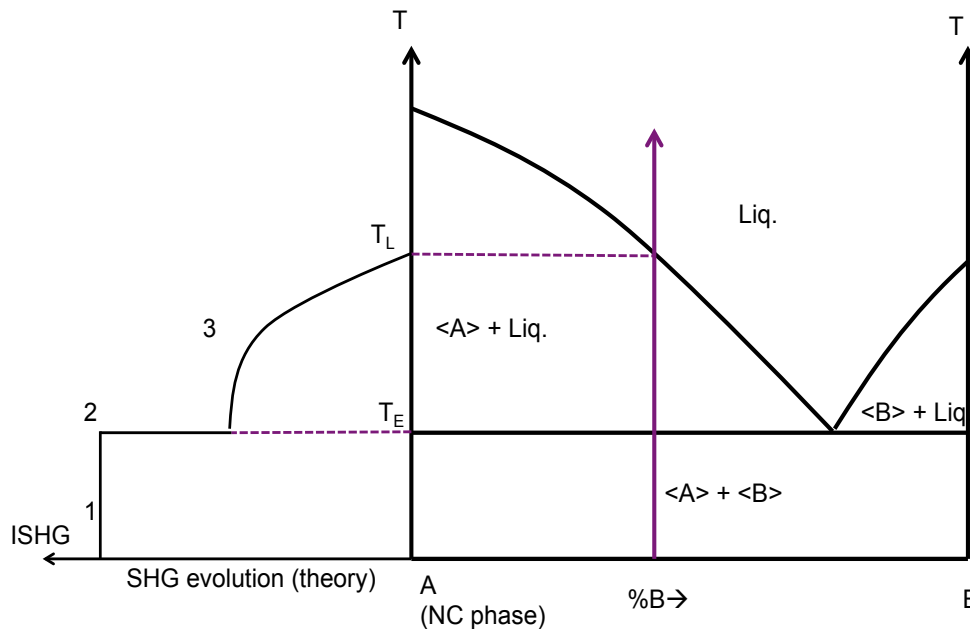


Figure 4.2 Expected (theoretical) TR-SHG curve for A/B mixture in the enrich NC phase composition

In rich NC phase domain, the theoretical evolution of the SHG signal could be described by:

(1) An evolution of the SHG efficiency with the temperature (mainly related to nonlinear properties of A crystal). The SHG signal could remain stable, increase or decrease with the temperature.

(2) At the eutectic temperature T_E , a sharp decrease of the SHG signal occurs because of the apparition of liquid phase (the scattering and/or the absorption of the liquid create a decrease of the SHG signal)

(3) A progressive decrease of SHG signal due to the disappearance of A crystals with heating. Finally, when the SHG signal becomes null, the liquidus temperature T_L is reached.

The same assumptions are valuable for an enrich B mixtures expect that after the sharp

decrease of the SHG signal at the eutectic temperature (2), the signal must vanish because the system is then only composed of centrosymmetric phases (liquid and B crystals).

By repeating these experiments for several compositions, it is thus possible to plot the liquidus and the eutectic lines. These hypotheses were confirmed through the investigation of the formic acid/water binary system.

1.3 Presentation of the Formic acid/ water system

The water molecule properties are well described in the literature and thus are not fully developed in the following. One can just notice that there are, up to date, 16 different crystal structures of the water. (Zheligovskaya and Malenkov 2007; Bartels-Rausch et al. 2012) Nevertheless, under normal atmospheric condition and at the equilibrium, water crystallizes in centrosymmetric hexagonal space group. The Table 4.1 summarized some physical data of both water and formic acid.

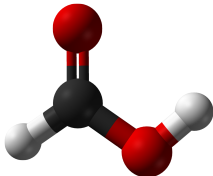
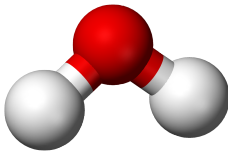
	Formic Acid (HCOOH)	Water (H ₂ O)
Molecule		
Molecular mass (g mol ⁻¹)	46	18
Melting Temperature T _m (°C)	8.35± 0.6 (Coolidge 1930; Dreisbach and Martin 1949; Kohler et al. 1981).	0
Melting enthalpy ΔH _{melting} (kJ.mol ⁻¹)	12.68 (Stout and Fisher 1941; Domalski and Hearing 1996)	6.01(Lide 2006)
Crystal structure	<i>Pna</i> 2 ₁ (Holtzberg et al. 1953; Albinati et al. 1978; Nahringbauer 1978)	<i>P</i> 6 ₃ / <i>mmc</i> (Ice I)

Table 4.1 Physical data for pure compounds

The formic acid is the simplest carboxylic acid. It is naturally found in the poison or defence systems of ants and bees and was detected, in the solid state, in interstellar and cometary ices and in the interstellar gas (Boechat-Roberty et al. 2005). It is completely miscible with water and many polar solvents. Formic acid does not increase in volume when it solidifies and has a tendency to undergo supercooling (Reutemann and Kieczka 1996).

Concerning possible polymorphism and solid-solid transition for the formic acid, the literature remains unclear on some aspects. The study of the formic acid in the solid state started as early as 1953 with the first crystal structure determination. Then it was widely studied, notably by means of infrared methods. Historic discoveries on solid formic acid are summarized in Table 4.2.

Date	Discoveries	References
1953	First SC-XRD study at -50°C Crystal structure: $Pna2_1$ (β_1 polymorph)	(Holtzberg et al. 1953)
1958	IR study: 77K to 20K no change on the spectrum assign to an α polymorph.	(Millikan and Pitzer 1958)
1966-67	Two polymorphic forms detected and suspicion of phase transition by means of IR. No temperature range was indicated and authors refer to the use of pressure cell. The experimental conditions were not properly specified	(Mikawa 1966; Jakobsen et al. 1967; Mikawa et al. 1967)
1970	Phase transition suspected and temperature determined at -66°C (cooling) and -55°C (heating) by IR & DSC thus classified as a first order transition. No change was detected by means of TR-XRPD. One can notice that DSC and TR-XRPD results are not shown in the paper. The authors suggest the existence of a new polymorphic form related to a “tautomeric polymorphism” with a coexistence of two phases β_1 and β_2 above T_c in a disordered structure (see Figure 4.3). They also suggest an order-disorder transition.	(Zelmann et al. 1970)
1978	SC-XRD studies at 278, 248, 223 and 98K No phase transition detected, the formic acid molecules are hydrogen bonded together to form planar chains β_1 (same structure than determined by Holtzberg in 1953).	(Nahringbauer 1978)
	Neutron diffraction at 4.5K. Same crystal structure	(Albinati et al. 1978)
1981	Raman investigation: “An intensity anomaly is seen around 220 K (-53°C) near a previously reported thermal anomaly, suggestive of a phase transition. A renewed thermal investigation is needed.” New IR studies in order to monitor a possible order-disorder transition. They conclude that « The crystallographic evidence is ambiguous »	(Grip and Samuelsen 1981) (Robertson and Lawrence 1981)
1999	SC-XRD: determination of high pressure polymorphic form. In the paper, no mention of historic episodes and possible phase transition.	(Allan and Clark 1999)
2008	Computational study: « The speculated polymorphism involving β_2 or α by Mikawa <i>et al.</i> is untenable from the energetic, structural, and spectroscopic viewpoints. The mixed and β_1 and β_2 state above 207 – 218 K proposed by Zelmann <i>et al.</i> is not necessarily incompatible with the predicted energetic and infrared spectroscopic characteristics. However, observed Raman and inelastic neutron scattering spectra do not show any signs of β_2 above these temperatures. The hitherto-inexplicable splitting of infrared bands of solid formic acid can be assigned to in-phase and out-of-phase vibrations of adjacent hydrogen-bonded formic acid molecules ».	(Hirata 2008)

Table 4.2 History of the formic acid in the solid-state

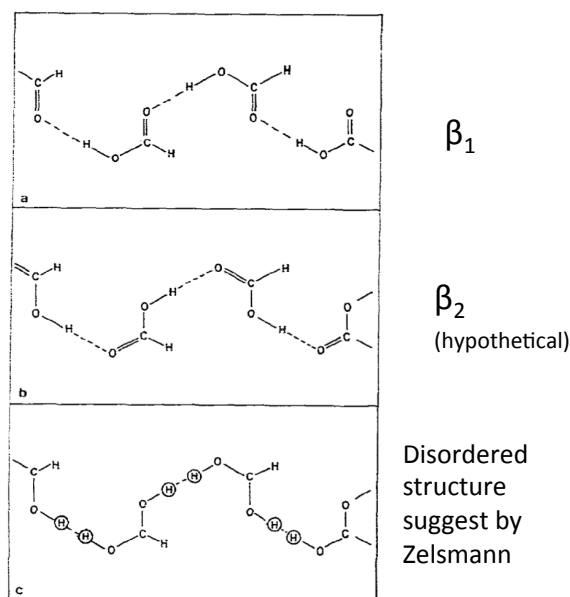


Figure 4.3 Different planar chains for β_1 and β_2 polymorphic forms and for the disordered form imagined by Zelsmann

To sum up, only the β_1 crystal structure has been observed at normal pressure (1 atm) by means of X-Ray diffraction. One can notice, based on calculated XRPD diffractograms from the literature data, that the crystal lattice contraction during the cooling is anisotropic (see Figure 4.4). The existence of other presume polymorphs is not consistent with recent energy an IR spectrum calculations (Hirata 2008). Moreover no phase transition was detected by XR diffraction. The suspicion of the existence of other formic acid polymorphs at normal pressure is based on optical investigations (IR and Raman) because of an anomaly appearing on spectra at circa $-55\pm 1^\circ\text{C}$ (Zelsmann et al. 1970) or -53°C (Grip and Samuelsen 1981). A thermal signature of this presumed phase transition also appears on DSC chart at $-66\pm 2^\circ\text{C}$ during the cooling and $-55\pm 0.5^\circ\text{C}$ during the heating (Zelsmann et al. 1970). Up to now, no clear answer to explain these anomalies has been given. An element of response is given in the conclusion of this part.

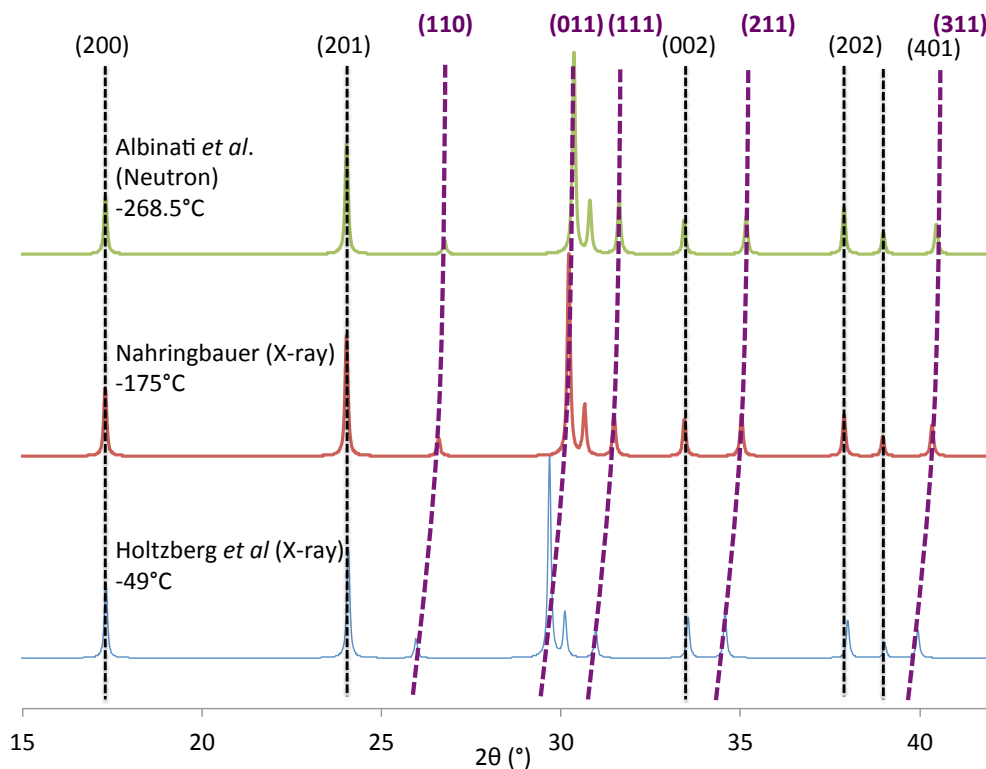


Figure 4.4 Powder x-ray diffractograms calculated at -49°C , -175°C and -268.5°C from the structure collected at the same respective temperatures. An anisotropic contraction occurs.

Note that in many studies as in our work, the formic acid used was not totally pure and often contained small amounts of water²¹. This changes slightly the mixture compositions.

Intensive research in literature was performed to find existing phase diagram of formic acid/water system and entries are plotted Figure 4.5 taken from (Timmermans 1960). One can notice that the original papers were not found with consequently unknown information about the experimental conditions and the purities. All data seem in agreement with the others except for the Glagoleva's values. From Kuznetsova & Bergman and Kremann data, the eutectic temperature T_E was determined at circa -49.5°C and -52.5°C , respectively. The eutectic composition was determined at circa 59 %mol. of water (*i.e.* circa 38%wt.).

²¹ There are some difficulties to obtain very pure formic acid since it decomposes in water and carbon monoxide (Schmeißer and Schuster 2011) and due to its hygroscopic behaviour

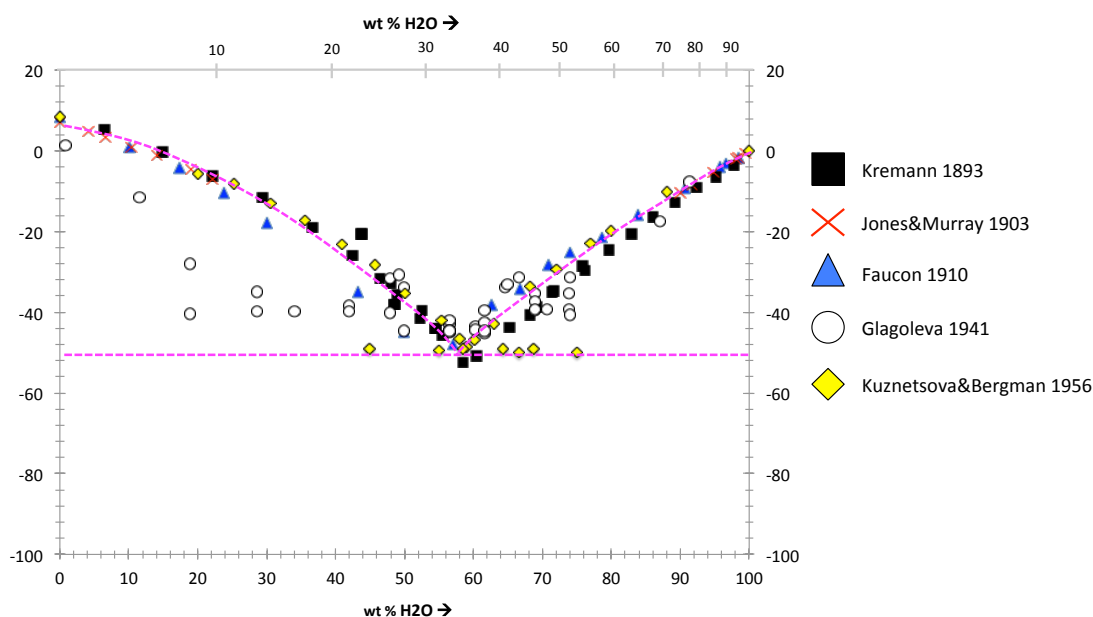


Figure 4.5 Binary formic acid/water phase diagrams found in literature taken from (Timmermans 1960)

1.4 TR-SHG phase diagram investigations

Several mixtures of formic acid and water (total mass of 10 g) were prepared and analyzed by TR-SHG. Firstly, the sample is cooled at -100°C at $10\text{K}/\text{min}$ and then heated at $1\text{K}/\text{min}$ with SHG measurements during the heating every 1 or 2 minutes (consequently the error on the temperature is approximately 0.05°C for a measure duration of 3sec). TR-SHG results are detailed for only some particular compositions.

Figure 4.6 shows the TR-SHG curve for a 80/20 (%wt.) composition. A first comment is that results fit pretty well the elaborated theory. A positive SHG signal is detected at -100°C confirming the non-centrosymmetric nature of the sample (attributed in this case to formic acid crystals). The SHG signal remains relatively stable from -100°C to -54°C . At circa -52°C , the signal decreases sharply (divided by four) and after that decreases progressively to totally vanish at circa -21°C .

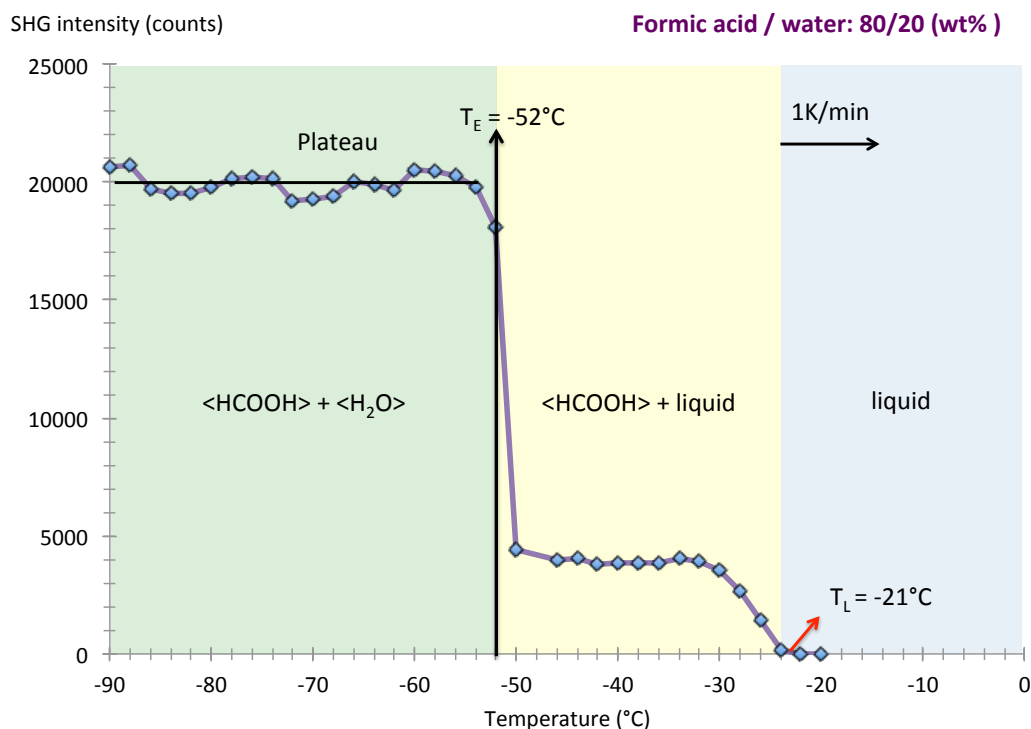


Figure 4.6 TR-SHG curve for 80/20 (wt%) mixture at $1\text{K}\cdot\text{min}^{-1}$. A plateau is observed before a drastic decrease of the SHG signal corresponding to the eutectic temperature. Color domains are determined from SHG signal interpretations: mixture of water and formic acid crystal (green); mixture of formic acid crystal and liquid (yellow); pure liquid (blue)

The same experiments were performed several times in order to ensure the reproducibility. In some it seems that the sample was not totally crystalline at -100°C (the sample was translucent). It is consistent with the fact that formic acid has a tendency to undergo supercooling. This can lead to some problems during TR-SHG experiments. For instance, the TR-SHG curve obtained for the 70/30 composition plotted Figure 4.7 shows that the sample exhibits a very weak SHG signal at -100°C compare to the 80/20 composition (one order of magnitude lower). An increase of the SHG signal is also observed during the heating. This is attributed to the recrystallization of the amorphous part of the sample. Nevertheless this increase is “stopped” at -52°C and the signal decreases significantly from -50°C . The SHG signal completely vanishes at -34°C .

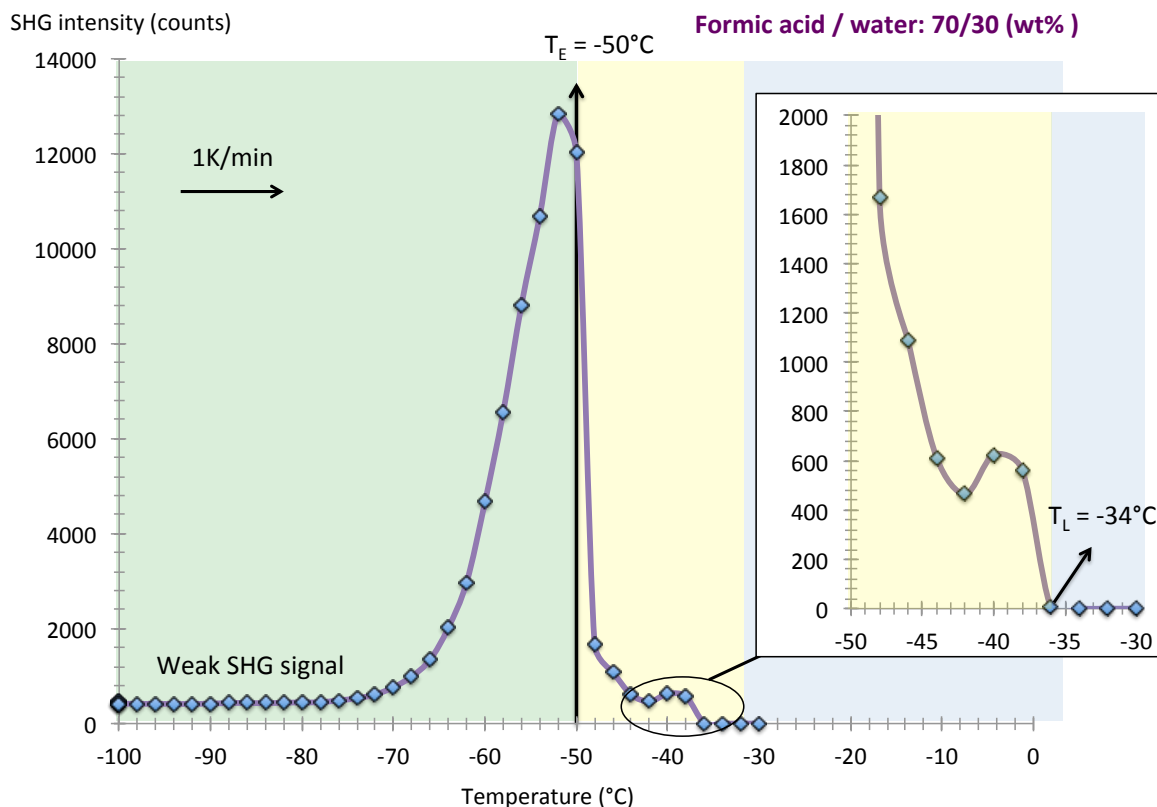


Figure 4.7 TR-SHG curves for 70/30 composition highlighting partial crystallization at -100°C with subsequent recrystallization during the heating. Eutectic and liquidus temperatures can be determined.

Through these two examples, it clearly appears that investigated compositions are made of mixtures of formic acid and water crystals from -100° up to circa -52°C (green part). Then, at this temperature, we enter in the liquid + formic acid binary domain up to the liquidus temperature (yellow part). The system is completely liquid when the SHG signal is null (blue part).

With the increase of water concentration, the temperature domain (between the beginning of the SHG decrease and its vanishing) decreases as shown on Figure 4.8 for the 60/40 composition. It means that compositions investigated are getting closer and closer to the eutectic composition.

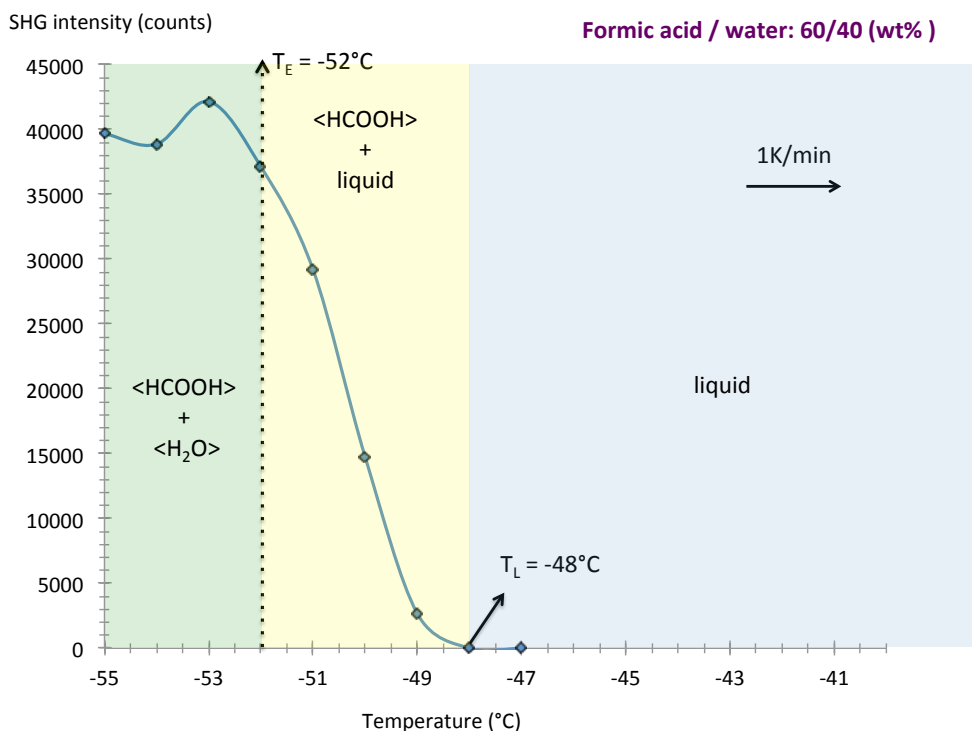


Figure 4.8 TR-SHG curves for 60/40 composition closes to the eutectic composition.

For the 50/50 composition, only the eutectic temperature is detected (at circa -53°C), then the signal completely vanishes. It means that above -53°C , the system is totally centrosymmetric (*i.e.* only composed of liquid and water crystals).

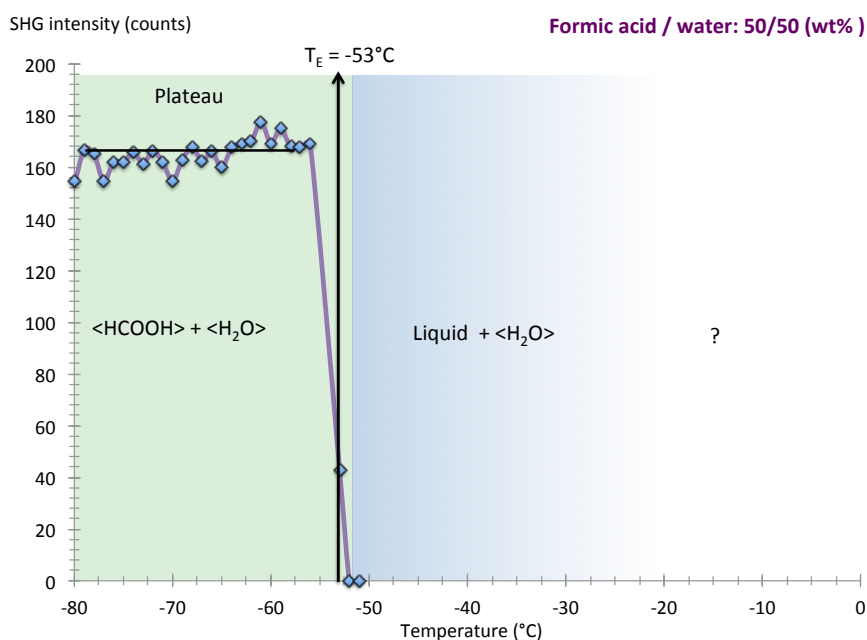


Figure 4.9 TR-SHG curves for 50:50 (wt.%) composition. Only the eutectic temperature is detected and above T_E , the SHG signal totally vanishes meaning that the investigated mixture is centrosymmetric (<water> + liquid binary domain).

The main limitation of the TR-SHG technique is the impossibility to fully investigate the phase diagram in water rich compositions due to the centrosymmetric crystal structure of

water.

DSC analyses were performed for the same compositions at 1K/min in order to compare the thermal analysis data to the TR-SHG results. DSC charts are plotted Figure 4.10 and all data are also summed in the Table 4.3.

Water composition (wt.%)	SHG results		DSC results	
	Liquidus (°C)	Eutectic (°C)	Liquidus (°C)	Eutectic (°C)
10.36	-4	-51	-5.2	-50.9
20	-21	-52	-24.8	-50.8
30.41	-34	-52	-40.2	-52.4
40.01	-48	-52	-	-51.1
49.89	-	-51	-36.4	-53.4
60.09	-	-	-24.4	-51.1
73.52	-	-	-15.4	-51
76.55	-	-	-9.6	-52.6
90	-	-53	-8.2	-
94.9	-	-51	-	-
99.06	-	-52	-	-

Table 4.3 Liquidus and Eutectic temperatures determined by TR-SHG and DSC analyses

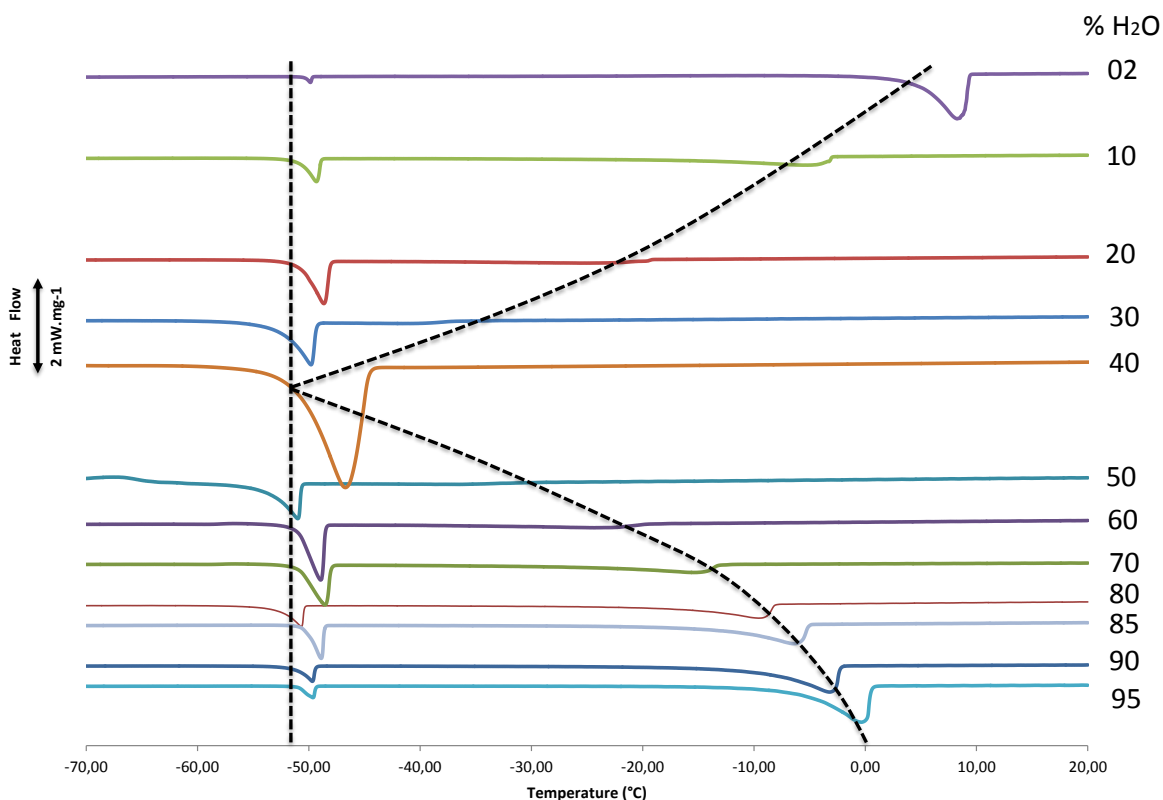


Figure 4.10 DSC charts of Formic Acid/water mixtures

To determine the eutectic and liquidus temperatures, the onset and the peak temperature are taken on the DSC chart, respectively. The phase diagram gathering DSC and TR-SHG results is plotted *Figure 4.11*.

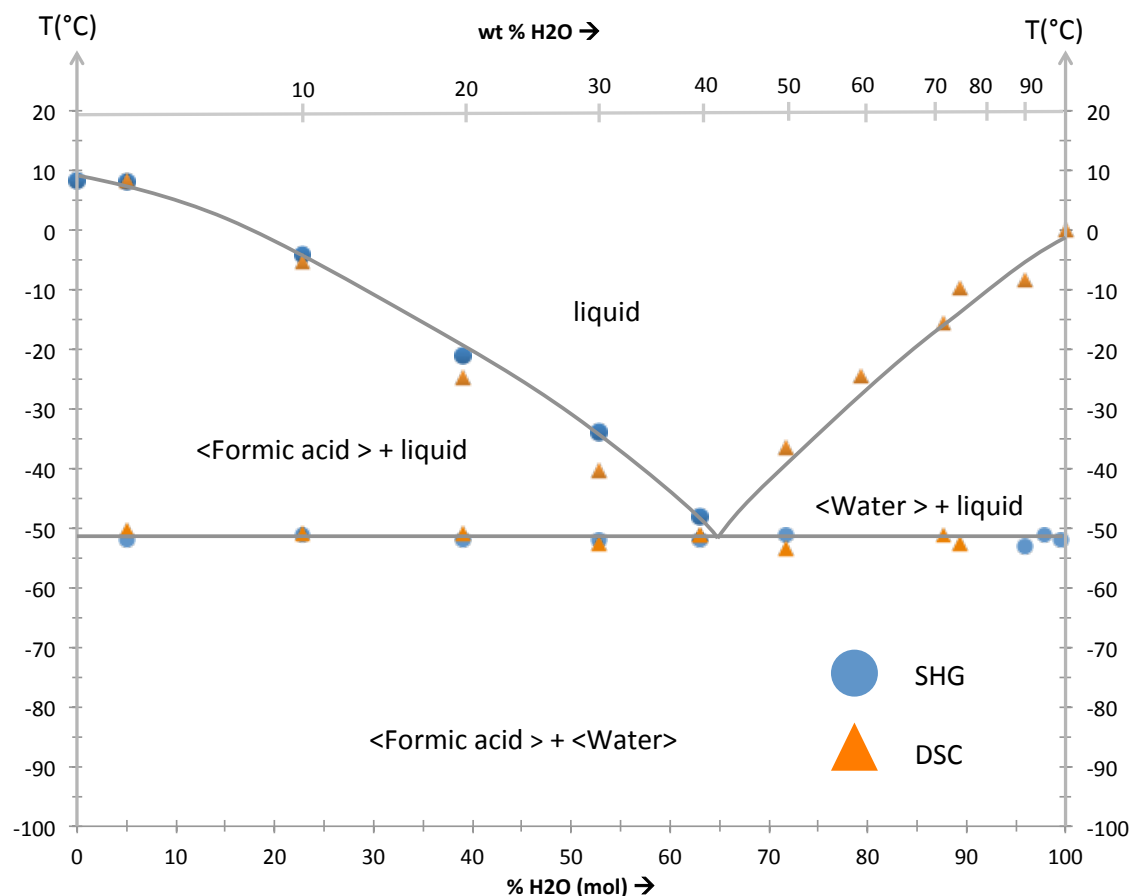


Figure 4.11 Formic Acid/ Water phase diagram from TR-SHG (blue circles) and DSC (orange triangles) data.

1.5 Conclusion and possible explanation for the suspected formic acid phase transition

Through the investigation of the formic acid/ water binary phase diagram, the TR-SHG technique reveals its usefulness to the rapid and sensitive determination of phase domains boundaries.

Eutectic temperatures determined by both methods are relatively close, nevertheless some differences in the liquidus temperatures are observed and are all the more pronounced that the water concentration is high. In this matter, DSC analyses can suffer of a lack of precision since it is difficult to decouple eutectic and liquidus endotherms for compositions close to the eutectic composition (due the shape of the liquidus peak). For instance, DSC chart for the composition 60/40 only presents one peak (Figure 4.10) although it is possible to differentiate eutectic and liquidus temperature by TR-SHG (Figure 4.8). It demonstrates the usefulness of SHG to accurately determine the eutectic composition.

An important result is the determination of the eutectic temperature at circa -52°C . One can notice that the eutectic endotherm on DSC charts is visible even for small amount of water. Moreover, at the eutectic temperature a sharp decrease is visible on the TR-SHG curves. These results and observations are of particular importance if we recall that phase transition was suspected at circa the same temperature than the eutectic invariant. Moreover, it is difficult to have formic acid free of any water traces. Consequently, the optical anomalies on Raman and IR spectra and on the endotherm on DSC chart reported in literature could be explained by the detection of the eutectic invariant (*i.e.* the apparition of the liquid phase during the heating could explain these phenomena) and then may not be associated to any phase transition.

The main limitation is that at least one NC phase is still required in the investigated domains. Moreover, some precaution must be taken to correctly crystallize the sample during the cooling. Protocol improvements are in progress, in order to find the better way to obtain reliable results and to investigate other phase diagrams.

Part.2 SHG measurements versus relative Humidity

Pharmaceutical compounds can exist in various solid phases such as different polymorphs, hydrates, solvates, co-crystals, host–guest associations, salts and hybrids of all sorts and are often administered in crystalline powder forms (Bernstein 2002). Water concentration in the atmosphere (RH) can drastically modify the nature of phases because of the possible formation of hydrate or anhydrate. Dynamic vapor sorption (DVS) analysis is particularly adapted to monitor the evolution of the water uptake by the crystal versus the relative humidity and is thus often used to characterize and monitor dehydration/rehydration or deliquescent kinetics. Other usual techniques are not particularly designed to monitor a process under various relative humidity. One can note the elaboration in the SMS laboratory of XRPD prototype to performed XRD under various RH and temperatures (Coquerel et al. 2014). In this part we report the use of SHG to monitor the evolution of a crystalline phase under various RH. The aim of this study was to assess the potential of this technique in the field to monitor processes related to the relative humidity changes. The potential of SHG is exemplified through the case of Strontium diformate dihydrate.

2.1 Polymorphic and hydrated forms of Strontium diformate

The strontium diformate (often noted in literature strontium formate) exhibits 3 known polymorphic forms (β -Sr(HCOO)₂ ($P4_12_12$) and δ -Sr(HCOO)₂ ($I4_1/amd$): Comel and Mentzen

1974; α -Sr(HCOO)₂ ($P2_12_12_1$): Watanabé and Matsui 1978) and one dihydrate ($P2_12_12_1$: Galigné 1971). The crystallographic data are summarized in Table 4.4.

Crystal form	Sr(HCOO) ₂ ·2H ₂ O	α -Sr(HCOO) ₂	β -Sr(HCOO) ₂	δ -Sr(HCOO) ₂
CCDC code	SRFORM10	SRFORA05	SRFORA06	SRFORA08
Reference	(Galigné 1971)		(Ståhl et al. 2009)	
Crystal system	Orthorhombic	Orthorhombic	Tetragonal	Tetragonal
Space group	$P2_12_12_1$	$P2_12_12_1$	$P4_12_12$	$I4_1/amd$
a (Å)	7.144	6.86744	7.13577	7.09042(10)
b (Å)	7.332	7.26091	7.13577	7.09042(10)
c (Å)	12.04	8.75087	9.5908	10.16973(15)
β (°)	90	90	90	90
Volume (Å ³)	650.653	436.352	488.356	511.274
Z, Z'	4, 1	4, 1	4, 0.5	4, 0.13
Analysis temperature (K)	283-303	283-303	334	605
Density	2.251	2.704	2.416	2.308
Rfactor (%)	2.1	2.3	1.3	2.0

Table 4.4 Crystallographic data of known hydrate and polymorphs of strontium diformate

2.2 Dehydration and hydration pathways (from literature)

The dehydration and phase transitions occurring during the heating of the dihydrate form are described Figure 4.12.

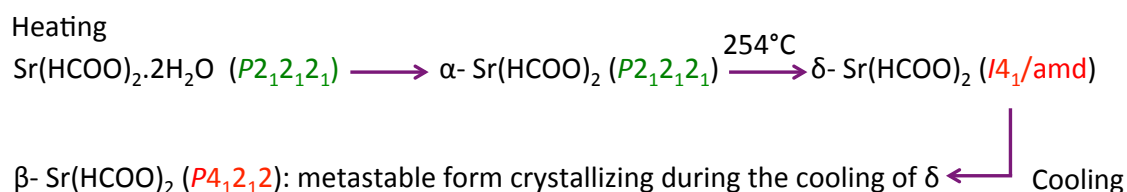


Figure 4.12 Thermal Dehydration of the dihydrate form and phase transitions occurring after dehydration in a dry atmosphere.

An interesting fact is the crystallization of a metastable β -Sr(HCOO)₂ ($P4_12_12$) form during the cooling of the δ -form (Comel and Mentzen 1974). One can notice that the β -form belongs to the crystal class 422 that can be SHG inactive if Kleinman condition applies. The existence of another modification in the $F4_132$ space group (thus NC but also SHG inactive) has also been suggested (Comel and Mentzen 1974; Mentzen and Comel 1974). Nevertheless this was not confirmed in a recent study (Ståhl et al. 2009). It should be also mentioned that in this latter study no attention was paid to the relative humidity contrary to the studies of Comel and Mentzen. In fact, it seems that the water concentration in the atmosphere acts considerably on the polymorphism of the strontium formate. Indeed, the relative humidity can change the heterogeneous equilibria. It has been shown that, in presence of water moisture, the β -form is

transformed into the α -form (with an associated exothermic peak on DSC) but in dry condition, the reversible $\beta \leftrightarrow \delta$ transformation (upon heating) can indefinitely be observed (only by XR diffraction) and without any thermal effect detected by DSC (Comel and Mentzen 1974; Mentzen and Comel 1974).

The supposed SHG activities of the various phases involved are summarized in Table 4.5.

Crystal form	Sr(HCOO) ₂ .2H ₂ O	α	β	δ
Space group	<i>P</i> 2 ₁ 2 ₁ 2 ₁	<i>P</i> 2 ₁ 2 ₁ 2 ₁	<i>P</i> 4 ₁ 2 ₁ 2	<i>I</i> 4 ₁ /amd
SHG activity	+	+	- (due to Kleinman Symmetry if no absorption)	-

Table 4.5 Expected SHG activity for the different structures of Sr(HCOO)₂.2H₂O

The dehydration of the dihydrate and the phase transitions occurring during the heating involve centric and acentric crystal structures; consequently this system can be monitored by TR-SHG.

2.3 TR-SHG experiments under dry atmosphere

A TR-SHG experiment under dry atmosphere was performed on Sr(HCOO)₂.2H₂O at 5K/min and results are plotted Figure 4.13.

During the heating, the first SHG increase starting at circa 60°C (until circa 85°C) can be attributed to the dehydration toward the anhydrous α -form. Then, the SHG signal remains almost stable (with a small decrease) until circa 200°C. At 200°C the SHG signal starts to decrease rapidly and completely vanishes at 250°C. It can be associated to the phase transition toward the δ -form (centrosymmetric). During the cooling of the sample, the SHG signal remains zero up to 25°C which probably indicates the presence of the metastable β -form (NC but giving no SHG signal due to Kleinman symmetry).

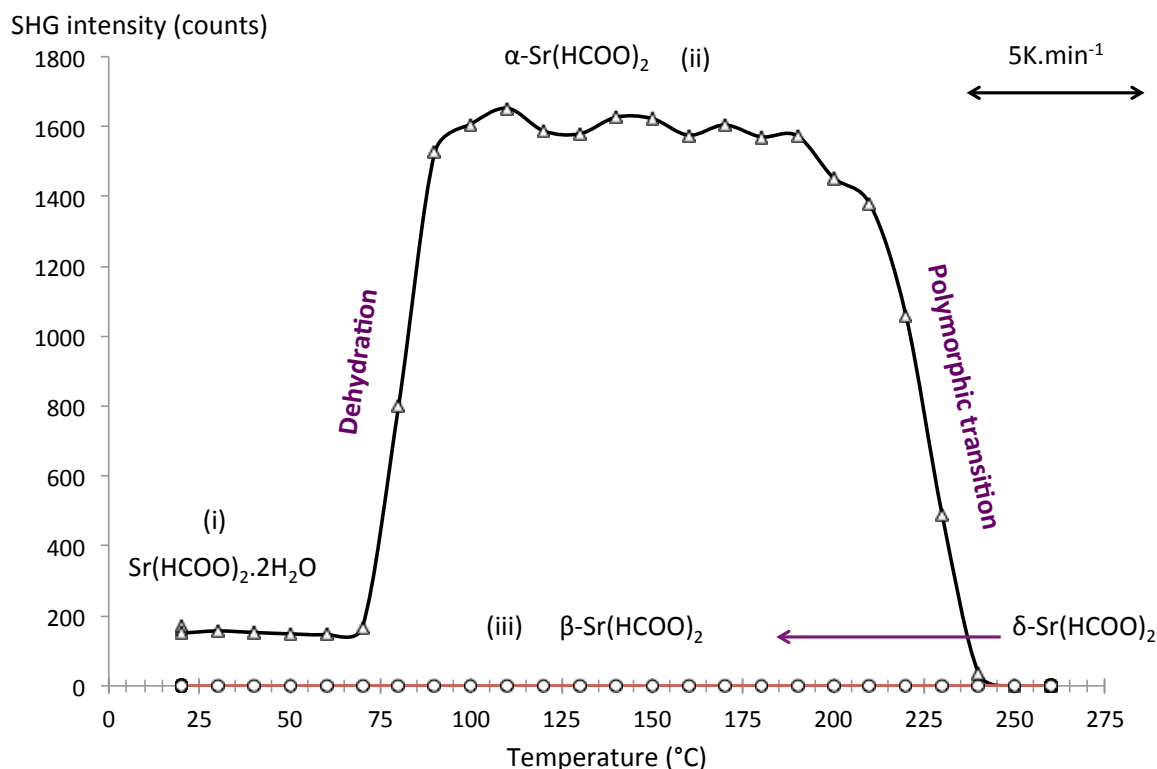


Figure 4.13 Heating (triangles) and cooling (circles) TR-SHG curves starting from the dihydrate form in a dry atmosphere. Diffractograms of sample (i), (ii) and (iii) are plotted Figure 4.14

2.4 Phase checking by XRPD

In order to confirm these hypotheses on the crystalline nature of the phases involved during the heating and the cooling, the experiment was stopped at the labeled (i), (ii), (iii) points on the Figure 4.13. The XRPD diffractograms of (i), (ii) and (iii) together with the calculated patterns of $\text{Sr}(\text{HCOO})_2 \cdot 2\text{H}_2\text{O}$, α -form and β -form are plotted Figure 4.14. It confirms that sample in (i) and (ii) correspond to the dihydrate and the α -form, respectively. The sample (iii) is a mixture of α and β forms. Nevertheless, before the XRPD (in dry atmosphere) the sample exhibits no SHG signal and after the diffraction analysis (at $\text{RH} > 0\%$) the sample exhibits a positive SHG signal. It suggests that, in the dry atmosphere, only the β -form (metastable one) was present in the sample. Further to the exposure to a $\text{RH} > 0$ during the XRPD measurements, the β phase was probably partly converted to the α -form. This is in agreement with the results reported by Comel *et al.* even if the associated mechanism remains unclear.

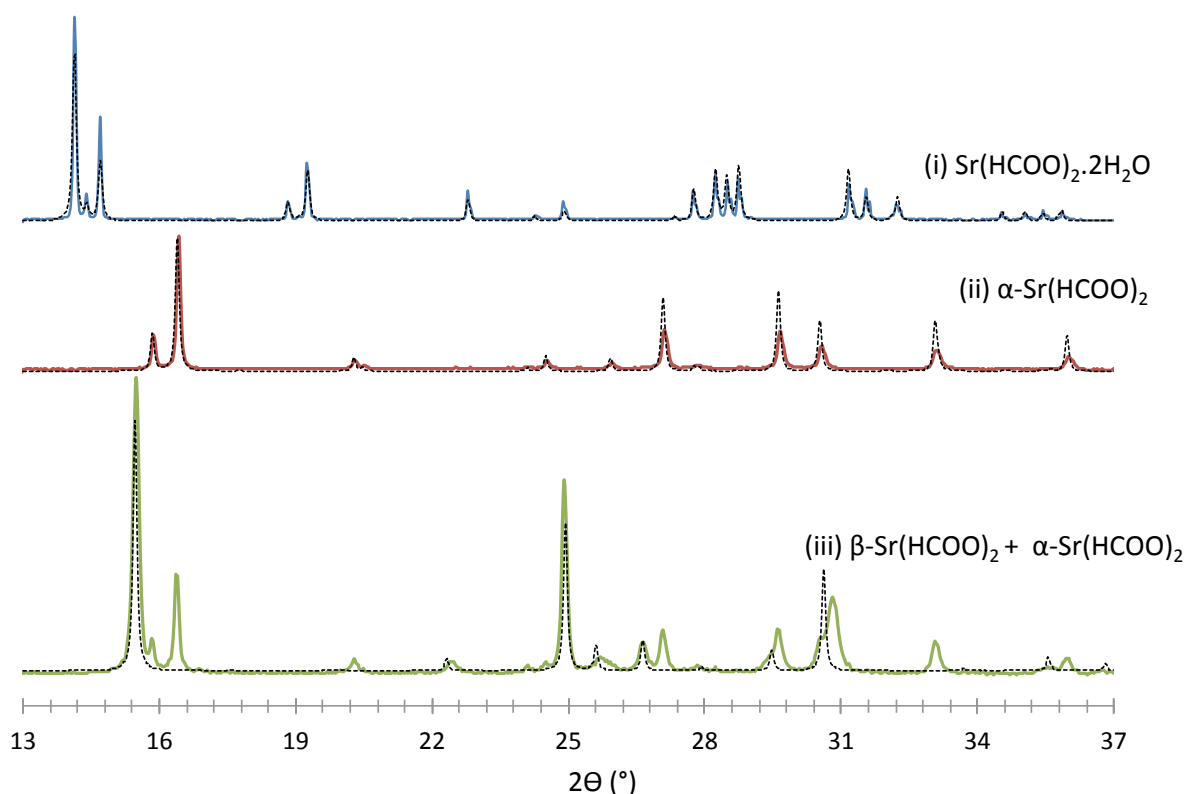


Figure 4.14 XRPD performed at room conditions (circa 1 atm, 25°C, 30-60%RH) on sample labeled (i), (ii) and (iii) (see Figure 4.13). Dash diffractograms plotted for the (i), (ii) and (iii) sample are respectively calculated from SRFORM10 ($\text{Sr}(\text{HCOO})_2 \cdot 2\text{H}_2\text{O}$), SRFORA05 ($\alpha\text{-Sr}(\text{HCOO})_2$) and SRFORA06 ($\beta\text{-Sr}(\text{HCOO})_2$) CCDC structures.

2.5 TR-SHG experiments under various relative humidity

In order to confirm the role of water in the phase transition from the β -form to the α -form, the following experiment steps were performed:

- (1) Formation of the β -form by cooling the sample from 250°C to 40°C in dry atmosphere
- (2) Sample kept at 40°C in dry atmosphere and monitoring of the evolution of the phase by SHG.
- (3) Increase of the water concentration in the atmosphere surrounding the sample by setting the RH at 20% monitoring by SHG measurements.

The SHG curves obtained along this experiment is plotted Figure 4.15. Results show that in dry atmosphere, the β -form does not undergo any phase transition neither for the whole duration of the cooling (from 250°C to 40°C and thus during 42min) nor at 40°C during 13 min. In step (3), the β -form undergoes a phase transition toward the α -form only 4 min after

the increase of the RH at 20%. The necessary time to complete the transition was estimated at circa 25 minutes.

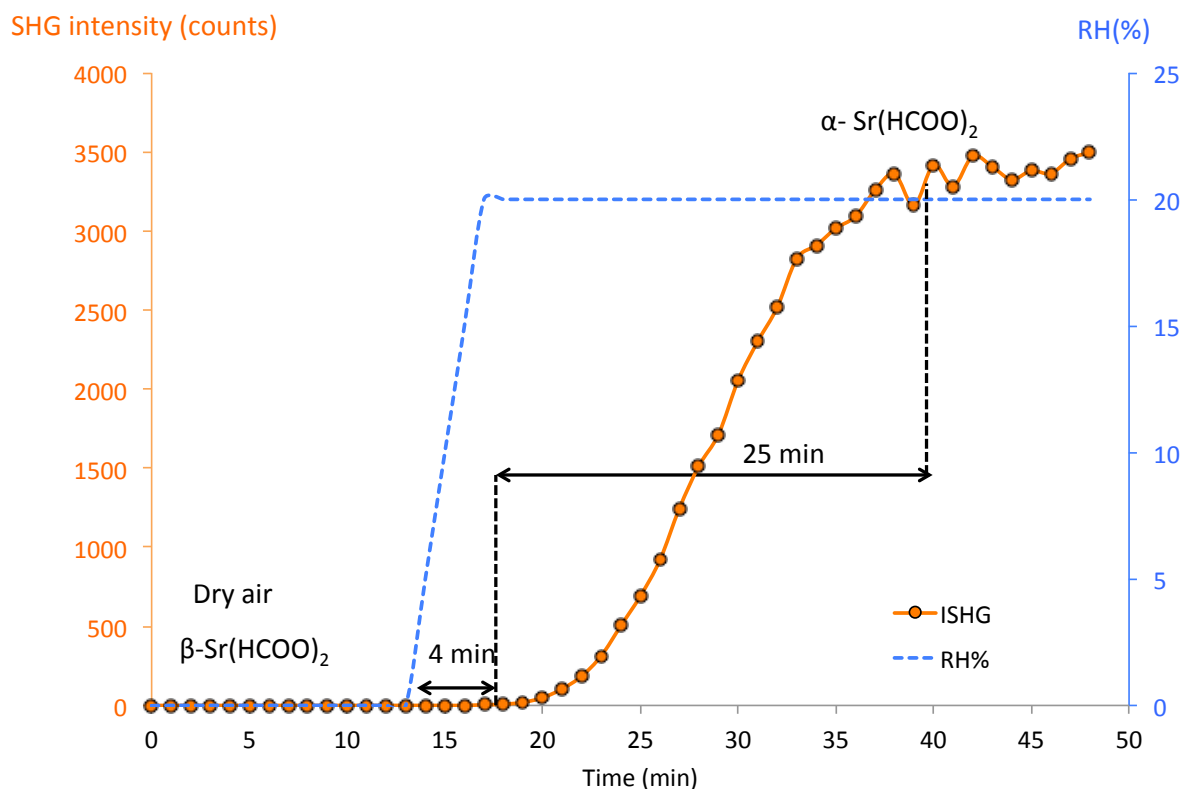


Figure 4.15 SHG measurement versus time and relative humidity for β -form at 40°C

At this point, we know that the thermal dehydration of the dihydrate leads to the α -form that exhibits a very high SHG signal compare to dihydrate form. It is thus easy to detect the dehydration by monitoring the enhancement of the SHG signal. Moreover, scanning electron microscopy (SEM) experiments performed on the dihydrate (before dehydration) and on the α -form were useful to gather more information on the mechanism. The SEM pictures are presented Figure 4.16. They show that the crystals of $\text{Sr}(\text{HCOO})_2 \cdot 2\text{H}_2\text{O}$ keep their crystal shape integrity after the dehydration. Nevertheless, crystal surfaces are rougher after the dehydration probably due to the water escape from the dihydrate crystals.

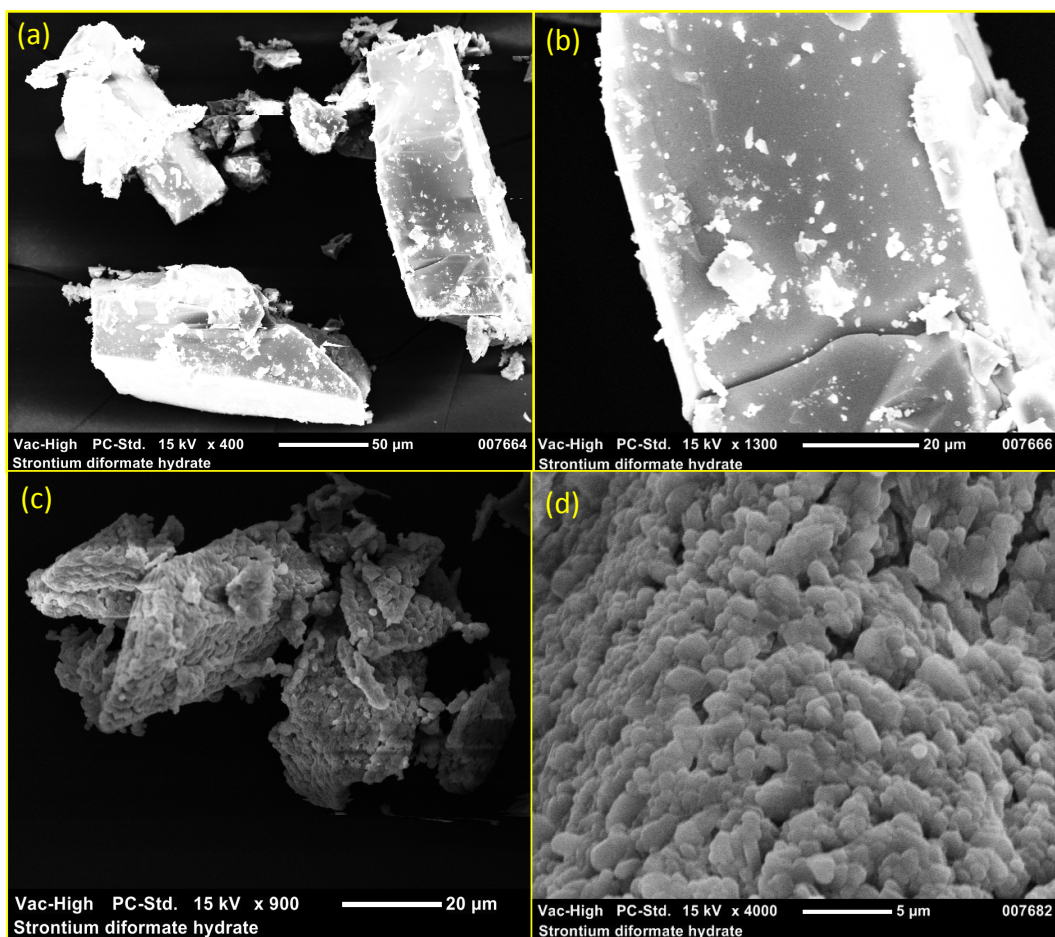


Figure 4.16 SEM pictures of the strontium diformate dihydrate (a), (b) and after dehydration (c) and (d) Crystals keep their shape integrity but the surface is totally modified.

A Dynamic Vapor Sorption (DVS) study was also performed on the dihydrate form. The DVS chart is plotted Figure 4.17. Results demonstrate the possibility to dehydrate the dihydrate form at 40°C under 0%RH in circa 850 min and that this process is totally reversible. The rehydration process starts after an increase of the RH at 90% and takes circa 250 minutes. It should be notice that de dehydration rehydration process becomes easier cycle after cycle. For instance, after the first cycle the dehydration occurs in 1300 min at 30% RH, and after the second cycle it takes only 200 minutes at 20%RH. The time required to rehydrate the sample remains relatively stable (250 min) at 90 % RH. This behavior could be related to the rough crystal surface observed after dehydration (see Figure 4.16.c).

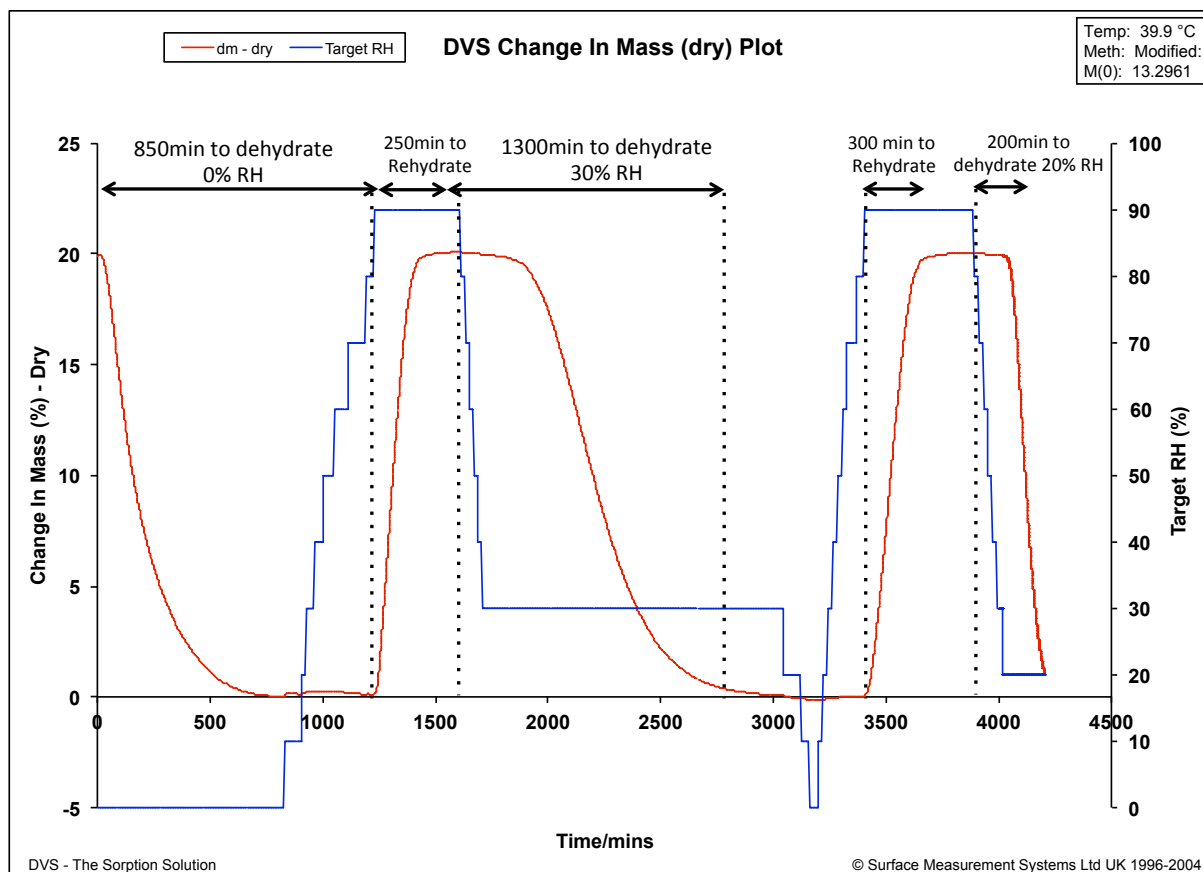


Figure 4.17 DVS chart showing the mass changes of the sample (red curve) with respect to the RH (blue curve) at 40°C for $\text{Sr}(\text{HCOO})_2 \cdot 2\text{H}_2\text{O}$

Similar SHG experiments were performed on the dihydrate form put in the heating/cooling stage with a temperature settled at 40°C under 0%RH. The SHG curves are plotted Figure 4.18.

Comparisons between DVS experiments are quite difficult because of technical differences such as the analysis cell volume and gas flow. Consequently, this could change the kinetics of dehydration in both experiments. Nevertheless, from DVS analyses, an increase of the SHG signal is expected due to the dehydration of the dihydrate under 0%RH. It is not the case on Figure 4.18. The SHG signal slightly increases at the beginning and then remains relatively stable during a long period (2500 minutes). Moreover, the SHG increase is very low if it is compared to the SHG enhancement detected during the thermal dehydration. It is relatively surprising since the mass loss of the sample during this experiment (17.5%) corresponds to the theoretical mass loss expected for a complete dehydration (16.8%). A XRPD analysis performed as quickly as possible on the sample kept during 2500 minutes at 0%RH reveals that the sample is composed of a mixture of dehydrate α and β forms. It is recalled that the β

form is referred as the metastable form but can be maintained “indefinitely” under dry atmosphere (Comel and Mentzen 1974).

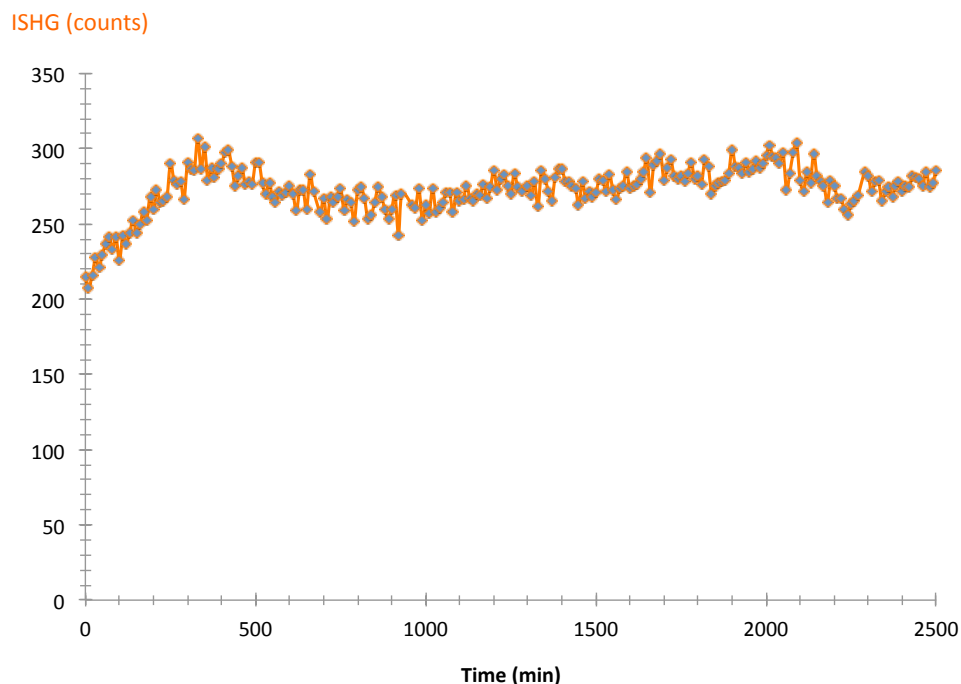


Figure 4.18 SHG monitoring of the strontium formate dihydrate form at 40°C and 0%RH. The signal, after a slight increase remains relatively stable.

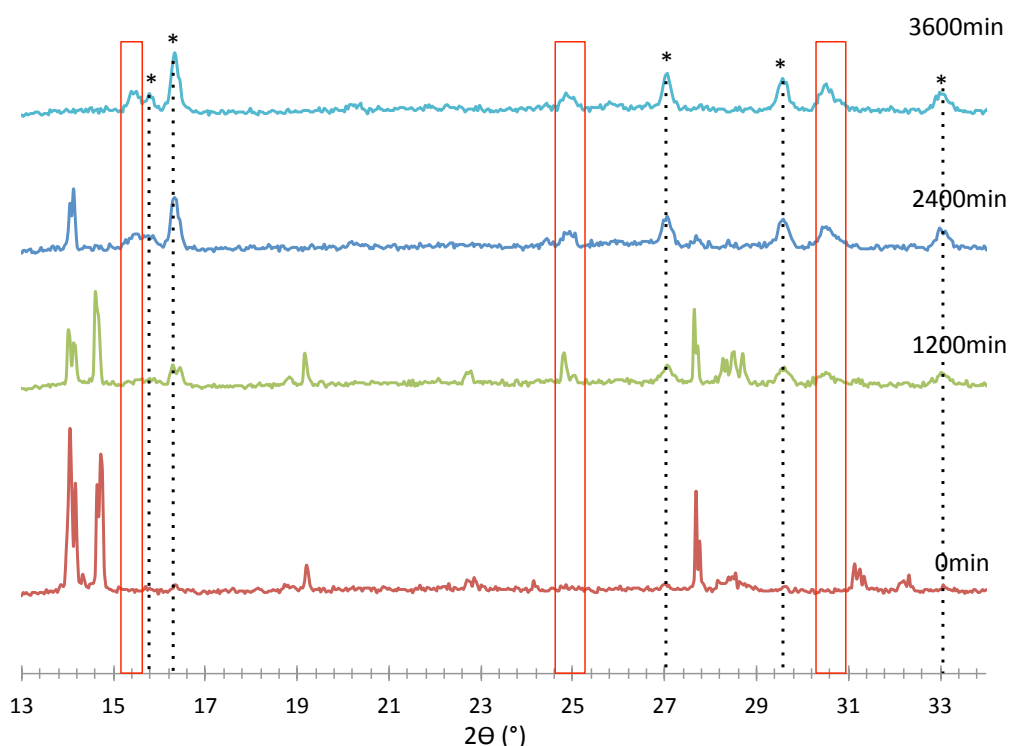


Figure 4.19 XRPD at 0%RH at 40°C on dihydrate form (diffractograms at 0min). Peaks highlighted by red rectangles belong to the β phase and those by dash lines and asterisks belong to the α -form.

The desolvation of the dihydrate form has also have been monitored versus the time at 0%RH by means of XRPD. The diffractograms are plotted Figure 4.19. On the diffractograms,

peaks of both α and β forms clearly appear during the dehydration highlighting the existence of the metastable phase in the dehydration mechanism.

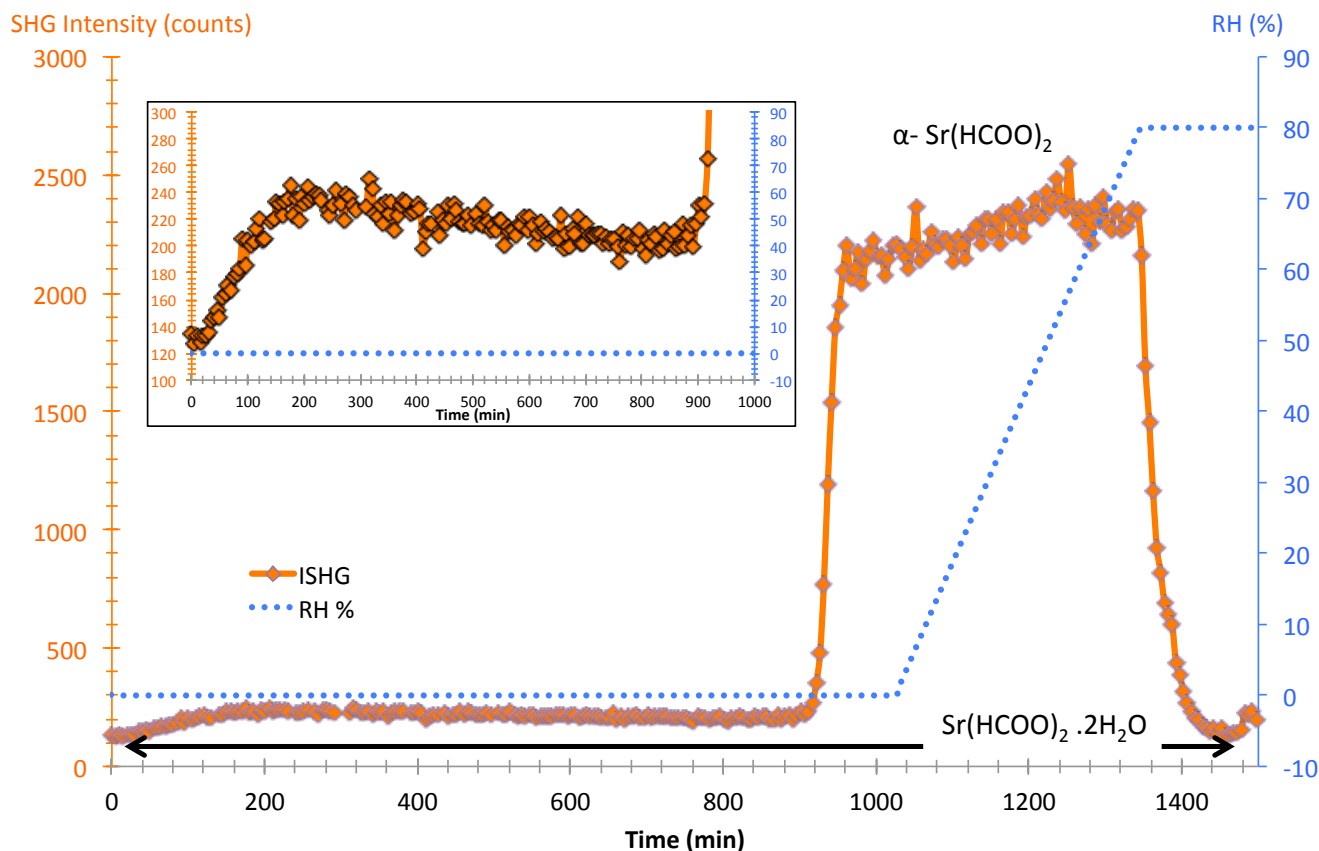


Figure 4.20 SHG dehydration monitoring of the dihydrate at 40°C under various RH.

Other dehydration experiments by means of SHG were performed, but it should be notice that the previously established results are not fully reproducible. For instance in Figure 4.20, although the SHG signal increases slightly under 0%RH at the beginning as in the previous experiment, a high enhancement of the SHG signal (similar to that detected during a thermal dehydration) produces after circa 900 minutes. The resulting product is a pure α -form. After this dehydration, if the RH is increased up to 80%, the SHG signal falls rapidly (in circa 150 min) to the SHG value exhibited by the dihydrate before the first dehydration. The sample is thus rehydrated. Let us just recall that the necessary time for the dehydration/rehydration cycle found by SHG monitoring are very similar to those found by DVS analysis (850 and 250 min, respectively).

2.5.1 Conclusion and results

Let us just sum up the previous experiments. From thermal dehydration of the strontium diformate dihydrate experiments, it is possible to easily differentiate the dihydrate and the α -form because their SHG efficiencies are completely different. The α -form exhibits a SHG

activity roughly seven times higher than that of the dihydrate form. It is thus possible to monitor the evolution of the dehydration/rehydration processes with logically a high increase of the SHG signal during the dehydration and a high decrease for the rehydration. Two dehydration experiments on the strontium diformate dihydrate at 0%RH and 40°C have been performed for comparison with the results obtained by DVS analyses.

In the first experiment (Figure 4.18), SHG and DVS results are inconsistent. The dehydration should take circa 850 min at 0%RH according to DVS results. During more than 2500 min the SHG signal remains constant with only a slight increase (circa +43%) at the beginning of the experiment. Nevertheless, the mass loss of the analyzed sample corresponds to its complete dehydration and XRPD reveals that the sample contains the metastable β -form.

In the second experiment, the SHG signal increases (likewise in thermal dehydration) in a similar time scale than in DVS for the complete dehydration. The main difference is that SHG signal increases suddenly after circa 900 minutes and reaches a maximum circa 60 minutes after that. In the DVS experiment the rate of mass loss is constant during circa 850 minutes. Moreover, at the beginning of the experiment a similar slight SHG signal increase (circa +73%) is observed as in the first experiment. This suggests that the same mechanism occurs at the beginning in both experiments. For the rehydration, the SHG signal decrease fits almost the mass uptake observed in DVS.

During these dehydration experiments, it clearly appears that the metastable β form must be involved in dehydration processed at 0%RH. Nevertheless, works are in progress to explain the inconsistencies between SHG and DVS results. The fact that the SHG efficiency of this dehydrated powder remains unchanged in some experiments is not explained for the moment. However, one element of explanation could be the formation of a transient anhydrate crystal isostructurally close to the dihydrate one, and thus exhibiting relatively the same SHG signal. It is also known that the metastable β -form can be maintained at 0%RH, with its possible crystallization and a “competition” between both phases. Let us just recall that the densities of the dihydrate, β -form and α -form are respectively 2.251; 2.416 and 2.704. The density of the stable α -form is much higher than that of the other forms and thus can act as a driving force to the crystallization of the stable form occurring after a stochastic induction time (as for example circa 900 minutes in the second experiment).

Part.3 SHG to study amorphous solids

Contrary to crystalline phase, an amorphous solid is not organized periodically and does not exhibit a SHG signal. It is thus possible to discriminate an amorphous sample from a NC crystal by SHG.

An amorphous sample is characterized by the glass transition temperature, T_g , above which it is possible to recrystallize the sample (below, the sample remains in the “glassy state”). This particular temperature depends on the history of the sample and can be also impacted by the relative humidity. In this part, the relevance of SHG to study crystallizations from amorphous at various relative humidity is investigated through the study of the amorphous lactose.

3.1 Lactose forms

Two molecular conformations (anomers) of lactose exist: (see Figure 4.21) The α -Lactose monohydrate, is the most common form of lactose and exists in 3 different crystalline structures (2 polymorphs and one monohydrate). The β -lactose is less stable and only one crystal form is known. Crystallographic data of these various crystalline structures are summarized in Table 4.6.

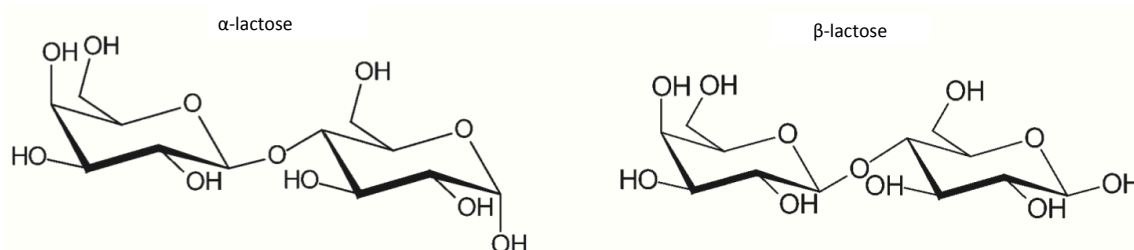


Figure 4.21 and conformations of lactose

Lactose exists partially as an open-chain form. The aldehyde group can form a hemi-acetal and, thus, a ring structure. The formation of a hemi-acetal creates a new chiral center (asymmetric carbon) that may exist as two isomers, α or β . By alternatively opening and forming the ring structure, the molecule can interchange between α and β anomers, a process referred to mutarotation. This process can occur easily in solution but also in the solid state (Lefort et al. 2006; Garnier et al. 2008).

Lactose is often used as excipient in pharmaceutical and enters in many food formulations notably in its amorphous state. Crystallization of amorphous lactose in dairy powders and in ice cream during storage is one of the principal causes of loss of product quality. Water

sorption by whey powders causes plasticization and subsequent hardening of the material owing to lactose crystallization. Crystallization during the storage is often detrimental to food quality and is a major cause of structural changes occurring in bread and other bakery products during storage. The proper control of amorphous solids is thus one of the key factors to maintain stability of food products. (Roos 1995)

Amorphous lactose may crystallize in a complex manner in a number of crystalline forms (see Table 4.6) depending on the relative humidity (RH), water content in the amorphous and temperature. It should be mentioned that several α/β defined molecular compounds are reported in literature (Earl and Parrish 1983) although crystal structures were not resolved. The amorphous lactose is in a non-equilibrium state with a high level of supercooling and a large driving force towards the crystalline state (*i.e.* the equilibrium). Lactose recrystallization is a glass transition-related and time-dependent phenomenon governed by the mobility of lactose molecules. Molecules in the glassy solid are not able to change their spatial arrangement to crystallize. At temperatures and water contents exceeding the critical values for the glass transition, molecular mobility increases rapidly and results in lactose crystallization. Thus, the crystal form obtained depends on temperature and water content. (Haque and Roos 2005).

CCDC code	α -lactose			β -lactose	α -lactose: β -lactose
	EYOCUQ	EYOCUQ01	LACTOS11	BLACTO02	LAKKEO
Reference	(Platteau et al. 2005)	(Platteau et al. 2004)	(Smith et al. 2005)	(Garnier et al. 2002)	(Lefebvre et al. 2005)
Form	α -stable	α -metastable	α -monohydrate	β -stable	1:1 compound
System	Monoclinic	Triclinic	Monoclinic	Monoclinic	Triclinic
Space Group	$P2_1$	$P1$	$P2_1$	$P2_1$	$P1$
a (Å)	7.7795	7.65217	4.7830	4.9325	7.6258(4)
b (Å)	19.6909	19.8337	21.540	13.2700(11)	19.6559(10)
c (Å)	4.90643	4.98773	7.7599	10.7792(9)	5.0613(3)
β (°)	103.6909(15)	106.2610(7)	105.911(2)	91.554(4)	105.430(2)
Volume (Å ³)	730.32	720.178	768.841	705.285	721.008
Z, Z'	2, 1	2, 2	2, 1	2, 1	2, 2
Density	1.557	1.579	1.556	1.612	1.577
R-Factor (%)	6.57	5.55	3.32	5.8	3.04

Table 4.6 Crystallographic data of the α -lactose and β -lactose

In the dairy industry, the degree of crystallization is often used as a measure of the potential of a lactose powder to cake (Schuck and Dolivet 2002). The T_g of dry amorphous lactose is 101 °C (Lloyd et al. 1996). It should be notice that the T_g decreases with the content of water in the sample. For instance, the T_g falls at circa 40°C for an amorphous sample containing

5%wt. of water because its plasticization effect decreases the T_g . In other terms, a higher water content causes lactose crystallization at a lower temperature. (Roos and Karel 1991; Roos 2009)

It has also been shown by Herrington (Herrington 1934) that lactose glasses were “kinetically stable” at room temperature if they were protected from water. For instance, lactose glasses containing low water contents may be kept in a desiccator for “indefinite periods” without crystallization. Once exposed to air, the glass takes up water until the crystallization begins (Herrington 1934). The lactose in dairy products is often present in the glassy state and its crystallization during storage at high humidity has been confirmed in numerous studies. These studies have used polarized light microscopy, electron microscopy, differential scanning calorimetry (DSC), nuclear magnetic resonance (NMR) and X-ray techniques to analyze the physical state of lactose in dairy powders (Earl and Parrish 1983; LAI and SCHMIDT 1990; Roos and Karel 1990; Aguilar and Ziegler 1994; Jouppila et al. 1998; Haque and Roos 2005). The potential of the SHG technique in the detection of crystalline particles in amorphous matrices has already been investigated (Lee et al. 2007). Although, monitoring of crystallization from amorphous solids has already been achieved by SHGM (Wanapun et al. 2010), it has never been achieved using a K&P apparatus.

In the following the effect of low energy milling on the dehydration of lactose is firstly investigated. Secondly, a high energy milling is used in order to amorphize the sample. The study of the recrystallization under various relative humidity is then studied by SHG.

3.2 Solid-state amorphization of lactose²²

Various ways exist to obtain amorphous solids. Generally rapid undercooling of molten crystals leads to the amorphous state (Ediger et al. 1996). However, in the case of lactose it cannot be done due to the possible mutarotation in the solid-state (at high temperature) and in the molten state (Garnier et al. 2002). Other pathways for solid state amorphization exist which do not require the melt of the crystal (Angell 1995) such as milling (Willart et al. 2001) or dehydration (Willart et al. 2008).

The (G,T) diagram plotted Figure 4.22 represents the two kind of pathways that milling can induce (out of equilibrium). Firstly, mechanical milling can cause structural changes in a stable initial crystal phase (crystal 1) and a transformation into a metastable crystalline phase

²² More details on the theory are available in the review on « Solid State amorphization of pharmaceuticals » (Willart and Descamps 2008)

(crystal 2). This polymorphic transformation that typically occurs when milling is carried out at a temperature above the glass transition temperature of the corresponding liquid. In this case molecules have enough energy to reorganize themselves and form another polymorph. On the other hand, the milling may also cause changes to the amorphous. Amorphization of a material is generally observed when the milling is carried out at a temperature below the glass transition temperature of the corresponding liquid. This is particularly true for lactose (Willart et al. 2004) and trehalose (Willart et al. 2006).

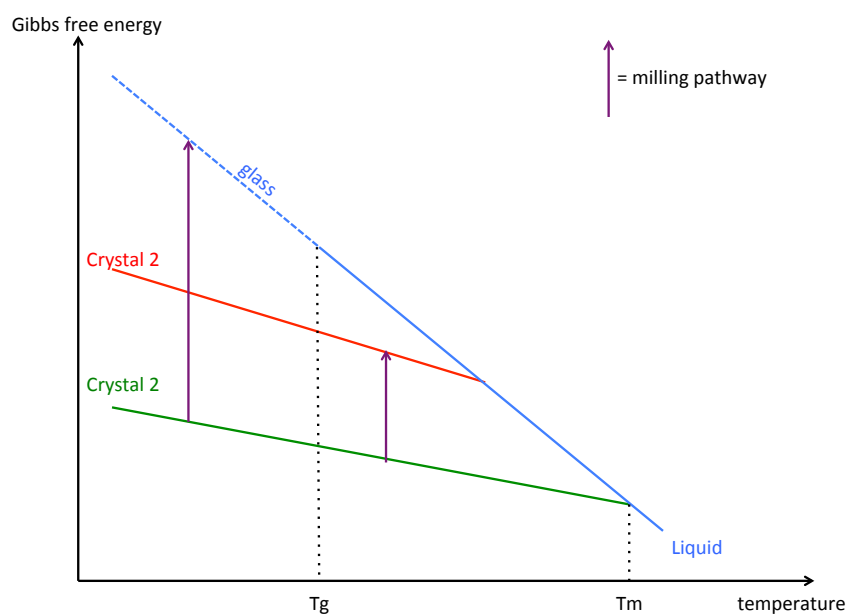


Figure 4.22 G,T diagram of two polymorphs and the liquid phase of a molecule. The different pathways encountered for milling above and below T_g are depicted by purple arrows. The possible existing rearrangement above T_g leads often to the formation of polymorphic form. Note that milling is an out of equilibrium process.

3.2.1 Size reduction by milling and its effect on the SHG signal.

Milling of 200mg of α -lactose monohydrate was performed using a Retsch apparatus (details in Appendix II). Milling time of 16 and 32 minute at a frequency of 3Hz was used. Samples are hereafter denotes M16 and M32, respectively and M0 for the α -lactose monohydrate.

This kind of milling is relatively smooth and can be compared to a gentle manual grinding of the sample. Nevertheless, it is sufficient to modify the crystal size distribution as shown by XRPD (Figure 4.23) and laser granulometry (Figure 4.24). A sharp decrease of the XRPD peak intensities and an increase of the peak widths are visible on the M32 diffractogram compare to the M0 sample. This is correlated to the reduction of the crystal size and it is confirmed by laser granulometry (see Figure 4.24).

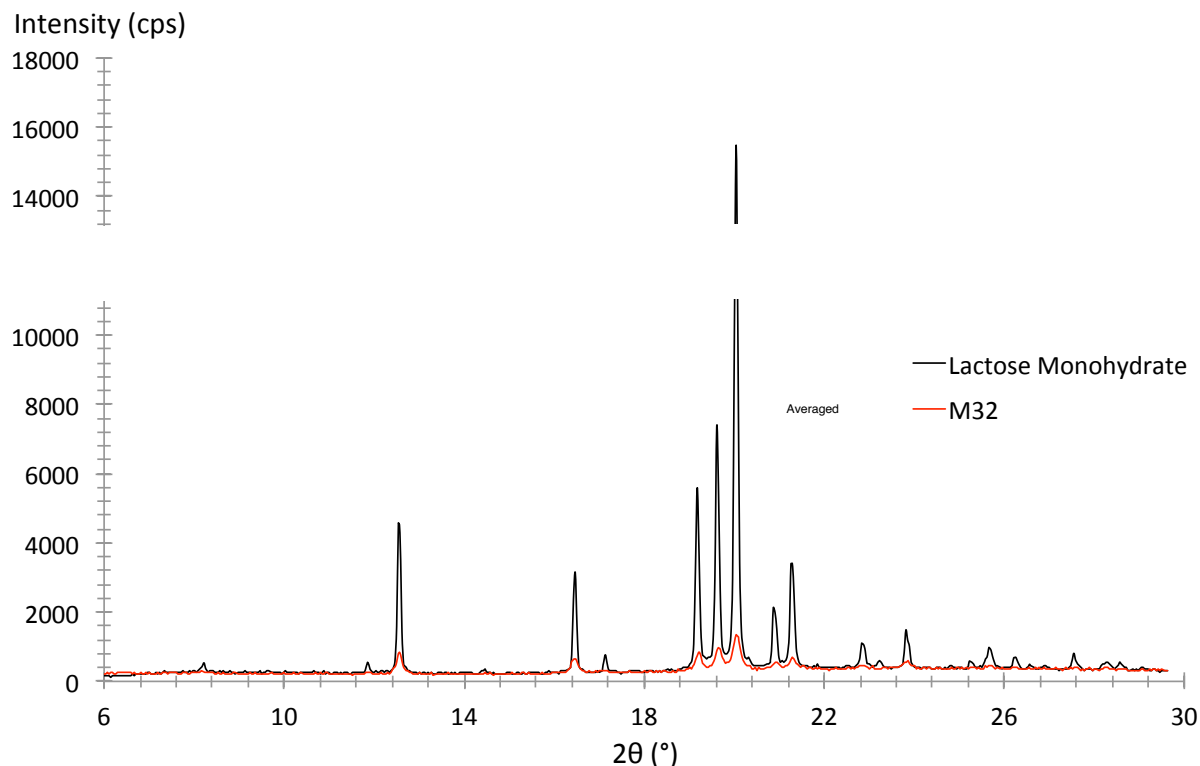


Figure 4.23 M32 and the calculated monohydrate XRPD patterns. A milling of 32 min at 3Hz leads to the

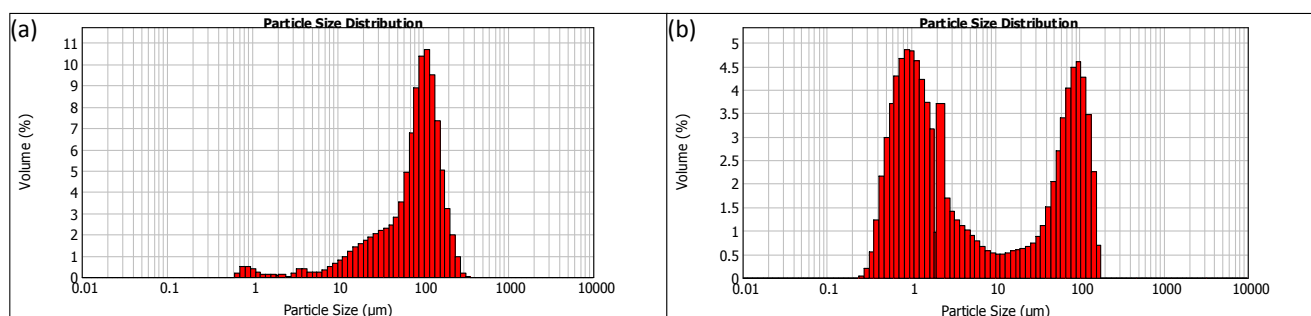


Figure 4.24 M0 (a) and M32 (b) PSD obtained from laser granulometry experiments. The crystal size is decreased for the milled sample.

Influence of milling on lactose has been well described in the literature (Garnier et al. 2002; 2008). For instance, the onset temperature of the dehydration peak in DSC analyses is strongly affected with a marked decrease of the temperature. The dehydration peak (around 150°C for an analysis at 5K/min) also exhibits a double event more pronounced for higher milling time. DSC chart of M0, M16 and M32 sample are plotted Figure 4.25. Results are in good agreement with Garnier et al. works. The exothermic peak around 155°C corresponds to the recrystallization (after dehydration) toward the anhydrous lactose. It should be noticed that no difference is visible on the DSC charts for M16 and M32 samples. For the dehydration peak, the onset temperature decreases and the visible shoulder is more pronounced, as expected, for a milled sample (Garnier et al. 2008).

Several dehydration pathways exist and are impacted by a smaller particle size distribution and by the formation of surface defects (or high energy surfaces).

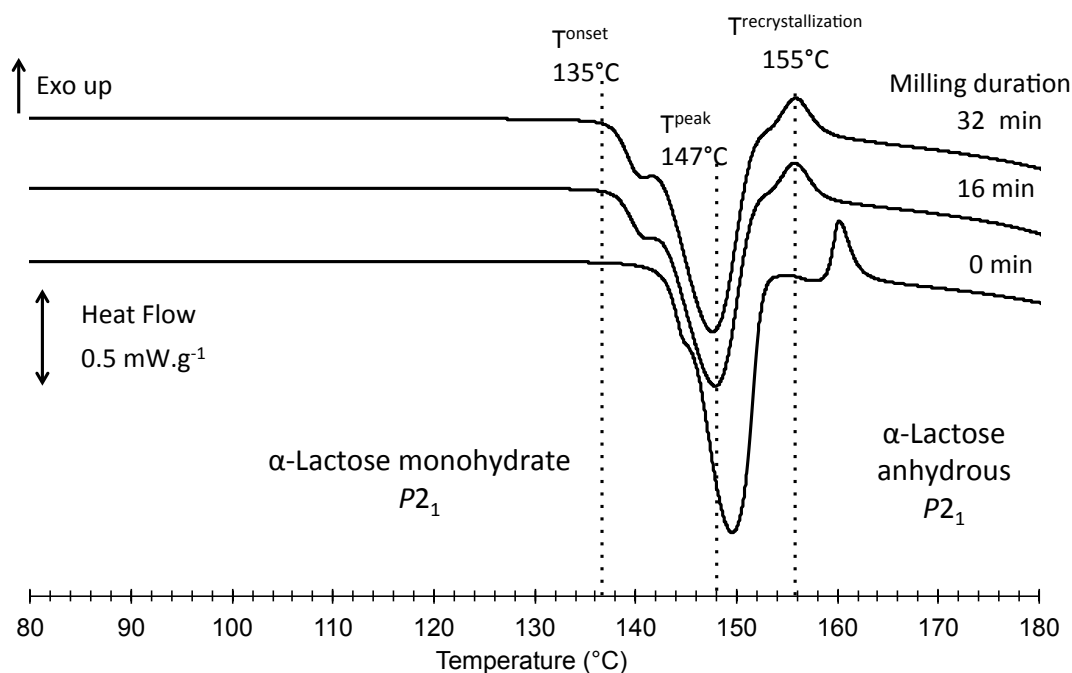


Figure 4.25 DSC of M0, M16 and M32 sample. Results are in good agreement with Garnier et al. works

TR-SHG was performed on the same samples and with the same conditions used for DSC. The evolution of the SHG signal (plotted Figure 4.26) for the 3 samples is similar:

- (1) the signal remains stable up to circa 50°C
- (2) then, it increases slightly and continuously with temperature.
- (3) around 147°C for M16 and M32 a sharp increase of the SHG signal is detected.

Results can be compared with DSC results and are in good agreement. For instance the temperatures of the disruption on the SHG curves correspond to the temperature of the dehydration peaks detected by DSC. Nevertheless, one can notice that the onset temperature is detected before (at circa 50°C) by SHG where the signal begins to increase. It highlights the sensitivity of the technique in the dehydration detection. Moreover, the TR-SHG curve of the M16, M32 sample differ from their DSC charts with an increase more marked of the SHG signal for the M32. It denotes that more particles underwent dehydration during the heating than in the M16 or M0 sample. This is due to a lower crystal size distribution in the M32 sample with consequently smaller particles that are preferentially dehydrated.

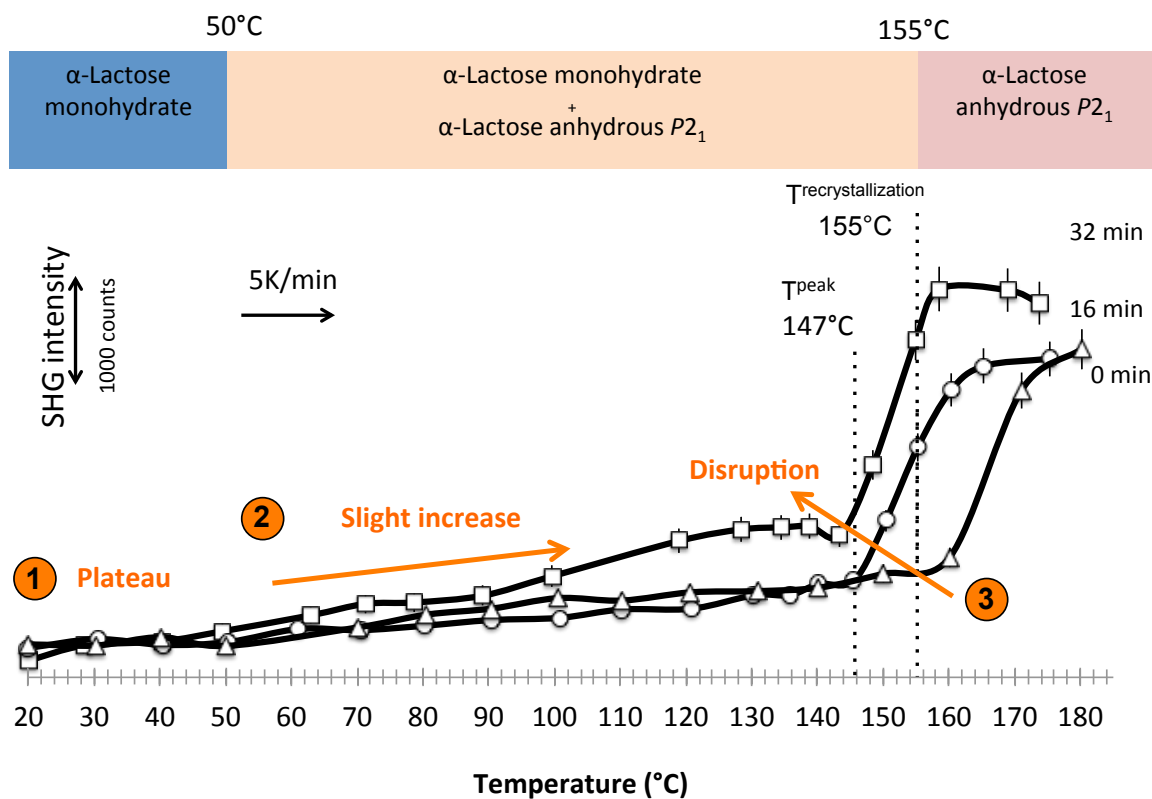


Figure 4.26 TR-SHG curves for M0, M16 and M32 samples

3.2.2 Complete amorphization

XRPD diffractograms of the product before and after 90 minutes of milling at a frequency of 30Hz (hereafter denotes M90 sample) are plotted Figure 4.27. No diffraction peak is detectable on the M90 diffractogram that clearly demonstrates that 90 min of milling leads to an amorphization of the α -lactose monohydrate. Moreover, contrary to the α -lactose monohydrate, the M90 sample exhibits no SHG signal that is attributed to a sample completely amorphized.

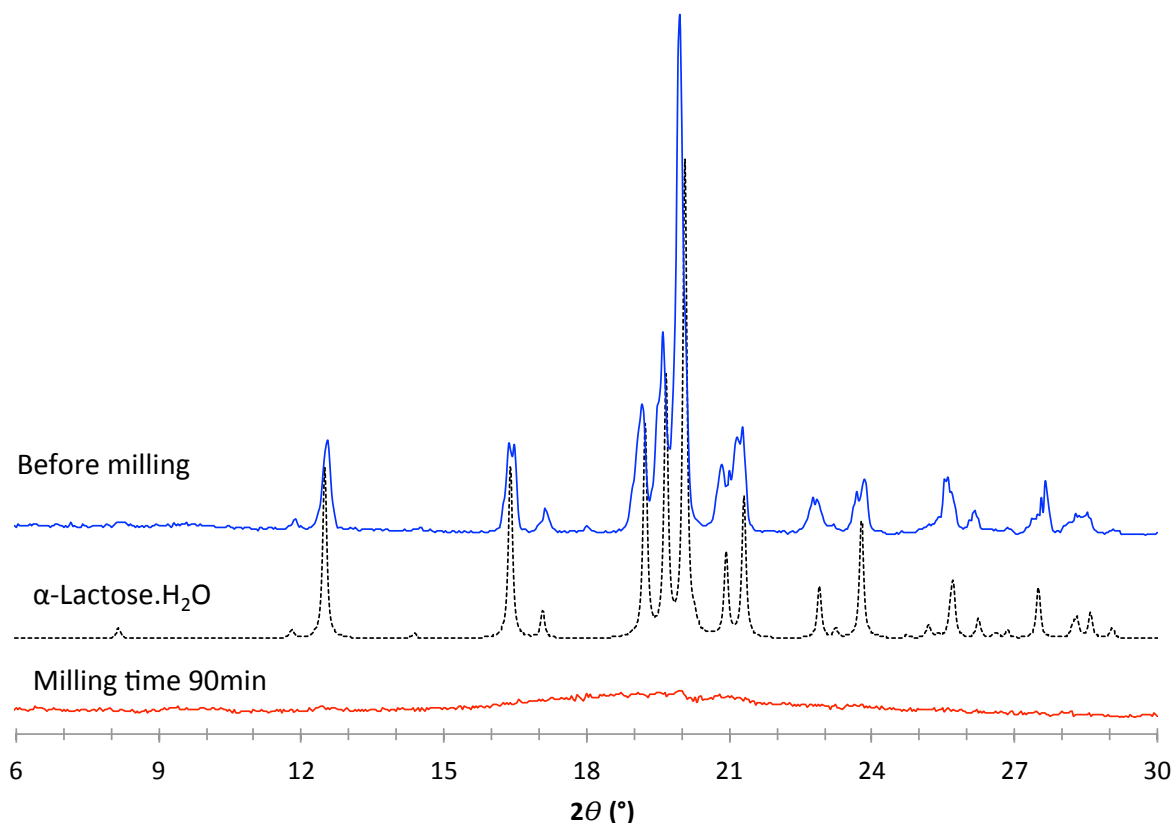


Figure 4.27 XRPD of the α -lactose before milling (blue) and after 90min of milling (red). The dash pattern is calculated from the CCDC structure.

3.3 Crystallization monitoring by SHG under various RH

Just after, the evolution of the milled sample M90 is monitored by SHG under normal condition (circa 25°C and 40%RH). The evolution of SHG signal versus time is plotted Figure 4.28. After 5 minutes a positive SHG signal is detected. The experiment was stopped in order to check the crystal phase. The XRPD pattern of the M90 sample (exhibiting a positive SHG signal) corresponds to the monohydrate phase. No other phase has been detected by means of XRPD.

The behavior of the M90 sample is reproducible. In a similar experiment (SHG curve is plotted Figure 4.29), a SHG signal is detected only 15 minutes after the storage of the sample at 25°C and 40%RH. The SHG signal continues to increase and finally reaches a maximum after circa 1400 min. The evolution of the SHG signal versus time exhibits the classical “S” shape of a recrystallization process. The end product is the α -lactose monohydrate.

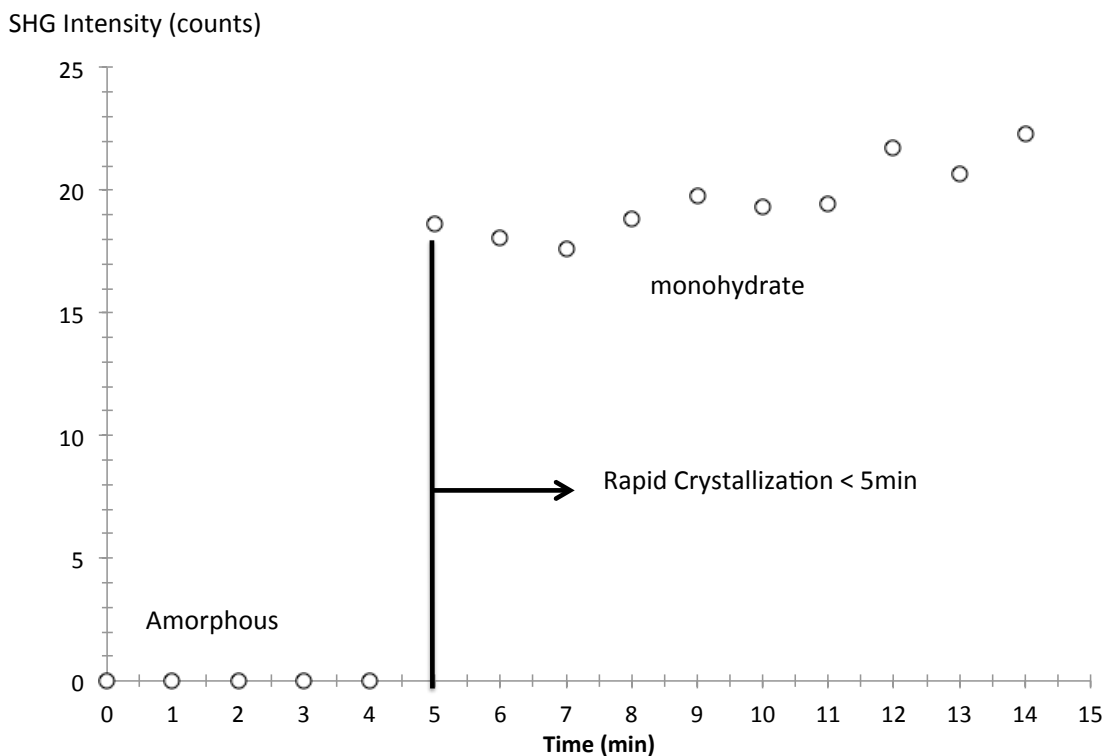


Figure 4.28 SHG monitoring the crystallization of amorphous lactose at 25°C and 40% RH – 1st Experiment

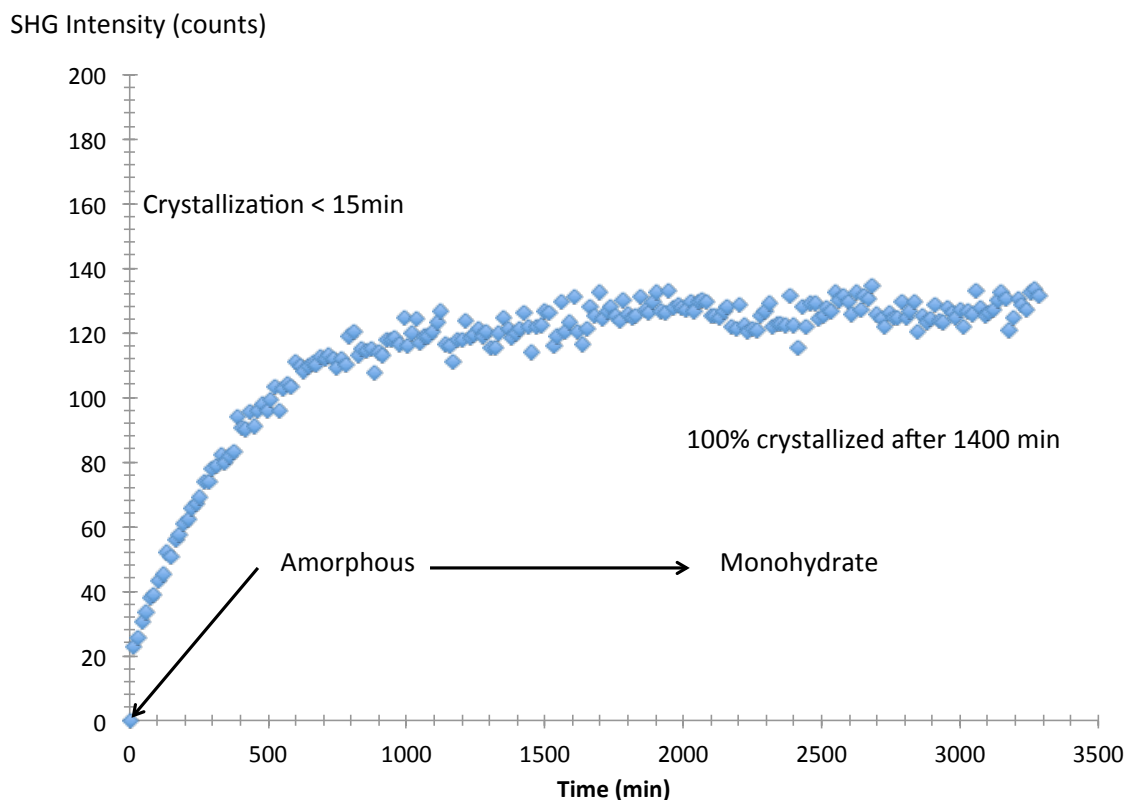


Figure 4.29 SHG monitoring of amorphous lactose at 25°C and 40% RH. The crystallization is completed after circa 1400 min- 2nd Experiment

Amorphous sample can be stabilized for relative long period of time in dry condition. For instance, amorphous lactose was kept 1845 minutes at 25°C in dry atmosphere without detected crystallization by means of SHG. A similar experiment was reproduced and is plotted Figure 4.30. For amorphous lactose, kept at 0%RH during 1345 minutes, no crystallization occurred. Only 15 minutes after an increase of the RH at 40%, a positive SHG signal is detected meaning that NC crystals are presents in the sample. The resulting crystal form is the α -lactose monohydrate. These results are in good agreement with observation of Herrington (Herrington 1934).

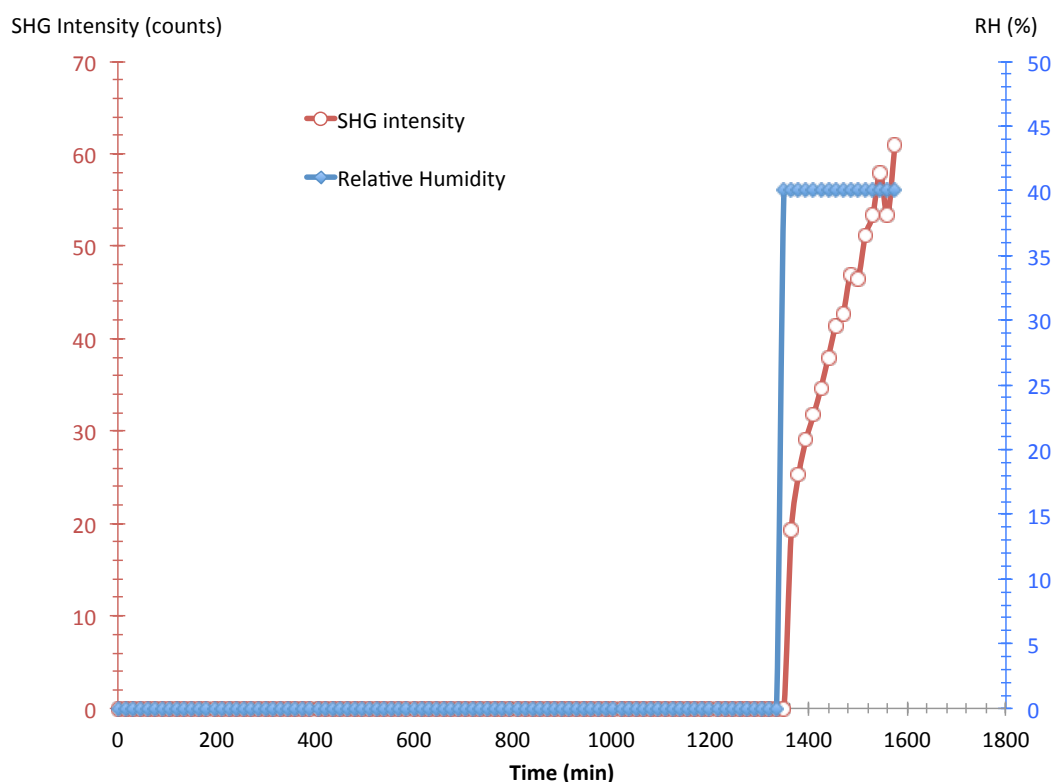


Figure 4.30 SHG monitoring of amorphous lactose at 25°C in dry condition and then with 40%RH. No crystallization occurs at 0%RH but crystallization toward the form is detected only 15 minutes after an increase of the RH at 40%.

Part.4 Conclusion

Through the investigation of the formic acid/ water binary phase diagram, the TR-SHG technique is promising and useful for the rapid determination of phase domains boundaries. Moreover, its sensitivity is a major asset to determine accurately the liquidus temperature. In addition the binary selectivity (the liquid does not give SHG signal contrary to the crystal) provides an unambiguous visualization of the liquidus line.

The first experiments under various relative humidity monitored by SHG demonstrate the possibility to extend the use of the SHG method to desolvation studies or recrystallization from amorphous solids. However, some inconsistencies observed in the SHG signal evolution are a sign of complex mechanisms and further investigation are needed to fully understand these processes.

These three examples demonstrate the versatility of the SHG technique. Nevertheless, it should be notice that only the non-centrosymmetry of the compounds is detected; the SHG signal does not bring in itself information on the crystal structure. Although it is sometimes possible to differentiate two forms by their SHG intensities (e.g. the anhydrous and dihydrate $\text{Sr}(\text{HCOO})_2$ phases), a XRPD experiment is, nonetheless, necessary to ensure the nature of the phase. In the next chapter, the first prototyping attempts of an X-Ray diffractometer are presented.

References

- Aguilar CA, Ziegler GR. Physical and Microscopic Characterization of Dry Whole Milk with Altered Lactose Content. 2. Effect of Lactose Crystallization. *Journal of Dairy Science*. 1994 May;77(5):1198–204.
- Albinati A, Rouse KD, Thomas MW. Neutron powder diffraction analysis of hydrogen-bonded solids. II. Structural study of formic acid at 4.5 K. *Acta Crystallogr B Struct Crystallogr Cryst Chem*. 1978 Jul 15;34(7):2188–90.
- Allan DR, Clark SJ. Impeded dimer formation in the high-pressure crystal structure of formic acid. *Physical Review Letters*. APS; 1999;82(17):3464.
- Angell CA. Formation of glasses from liquids and biopolymers. *Science*. 1995 Mar 31;267(5206):1924–35.
- Bartels-Rausch T, Bergeron V, Cartwright JHE, Scribing R, Finney JL, Grothe H, et al. Ice structures, patterns, and processes: A view across the icefields. *Rev. Mod. Phys*. 2012 May;84(2):885–944.
- Bayarjargal L, Wiehl L, Winkler B. Influence of grain size, surface energy, and deviatoric stress on the pressure-induced phase transition of ZnO and AlN. *High Pressure Research*. 2013 Aug 20;33(3):642–51.
- Bayarjargal L, Winkler B. High (pressure, temperature) phase diagrams of ZnO and AlN from second harmonic generation measurements. *APPLIED PHYSICS LETTERS*. AIP Publishing; 2012;100(2):021909.
- Bayarjargal L, Winkler B, Haussühl E, Boehler R. Influence of deviatoric stress on the pressure-induced structural phase transition of ZnO studied by optical second harmonic generation measurements. *APPLIED PHYSICS LETTERS*. AIP Publishing; 2009;95(6):061907.
- Bernstein J. *Polymorphism in molecular crystals*. Clarendon Press/International Union of Crystallography; 2002.
- Boechat-Roberty HM, Pilling S, Santos ACF. Destruction of formic acid by soft X-rays in star-forming regions. *A&A*. 2005 Aug;438(3):915–22.
- Comel C, Mentzen BF. Comparative study of the polymorphic species of strontium and calcium formates. I. Differential thermal analysis (DTA). *Journal of Solid State Chemistry*. 1974 Mar;9(3):210–3.

- Coolidge AS. THE VAPOR PRESSURE AND HEATS OF FUSION AND VAPORIZATION OF FORMIC ACID. *J. Am. Chem. Soc.* 1930 May;52(5):1874–87.
- Coquerel G, Sanselme M, Lafontaine A. Method of measuring scattering of x-rays, its applications and implementation device. *google.com*. 2014 Jul 3.
- Domalski ES, Hearing ED. Heat capacities and entropies of organic compounds in the condensed phase. Volume III. *J. Phys. Chem. Ref. Data*. AIP Publishing; 1996;25(1):1–525.
- Dreisbach RR, Martin RA. Physical Data on Some Organic Compounds. *Ind. Eng. Chem.* 1949 Dec;41(12):2875–8.
- Earl WL, Parrish FW. A cross-polarization—magic-angle sample spinning n.m.r. study of several crystal forms of lactose. *Carbohydrate Research*. 1983 Apr;115:23–32.
- Ediger MD, Angell CA, Nagel SR. Supercooled Liquids and Glasses. *The Journal of Physical Chemistry*. 1996 Jan;100(31):13200–12.
- Galigné JL. Affinement de la structure cristalline du formiate de strontium dihydraté, Sr(HCOO)₂·2H₂O. *Acta Crystallogr B Struct Crystallogr Cryst Chem. International Union of Crystallography*; 1971 Dec 15;27(12):2429–31.
- Garnier S, Petit S, Coquerel G. Dehydration mechanism and crystallisation behaviour of lactose. *Journal of Thermal Analysis and Calorimetry*. Akadémiai Kiadó, co-published with Springer Science+ Business Media BV, Formerly Kluwer Academic Publishers BV; 2002;68(2):489–502.
- Garnier S, Petit S, Mallet F, Petit MN, Lemarchand D, Coste S, et al. Influence of ageing, grinding and preheating on the thermal behaviour of α -lactose monohydrate. *International Journal of Pharmaceutics*. 2008 Sep;361(1-2):131–40.
- Grip J, Samuelsen EJ. Raman Spectroscopic Search for Phase Transition in Solid Formic Acid, and Lattice Dynamics. *Phys. Scr.* IOP Publishing; 1981 Dec 22;24(1A):52–6.
- Haque MK, Roos YH. Crystallization and X-ray diffraction of spray-dried and freeze-dried amorphous lactose. *Carbohydrate Research*. 2005 Feb 7;340(2):293–301.
- Herrington BL. Some Physico-Chemical Properties of Lactose. *Journal of Dairy Science*. 1934 Jul;17(7):501–18.
- Hirata S. Fast electron-correlation methods for molecular crystals: An application to the α , β [sub 1], and β [sub 2] modifications of solid formic acid. *J. Chem. Phys.* 2008;129(20):204104.
- Holtzberg FV, Post B, Fankuchen I. The crystal structure of formic acid. *Acta Cryst. International Union of Crystallography*; 1953;6(2):127–30.
- Jakobsen RJ, Mikawa Y, Brasch JW. Far infrared studies of hydrogen bonding in carboxylic acids—I formic and acetic acids. *Spectrochimica Acta Part A: Molecular Spectroscopy*. 1967 Jul;23(7):2199–209.
- Jouppila K, Kansikas J, Roos YH. Crystallization and X-ray diffraction of crystals formed in water-plasticized amorphous lactose. *Biotechnol. Prog.* 1998 Mar;14(2):347–50.
- Kohler F, Atrops H, Kalali H, Liebermann E, Wilhelm E, Ratkovics F, et al. Molecular interactions in mixtures of carboxylic acids with amines. 1. Melting curves and viscosities. *The Journal of Physical Chemistry*. American Chemical Society; 1981 Aug;85(17):2520–4.
- Kurtz SK, Perry TT. A Powder Technique for the Evaluation of Nonlinear Optical Materials. *J. Appl. Phys.* AIP; 1968;39(8):3798–813.
- LAI H-M, SCHMIDT SJ. Lactose Crystallization in Skim Milk Powder Observed by Hydrodynamic Equilibria,

- Scanning Electron Microscopy and ²H Nuclear Magnetic Resonance. *J Food Science*. 1990 Jul;55(4):994–9.
- LeCaptain DJ, Berglund KA. The applicability of second harmonic generation for in situ measurement of induction time of selected crystallization systems. *Journal of Crystal Growth*. 1999 May 24;203:564–9.
- Lee CJ, Strachan CJ, Manson PJ, Rades T. Characterization of the bulk properties of pharmaceutical solids using nonlinear optics - a review. *Journal of Pharmacy and Pharmacology*. 2007 Feb;59(2):241–50.
- Lefebvre J, Willart J-F, Caron V, Lefort R, Affouard F, Danède F. Structure determination of the 1/1 α/β mixed lactose by X-ray powder diffraction. *Acta Crystallogr B Struct Sci. International Union of Crystallography*; 2005 Jul 19;61(4):455–63.
- Lefort R, Caron V, Willart J-F, Descamps M. Mutarotational kinetics and glass transition of lactose. *Solid State Communications. Elsevier*; 2006;140(7):329–34.
- Lide D. *CRC Handbook of Chemistry and Physics*-Editorial Board. 2006 May 8;:1–2317.
- Lloyd RJ, Dong Chen X, Hargreaves JB. Glass transition and caking of spray-dried lactose. *Int J Food Sci Tech*. 1996 Aug;31(4):305–11.
- Mentzen BF, Comel C. Comparative study of the polymorphic species of strontium and calcium formates. II. X-Ray diffraction. *Journal of Solid State Chemistry*. 1974 Mar;9(3):214–23.
- Mikawa Y. Infrared Evidence of Polymorphism in Formic Acid Crystals. *J. Chem. Phys*. 1966;45(12):4750.
- Mikawa Y, Brasch JW, Jakobsen RJ. Infrared spectra and normal coordinate calculation of crystalline formic acid. *Journal of Molecular Spectroscopy*. 1967 Jan;24(1-4):314–29.
- Millikan RC, Pitzer KS. The Infrared Spectra of Dimeric and Crystalline Formic Acid. *J. Am. Chem. Soc. American Chemical Society*; 1958 Jul;80(14):3515–21.
- Nahrngbauer I. A reinvestigation of the structure of formic acid (at 98 K). *Acta Crystallogr B Struct Sci. International Union of Crystallography*; 1978 Jan;34(1):315–8.
- Platteau C, Lefebvre J, Affouard F, Derollez P. Ab initio structure determination of the hygroscopic anhydrous form of α -lactose by powder X-ray diffraction. *Acta Crystallogr B Struct Sci*. 2004 Jul 19;60(4):453–60.
- Platteau C, Lefebvre J, Affouard F, Willart J-F, Derollez P, Mallet F. Structure determination of the stable anhydrous phase of α -lactose from X-ray powder diffraction. *Acta Crystallogr B Struct Sci. International Union of Crystallography*; 2005 Mar 16;61(2):185–91.
- Reutemann W, Kieczka H. Formic acid. *Ullmann's Encyclopedia of Industrial Chemistry. Wiley Online Library*; 1996.
- Richardson JH. *Systematic Materials Analysis*. Elsevier; 1978.
- Robertson GN, Lawrence MC. Do protons tunnel in the formic acid dimer and in the crystal? *Chemical Physics*. 1981 Nov;62(1-2):131–44.
- Roos. *phase transitions in foods*. Academic Press; 1995.
- Roos Y, Karel M. Differential scanning calorimetry study of phase transitions affecting the quality of dehydrated materials. *Biotechnol. Prog*. 1990 Mar;6(2):159–63.
- Roos Y, Karel M. Plasticizing Effect of Water on Thermal Behavior and Crystallization of Amorphous Food Models. *J Food Science*. 1991 Jan;56(1):38–43.
- Roos YH. *Solid and Liquid States of Lactose*. New York, NY: Springer New York; 2009. pp. 17–33.

- Schmeißer M, Schuster J. Decomposition of formic acid. arXiv preprint arXiv:1108.5891. 2011.
- Schuck P, Dolivet A. Lactose crystallization: determination of α -lactose monohydrate in spray-dried dairy products. *Lait*. EDP Sciences; 2002;82(4):413–21.
- Schulze WA. dielectric properties of lead-zirconate - lead-titanate - lanthanum-oxide. proquest, umi dissertations publishing; 1973.
- Smith JH, Dann SE, Elsegood MRJ, Dale SH, Blatchford CG. α -Lactose monohydrate: a redetermination at 150 K. *Acta Crystallogr Sect E Struct Rep Online*. International Union of Crystallography; 2005 Aug 1;61(8):2499–501.
- Stähl K, Andersen JET, Shim I, Christgau S. Structures of strontium diformate and strontium fumarate. A synchrotron powder diffraction study. *Acta Crystallogr B Struct Sci*. 2009 Jul 16;65(4):481–7.
- Stout JW, Fisher LH. The Entropy of Formic Acid. The Heat Capacity from 15 to 300°K. Heats of Fusion and Vaporization. *J. Chem. Phys.* 1941;9(2):163.
- Timmermans J. The Physico-chemical Constants of Binary Systems in Concentrated Solutions, Volume 4: Systems with Inorganic+Organic Or Inorganic Compounds. 1960.
- Wanapun D, Kestur US, Kissick DJ, Simpson GJ, Taylor LS. Selective Detection and Quantitation of Organic Molecule Crystallization by Second Harmonic Generation Microscopy. *Anal. Chem. American Chemical Society*; 2010 Jul;82(13):5425–32.
- Watanabé T, Matsui M. A redetermination of the crystal structures of α -calcium formate, α -strontium formate and barium formate by X-ray analyses. *Acta Crystallogr B Struct Crystallogr Cryst Chem*. 1978 Sep 15;34(9):2731–6.
- Willart JF, Caron V, Lefort R, Danède F, Prévost D, Descamps M. Athermal character of the solid state amorphization of lactose induced by ball milling. *Solid State Communications*. 2004 Dec;132(10):693–6.
- Willart JF, De Gussemé A, Hemon S, Odou G, Danède F, Descamps M. Direct crystal to glass transformation of trehalose induced by ball milling. *Solid State Communications*. Elsevier; 2001;119(8):501–5.
- Willart JF, Descamps M. Solid State Amorphization of Pharmaceuticals. *Mol. Pharmaceutics*. American Chemical Society; 2008 Dec;5(6):905–20.
- Willart JF, Descamps M, Caron V. Direct crystal to glass transformations of trehalose induced by milling, dehydration and annealing. *AIP Publishing*; 2008;982(1):108–13.
- Willart JF, Hédoux A, Guinet Y, Danède F, Paccou L, Capet F, et al. Metastability release of the form α of trehalose by isothermal solid state vitrification. *J. Phys. Chem. B*. 2006 Jun 15;110(23):11040–3.
- Zelmann HR, Bellon F, Marechal Y, Bullemer B. Polymorphism in crystalline formic acid. *Chemical Physics Letters*. Elsevier; 1970;6(5):513–5.
- Zheligovskaya EA, Malenkov GG. Crystalline water ices. *Russ. Chem. Rev.* 2007 Oct 17;75(1):57–76.

Chapter 5. DIXCUR Project

This chapter is devoted to the first attempts of the prototyping of a diffractometer in order to monitor precipitation processes in organic chemistry. It should be notice that this work represents only a small part of this thesis and, consequently, is not intended to be complete.

Part.1 Introduction

In chemistry, it is estimated that 70% of sold products are solids. Most of the chemical processes are carried out in the liquid phase from the laboratory to large-scale industrial production. It is especially the case for the production or purification of crystallized products that must be obtained by nucleation and growth from solution. The final crystal structure can considerably vary within the conditions under which crystallization is performed such as temperature, heating/cooling rate, pressure, solvent, concentrations, pH, mixing rate, etc. It could be problematic in pharmaceutical industry as many APIs are commercialized as crystallized products. Indeed, polymorphs have specific physicochemical properties such as dissolution rate, solubility and bioavailability. In order to achieve the required crystal properties and to ensure reproducibility, crystallization must be controlled. Thus, there is a need for a method that can monitor crystallization from its early step. In most cases, the monitoring is based on off-line characterization that suffers many limitations. Sample preparation (extracting, filtering, washing and drying) is the key reason and thus can't provide real-time information. Moreover, some phases may only exist *in-situ* because they are only stable in solvent or can react with the air. Furthermore, off-line measurements may required special precautions when an operator must manipulate APIs or toxic materials. In-line monitoring overcomes these limitations. Several in-line technics exist such as Raman spectroscopy, ATR-FTIR, refractometry, imaging, *etc.* but the usual method for the analysis of crystal structure and crystallization processed is X-ray diffraction. The increase of the detector sensitivity and X-ray sources power make feasible to prototype an X-Ray laboratory diffractometer for *in-situ* monitoring of fast crystallization (i.e. precipitation). Such device could provide valuable real-time information on crystallization processes and could reveal the crystallization of new phases or new transient phases. Herein, we present the possibilities of a prototype for *in-situ* monitoring through crystallization studies of molecular and inorganic materials.

Among the processes to obtain a crystalline material, the precipitation (*i.e.* the crystallization in very short time) is used from the laboratory to large-scale industrial production. The early

step of crystallization, that is to say the nucleation, remains largely unexplored, but it is clear that rationalization of nucleation would afford valuable insights in solid-state chemistry. The physicochemical properties of a crystal are closely related to the spatial arrangement of atoms or molecules. Understanding and controlling the crystallization is a necessary step in order to develop new materials or drugs. According to current theories, the formation of a crystal is divided into two main stages: nucleation (first step) and crystal growth (second step). It is easy to imagine the growth of a crystal in solution: atoms or molecules aggregate on a seed (nucleus) appeared in solution. It is less easy to understand how and why this first germ appears. For many years, experimental observations and theories have led to a steady increase in our understanding of the phenomena of nucleation-growth. However, questions remain about the processes and mechanisms involved in particular during the first stage. The stochastic nature of nucleation and the importance of purity in the experiments make interpretations difficult. The purpose, here is to contribute to the understanding of the kinetics and thermodynamics of nucleation in studying the formation of the first crystal resulting of nuclei in solution. Nevertheless, it is rather complex to study the precipitation process due to the extremely fast phenomena, such as nucleation (less than one second) involved. Hence, although many theories exist to describe nucleation (Erdemir et al. 2009; Vekilov 2010) no complete experimental validations were performed notably to determine the critical radius of stability.

Off-line characterization (requiring extraction, filtration, washing and drying) is obviously unsuitable in this context and may overlook some transient phase.

In-line monitoring could overcome these limitations. The usual method for phase identification is X-ray diffraction. For this purpose the development of an experimental device (based on X-ray diffraction) for in situ monitoring of the crystallization process (DIXCUR Project) was proposed. It was expected that due to the increase of detectors sensitivity and X-ray source power, an X-Ray laboratory diffractometer prototype should:

- (1) Detect the first crystal phase within the liquid
- (2) Track and monitor in all stages of the crystallization processes the induction times, the crystalline structure of appearing phases and their evolution versus time
- (3) Help to validate (or not) a number of theories and provide a better understanding of crystallization

- (4) Reveal the existence of unknown crystal structures (transient phases). These could have interested applications in many areas (materials, magnetism, drug development).

In the following, we report our first attempts to develop a device that corresponds to these demands.

Part.2 Principle

The principle of the prototype consists in mixing two solutions to precipitate a compound that passes in the measuring cell to be analyzed by X-ray diffraction. This principle is schematically represented Figure 5.1.

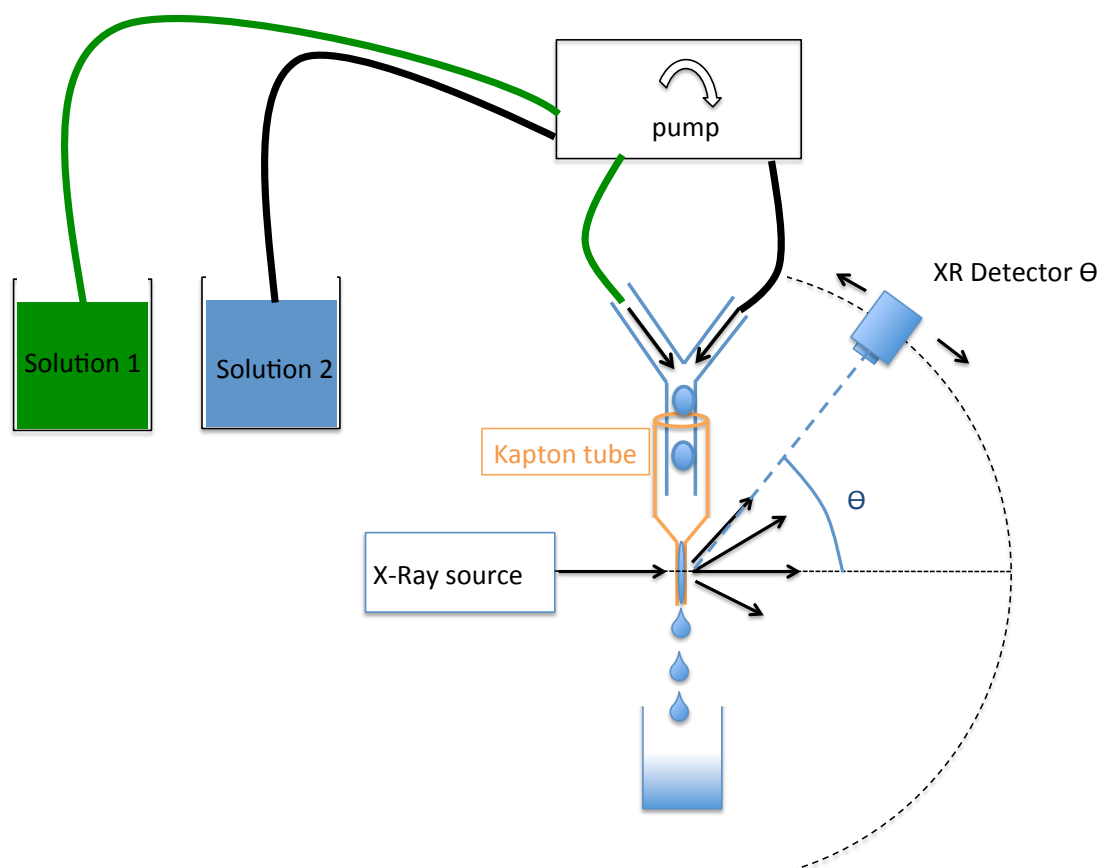


Figure 5.1 Schematic presentation of the DIXCUR prototype

A solution containing the molecules is adequately prepared (concentration, viscosity ...) to ensure its crystallization in the measuring cell. The cell is transparent with respect to the X-

rays used in this device. When adding the precipitating agent (the anti-solvent, a pH modifier, reactive...) the phenomenon of precipitation begins. Depending on the rate of introduction of the solutions into the system, it is thus possible to analyze the sample at different crystallization times. Indeed, the height z (corresponding to the distance from where the two solutions are mixed) is directly related to the reaction time (see Figure 5.2).

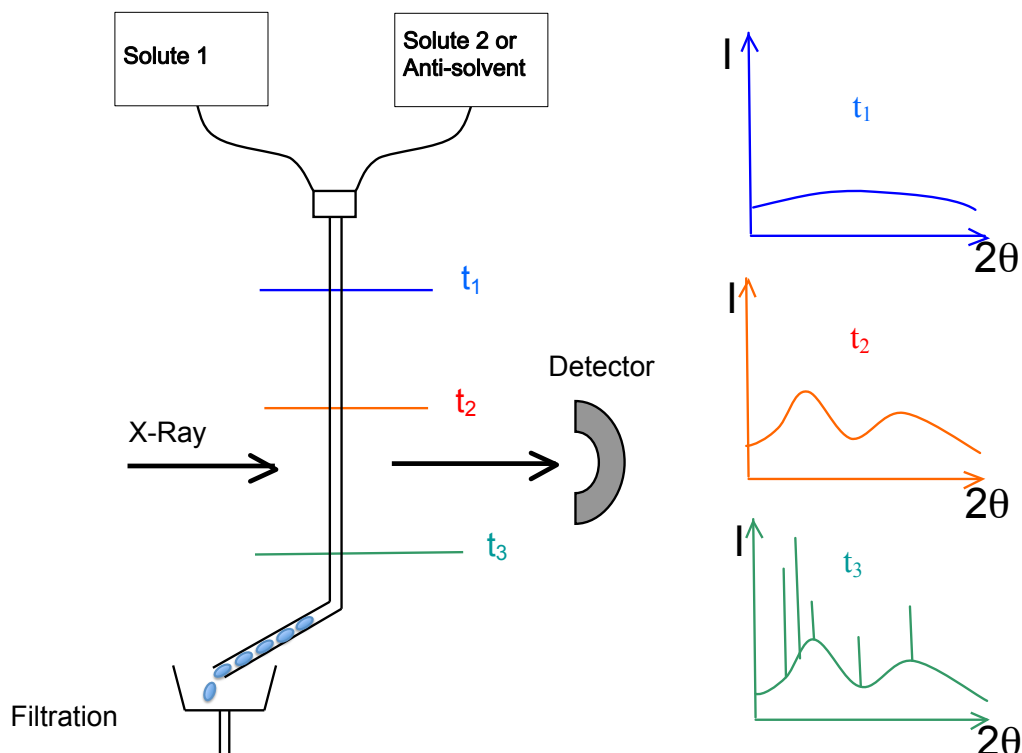


Figure 5.2 Correspondence between the distance z and the time.

This work was initially focused on the design of the mixing cell and the choice of the windows. It determines the optimal experimental conditions such as the concentration of reactants, the homogenization of solutions, the speed flow. This preliminary work is essential in order to begin the study the crystallization of compounds defined in the literature. A device for controlling the temperature of the solutions and homogenization of the mixture is placed upstream of the measure cell.

Part.3 X-ray source and beam shape

The anode produces X-rays is in Molybdenum. The radiation wavelength is 0.70930 \AA ($K\alpha_1$). Consequently, diffractograms are "compressed" in 2θ compare to other more usual anode

source (cobalt or copper). The advantage is clear for the acquisition time because of the 2θ space reduction, but it could be a drawback due to possible recovery of diffraction peaks.

This X-Ray source provides a high power 50 kV, 40 mA (2000W) with photon energy of 17.5 keV. A collimator (see Figure 5.3) can be used in order to reduce the effects of noise-induced diffusion of the liquid. However, tests have shown that the use of a slit of 1.2 mm (with a wider beam) lead to more intense detected intensities; therefore, in most cases this will be the geometry chosen.

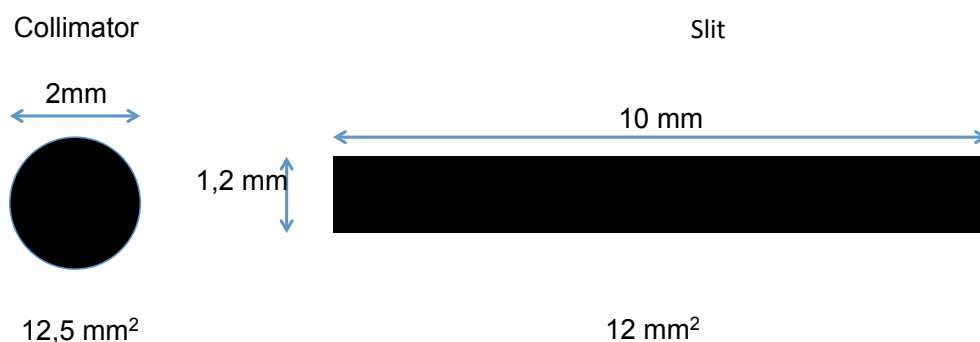


Figure 5.3 X-Ray beam shape and corresponding area of irradiation

Part.4 Measurement cell: the choice of Kapton

Two main key parameters must be taken into account in the choice of the cell window:

- (1) The resistance to the degradation. Generally it includes resistance to:
 - Chemical degradation by solvent or product formed during the process
 - Thermal degradation
 - X-Ray radiation

The cell must keep its integrity and exhibit a low thermal expansion and contraction, fragility, tearing and stretching.

- (2) The transmittance efficiency of the X-ray beam. The transparency of the window is an important point given that the transmission geometry of the device in addition to the presence of a solvent will cause absorption and scattering of a significant part of the incident beam.

Of course, the windows must be non-crystalline and, generally, a good choice is to use polymer materials that are totally amorphous and exhibit good chemical properties. The main resistances for polymer to usual solvent or solution that could be used in precipitation experiments are summarized in the Table 5.1.

Chemical classification	Prolene	Polypropylene	Polyester	Polycarbonate	Kapton	Mylar	Etnome
Acid (weak)	+	+	+	+	+	+	+
Acid (concentrated)	+	+	+	+	+	+	+
Alcohols	+	+	+	-	+	+	+
Aldehydes	-	-	+	-	+	+	-
Alkalis (concentrated)	+	+	+	+	+	+	+
Esters	+	+	+	-	+	+	+
Ether	-	-	+	+	+	+	+
Hydrocarbon (aliphatic)	-	-	+	-	+	+	-
Hydrocarbon (aromatic)	-	-	+	-	+	+	-
Ketones	-	-	+	-	+	+	-
Oxidizing agent	+	+	+	+	+	+	+

Table 5.1 Chemical resistance of various polymers with respect to usual solution. '+' denotes a well chemical resistance and '-' a possible cause of damage.

Among common polymers, the Kapton is a polyimide film developed by DuPont® that remains stable across a wide range of temperatures, from -269 to +400 °C.

Its chemical name is poly(4,4'-oxydiphenylene-pyromellitimide) and the monomer unit is schemed Figure 5.1.

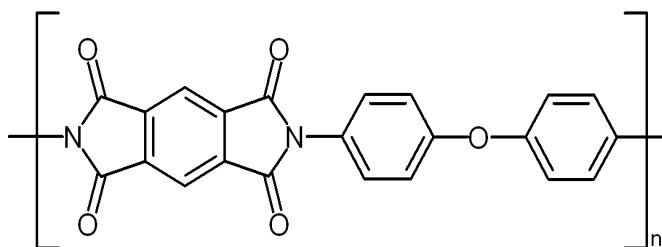


Figure 5.4 Structure of poly-oxydiphenylene-pyromellitimide.

Kapton is also commonly used as a material for windows of all kinds at X-ray sources (synchrotron beam-lines and X-ray tubes) and X-Ray detectors. Its high mechanical and thermal stability and high transmittance to X-Rays make it the preferred material. It is also relatively insensitive to radiation damage. (Megusar 1996)

Figure 5.5 shows the transmission of the incident X-Ray beam through a thickness of 152.4 μm of Kapton. The transmission is almost complete (about 98%) for the photon energy of our X-Ray source (17.5 keV).

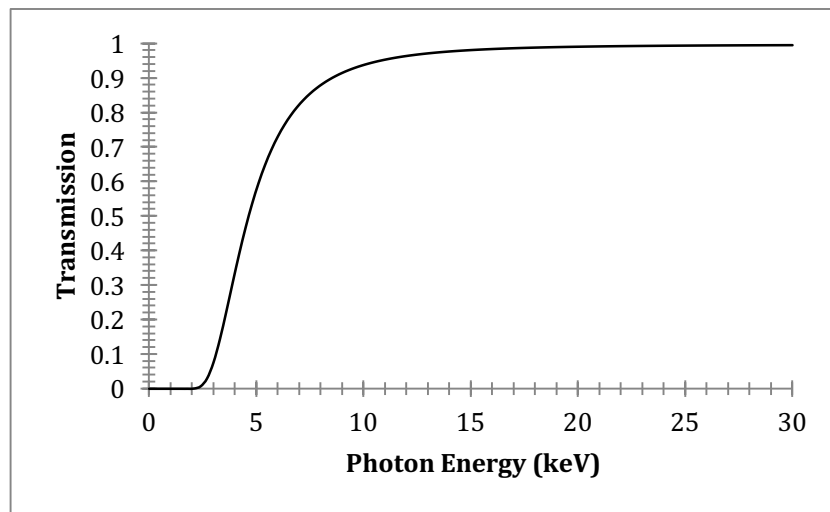


Figure 5.5 Transmission of X-ray incident beam through Kapton film (thickness 152.4 μm)

Kapton is of particular interest that it is commercially available in tube (see Figure 5.6).

Kapton tubings having an inside diameter of 12 mm and manufacturer-specified wall thicknesses of 76.2 μm were obtained from The Precision Paper Tube Company.



Figure 5.6 Kapton tubes commercially available (Precision Paper Tube Company $\text{\textcircled{R}}$)

The first design of the cell is presented Figure 5.7.

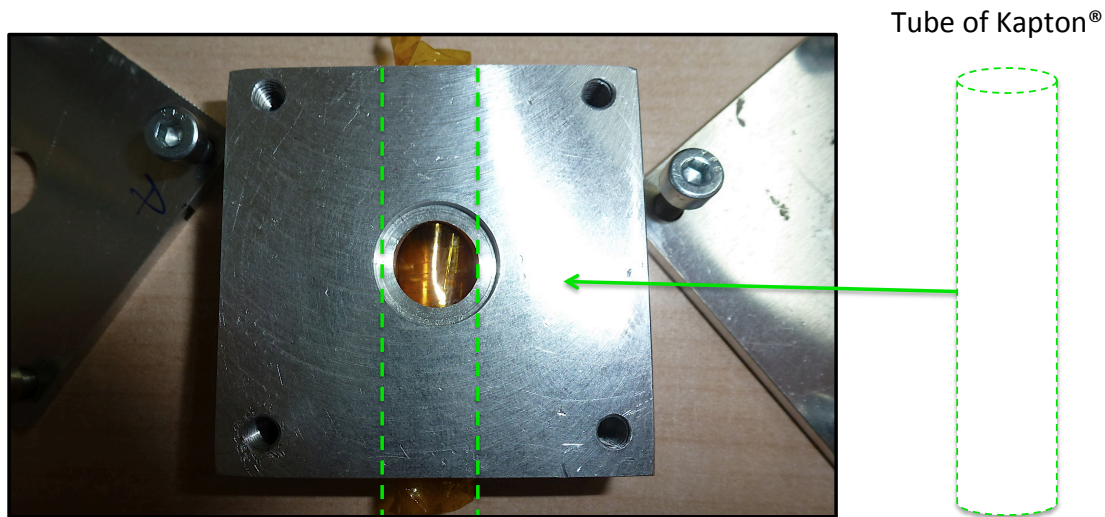


Figure 5.7 First design of the measurement cell.

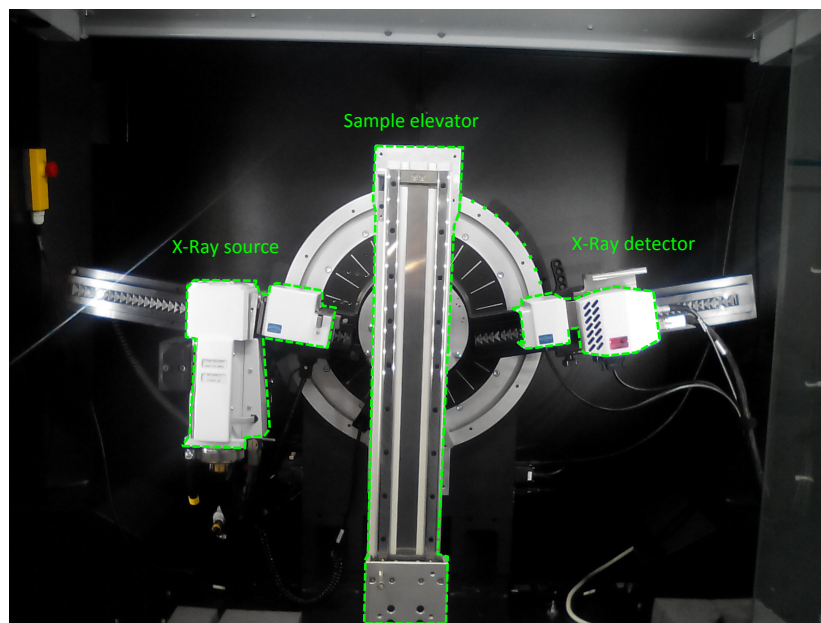


Figure 5.8 Bruker X-Ray diffractometer to monitor in-situ precipitation.

A picture of the X-ray diffractometer (Bruker) prototype to monitor in-situ the precipitation is presented Figure 5.8. Such device was design to provide valuable real-time information on crystallization processes and to highlight the formation of transient phases

Part.5 Preliminary results

Two different measuring modes were used:

- Static: the flow was stopped after precipitation and the diffractograms collected
- Dynamic: continuous flow with real time acquisition.

The possibilities of the prototype for in-situ monitoring are presented through crystallization studies of molecular and inorganic compounds. The thickness of the Kapton tube is relatively large compared to the thicknesses of Kapton films available on the market (approximately $7\mu\text{m}$). However, the transmittance is about 98% for this thickness (see Figure 5.5). Moreover, the tube is extremely resistant thereby bend smoothly; this is required to detect a signal. Indeed, the first tests showed that it is impossible to detect any signal through a thickness of $(12 + 0.1524)$ mm of sample. The sensor simply detects no photon. In order to decrease the sample section crosses by the X-Ray beam, the tube was folded to reduce the thickness around 1 or 2 mm and form a funnel (Figure 5.9). In general, sample thicknesses greater than 5 mm or so should be avoided in transmission geometry. Unfortunately, the Kapton gave rise to parasitic scattering particularly significant at low angle, but relatively easy to remove by measuring the background (*i.e.* the intensity scattered from solution). (Egami and Billinge 2012)

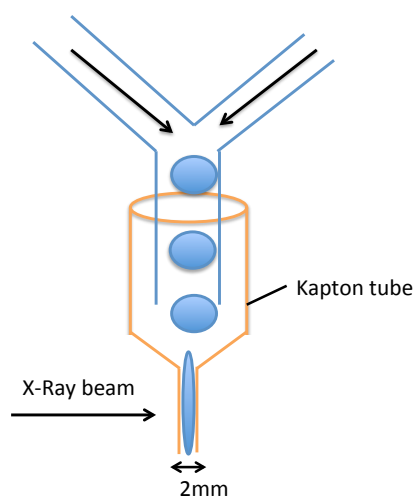


Figure 5.9 Funnel formed to ensure a good transmittance of X-Ray scattering beam through the sample.

5.1 Static mode

Experimental XRPD diffractogram of NaCl obtained on dry powder of NaCl fits the calculated one. Nevertheless, one can notice an anomalous shift of the diffraction peaks for high 2θ probably induced by the Kapton. (Egami and Billinge 2012))

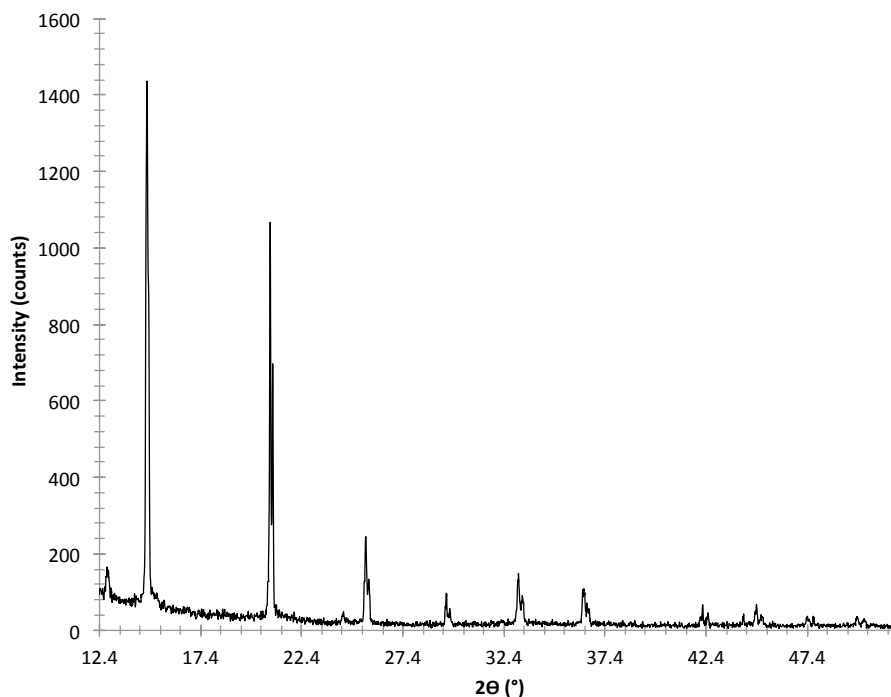


Figure 5.10 XRPD in static mode for dry powder of NaCl. Counting time of 8s and each 0.02° step.

Figure 5.11 shows the diffractograms obtained in the static mode for a dry NaCl powder sample (blue) and NaCl crystal in a saturated solution of ethanol (red) for a same counting time. For both cases it is possible to obtain a diffractogram nevertheless it should be mentioned that in the case of the Ethanol and NaCl mixture the detected intensity is about 21 times lower than for the dry powder. This decreases considerably the detection threshold and forced us to increase the counting time.

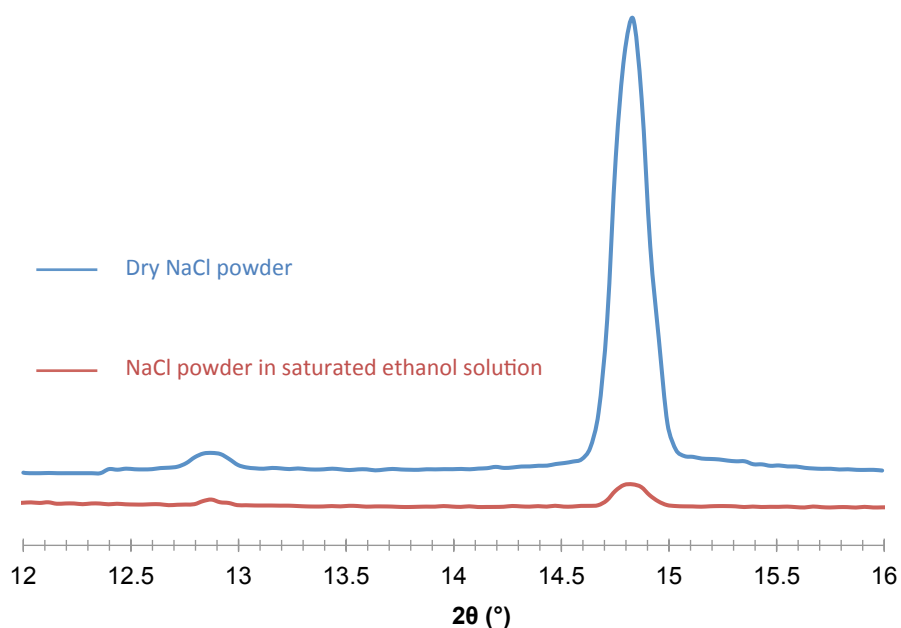


Figure 5.11 NaCl XRPD patterns performed in a static mode of dry powder and in a saturated ethanol solution.

5.2 Dynamic mode

This part described, through the study of calcium oxalate (CaC_2O_4) precipitation, our first trials to monitor a precipitation process.

In this experiment, $\text{NH}_4\text{C}_2\text{O}_4$ and CaCl_2 aqueous solutions were mixed to precipitate CaC_2O_4 (insoluble in water).

From the recorded diffractograms (see Figure 5.12), at least two solid phases were detected:

- The monohydrate phase (one peak detected after 855 sec): $\text{CaC}_2\text{O}_4 \cdot \text{H}_2\text{O}$
- The trihydrate phase (Two peaks detected after 2090 sec): $\text{CaC}_2\text{O}_4 \cdot 3\text{H}_2\text{O}$

It suggests that the monohydrate was the first to precipitate.

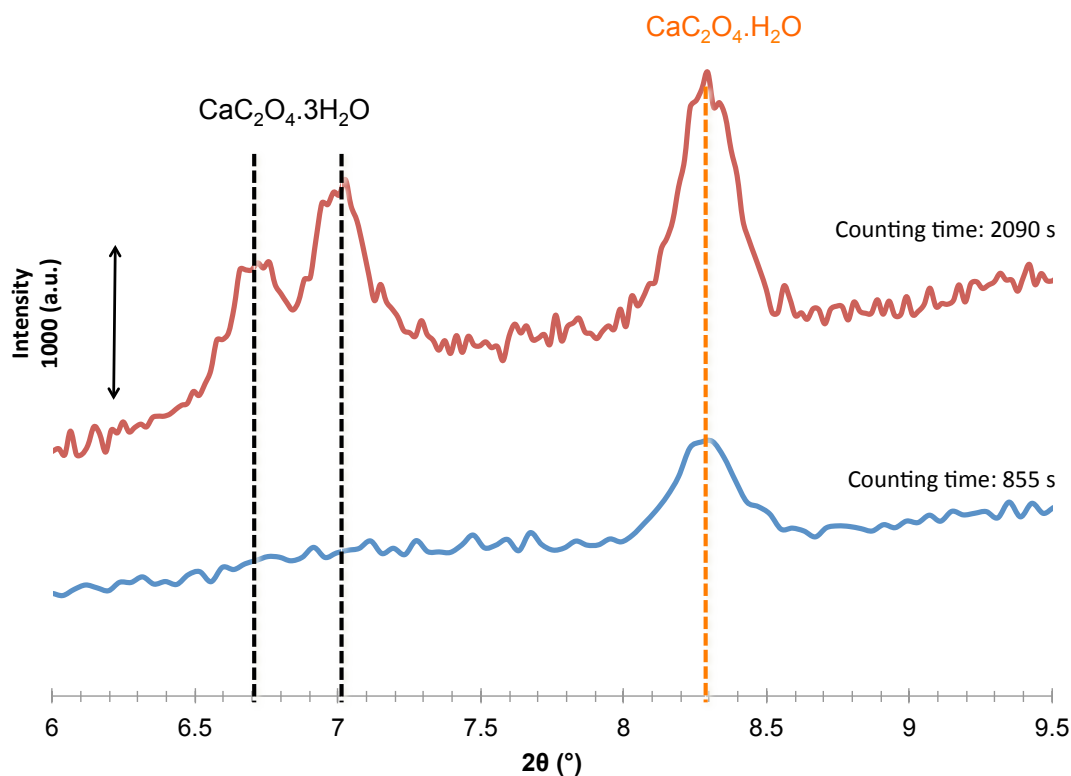


Figure 5.12 Diffractograms obtain for in-situ precipitation of CaC_2O_4

It should be mentioned that some problems of crystal incrustation in the measurement cell occurred during these first experiments. Further works are in progress in order to fix this problem.

Part.6 Conclusion

The development of the DIXCUR project is in its first stages. Further works are necessary to reveal all the potential of this device. The design of a new measurement cell is in progress to ensure a better flow of the solution through the cell.

First trials are promising because they highlight the feasibility of the experiment and some interesting results on the appearance of phases in solution. Nevertheless, the intensities detected are, for the moment, too low to ensure detection in a reasonable time in order to study the precipitation process since its early stages. To this purpose, a reduction of the cell volume is envisaged.

References

- Egami T, Billinge SJ. *Underneath the Bragg peaks: structural analysis of complex materials*. Pergamon; 2012.
- Erdemir D, Lee AY, Myerson AS. Nucleation of Crystals from Solution: Classical and Two-Step Models. *Acc. Chem. Res. American Chemical Society*; 2009 May 19;42(5):621–9.
- Megusar J. Low temperature fast-neutron and gamma irradiation of glass fiber-epoxy composite. Part 2: Structure and chemistry. *JNM*. 1996 Jun 1;230(3):233–41.
- Vekilov PG. Nucleation. *Crystal Growth & Design*. 2010 Dec;10(12):5007–19.

Chapter 6. Conclusion Générale

L'objectif premier de ce travail était l'élaboration de technique optiques *in-situ* pour la caractérisation de composés organiques cristallisés. La complexité des phénomènes mis en jeux dans les mécanismes de transition entre phases, de désolvatation et des équilibres hétérogènes en règle générale nécessite le développement de techniques analytiques capables de sonder l'état de la matière en un temps très court. Le développement d'un appareil basé sur la génération de seconde harmonique (SHG) nous est apparu pourvoir répondre à ces besoins.

La principale restriction de cette technique est la nécessité qu'au moins une des phases étudiées cristallise dans un groupe d'espace non-centrosymétrique. Dans les matériaux organiques et organométalliques la proportion de phases NC est constante depuis une dizaine d'année (24.1% (Allen 2002) des structures répertoriées dans la CSD en 2002, 22% en 2014). Il est cependant à noter que les composés non centrosymétriques ont une grande portée industrielle en terme d'application. On citera par exemple, tous les matériaux piezzo ou pyroélectriques qui seront amenés à être de plus en plus étudiés dans les prochaines années afin de développer de nouvelles technologies vertes permettant des gains énergétiques. Bien sûr, les matériaux NC, du fait de leur propriété à générer de nouvelles harmoniques, sont depuis longtemps utilisés dans les télécommunications et dans le développement de nouvelles sources lasers.

Une autre restriction est la possible absorption du rayonnement incident et/ou SHG qui conduit à un endommagement de l'échantillon. Pour palier ce problème l'utilisation de laser accordable en longueur d'onde est une solution envisageable mais est couteuse en 2014. De plus, l'énergie apportée par les lasers accordables est souvent moins importante. La source laser doit donc :

- (1) émettre dans la gamme de longueur d'onde de transparence de la plupart des solides organiques (*NB* une très légère absorption peut être bénéfique pour contourner les règles de Kleinman)
- (2) permettre une émission de SHG en adéquation avec les détecteurs spectraux utilisés
- (3) avoir un coût acceptable et être simple d'utilisation
- (4) fournir une énergie constante et suffisamment importante pour entrer dans le domaine de réponse non linéaire des matériaux ainsi que générer des signaux SHG suffisamment élevés pour être détectables

Le choix d'une source laser émettant à 1064nm a répondu à la plupart de ces prérequis.

L'utilisation d'un spectromètre dans notre montage a permis une détection spectrale ainsi une qu'une intégration plus rapide du signal bien que cela ait introduit une diminution de la sensibilité comparé à l'utilisation de photomultiplicateurs dans des montages plus élaborés (LeCaptain and Berglund 1999; Rechsteiner et al. 2000; Wanapun et al. 2010).

Néanmoins, tout au long de ce travail la méthode SHG développée s'est révélée être une technique de choix pour détecter de la non centrosymétrie des cristaux ; elle est d'ailleurs régulièrement utilisée au sein du laboratoire SMS sur poudre sèche dans le but de détecter des systèmes énantiomériques cristallisants sous la forme de conglomérat (Galland et al. 2009). Les niveaux de détection ont été améliorés par rapport au montage originellement développé au sein du laboratoire SMS en 2009 passant d'une détection de 1/100 à 1/1000 de l'intensité SHG produite par le quartz α . Cette amélioration est essentiellement due à un meilleur réglage des optiques (miroir, alignement laser) mais surtout à un changement de géométrie du montage (utilisation de piluliers et détection en réflexion par le dessous : Cf montage voie sèche, page 83). Cette géométrie a également permis une mesure plus fiable (l'échantillon reste dans le pilulier et ne risque pas d'être contaminé) ainsi que la possibilité de manipuler de manière plus sûre des produits toxiques ou n'existant qu'en solution (cas des composés efflorescents).

En plus de la discrimination entre cristaux centrosymétrique et NC, les niveaux de sensibilité de la technique SHG sont bien plus élevés que les méthodes de caractérisation conventionnelles telle que la diffraction des rayons X ou l'analyse thermique différentielle et ce pour un temps de mesure négligeable par rapport aux autres techniques (environ 3 sec). Ainsi, dans le cas particulier (et favorable) de l'acide 3-hydroxybenzoïque, seulement 2ppm d'impuretés structurales ont été détectées. Ceci met en évidence la haute sensibilité de la technique avec des applications notables pour la détection d'impureté structurale NC dans le domaine pharmaceutique. Il est à noter, que la présence d'impuretés structurales peut grandement modifier la cinétique de transition de phase du polymorphe métastable vers la forme stable avec des conséquences qui peuvent être dramatiques si la forme métastable est celle commercialisées. (Chemburkar et al. 2000).

Outre la détection de cristaux NC, l'adjonction au montage SHG d'une platine chauffante ainsi qu'un contrôleur d'humidité a permis l'étude *in-situ* de nombreux processus se produisant à l'état solide (transition polymorphiques, déshydratation, recristallisation depuis l'amorphe) mais aussi entre les différents états de la matière (cristallisation depuis une

solution, études de transitions de phase dans un système binaire). La plupart des processus étudiés par SHG et les informations qui ont pu en être déduites sont résumés dans la Figure 6.1.

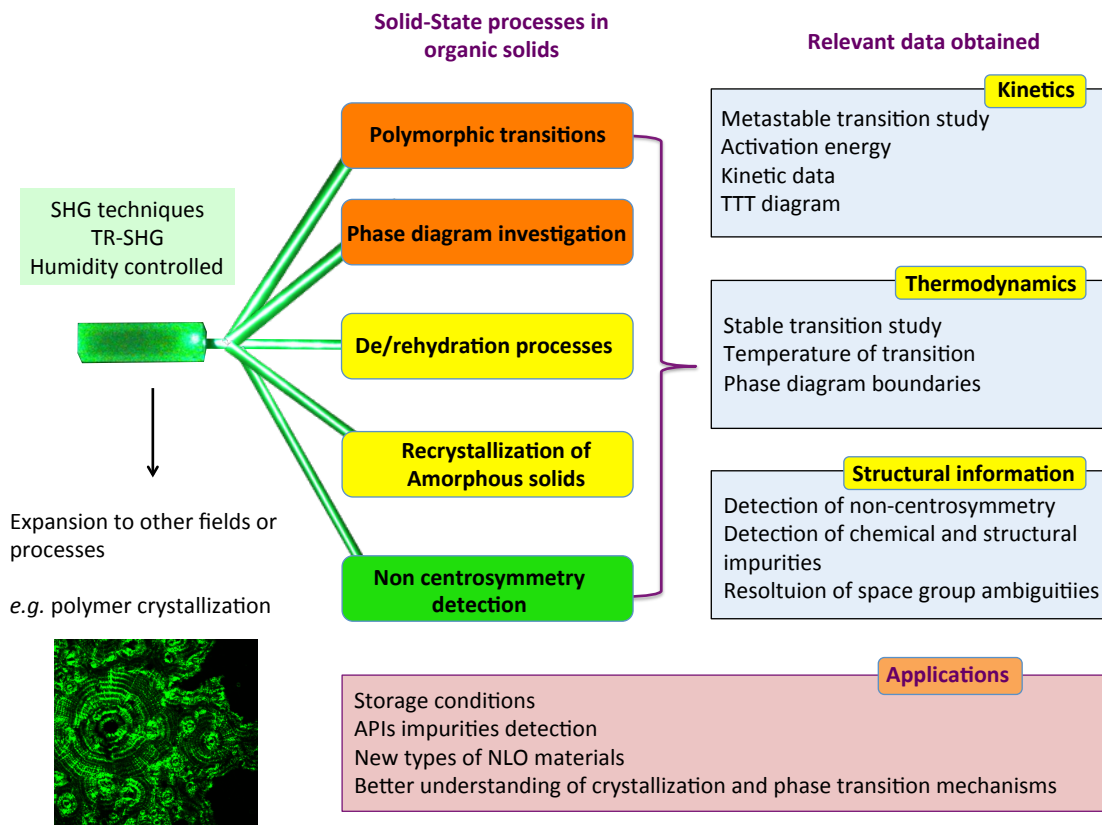


Figure 6.1 Résumé des processus étudiés au cours de ces travaux de thèse et des paramètres pertinents associés

Il y a ainsi un grand nombre de domaines de recherche dans lesquels la méthode SHG pourrait être utilisée pourvu que les phases sondées soient NC avec des applications telles que :

- la détection d'impureté cristalline dans les domaines pharmaceutique et agroalimentaire
- l'aide à détermination de groupes d'espace
- la détection rapide de matériaux NC et de leur efficacité SHG
- le suivi de désolvatations (pharmaceutique et agroalimentaire)
- l'étude des transitions de phase et de la nucléation
- l'étude du désordre moléculaire à l'état solide comme les changements de conformations induits par la température ou la pression
- l'étude de diagrammes de phases

Ainsi au cours de cette thèse, le suivi de la transition monotropique dans le cas du MHBA et ordre désordre dans le cas des TAK a été réalisé au moyen de la méthode SHG. Il a également été montré dans le cas du système binaire acide formique /eau, la pertinence de l'utilisation du SHG pour déterminer précisément les frontières des domaines dans un diagramme de phases. Des processus suivis en SHG et en humidité contrôlée tels que la déshydratation de composés organiques ou inorganiques peuvent également être envisagés. Enfin la recristallisation depuis l'état amorphe du lactose permet d'envisager d'exporter la technique dans d'autres domaines tels que celui des polymères semi-cristallins.

Le technique SHG mise au point se révèle donc être extrêmement sensible à de nombreux paramètres tels que la structure cristalline, la nature de molécules (conformation, disposition dans la maille cristalline), la taille des particules. Cette sensibilité de détection et la rapidité de la mesure en font une technique des choix pour étudier de nombreux phénomènes physiques. Néanmoins, le nombre important de paramètres qui peuvent influencer la mesure peut aussi se révéler un frein à l'interprétation des résultats. L'interprétation des résultats SHG gagne ainsi en pertinence lorsque cette technique est utilisée en combinaison avec d'autres techniques analytiques comme cela a été fait par exemple dans l'étude des HMX. (Smilowitz et al. 2009a; 2009b). Le développement de méthodes optiques couplées telle que le SHG et la diffraction des RX (projet DIXCUR) pourrait se révéler particulièrement intéressant.

Le nombre grandissant de citations de la publication de Kurtz & Perry est à mettre en perspective avec ce travail puisque, parmi les 3200 citations depuis 1968, la plupart sont essentiellement des mesures qualitatives des propriétés optiques non linéaires de nouveaux matériaux. Seulement 59 publications contiennent le terme « transition(s) », « transformation(s) » ou « polymorph(s) » dans leurs titres (dont 3 issus de ce travail de thèse). Au vu du nombre d'applications possibles, de sa sensibilité et de sa rapidité, cette technique, dont les possibles applications ont été démontrées à travers ce travail, mériterait d'être mieux reconnue dans des domaines tels que la cristallographie ou la chimie organiques pour occuper une place de choix parmi les techniques usuelles lorsque la phase étudiée est non-centrosymétrique.

Les travaux présentés dans ce mémoire ont à ce jour conduit à la publication d'articles et ont également été présentés en congrès. Le détail des communications et des articles est disponible en Annexe VI.

References

- Allen FH. The Cambridge Structural Database: a quarter of a million crystal structures and rising. *Acta Crystallogr B Struct Sci. International Union of Crystallography*; 2002 May 29;58(3):380–8.
- Chemburkar SR, Bauer J, Deming K, Spiwek H, Patel K, Morris J, et al. Dealing with the Impact of Ritonavir Polymorphs on the Late Stages of Bulk Drug Process Development. *Org. Process Res. Dev.* 2000 Sep;4(5):413–7.
- Galland A, Dupray V, Berton B, Morin-Grognet S, Sanselme M, Atmani H, et al. Spotting Conglomerates by Second Harmonic Generation. *Crystal Growth & Design.* 2009 Jun 3;9(6):2713–8.
- LeCaptain DJ, Berglund KA. The applicability of second harmonic generation for in situ measurement of induction time of selected crystallization systems. *Journal of Crystal Growth.* 1999 May 24;203:564–9.
- Rechsteiner P, Hulliger J, Flörsheimer M. Phase-Sensitive Second Harmonic Microscopy Reveals Bipolar Twinning of Markov-Type Molecular Crystals. *Chem. Mater. American Chemical Society*; 2000 Nov;12(11):3296–300.
- Smilowitz L, Henson BF, Romero JJ. Intercomparison of Calorimetry, Raman Spectroscopy, and Second Harmonic Generation Applied to Solid–Solid Phase Transitions. *J. Phys. Chem. A.* 2009a Sep 3;113(35):9650–7.
- Smilowitz LB, Henson BF, Romero JJ. A comparison of observables for solid-solid phase transitions. Los Alamos National Laboratory (LANL); 2009b.
- Wanapun D, Kestur US, Kissick DJ, Simpson GJ, Taylor LS. Selective Detection and Quantitation of Organic Molecule Crystallization by Second Harmonic Generation Microscopy. *Anal. Chem. American Chemical Society*; 2010 Jul;82(13):5425–32.

Appendices

Appendix. I Tables of susceptibility tensors²³

Following are supplements to and explanation for tables I-1, I-2

The set of all the symmetry element of a crystal is called its crystal class. There are 32 different crystal classes (or point group). They are classified into seven crystal systems: triclinic, monoclinic, orthorhombic, tetragonal, hexagonal, trigonal and cubic. The different classes are characterized by the generating symmetry elements: n denotes, for example, an n-fold axis (a rotation of $2\pi/n$ leaves the crystal invariant), ' \bar{n} ' an n-fold rotation followed (or preceded) by an inversion, 'm' a mirror plane ($=\bar{2}$), 'n/m' an n-fold rotation axis with mirror plane perpendicular to it.

References

P.N. Butcher. Nonlinear Optical Phenomena. Bulletin 200; Engineering Experimental Station, Ohio State University, Columbus, Ohio, 1965

C. C. Shang and H. Hsu. The spatial symmetric forms of third-order nonlinear susceptibility. J. Quant. Elect. IEEE-QE 23 (1987): 177-179

Table AI-1 First Order Susceptibility Tensors

Hereafter, the first-order susceptibility tensor $\chi^{(1)}$ for the seven crystal systems and for isotropic media. Each element is denoted only by its subscripts (e.g. $\chi^{(1)}_{xxx} = xxx$). The number in brackets is the number of independent nonzero elements.

Triclinic	$\begin{bmatrix} xx & xy & zx \\ xy & yy & yz \\ zx & yz & zz \end{bmatrix}$	(6)
Monoclinic	$\begin{bmatrix} xx & 0 & zx \\ 0 & yy & 0 \\ zx & 0 & zz \end{bmatrix}$	(4)
Orthorhombic	$\begin{bmatrix} xx & 0 & 0 \\ 0 & yy & 0 \\ 0 & 0 & zz \end{bmatrix}$	(3)
Tetragonal Trigonal Hexagonal	$\begin{bmatrix} xx & 0 & 0 \\ 0 & xx & 0 \\ 0 & 0 & zz \end{bmatrix}$	(2)
Cubic	$\begin{bmatrix} xx & 0 & 0 \\ 0 & xx & 0 \\ 0 & 0 & xx \end{bmatrix}$	(1)

²³ Taking from E. G. Sauter, Nonlinear Optics. Wiley, 1996.

Table AI-2 Second-Order Susceptibility Tensors

Hereafter are listed the second-order susceptibility tensor $\chi^{(2)}$ for those crystal classes with no center of symmetry. Each element is denoted only by its subscripts (e.g. $\chi^{(2)}_{xxx} = xxx$) and bar denotes the negative. The number in parenthesis is the number of independent nonzero elements. All the elements of the tensor are identically zero for the classes that do not appear.

Triclinic

$$\text{Class 1} \quad \begin{bmatrix} xxx & xyy & xzz & xyz & xzy & xzx & xxz & xxy & xyx \\ yxx & yyy & yzz & yyz & yzy & yzx & yxz & yxy & yyx \\ zxx & zyy & zzz & zyz & zzy & zzx & zxz & zxy & zyx \end{bmatrix} \quad (27)$$

Monoclinic

$$\text{Class 2} \quad \begin{bmatrix} 0 & 0 & 0 & xyz & xzy & 0 & 0 & xxy & xyx \\ yxx & yyy & yzz & 0 & 0 & yzx & yxz & 0 & 0 \\ 0 & 0 & 0 & zyz & zzy & 0 & 0 & zxy & zyx \end{bmatrix} \quad (13)$$

$$\text{Class m} \quad \begin{bmatrix} xxx & xyy & xzz & 0 & 0 & xzx & xxz & 0 & 0 \\ 0 & 0 & 0 & yyz & yzy & 0 & 0 & yxy & yyx \\ zxx & zyy & zzz & 0 & 0 & zzx & zxz & 0 & 0 \end{bmatrix} \quad (14)$$

Orthorhombic

$$\text{Class 222} \quad \begin{bmatrix} 0 & 0 & 0 & xyz & xzy & 0 & 0 & 0 & 0 \\ 0 & 0 & 0 & 0 & 0 & yzx & yxz & 0 & 0 \\ 0 & 0 & 0 & 0 & 0 & 0 & 0 & zxy & zyx \end{bmatrix} \quad (6)$$

$$\text{Class mm2} \quad \begin{bmatrix} 0 & 0 & 0 & 0 & 0 & xzx & xxz & 0 & 0 \\ 0 & 0 & 0 & yyz & yzy & 0 & 0 & 0 & 0 \\ zxx & zyy & zzz & 0 & 0 & 0 & 0 & 0 & 0 \end{bmatrix} \quad (7)$$

Tetragonal

$$\text{Class 4} \quad \begin{bmatrix} 0 & 0 & 0 & xyz & xzy & xzx & xxz & 0 & 0 \\ 0 & 0 & 0 & xxz & xzx & \overline{xyz} & \overline{xyz} & 0 & 0 \\ zxx & zxx & zzz & 0 & 0 & 0 & 0 & zxy & \overline{zxy} \end{bmatrix} \quad (7)$$

$$\text{Class } \bar{4} \quad \begin{bmatrix} 0 & 0 & 0 & xyz & xzy & xzx & xxz & 0 & 0 \\ 0 & 0 & 0 & \overline{xxz} & \overline{xzx} & xzy & xyz & 0 & 0 \\ zxx & \overline{zxx} & 0 & 0 & 0 & 0 & 0 & zxy & zxy \end{bmatrix} \quad (6)$$

$$\text{Class 422} \quad \begin{bmatrix} 0 & 0 & 0 & xyz & xzy & 0 & 0 & 0 & 0 \\ 0 & 0 & 0 & 0 & 0 & \overline{xyz} & \overline{xyz} & 0 & 0 \\ 0 & 0 & 0 & 0 & 0 & 0 & 0 & zxy & \overline{zxy} \end{bmatrix} \quad (3)$$

$$\text{Class 4mm} \quad \begin{bmatrix} 0 & 0 & 0 & 0 & 0 & xzx & xxz & 0 & 0 \\ 0 & 0 & 0 & xxz & xzx & 0 & 0 & 0 & 0 \\ zxx & zxx & zzz & 0 & 0 & 0 & 0 & 0 & 0 \end{bmatrix} \quad (4)$$

$$\text{Class } \bar{4}2m \quad \begin{bmatrix} 0 & 0 & 0 & xyz & xzy & 0 & 0 & 0 & 0 \\ 0 & 0 & 0 & 0 & 0 & xzy & xyz & 0 & 0 \\ 0 & 0 & 0 & 0 & 0 & 0 & 0 & zxy & zyx \end{bmatrix} \quad (3)$$

Cubic

$$\text{Class } 432 \quad \begin{bmatrix} 0 & 0 & 0 & xyz & \overline{xyz} & 0 & 0 & 0 & 0 \\ 0 & 0 & 0 & 0 & 0 & xyz & \overline{xyz} & 0 & 0 \\ 0 & 0 & 0 & 0 & 0 & 0 & 0 & xyz & \overline{xyz} \end{bmatrix} \quad (1)$$

$$\text{Class } \bar{4}3m \quad \begin{bmatrix} 0 & 0 & 0 & xyz & xzy & 0 & 0 & 0 & 0 \\ 0 & 0 & 0 & 0 & 0 & xyz & xzy & 0 & 0 \\ 0 & 0 & 0 & 0 & 0 & 0 & 0 & xyz & xzy \end{bmatrix} \quad (1)$$

$$\text{Class } 23 \quad \begin{bmatrix} 0 & 0 & 0 & xyz & xzy & 0 & 0 & 0 & 0 \\ 0 & 0 & 0 & 0 & 0 & xyz & xzy & 0 & 0 \\ 0 & 0 & 0 & 0 & 0 & 0 & 0 & xyz & xzy \end{bmatrix} \quad (2)$$

Trigonal

$$\text{Class } 3 \quad \begin{bmatrix} xxx & \overline{xxx} & 0 & xyz & xzy & xzx & xxz & \overline{yyy} & \overline{yyy} \\ \overline{yyy} & yyy & 0 & xxz & xzx & \overline{xzy} & \overline{xyz} & \overline{xxx} & \overline{xxx} \\ zxx & zxx & zzz & 0 & 0 & 0 & 0 & zxy & \overline{zxy} \end{bmatrix} \quad (9)$$

$$\text{Class } 32 \quad \begin{bmatrix} xxx & \overline{xxx} & 0 & xyz & xzy & 0 & 0 & 0 & 0 \\ 0 & 0 & 0 & 0 & 0 & \overline{xzy} & \overline{xyz} & \overline{xxx} & \overline{xxx} \\ 0 & 0 & 0 & 0 & 0 & 0 & 0 & zxy & \overline{zxy} \end{bmatrix} \quad (4)$$

$$\text{Class } 3m \quad \begin{bmatrix} 0 & 0 & 0 & 0 & 0 & xzx & xxz & \overline{yyy} & \overline{yyy} \\ \overline{yyy} & yyy & 0 & xxz & xzx & 0 & 0 & 0 & 0 \\ zxx & zxx & 0 & 0 & 0 & 0 & 0 & 0 & 0 \end{bmatrix} \quad (5)$$

Hexagonal

$$\text{Class } 6 \quad \begin{bmatrix} 0 & 0 & 0 & xyz & xzy & xzx & xxz & 0 & 0 \\ \overline{yyy} & yyy & 0 & xxz & xzx & \overline{xzy} & \overline{xyz} & 0 & 0 \\ zxx & zxx & zzz & 0 & 0 & 0 & 0 & zxy & \overline{zxy} \end{bmatrix} \quad (7)$$

$$\text{Class } \bar{6} \quad \begin{bmatrix} xxx & \overline{xxx} & 0 & 0 & 0 & 0 & 0 & \overline{yyy} & \overline{yyy} \\ \overline{yyy} & yyy & 0 & 0 & 0 & 0 & 0 & \overline{xxx} & \overline{xxx} \\ 0 & 0 & 0 & 0 & 0 & 0 & 0 & 0 & 0 \end{bmatrix} \quad (2)$$

$$\text{Class } 622 \quad \begin{bmatrix} 0 & 0 & 0 & xyz & xzy & 0 & 0 & 0 & 0 \\ 0 & 0 & 0 & 0 & 0 & \overline{xzy} & \overline{xyz} & 0 & 0 \\ 0 & 0 & 0 & 0 & 0 & 0 & 0 & zxy & \overline{zxy} \end{bmatrix} \quad (3)$$

$$\text{Class } 6mm \quad \begin{bmatrix} 0 & 0 & 0 & 0 & 0 & xzx & xxz & 0 & 0 \\ 0 & 0 & 0 & xxz & xzx & 0 & 0 & 0 & 0 \\ zxx & zxx & zzz & 0 & 0 & 0 & 0 & 0 & 0 \end{bmatrix} \quad (4)$$

$$\text{Class } \bar{6}m2 \quad \begin{bmatrix} 0 & 0 & 0 & 0 & 0 & 0 & 0 & \overline{yyy} & yyy \\ \overline{yyy} & yyy & 0 & 0 & 0 & 0 & 0 & 0 & 0 \\ 0 & 0 & 0 & 0 & 0 & 0 & 0 & 0 & 0 \end{bmatrix} \quad (1)$$

Appendix. II Experimental details

Single Crystal X-ray Diffraction (SC-XRD)

Single Crystal X-ray Diffraction (SC-XRD) experiments were performed by fixing the selected single crystal on a glass fiber which was mounted on the full three circle goniometer of a Bruker SMART APEX diffractometer (Figure.A. II-1) equipped with a CCD area detector (with Mo K α_1 $\lambda=0.71071$ Å). The SMART²⁴ software was used to determine the cell parameters and the orientation matrix for each crystal. Intensities were integrated and corrected for Lorentz polarization and adsorption effects using SAINT²⁵ software. Crystal structures were solved by direct methods, using the SHELX-97 program,²⁶ and anisotropic displacement parameters were refined for non- hydrogen atoms. All hydrogen atoms were located by Fourier difference synthesis and fixed geometrically according to their environment with a predefined isotropic thermal factor.



Figure.A. II-1 Photography of the typical device used for SC-XRD in this work.

X-ray Powder Diffraction (XRPD)

XRPD analyses were performed using a D8 diffractometer (Bruker, Germany, Figure.A. II-2) equipped with a modified goniometer of reverse-geometry (- Θ /- Θ).²⁷ The incident X-ray beam consisted of the Cu K α ($\lambda=1.5418$ Å) with a tube voltage and amperage set at 40 kV and 40 mA respectively. The diffraction patterns were collected with a Lynx Eyes® linear detector (Bruker, Germany). Routine XRPD analyses were performed with a step of 0.04° (2 Θ), and a 12 s per step counting time from 3° to 30° (2 Θ). High-quality XRPD patterns

²⁴ Bruker AXS Inc., “Bruker SMART (5.059) and SAINT (6.01),” (Madison, Wisconsin: Madison, Wisconsin, November 20, 1997).

²⁵ *ibid.*

²⁶ G.M. Sheldrick, “SHELXS97 and SHELXL97,” (Institut für Anorganische Chemie der Universität: Göttingen, Germany: Institut für Anorganische Chemie der Universität: Göttingen, Germany, November 20, 1997).

²⁷ G. Coquerel, M. Sanselme, and A. Lafontaine, “Method and Measuring Scattering of X-Rays, Its Applications and Implementation Device,” n.d.

were collected using a step of $0.018^\circ(2\theta)$ with a 40 s per step counting time from 3° to $80^\circ(2\theta)$.



Figure.A. II-2 Photography of the diffractometer used for XRPD in this work

Temperature Resolved X-Ray Powder Diffraction (TR-XRPD)

Crystalline solid phases were analyzed at room temperature by means of X-ray powder diffraction (XRPD) on a Bruker Siemens D5005 apparatus ($\theta - \theta$) set, with Cu $K_{\alpha 2}$ radiation (1.54056 \AA) (Kb filter) under 40 kV and 30 mA and collected on a scintillation detector. The θ angle calibrations were carried out by using Siemens slits and a quartz sample (secondary standard). Temperature was controlled and monitored using an Anton Paar TTK450. The intensity was measured with a 2θ step of 0.04° during 4s.

Determination of unit cell parameters by (TR-XRPD)²⁸

The TR-XRPD patterns have been performed at the X-ray diffraction facility of the Institute Jean Barriol of "Université de Lorraine (Nancy, France)", using a Panalytical X'Pert Pro diffractometer equipped with a Cu $K\alpha$ radiation, a Ge(111) incident beam monochromator ($\lambda = 1.5406 \text{ \AA}$) and an X'Celerator detector. Temperature-controlled diffractograms were collected by using an Oxford cryostat (Oxford cryosystems Phenix). A measurement was performed every 2°C increments (after 2 minutes of temperature stabilization) upon cooling and heating from the room temperature down to -50°C (under vacuum) at the $6 \text{ K}\cdot\text{min}^{-1}$ cooling/heating rate. Data collection was carried out in the scattering angle range 5° – $32^\circ(2\theta)$ with a 0.0167° step over 60 min. The Material Studio software by Accelrys, Inc. was used in order to obtain the lattice parameters. The unit cell dimensions and space group were

²⁸ The XRPD data collections have been performed at the X-ray diffraction facility of the Institute Jean Barriol of Université de Lorraine, <http://www.crystallography.fr/crm2/fr/services/servicecommun/index.php>. Pierrick Durand is gratefully acknowledged for XRPD experiments.

determined by using the X-Cell algorithm²⁹ at 20°C and then the dimensions of the obtained unit cell and the profile parameters were refined by the Pawley method³⁰ ($7.5^\circ < 2\theta < 29^\circ$) at each temperature.

Differential Scanning Calorimetry (DSC)

DSC experiments in the temperature range 0 °C to 200 °C were performed using a Netzsch DSC 204 F1 apparatus (Figure.A. II-3) equipped with an intracooler. Each DSC run was performed with few mg of a powdered sample (± 0.05 mg) in aluminum pans with pierced lids at 1, 2, 5, and 10 K/min heating rates. The atmosphere of the analyses was regulated by a helium flux (40 mL/min). Onset (respectively endset) temperatures are calculated from the intersection between the baseline and the slope of the first (respectively last) part of the endotherm.



Figure.A. II-3 Photography of the DSC apparatus used in this work.

DSC experiments below 0°C were performed using a TG/DSC NETZSCH STA 449 C instrument (Figure.A. II-4). Enthalpy and temperature calibrations were performed with biphenyl and indium and liquid nitrogen was used as a refrigerant to afford sub ambient temperatures. Each DSC run was performed with few mg of a powdered sample (± 0.05 mg) in sealed aluminium pans with pierced lids. Measurements were carried out with heating/cooling rates in the range 5-15 K/min under a helium atmosphere (constant flow of 40 mL/min) and repeated at least twice to check the reproducibility of the measurements. The Netzsch-TA Proteus Software v4.8.4 was used for data processing.

²⁹ Neumann MA. X-Cell: a novel indexing algorithm for routine tasks and difficult cases. *J Appl Crystallogr.* 2003 Mar 15;36(2):356–65.

³⁰ Pawley GS. Unit-cell refinement from powder diffraction scans. *J Appl Crystallogr.* 1981 Dec 1;14(6):357–61.



Figure.A. II-4 Photography of the TGA-DSC apparatus used in this work for subambient measurements.

Hot & Cold Stage Microscopy (HSM, CSM)

For microscopy observations with controlled temperature, samples (either powder, thin-films or single crystals) were loaded into a quartz cell with a cylindrical geometry (d=13 mm, h=1.3 mm)

and sampled in a THMS 600 temperature stage setup (Linkam) allowing accurate control of the sample temperature (± 0.1 °C). Liquid nitrogen was used as the refrigerant for cooling ramp down to -120 °C and the nitrogen flux into the cell was regulated via an automatic pump. The setup is coupled with a Nikon Eclipse LV100 microscope (maximum magnification: x1000) connected to a computer for image captures by using a CCD camera (Figure.A. II-5).



Figure.A. II-5 Photography of the optical microscope used in this study.

Multiphoton microscopy³¹

A laser scanning microscope LSM 710 NLO Zeiss (Iena, Germany) has been used. Excitation was provided by a CHAMELEON femtosecond Titanium-Sapphire laser (Coherent, Santa Clara, USA) set at 860 nm. Samples were put in glass bottom box and were imaged with a

³¹ Acknowledgments Plateforme Imagerie Cellulaire et Tissulaire IBISA de l'université de Reims Champagne Ardenne. Dr Christine TERRY is greatly acknowledged for her contribution to this study

63X, 1.4 NA oil (or 20x, 0.8 NA) objective lens. Emitted SHG signal was collected with a bandpass filter (420-440 nm). Z stacks images were acquired with 0.8 μm Z step.

Ball-Milling

The milling of the samples was performed using a Retsch® apparatus (Figure.A. II-6). It consists in a oscillation of a zirconium ball in jar in order to break crystals. Circa 200 mg of powder were used and the frequencies of ball oscillation were set either at 3 or 30 Hz for.



Figure.A. II-6 Retsch® ball milling apparatus

Laser Granulometry

A Mastersizer 2000 ® (see Figure.A. II-7) was used to determine the particles size of our samples (accuracy better than 1%). The apparatus uses the technique of laser diffraction to measure the size of particles. It does this by measuring the intensity of light scattered as a laser beam passes through a dispersed particulate sample. Data are then analyzed to calculate the size of the particles that generated the scattering pattern. Sample dispersion is controlled by a wet dispersion unit. This ensures that the particles are delivered to the measurement area of the optical bench at the correct concentration and in a suitable, stable state of dispersion. The solvent used to disperse the powder depends on the solubility properties of the sample.



Figure.A. II-7 Photography of the particle size analyzer Mastersizer 2000®

Curve fitting

Data were fitted to specific expressions by application of the Levenberg–Marquardt (least square method) algorithm to minimize χ^2 using the program Gnuplot.

Appendix. III Softwares

I.1 Determination of the SHG signal

The following software was developed in Scilab® programming language in order to treat a large number of spectra. It extracts the SHG signal values and plots automatically the spectra.

```

0001 // Ce programme a été élaboré au sein du Laboratoire SMS
0002 //Créateur Simon Clevers
0003 //Programme permettant l'ouverture d'une suite de fichiers du
type NOMdefichiersanszeronb.txt où nb
 sera la variable permettant de repérer le numero fichier.
0004
0005 //définition des fonctions
0006
////////////////////////////////////
////////////////////////////////////
0007 //fonction permettant la récupération du numéro du fichier
0008
0009 function nb=recuperation(Nom_Fichier)
0010
0011 avant=strindex(Nom_Fichier,'0');//position dans le nom de
fichier du "0"
0012 //
0013 nzero=size(avant);// renvoi une matrice définissant la taille
de la matrice avant (normalement 1
 ligne et nzero colonnes)
0014 nzero=nzero(1,$);//renvoi le nombre de colonne correspondant au
nombre de zero
0015 avant=avant(1,nzero-1);//selection du premier zero
0016 //attention il faut impérativement qu'il n'y ait pas de zero
dans la chaine de caractère précédant nb
0017 apres=strindex(Nom_Fichier, '.');// position du point dans le
nom de fichier
0018 numero=part(Nom_Fichier,[avant+1:1:apres]);//récupération de la
portion de chaine de caractere
 définissant le numero.les nbr correspondent à la distance à
laquelle on veut scanner.
0019 nb=evstr(numero) // conversion de la chaine en nombre
0020 endfunction
0021
0022 //fonction permettant de récupérer le nom de fichier précédant
le numéro
0023 function nomf=recuperationnb(Nom_Fichier)
0024
0025 avantb=strindex(Nom_Fichier, '/');//position dans le nom de
fichier de "/"
0026 avantb=avantb(1,$);
0027 apresb=strindex(Nom_Fichier, '.');// position du point
0028 nomf=part(Nom_Fichier,[avantb+1:1:apresb]);//récupération de la
portion de chaine de caractere

```

```

    definissant le numero.les nbr correspondent à la distance à
    laquelle on veut scanner.
0029
0030 endfunction
0031
0032 //fonction permettant de remplacer les virgules par des points
    dans un fichier de données
0033
0034 function spt=adapte_nom(NomEntree)
0035
0036 spt=strsubst(NomEntree,',','.');// recherche dans la chaine de
    caractère NomEntree , la VIRGULE
    et la remplace par un POINT.
0037
0038 endfunction
0039 //
0040
    //////////////////////////////////////
    //////////////////////////////////////
0041
0042 //chemin du dossier contenant les fichiers à traiter
0043
0044
chemin=uigetdir('/Users/simonclevers/CloudStation/these/SHG/resultat
s/Analyses/
MesureMSA',[,'Choisissez le dossier à traiter'])+'//';
0045
0046 mchemin= lex_sort(ls(chemin + '*.lvm')) //génère une matrice des
chemins des fichiers textes contenus
    dans le dossier
0047 mkdir(chemin+'scilab'); //creation d'un repertoire scilab
0048 cd (chemin+'scilab/')// on se place dans ce repertoire
0049
0050 mshg=[];//initialisation de la matrice
0051 nbff=[];//initialisation de la matrice
0052 nomff=[]//initialisation de la matrice
0053 a=[];
0054 b=0;//variable permettant l'ecriture dans fichierr
0055 erreurfichier=0;
0056
0057 //boucle while = permet de remanier la matrice mchemin et de
    supprimer les noms de fichiers non
    conformes- fonction désactivée
0058
0059
0060
0061
0062
0063
0064
0065
//while strindex(mchemin(i),'-') == a then
//b=b+1
//fichierr(b)=mchemin(i)
//mchemin(i)= []

```

```

//erreurfichier=1
0066 //end
0067
0068
0069 t=size(mchemin); //renvoi la taille de la matrice mchemin, le
nombre de ligne correspond au nombre de
fichiers texte.
0070
0071 //dans la boucle for nous allons donc de 1 au nombre de fichier
total, cette boucle ouvre chaque
fichier texte, appelle les fonctions necessaires à leur traitement
0072
0073 for i=1:t(1,1)
0074
0075 sp = mopen(mchemin(i), 'r'); //ouverture en mode lecture du
fichier (le fichier original ne sera
aucunement modifié)
0076
0077 s1=mgetl(sp); //affectation
0078
0079 mclose (sp); //fermeture du fichier
0080
0081 slpt=adapte_nom(s1); //remplacer virgule par point par la
fonction adapte_nom, slpt est donc le
fichier de point transformé
0082
0083 //disp (slpt)//affiche la matrice transformée (désactivé pour
gain de tps)
0084
0085 //jusqu'ici scilab traitait des chaines de caractères que nous
allons transformer en chaines
numériques

. 0086 nslpt=evstr(slpt); //convertie la matrice en fichier de
points numériques
.
. 0087 //disp(nslpt) // affiche cette nouvelle matrice (désactivé
pour gain de tps)
.
. 0088 //disp(size(nslpt), "la taille de la matrice est :")//
controle de la taille de la matrice valeur
.
attendue : 1024 2 (désactivé pour gain de tps)
0089
0090
0091
0092 nb=recuperation(mchemin(i)); //récupération du numéro du fichier
dans la matrice
0093
0094
0095
0096 //Calcul de l'intensité SHG
0097
////////////////////////////////////
//
0098

```

```

0099 ibase=ns1pt(380,2); //intensité de la ligne de base est prise à
530,6nm
0100
. 0101 //disp(ibase, 'Intensité ligne de base :')
.
. 0102 fenetre=ns1pt(398:400,:) //la fenetre choisie pour le calcul
de l'intensité est comprise entre
.
531,88 et 532,08nm

0115
0116
0117 //disp(nb)
0118
////////////////////////////////////
//
0119 //concaténation des resulats pour chaque valeur de i
. 0120 mshg=cat(1,mshg,ishg); //mshg sera la matrice finale
contenant les intensités SHG
.
. 0121 nbf =cat(1,nbf,nb); //nbf sera la matrice finale contenant les
numero de fichier
.
0122
0123
////////////////////////////////////
//
0124 //plot des graphiques&exportation fichier
0125
0126
. 0127 f=scf(nb); //cree une nouvelle fenetre (n°du fichier)
.
. 0128 //h=gca(nb)
.
. 0129 //définition des légendes des axes
.
. 0130 xtitle('SHG Spectrum', ['wavelenght (nm)'], ['SHG Intensity
(cps)'])
.
0131
. 0132 plot(ns1pt(:,1),ns1pt(:,2)) //nouvelle figure dans la fenetre
courante
.
. 0133          posity=max(ns1pt(:,2))-(max(ns1pt(:,2))-
min(ns1pt(:,2)))*0.2 //position du texte en y
.
. 0134 posity2=max(ns1pt(:,2))-(max(ns1pt(:,2))-min(ns1pt(:,2)))*0.1
.
. 0135 positx=500; //position du texte en x
.
. 0136 xstring(positx, posity, 'ISHG='+string(ishg)+'cps') //écriture
du texte dans le graph
.
0137

```

```

0138 nomf=recuperationb(mchemin(i))//recupération du nom de fichier
0139
. 0140 xstring(positx,posit2,nomf)
.
. 0141 nchemin=chemin+'scilab/figure'+string(nb)+'.png'
.
. 0142 xs2png(f,nchemin)//écriture du graphique f au format png dans
      nchemin
.
. 0143 close;
.
. 0144 clf();
.
. 0145 //disp(nb,i)
.
. 0146 nomff=cat(1,nomff,nomf);
.
0147 end
0148
0149 // matrice finale contenant en 1ere colonne le numéro ou le nom
de fichier et en seconde l'intensité
shg

. 0150 //final=[nbf,mshg] //version numero/intensité
.
. 0151 //

. 0152 nmshg=string(mshg);
.
--
0153 final=[nomff+
0154
0155
0156
; '+nmshg]; //version nom de fichier/intensité
0157
0158 //disp(mchemin)
0159 //disp(nb)
0160 //disp(size(mchemin(:,1)))
0161 disp(final) // affiche la matrice finale
0162
0163 if 1 == erreurfichier then
0164 disp('nom de fichier non conforme (pas de tiret)='+fichier)
0165 end
0166
0167 verif=ls(chemin+'scilab/'+'*txt')
0168 tverif=size(verif);
0169 if verif==[] then write('resultat.txt', final);//enregistre le
fichier de résultats contenant la
matrice 'final'
0170 //fprintfMat(chemin+'scilab/'+ 'resultat.txt',
final);//enregistre le fichier de résultats contenant
la matrice 'final'
0171 else i=tverif(1,1)+1;
0172

```

```

. 0173 write('resultat'+string(i)+'.txt', final);
.
. 0174 disp('le dossier contient déjà un fichier nommé
résultat'+string(tverif(1,1))+'.txt, création
.
d'un nouveau fichier : resultat'+string(i)+'.txt' );
0175
0176 end
0177
0178 //resultat=mopen(chemin+'scilab/'+ 'resultat.txt');
0179 //resultat2=mgetl(resultat);
0180 //mclose (resultat); //fermeture du fichier
0181
0182 //resultat2=adapte_nom(resultat2);//remplacer virgule par point

```

I.1 Laser control and SHG monitoring

The following program was developed in graphical programming language: Labview®.

The first image (Figure.A. III-1) represents the graphical user interface then the code is given (. The program communicates with the laser and the spectrometer. It is possible to fully control the laser: intensity, on/off, time of irradiation, and time between two measurements. In parallel, the SHG spectrum is automatically recorded and saves on the computer.

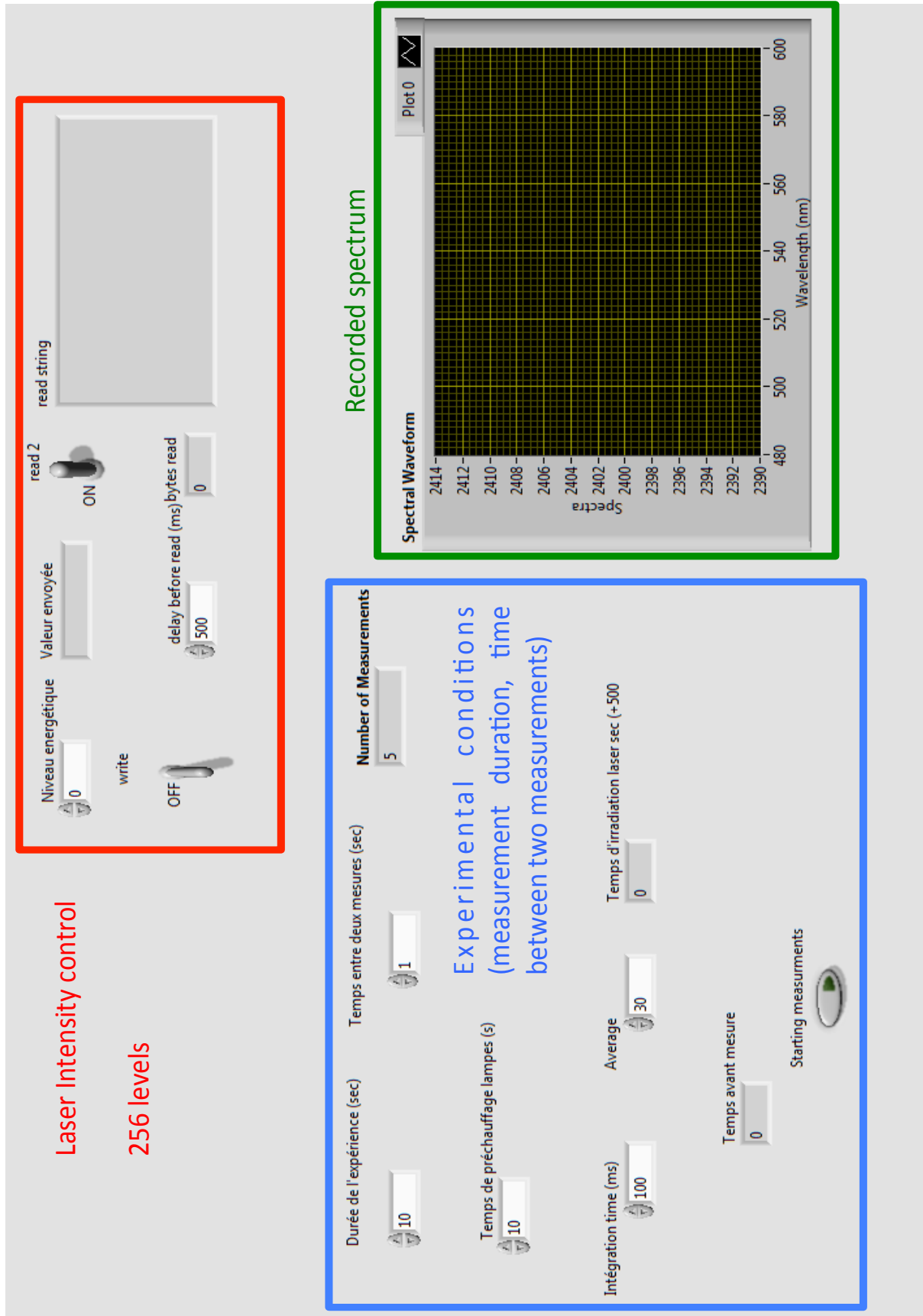


Figure.A. III-1 Graphical user interface of the software

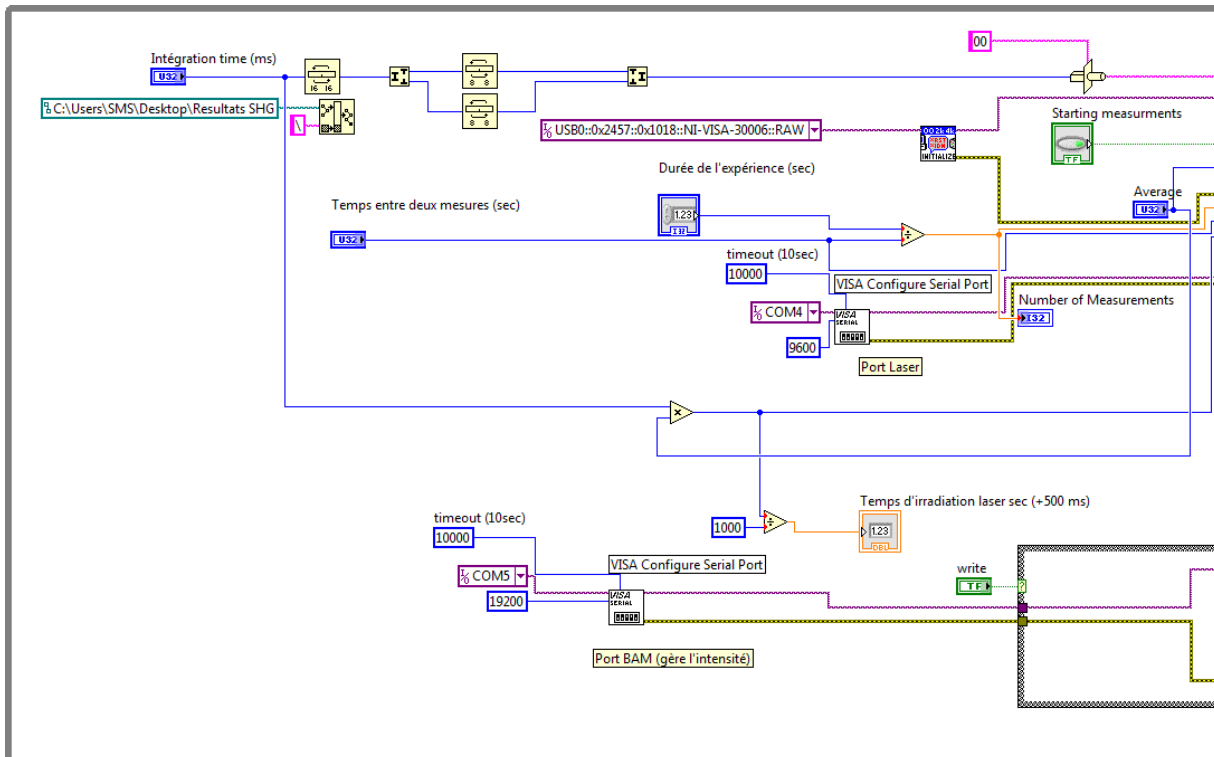


Figure.A. III-2 Programming code to set serial communication ports for laser, laser intensity controller and spectrometer

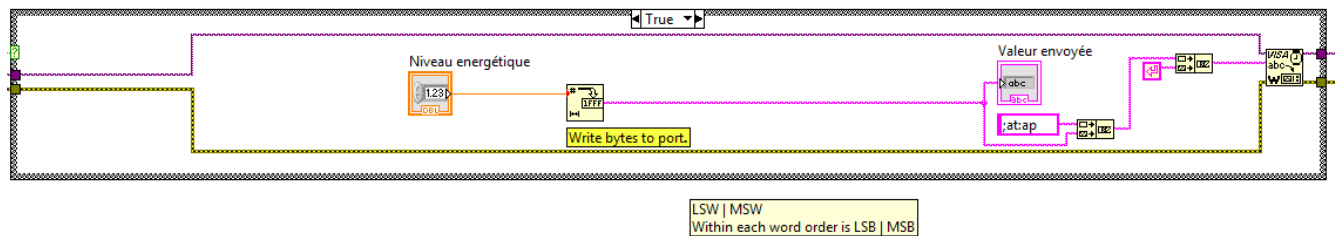


Figure.A. III-3 Part of code to control the laser intensity. A hexadecimal code is sending to laser intensity controller (corresponding to a energetic level comprises between 0 and 255). The user enters a number between 0 and 255.

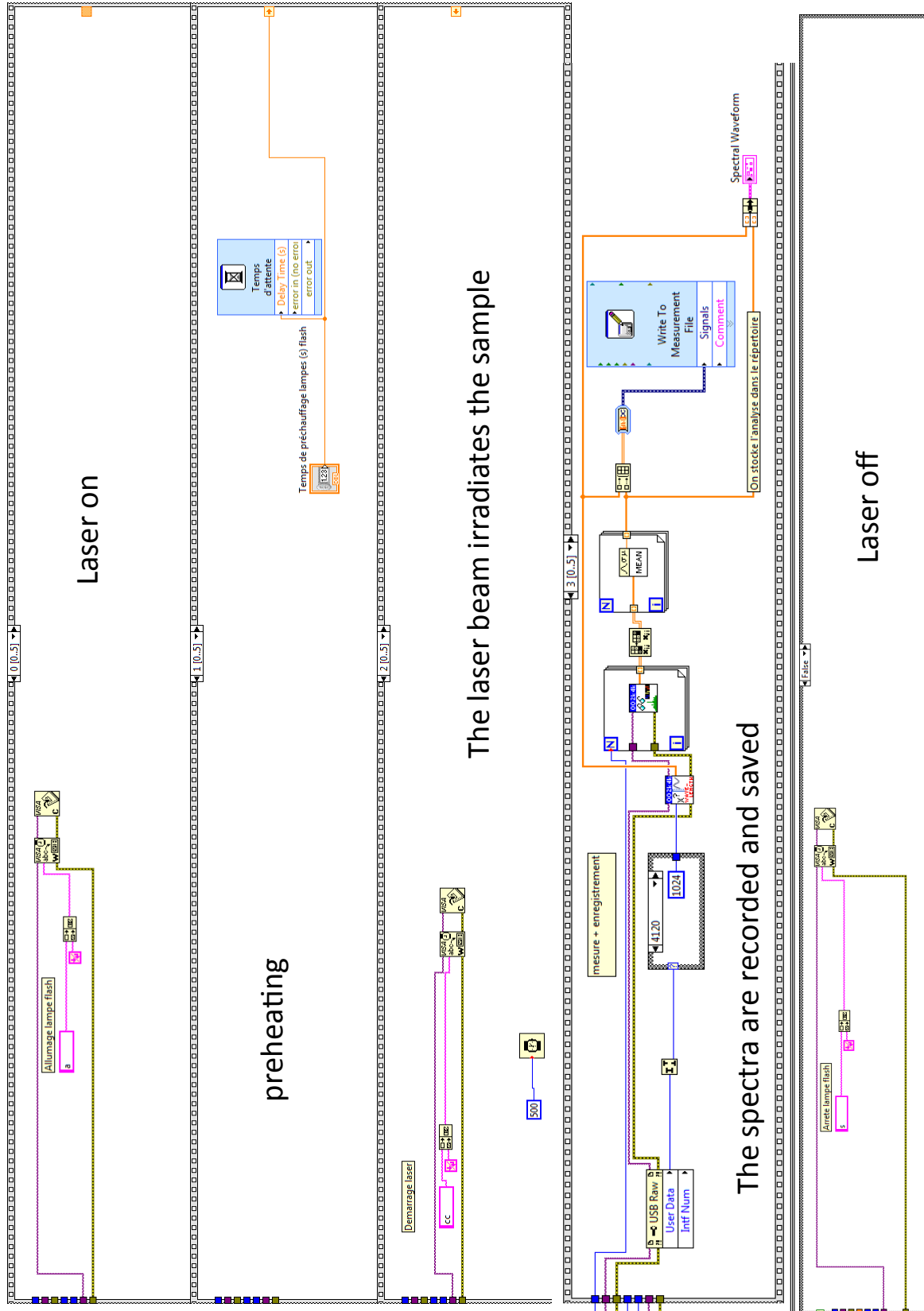


Figure.A. III-4 Sequence to start the laser and record a SHG spectrum every x minutes

Appendix IV Additional Considerations on X-ray Diffraction

Theory of X-ray Diffraction

Superimposition and Interference between Electromagnetic Waves

Let us consider a single electromagnetic wave spreading from a given point in space that we consider as the origin O. At O, the electric field $E_0 \cos 2\pi\nu t$ at $t=0$ is equals to E_0 since the phase is 0. Let us consider that the wave has travelled through the medium (progressive wave) with a velocity of c to a radial distance R from the source and that this distance is sufficiently large to approximate the wave front as a planar. The phase of the wave at time t is the same as that emitted at time $t-R/c$ and is therefore $2\pi\nu \left(t - \frac{R}{c}\right) = 2\pi \left(\nu t - \frac{R}{\lambda}\right)$ where λ is the wavelength of the electromagnetic wave.

Let us consider two waves E_1 and E_2 , with the same frequency and same origin but with different phases induced by two different phase shifts δ_1 and δ_2 with reference to a δ_0 of 0 (no dimensionality assumed here). The superimposition of these two waves gives a third wave, whose field E is given by:

$$E_1 \cos 2\pi(\nu t + \delta_1) + E_2 \cos 2\pi(\nu t + \delta_2) = E \cos 2\pi(\nu t + \delta)$$

Or in complex exponential notation:

$$\begin{aligned} E_1 \cos 2\pi(\nu t + \delta_1) + E_2 \cos 2\pi(\nu t + \delta_2) &= E_1 e^{2\pi i(\nu t - \delta_1)} + E_2 e^{2\pi i(\nu t - \delta_2)} \\ &= [E_1 e^{2\pi i\delta_1} + E_2 e^{2\pi i\delta_2}] \cdot e^{2\pi i\nu t} \end{aligned}$$

where $e^{2\pi i\nu t}$ is the phase shift in complex form of the resultant wave.

The intensity of a wave resulting from two other waves is the square of E but is modulated by the phase shift between the parent waves.

Electromagnetic waves scattered (see Chapter 1) at different points in space by electrons can interact with each other and give rise to either destructive or constructive interferences, depending on the differences between the path lengths and phase shifts of the waves. Let us consider a volume $d\vec{r}$ containing $\rho(\vec{r})d\vec{r}$ electrons at a distance \vec{r} from an arbitrary chosen origin, irradiated by a electromagnetic wave with a wavelength of λ . Consider the direction of propagation of the scattered and incident waves \vec{s} and \vec{s}_0 , respectively. The field of the wave scattered at \vec{r} is then of:

$$\rho(\vec{r})e^{2\pi i\vec{r}\left(\frac{\vec{s}-\vec{s}_0}{\lambda}\right)}d\vec{r} = \rho(\vec{r})e^{2\pi i\vec{r}\vec{R}}d\vec{r} \text{ with } \vec{R} = \left(\frac{\vec{s}-\vec{s}_0}{\lambda}\right)$$

Where \vec{R} is the scattering vector. It is possible to show that:

$$\vec{R} = \frac{2 \sin \theta}{\lambda}$$

where θ is the scattering angle. If λ is about the same order of magnitude than the distances between scattering points, then interferences occur at measurable scattering angles θ .

The complex amplitude corresponding to the superimposition of all the waves scattered at \vec{r} can be obtained by integration:

$$F(\vec{R}) = \int \rho(\vec{r}) e^{2\pi i \vec{r} \cdot \vec{R}} d\vec{r} \quad (\text{Eq AIV-a})$$

The complex quantity $F(\vec{R})$ is the structure factor of the volume $d\vec{r}$. The intensity of scattering $I(\vec{R})$ along \vec{R} is given by $F(\vec{R}) \cdot F^*(\vec{R})$ and is experimentally measurable. By contrast, the phase associated with $F(\vec{R})$ is not an observable quantity (this is the so called “phase” problem). Additionally, if $\rho(\vec{r}) = \rho(-\vec{r})$, (*i.e.* if the distribution is centrosymmetric) then $F(\vec{R})$ is real (but an ambiguity on its sign remains).

Fourier Transform

$$F(\vec{R}) = \int \rho(\vec{r}) e^{2\pi i \vec{r} \cdot \vec{R}} d\vec{r} \quad (\text{Eq AIV-b})$$

is an example of a Fourier transformation. The structure factor $F(\vec{R})$ is the Fourier transform of the scattering density $\rho(\vec{r})$. The relationship between $F(\vec{R})$ and $\rho(\vec{r})$ is remarkable and is reciprocal:

$$\rho(\vec{r}) = \int F(\vec{R}) e^{-2\pi i \vec{r} \cdot \vec{R}} d\vec{R}$$

Scattering by a Point Atoms, by an Assemblage of Point Atoms, by a Periodic Array

In the previous case (*i.e.*, volume $d\vec{r}$ containing $\rho(\vec{r})d\vec{r}$ electrons), the distribution of $\rho(\vec{r})$ in space is given by the Gaussian distribution:

$$\rho(\vec{r}) = \frac{x}{\sqrt{\pi}} \lim_{x \rightarrow \infty} e^{-x^2 r^2}$$

Consider a point atom with atomic number c , the distribution of $\rho(\vec{r})$ is given by the limiting case of the Gaussian distribution, the Dirac function:

$$\rho(\vec{r}) = 0 \text{ except when } \vec{r} = 0, \text{ where } \rho(\vec{r}) = c$$

$$\text{then } \int \rho(\vec{r}) d\vec{r} = c$$

If the point atom is located at vector distance \vec{r}' from O, then its structure factor is written:

$$\begin{aligned} F(\vec{R}) &= \int \rho(\vec{r} - \vec{r}') e^{2\pi i \vec{r} \cdot \vec{R}} d\vec{r} \\ &= c e^{2\pi i \vec{r}' \cdot \vec{R}} \quad (\text{Eq AIV-b}) \end{aligned}$$

If the point atom is located at O, then $F(\vec{R}) = c$, the amount of scattered beams does not depends on the scattering angle as far as the “concept” of point atom is concerned.

Let us consider an assemblage of i point atoms at distances $\vec{r}_1, \vec{r}_2, \dots, \vec{r}_i$ from O, then:

$$F(\vec{R}) = \sum c_i e^{2\pi i \vec{R} \cdot \vec{r}_i} \quad (\text{Eq AIV-c})$$

Let us define a lattice of point atoms defined by the translation $\vec{r}(u,v,w) = u \cdot \vec{a} + v \cdot \vec{b} + w \cdot \vec{c}$ where

u, v, w are integers). Be $\vec{a}^*, \vec{b}^*, \vec{c}^*$, the corresponding reciprocal vectors defining the reciprocal lattice characterized by the translation $\vec{R}(h,k,l) = h \cdot \vec{a}^* + k \cdot \vec{b}^* + l \cdot \vec{c}^*$. The structure factor of the lattice of point atoms is thus given by:

$$F(\vec{R}) = c \sum e^{2\pi i (uh + vk + wl)} \quad (\text{Eq AIV-d})$$

Point atoms have no physical significance since scattering electrons cannot be concentrated at a point. Let us now consider true atoms.

Scattering by an Assemblage of Atoms

Let us consider a single molecule made of i atoms located at distances $\vec{r}_1, \vec{r}_2, \dots, \vec{r}_i$ from the arbitrary chosen origin. Then, it can be written:

$$F(\vec{R}) = \sum_i f_i(\vec{r}) e^{2\pi i \vec{R} \vec{r}_i} \quad (\text{Eq AIV-e})$$

$$\text{where } f_i(\vec{r}) = \int \rho_i(\vec{r}) e^{2\pi i \vec{r} \vec{R}} d\vec{r} \quad (\text{Eq AIV-f})$$

$f_i(\vec{r})$ is thus the Fourier transform of the electronic distribution of the i^{th} atom and represents the scattering power of the considered atom. It depends on the scattering angle.

Consider a monoatomic crystal lattice constructed on the lattice translation $\vec{r}(u,v,w) = u.\vec{a} + v.\vec{b} + w.\vec{c}$ (where u,v,w are integers), then one would write:

$$F(\vec{R}) = \sum f(\vec{r}) e^{2\pi i (uh+vk+wl)} \quad (\text{Eq AIV-g})$$

In actual crystal structures however, atoms are not at rest and vibrates because of thermal motions. Structure factors must be modulated by the Debye-Waller temperature factor.

$$F(\vec{R}) = F^0(\vec{R}) e^{\left(\frac{-B_{\text{iso}} \sin^2 \theta}{\lambda^2}\right)} \quad (\text{Eq AIV-h})$$

where B_{iso} is the quadratic average amplitude of thermal vibration. In the isotropic model, B_{iso} is a scalar value. In the anisotropic model, B_{iso} is vectorial.

Extinction Conditions

The space group (SG) determination of a crystal structure is an important part of structural resolution. The procedure, nowadays automatized, consists in indexation of the diffraction pattern, *i.e.* assignation of integer values to h, k and l to each spot detected in the reciprocal lattice. The extinction conditions refers to the condition where h, k and l result in $F(\vec{R}) = 0$ and are directly related to the Bravais mode and to the symmetry elements (screw axes and glide planes) present in the crystal structure. The list of extinction conditions associated to a specific diffraction experiment allows one to determine the SG of the crystal structure.

Appendix. V Basic Notions of Thermodynamics

Definitions

Thermodynamics is the science of the macroscopic manifestations of the very large number of atoms constituting “systems”. A system consists of a quantity of matter separated from its surrounding by boundaries. These boundaries may be fixed or movable, imaginary or real. According to the properties of these boundaries, several types of systems can be identified:

- An open system can exchange both matter and energy with surrounding.
- A closed system can only exchange energy with surrounding.
- An isolated system exchange neither energy nor matter with surrounding.
- An adiabatic system cannot exchange heat with surrounding.

In this contribution, it is approximated that most systems are closed since they consist of condensed matter (crystalline solids, liquid systems, glasses...). However, the systems should be considered as open in case of sublimation or evaporation.

The convenience and wide applicability in many scientific fields of the thermodynamic formalism rely on the use of state variables. Most of these state variables are quantities relative to the system that are measurable at the macroscopic scale (*e.g.* pressure P, volume V, temperature T, quantity of matter n). If a system transforms from an initial to a final state, a specific type of variables should be considered that does not depend on the path followed by the transformation: these are called the state functions. State functions that are proportional to the system size are extensive (*e.g.* V, n). State functions that are not proportional to system size are intensive (*e.g.* P,T).

A phase³² is a portion of a system that presents homogeneous properties (*e.g.* density, refractive index, polarizability or symmetry in case of crystallized solids) and chemical compositions. The interfaces of a phase are related to a discontinuity in at least one of its intensive variables. Thus, a system consisting of several phases is a heterogeneous system. It should be noted however that each phase could be considered as an open sub-system.

The First and Second Laws of Thermodynamic and the Gibbs Free Energy

Let us consider a closed system consisting of a single phase made of a single constituent *a* (*i.e.* $\mu_a dn_a = 0$). The internal energy U of this system is a state function referring to the sum of the potential and kinetic energies related to each molecule present in the phase. It is therefore an extensive variable.

During transformation from a state U_1 to a state U_2 , the system can exchange energy with surrounding either as heat Q or as work W (which are not state functions), but cannot lead to a change in the energy of the universe (*i.e.* system + surrounding): the energy of the universe is constant, this is the first principle of thermodynamic. In differential form:³³

³² J. E. Ricci, *The Phase Rule and Heterogeneous Equilibrium*, (Dover Publications, 1966).

³³ Note: By convention, an infinitesimal variation of a state function is noted with “d”. For state variables that do not depend on the path followed by the transformation, the differential is noted with “d”.

$$dU = \delta Q + \delta W \quad (\text{Eq AV-a})^{34}$$

Let us consider that the work exchanged during the transformation is only mechanical, then Eq AV-a becomes:

$$dU = \delta Q - PdV \quad (\text{Eq AV-b})$$

The second law of thermodynamic introduces the notion of entropy S that can be roughly defined as the degree of “disorder” of the system. It states that the entropy of the universe can only increase upon transformations. In particular, if a system reversely exchange heat with surrounding, the entropy variation of the system must increase, as expressed in the Clausius inequality:

$$dS_{\text{system}} \geq \frac{\delta Q_{\text{rev}}}{T} \quad (\text{Eq AV-c})^{35}$$

Then, Eq AV-b becomes:

$$dU = TdS - PdV \quad (\text{Eq AV-d})$$

The system is considered at equilibrium when $dU=0$, U is therefore called a thermodynamic potential associated to S and V.³⁶ Since entropy cannot be measured experimentally, Legendre transforms are employed here to create other thermodynamic potentials associated to convenient natural state variables (P or T, instead of S). The following functions are relevant for this contribution:

$$H = U + PV \quad (\text{Eq AV-e})$$

$$G = H - TS \quad (\text{Eq AV-f})$$

H is the enthalpy and G is the Gibbs free energy of the system. Development of Eq AV-e and AV-f lead to:

$$dH = TdS + VdP \quad (\text{Eq AV-g})$$

$$dG = -SdT + VdP \quad (\text{Eq AV-h})$$

G and H are therefore thermodynamic potentials associated to P and T and to S and P respectively. Then, concerning dG, it comes:

$$dG = \left(\frac{\partial G}{\partial T}\right)_P dT + \left(\frac{\partial G}{\partial P}\right)_T dP \quad (\text{Eq AV-i})$$

so that:

$$S = -\left(\frac{\partial G}{\partial T}\right)_P \quad (\text{Eq AV-j})$$

Which shows that entropy is actually a first derivative of the Gibbs free energy. By a similar procedure, the Gibbs-Helmholtz equation highlights that enthalpy is also a first derivative of G:

$$H = -T^2 \left(\frac{\partial \left(\frac{G}{T}\right)}{\partial T}\right)_P \quad (\text{Eq AV-k})$$

³⁴ P Atkins, *Four Laws That Drive the Universe*, (Oxford: Oxford University Press, 2007).

³⁵ P Atkins, *The 2nd Law: Energy, Chaos, and Form*, ed. W H Freeman, 2nd ed., (Scientific American Library Paperback, 1994).

³⁶ H.A.J. Oonk, *Phase Theory*, (Amsterdam - Oxford - New York: Elsevier Scientific Publishing Company, 1981); David A Porter and Kenneth E Easterling, *Phase Transformations in Metals and Alloys, Third Edition (Revised Reprint)*, (CRC Press, 1992).

In material sciences, heat capacity (C_p) measurements at constant P are used to derive G , H and S . Since:

$$C_p = \left(\frac{\partial H}{\partial T} \right)_P = T \left(\frac{\partial S}{\partial T} \right)_P \quad (\text{Eq AV-l})$$

it comes:

$$C_p = -T \left(\frac{\partial^2 G}{\partial T^2} \right)_P \quad (\text{Eq AV-m})$$

Hence, C_p is a second derivative of the Gibbs free energy.³⁷

The Equilibrium Condition

In case of a monophasic open system made of N constituents (*e.g.* an open-subsystem of a closed system), Eq AV-h becomes:

$$dG = -SdT + VdP + \sum_{i=1}^N \mu_i dn_i \quad (\text{Eq AV-n})$$

to account for outflow or inflow of matter, where μ_i is the chemical potential of constituent i and n_i is the number of mole of i .

Moreover it possible to show that the Gibbs free energy of such system is equals to the sum of the molar partial Gibbs free energies of the system, namely the chemical potentials:

$$G = \sum_{i=1}^N \mu_i n_i \quad (\text{Eq AV-o})$$

The total differential of Eq AV-o is:

$$dG = \sum_{i=1}^N \mu_i dn_i + \sum_{i=1}^N n_i d\mu_i \quad (\text{Eq AV-p})$$

Combining Eq AV-p and AV-n leads to:

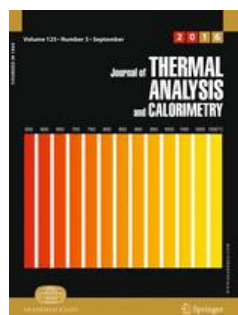
$$-SdT + VdP = \sum_{i=1}^N n_i d\mu_i \quad (\text{Eq AV-q})$$

Equation AV-q is known as the Gibbs-Duhem relation. It is the equilibrium condition ($dG=0$) and gives a relation between intensive properties of the system.

³⁷ H E Stanley, *Introduction to Phase Transitions and Critical Phenomena*, (Oxford: Clarendon Press, 1971).

Appendix. VI Valorisations scientifiques

The following papers are directly related to this PhD thesis and are available upon request.



Temperature resolved second harmonic generation to probe the structural purity of *m*-hydroxybenzoic acid

Volume 112, Issue 1, pp 271–277, April 2013

S. Clevers, F. Simon, V. Dupray, G. Coquerel

doi:[10.1007/s10973-012-2763-y](https://doi.org/10.1007/s10973-012-2763-y)

Keywords : Hydroxybenzoic acid; Monotropy; Phase transition; Polymorphism; Second harmonic generation; Structural impurity

Abstract

We report the use of second harmonic generation (SHG) and temperature resolved second harmonic generation (TR-SHG) for *in-situ* probing and monitoring the structural purification of *m*-hydroxybenzoic acid (MHBA). Pure and mixtures of the two polymorphic forms of MHBA (metastable $Pna2_1$ and stable $P2_1/c$) and commercial MHBA were analysed by: DSC, XRPD and SHG. Results obtained with these three techniques are compared and demonstrate for that particular component, the high sensitivity and accuracy of SHG in assessing the polymorphic purity of MHBA. The SHG detection threshold for the metastable polymorph is circa 2 ppm and is several orders of magnitude better than the sensitivity of XRPD (1 wt%) and DSC (only 17 wt%). The proportion of the metastable phase in the commercial MHBA was evaluated to 1 wt% by SHG. Results of TR-SHG measurements performed on commercial MHBA at 5 K min⁻¹ heating rate show that TR-SHG is a good technique for an *in situ* monitoring of the structural purity. The present study clearly demonstrates that SHG and TR-SHG are relevant and accurate techniques for probing the structural purity and for the monitoring of solid–solid phase transitions provided one of the two varieties crystallizes in a non-centrosymmetric space group.

Relevance of the Second Harmonic Generation to Characterize Crystalline Samples

Volume 38, Issue 6, Pages 971–983, June, 2015

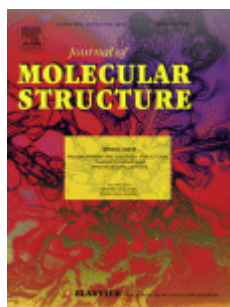
F. Simon, S. Clevers, V. Dupray, G. Coquerel

DOI: [10.1002/ceat.201400756](https://doi.org/10.1002/ceat.201400756)

Keywords : Crystallization; Phase equilibrium; Polymorphism; Purification; Second harmonic generation

Abstract

The application of powder second harmonic generation (P-SHG), temperature-resolved SHG (TR-SHG), and SHG microscopy (SHGM) in the characterization of bulk crystalline samples is illustrated. P-SHG applied to powder samples can be an extremely sensitive approach to detect the absence of an inversion center in crystalline structures, TR-SHG serves to monitor temperature-induced phase transitions, and SHGM is used in the detection of non-centrosymmetric zones inside a heterogeneous material. These methods are of great relevance, e.g., in the pharmaceutical industry where crystalline active pharmaceutical ingredients are often made of a single enantiomer and are therefore non-centrosymmetric. Herein, several examples are provided to describe how a given SHG signal should be interpreted. A general procedure to carry out a P-SHG experiment is illustrated in detail.



Detection of order–disorder transition in organic solids by using temperature resolved second harmonic generation (TR-SHG)

Volume 1078, Pages 61–67, 25 December 2014,

S. Clevers, C. Rougeot, F. Simon, M. Sanselme, V. Dupray, G. Coquerel

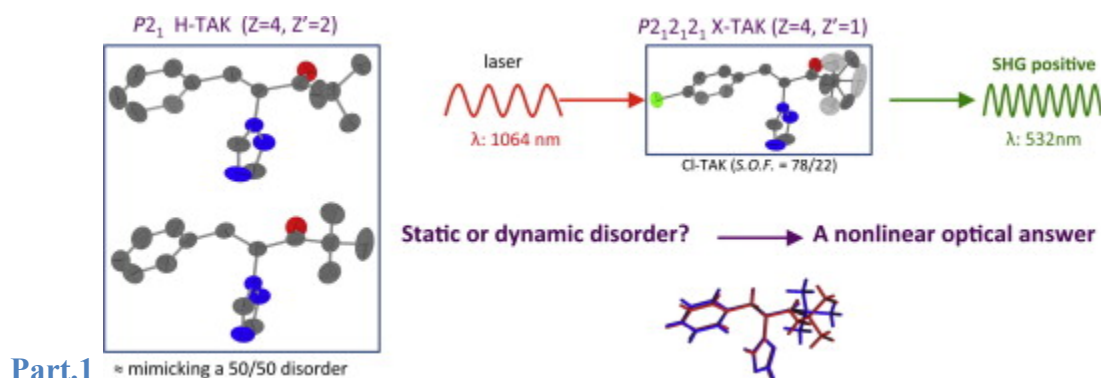
[doi:10.1016/j.molstruc.2014.04.007](https://doi.org/10.1016/j.molstruc.2014.04.007)

Keywords : Dynamic disorder; Temperature resolved second harmonic generation; Order disorder transition

Highlights

- The crystallographic studies of a series of triazol ketones reveal a disorder of the *tert*-butyl group.
- TR-SHG confirms the nature of the disorder as a dynamic disorder.
- TR-SHG detects the freezing temperature of the *tert*-butyl motion at circa $-30\text{ }^{\circ}\text{C}$.
- The lack of hysteresis effect in the TR-SHG results confirms the second-order like transition.

Abstract



We show the detection of an order–disorder like transition by temperature-resolved second harmonic generation (TR-SHG) in a series of triazolyl ketone (X-TAK derivatives). These compounds have the particularity to exhibit a disorder on the *tert*-butyl (*t*-Bu) group that was highlighted by single crystal X-Ray diffraction (SC-XRD). TR-SHG confirms the nature of this disorder as a dynamic disorder and allows to determine the freezing temperature of the *t*-Bu motion.

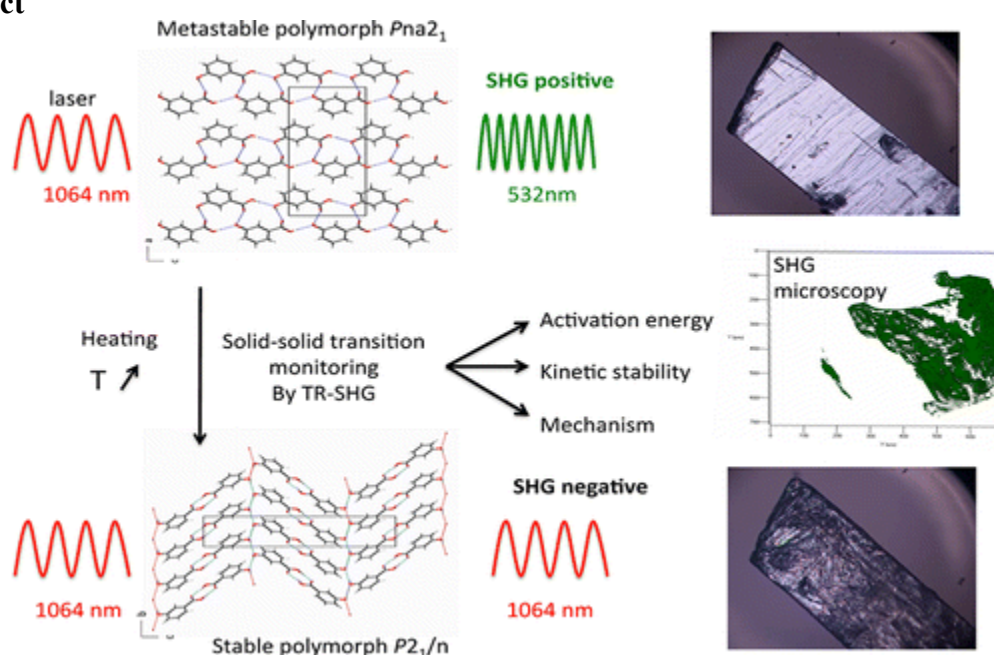
Monotropic Transition Mechanism of *m*-hydroxybenzoic Acid Investigated by Temperature-Resolved Second Harmonic Generation

Volume 13 (8), pp 3697–3704., 2013

[Simon Clevers](#), [Florent Simon](#), [Morgane Sanselme](#), [Valerie Dupray*](#), and [Gerard Coquerel](#)

DOI: [10.1021/cg400712s](https://doi.org/10.1021/cg400712s)

Abstract



Temperature-resolved second harmonic generation (TR-SHG) and SHG microscopy were used to study under normal pressure the solid–solid transition mechanism occurring between the two monotropically related polymorphic forms (metastable $Pna2_1$ and stable $P2_1/n$) of 3-hydroxybenzoic acid (MHBA). The activation energy E_a (as a measure of the barrier energy) of the irreversible transition was determined via isothermal TR-SHG ($137\text{--}144\text{ kJ}\cdot\text{mol}^{-1}$). It fits well with that determined from differential scanning calorimetry ($139\text{ kJ}\cdot\text{mol}^{-1}$). Regarding the two crystal structures, optical microscopy observations, and kinetics parameters from TR-SHG, a destructive/reconstructive mechanism is proposed for the solid–solid transition. The present study clearly demonstrates that TR-SHG is a relevant and accurate technique for monitoring solid–solid phase transitions.

As co-author:

- "Influence of the Cation Size on the Second Harmonic Generation Response of Chiral $A(\text{VO}_2)_2(\text{PO}_4) \cdot 3\text{H}_2\text{O}$ ($A = \text{K}^+, \text{NH}_4^+$ and Rb^+), R. Gautier, S. Auguste, S. Clevers, Valerie Dupray, G. Coquerel and E. Le Fur, *CristEngComm* 2014, Just accepted, In Proof

- "Racemic and Enantiopure Unsymmetric Diiron(III) Complex with a Chiral o-Carborane-based Pyridylalcohol Ligand: Combined Chiroptical, Magnetic and Non Linear Optical Properties" F.D.Salvo, M.Y. Tsang, F. Teixidor, C. Viñas, J.G. Planas, J. Crassous, N. Vanthuyne, N. Aliaga-Alcalde, E. Ruiz, G. Coquerel, S. Clevers, V. Dupray, D. Choquesillo-Lazarte, M.E. Light, M.B. Hursthouse. *Chemistry European Journal*, 2013 accepted. Impact factor 2012: 5.831

Oral communications:

- CGOM11 (Nara, Japan, June 2014): "*Temperature resolved second harmonic generation (TR-SHG) to investigate desolvation processes among organic solvates*" S. Clevers, V. Dupray, G. Coquerel.

- BIWIC 2013 (Odense, Denmark): "*Detection of order-disorder transition in organic solids by using Temperature Resolved Second Harmonic Generation (TR-SHG)*", September 2013. S. Clevers, C. Rougeot, F. Simon, M. Sanselme, V. Dupray, G. Coquerel.

- JEEP 2013 (Nancy, France) : "*Temperature-resolved second harmonic generation: a tool designed to study solid-solid transition,*" MATEC Web of Conferences, vol. 3, p. 01019, Jul. 2013. S. Clevers, F. Simon, V. Dupray, and G. Coquerel.

Poster communication:

- CGOM11 (Nara, Japan, 2014): « *Order-Disorder transitions: investigations in a series of triazole ketones* », S. Clevers, C. Rougeot, F. Simon, M. Sanselme, V. Dupray, G. Coquerel. (poster price)

- JCAT45 (Rouen, France, 2014) « *Phase Diagram Determination by Means of Temperature Resolved Second Harmonic Generation* », Simon CLEVERS, Florent SIMON, Nicolas Couvrat, Valerie Dupray, Gerard Coquerel (poster price)

- JEEP 2014 (Lyon, France): « *in situ monitoring of fast crystallization by means of x-ray diffraction* », March 2014, Simon Clevers, Virginie Nachbaur, Morgane Sanselme, Valérie Dupray, Gérard Coquerel, Jean-Marie Le Breton.

- JEEP 2012 (Rouen, France): "*Is second harmonic generation a reliable tool for studying solid-solid phase transitions?*" March 2012. S. Clevers, V. Dupray, F. Simon and G. Coquerel. (poster price)

